

# Micromechanical modelling of self-healing cementitious materials

Doctor of Philosophy Thesis

Robert Elfed Davies

School of Engineering, Cardiff University

2014



For Jenny and Evan  
Thank you for your love and support



## Summary

A self-healing cementitious material could provide a step change in the design of concrete structures. There is a need to understand better the healing processes, to predict accurately experimental behaviour and to determine the impact on mechanical properties. Micromechanical modelling, with a two-phase Eshelby inclusion solution, is chosen as a suitable framework within which to explore self-healing. The impact of micro-cracking and other time-dependent phenomena are considered alongside self-healing experiments and the numerical mechanical strength response.

A new approach describes simulating inelastic behaviour in the matrix component of a two-phase composite material. Quasi-isotropic distributed micro-cracking, accompanying volumetric matrix changes, is combined with anisotropic micro-cracking arising from directional loading. Non-dilute inclusions are homogenised and an exterior point Eshelby solution is used to obtain stress concentrations adjacent to inclusions. The accuracy of these solutions is assessed using a series of three dimensional finite element analyses and a set of stress/strain paths illustrate the model's characteristics. The problem of autogenous shrinkage in a cementitious composite is applied using a volumetric solidification and hydration model, which quantifies the effects of micro-cracking. Experiments on early age concrete and mortar beams showed that autogenous healing is primarily due to continued hydration. A novel self-healing model focuses on mechanical strength recovery of micro-cracked material and considers healing whilst under strain as well as allowing for re-cracking the healed material. The constitutive model is combined with a layered beam model to allow successful comparisons with experimental results.



**Declaration**

This work has not been submitted in substance for any other degree or award at this or any other university or place of learning, nor is being submitted concurrently in candidature for any degree or other award.

Signed ..... Date .....

**Statement 1**

This thesis is being submitted in partial fulfilment of the requirements for the degree of Doctor of Philosophy.

Signed ..... Date .....

**Statement 2**

This thesis is the result of my own independent work / investigation, except where otherwise stated. Other sources are acknowledged by explicit references. The views expressed are my own.

Signed ..... Date .....

**Statement 3**

I hereby give consent for my thesis, if accepted, to be available for photocopying and for inter-library loan, and for the title and summary to be made available to outside organisations.

Signed ..... Date .....

**Statement 4**

I hereby give consent for my thesis, if accepted, to be available for photocopying and for inter-library loans after expiry of a bar on access previously approved by the Academic Standards & Quality Committee.

Signed ..... Date .....



## Acknowledgements

I would like to express my sincere gratitude to Professor Tony Jefferson. His enthusiasm for my topic, expert guidance and wealth of experience is unsurpassed. By instilling a ‘can do’ attitude, whilst always remembering to consider the basic ‘engineering’ checks at every step, he has helped me through this chapter in my career. His infectious attention to detail and authoring skills, alongside continual encouragement, is very much appreciated. Diolch yn fawr.

I would also like to express my gratitude to Dr Diane Gardner. Her wisdom in the lab, objective discussions and her passion for organisation have been most valuable. Other research group members, I would like to mention, include Professor Bob Lark who welcomed me back to Cardiff University and Dr Iulia Mihai who has always been open to discussions.

To past and current colleagues in room W1.31/32 and friends completing a PhD, I am proud to be sharing this journey with you. There are too many to include here, you know who you are. The lab technicians, support staff and the Engineering department have all played their part in making the experience at Cardiff University an enjoyable and fulfilling one. Youssef, thank you for your assistance with some of the experiments and Carl, Ian, Harry and Steffan thank you for humouring me.

This research would not have been possible without the generous financial support and foresight of Alun Griffiths Civil Engineering Contractors. Their industrial collaboration, alongside Cardiff University’s President Scholarship, has allowed a broader research impact to be visualised, in particular, when addressing the ‘challenges of 2020’.

Finally, I would like thank my family for their ever-present love, support and enjoyment. My wife, Jenny, to whom I am eternally grateful, thank you for the encouragement to rely on my intuition and to follow my dream. Evan, your innocence, inquisitiveness and joy has helped to keep my thoughts in perspective. The courage shown by absent family members continues to inspire me.



# Contents

List of Figures . . . . .	xi
List of Tables . . . . .	xv
List of Symbols . . . . .	xvii
<b>1 Introduction</b>	<b>1</b>
1.1 Concrete, durability and the role of self-healing . . . . .	1
1.2 Overall objectives and aims . . . . .	3
1.3 Publications . . . . .	4
1.4 Outline of the thesis . . . . .	5
<b>2 Micromechanics State-of-the-art</b>	<b>7</b>
2.1 Modelling framework . . . . .	8
2.2 Micromechanical modelling of cementitious materials . . . . .	16
2.3 Micro-cracking considerations in concrete . . . . .	19
2.4 Self-healing cementitious composites . . . . .	22
<b>3 Inelastic Strain Modelling</b>	<b>39</b>
3.1 Constitutive model theory . . . . .	40
3.2 Micro-cracking . . . . .	47
3.3 Micro-crack criterion and evolution . . . . .	52
3.4 Numerical implementation . . . . .	56
<b>4 Model Validation, Performance and Application</b>	<b>59</b>
4.1 FE Validation of homogenised solution . . . . .	59
4.2 Characteristic model predictions . . . . .	64
4.3 Autogenous shrinkage during curing . . . . .	73
<b>5 Experimental Study on Autogenous Cementitious Healing</b>	<b>83</b>
5.1 Preliminary investigations . . . . .	83
5.2 Experimental procedure . . . . .	87
5.3 Results and discussions . . . . .	95
<b>6 Self-healing Micromechanical Model</b>	<b>117</b>
6.1 Micro-crack healing in a two-phase composite . . . . .	118
6.2 Numerical implementation . . . . .	124
6.3 Illustrative model performance . . . . .	127
6.4 Comparison with experimental data . . . . .	134
<b>7 Conclusions and Future Work</b>	<b>147</b>
7.1 Conclusions . . . . .	147
7.2 Recommendations for future work . . . . .	150
<b>A Direct Tensor Notation</b>	<b>153</b>
<b>B Experimental results</b>	<b>155</b>
<b>References</b>	<b>169</b>



# List of Figures

2.1	RVE of concrete . . . . .	13
2.2	Idealisation of a homogeneous concrete material . . . . .	14
2.3	Venn diagram to explain terminology of self-healing according to JCI TC-075B . . . . .	23
2.4	Different causes that can lead to autogenic self-healing . . . . .	25
2.5	Schematic of the relationship between tensile stress and tensile elongation of FRCC . . . . .	29
2.6	Comparison of numerical and experimental bending test on healed concrete specimens (Granger et al. 2007b) . . . . .	34
2.7	Comparison of Hilloulin et al. (2013) numerical self-healing model with experimental data . . . . .	35
3.1	Two-phase composite with illustrative rationale . . . . .	41
3.2	Reference system for crack planes . . . . .	49
3.3	Volumetric and directional tensile softening functions . . . . .	54
4.1	3D FE plot and stress spatial distribution plot for one inclusion . . . . .	62
4.2	3D FE plot and stress spatial distribution plot for multi-inclusion . . . . .	63
4.3	Time dependent matrix shrinkage with associated matrix micro-cracking (MC) and without matrix micro-cracking (NMC) . . . . .	66
4.4	Matrix shrinkage restrained uniaxially with micro-cracking (MC) and without micro-cracking (NMC) . . . . .	67
4.5	An uniaxial tensile strain path and selected micro-cracking directions . . . . .	68
4.6	An uniaxial tensile strain path with matrix shrinkage strain (SS) and without matrix shrinkage strain (NSS) . . . . .	69
4.7	Micro-cracking parameter response with/without matrix shrinkage . . . . .	70
4.8	Matrix shrinkage during the Willam et al. (1989) strain path which involves micro-crack formation under uniaxial tension followed by a rotating principal strain path . . . . .	71
4.9	Matrix shrinkage during the Willam et al. (1989) strain path results of the stress, principal stress and shear strain . . . . .	72
4.10	Pickett (1956) experimental results compared to model with/without micro-cracking . . . . .	79
4.11	Baroghel-Bouny (1994) experimental results compared to model with/without micro-cracking . . . . .	79
4.12	Parametric study of total shrinkage/matrix shrinkage with/without micro-cracking . . . . .	80
5.1	Specimen general arrangement . . . . .	89
5.2	Plate configuration before casting shown with twin moulds . . . . .	90
5.3	Flexural test arrangement . . . . .	92

5.4	Rockwell hardness test arrangement . . . . .	93
5.5	Plots of force against time and indenter-depth against time (Low 2001)	94
5.6	Hardness test indenter position within sample region . . . . .	95
5.7	Selection of self-healing evidence on external surfaces . . . . .	96
5.8	Selection of self-healing evidence on internal surfaces . . . . .	97
5.9	Selected SEM images Set 7 Beam A . . . . .	99
5.10	Photographs of self-healing development with time for Set 7 . . . . .	100
5.11	Plot of computed diffractogram Set 7 . . . . .	102
5.12	Plot of identified samples Set 7 . . . . .	103
5.13	Typical response 28 days autogenous healing Set 1 Beam C . . . . .	104
5.14	Typical response 35 days self-healing 0.2 mm half depth plate Set 5 Beam A . . . . .	106
5.15	SH strength recovery of samples with different natural cracks . . . . .	107
5.16	SH strength recovery of samples with different narrow notches Sets 4, 5 and 6 . . . . .	108
5.17	Self-healing strength recovery of samples with different narrow notches with time set 7 and set 8 . . . . .	109
5.18	Peak load against Self-healing time for Set 7 and 8 . . . . .	110
5.19	Fracture Energy CMOD against Self-healing time for Set 7 and 8 . . . . .	111
5.20	Rockwell Hardness test individual and average results Set 7 . . . . .	112
5.21	Rockwell Hardness test plotted against compressive strength Set 7 . . . . .	115
6.1	Self-healing algorithm . . . . .	124
6.2	Typical volumetric healing response . . . . .	128
6.3	Model response with standard material properties . . . . .	130
6.4	Micro-cracking parameter response . . . . .	130
6.5	Parametric study of model performance . . . . .	131
6.6	Healing under load . . . . .	133
6.7	Volumetric healing under load . . . . .	134
6.8	Layered beam model schematic . . . . .	135
6.9	Simplified representation of beam . . . . .	136
6.10	Self-healing micromechanical and layered beam model interaction . . . . .	138
6.11	Load CMOD plots for micromechanical model and experimental data	141
6.12	Load CMOD plots comparison of model and experimental results . . . . .	143
6.13	Micro-cracking parameter and effective stain parameter distribution through beam section . . . . .	144
6.14	The effect of the ageing material properties on the strength increase in the uncracked ligament . . . . .	145
B.1	Autogenous healing 0.0 mm natural crack (NC) Set 1 Load-CMOD . . . . .	156
B.2	Autogenous healing 0.18 mm natural crack (NC) Set 2 Load-CMOD . . . . .	157
B.3	Autogenous healing 0.30 mm natural crack (NC) Set 3 Load-CMOD . . . . .	158
B.4	Autogenous healing 0.1 mm narrow notch (NN) Set 4 Load-CMOD . . . . .	159
B.5	Autogenous healing 0.2 mm narrow notch (NN) Set 5 Load-CMOD . . . . .	160
B.6	Autogenous healing 0.3 mm narrow notch (NN) Set 6 Load-CMOD . . . . .	161
B.7	Load-CMOD for 13 days self-healing narrow notch (NN) Set 7 and 8 . . . . .	162
B.8	Load-CMOD for 27 days self-healing narrow notch (NN) Set 7 and 8 . . . . .	163
B.9	Load-CMOD for 41 days self-healing narrow notch (NN) Set 7 and 8 . . . . .	164
B.10	Load-CMOD for 55 days self-healing narrow notch (NN) Set 7 and 8 . . . . .	165

B.11 SEM Images Set 7 . . . . .	166
B.12 Time lapse Set 7 . . . . .	167



# List of Tables

3.1	Constitutive driver algorithm . . . . .	56
3.2	Computational algorithm for specified stress path with matrix shrinkage . . . . .	57
4.1	Material properties used for the FE validation . . . . .	60
4.2	Typical cementitious composite material properties . . . . .	64
4.3	Typical cementitious composite material properties Pickett (1956) . . . . .	78
4.4	Hydration model parameters used for Pickett (1956) . . . . .	78
4.5	Typical cementitious composite material properties Baroghel-Bouny (1994) . . . . .	78
4.6	Hydration model parameters used for Baroghel-Bouny (1994) . . . . .	79
5.1	Composition of concrete and mortar beams . . . . .	88
5.2	Summary of experimental study . . . . .	91
5.3	Identified patterns list . . . . .	101
5.4	Summary of Rockwell hardness number experimental results . . . . .	113
6.1	Computational algorithm for iterative local micro-cracking to update stress before healing . . . . .	125
6.2	Computational algorithm for iterative local micro-cracking to update stress after healing . . . . .	126
6.3	Material properties for volumetric model response . . . . .	128
6.4	Material properties fixed for parametric study . . . . .	129
6.5	Material properties varied for parametric study . . . . .	129
6.6	Composition of SSC (Granger et al. 2007b) and UHPC (Mounanga et al. 2012) . . . . .	139
6.7	Model material properties for experimental comparison study . . . . .	140
6.8	Model material properties when examining effect of ageing . . . . .	143
6.9	Hydration model parameters . . . . .	143
6.10	Load at various positions on Figure 6.14 . . . . .	146
A.1	Direct tensor notation font . . . . .	153
A.2	Tensor operation notation . . . . .	153
B.1	Anchor Scan Parameters: X’Pert Highscore PANalytical software . . . . .	168



# List of Symbols

$A_E$	Activation energy
$\mathbf{A}_\Omega$	As defined in equation (3.7)
$\mathbf{A}_{\Omega\omega_v}$	As defined in equation (3.46)
$A_{\Omega v}$	As defined in equation (4.10)
$a$	Radius of the spherical inclusion
$a_o$	Single crack radius
$B$	Ratio between the healed and original elastic tensor
$b_b$	Width of beam
$c_\gamma$	Strength recovery ratio
$\mathbf{C}_\alpha$	Micro-cracking elastic compliance terms
$\mathbf{C}_{addh}$	Total added healed compliance tensor
$\mathbf{C}_{add}$	Total added compliance tensor
$\mathbf{C}_{LM\Omega}$	Composite compliance tensor
$\mathbf{C}_{LM}$	Matrix compliance tensor
$\mathbf{C}_L$	Elastic compliance tensor
$C_{cem}$	Cementitious material content
$c_E$	Constant as defined for equation (4.29)
$c_{fc}$	Constant as defined for equation (4.31)
$c_{fi}$	Constant as defined for equation (4.32)
$c_\beta$	Evolution constant
$\mathbf{D}_{el}$	Elasticity tensor
$\mathbf{D}_M$	Matrix elastic tensor
$\mathbf{D}_{M\omega_v}$	Volumetric micro-cracked matrix tensor
$\mathbf{D}_{M\Omega}$	Composite elastic tensor, see equation (3.9)
$\mathbf{D}_{M\Omega\omega_v}$	Volumetric micro-cracked composite tensor
$\mathbf{D}_\Omega$	Inclusion elastic tensor
$\mathbf{D}_{Sec}$	Secant constitutive matrix
$\mathbf{D}_{sec}$	Secant elastic tensor
$\mathbf{D}_{Lh}$	Local healed elastic tensor
$\mathbf{D}_L$	Local elastic tensor
$E_\Omega$	Inclusion Young's modulus
$E_d$	Composite Young's modulus
$E_M$	Matrix Young's modulus
$E_s$	Secant Young's modulus
$\mathbb{F}$	Crack density parameter
$f_\Omega$	Volume fraction inclusion
$F_{\zeta_d}$	Directional micro-cracking function
$F_{\zeta_m}$	Volumetric micro-cracking function
$f_c$	Compressive strength

$f_M$	Volume fraction matrix
$f_{td}$	Local directional tensile strength at the aggregate/cement paste interface
$f_{th}$	Local volumetric tensile strength at the aggregate/cement paste interface in healed material
$f_{tv}$	Local volumetric tensile strength at the aggregate/cement paste interface
$f_t$	Tensile strength
$G_f$	Specific fracture energy
$h_b$	Height of beam
$H_{cem}$	Heat of hydration for cement
$h_d$	Three times the diameter of coarse aggregate
$H_{FA}$	Heat of hydration for fly ash
$h_h$	Size of the coarse aggregate
$h_n$	Height of notch
$H_{slag}$	Heat of hydration for slag
$H_{uls}$	Ultimate heat of hydration
$H_u$	Total heat of hydration
$h_v$	Diameter of the coarse aggregate
$h$	Healing proportion
$\mathbf{I}^{4s}$	Fourth order identity tensor
$i$	Integration direction
$j$	Beam layer
$K_M$	Bulk modulus of matrix
$K_{M\Omega v}$	Bulk modulus of composite as a function of solidification
$K_{Mv}$	Bulk modulus of matrix as a function of solidification
$K_\Omega$	Bulk modulus of inclusion
$k$	Plastic variable
$K$	Material stiffness
$L$	Length of beam
$L_e$	Elastic section of beam
$M$	Bending moment in beam
$\mathbf{N}$	Stress transformation tensor
$\mathbf{N}_\epsilon$	Strain transformation tensor
$N$	Axial force in beam
$n_i$	Total number of integration directions
$N_c$	Number of cracks per unit volume
$nlay$	Number of layers in beam
$P$	Load
$p_{cem}$	Total cement fraction
$p_i$	Fraction by weight of cement
$r, s, t$	Local coordinate system
$R$	Universal gas constant
$r_{\zeta_d}$	As defined for equation (3.71)
$s_{Lh}$	Equivalent local healed stress
$s_L$	Equivalent local stress
$\mathbb{S}$	Plane area of the crack
$\mathbf{S}^E(\mathbf{x})$	Exterior point Eshelby tensor
$\mathbf{S}$	Interior point fourth order Eshelby tensor, see equation (3.5)
$S_v$	Volumetric interior point Eshelby scalar

$\mathbf{S}_{Sec}$	Secant Eshelby tensor
$s_{hI}$	Local healed principal stress
$s_I$	Local principal stress
$s_{Lth}$	Local stress at time of healing
$s_{M\Omega h}(\mathbf{x})$	Local transformed amplified healed stress
$s_{M\Omega}$	Transformed amplified stress adjacent to inclusion
$textbfs$	Local stress vector
$\Delta t$	Time step interval
$\mathbf{T}^E(\mathbf{x})$	As defined in equation (3.40)
$\mathbf{T}_\Omega$	As defined in equation (3.10)
$\mathbf{T}_{\Omega\omega_v}$	As defined in equation (3.45)
$T_{\Omega_v}$	As defined in equation (4.8)
$t$	Time
$T_c$	Current temperature
$t_e$	Equivalent maturity (or age)
$T_r$	Reference temperature
$t_{th}$	Time of healing
$u$	Crack opening
$u_{0d}$	Relative displacement for directional fully micro-cracked
$u_{0h}$	Relative displacement for healed material when volumetric is fully micro-cracked
$u_{0m}$	Relative displacement for volumetric fully micro-cracked
$u_d$	Relative displacement across a zone of material
$u_m$	Relative displacement across a zone of material
$u_{td}$	Relative displacement for directional at first uniaxial micro-cracking
$u_{th}$	Crack opening at time of healing
$u_{tm}$	Relative displacement for volumetric at first uniaxial micro-cracking
$\Delta v$	Solidified volume increment
$v$	Solidified volume
$w_c$	Central Fracture Process Zone
$\mathbf{x}$	Position vector from the centre of a spherical aggregate particle
$x$	Continued hydration of cement
$z$	Layer depth in beam
$\alpha_L$	As defined for equation (3.68)
$\beta_h$	Hydration shape factor
$\bar{\epsilon}$	Composite average strain tensor
$\Delta\epsilon$	Out of balance strain increment
$\Delta\epsilon_a$	Strain path increment
$\Delta\epsilon_{s\Omega}$	Incremental volumetric solidification strain in inclusion
$\Delta\epsilon_{sM}$	Incremental volumetric solidification strain in matrix
$\Delta\epsilon_{shr}$	Applied shrinkage strain increment
$\epsilon_{\alpha h}$	Additional healed strain tensor in a single direction
$\epsilon_\alpha$	Additional strain tensor in a single direction
$\epsilon_\tau$	Transformation eigenstrain
$\epsilon_{ac}$	As defined in equation (6.12)
$\epsilon_{ah}$	Total additional healed strain tensor due to micro-cracking
$\epsilon_{as}$	As defined in equation (6.14)
$\epsilon_a$	Total additional strain tensor due to micro-cracking

$\epsilon_c$	Disturbance (or constrained) strain
$\epsilon_{INEQ\omega_v}$	As defined for equation (3.43)
$\epsilon_{INEQ}$	As defined for equation (3.35)
$\epsilon_{IN}$	Inelastic strains
$\epsilon_{Lh}$	Directional (equivalent) local healed strain
$\epsilon_{LMe}$	Peak elastic strain in the matrix
$\epsilon_L$	Directional (equivalent) local strain component
$\epsilon_{M\Omega}$	Amplified strain adjacent to inclusion
$\epsilon_{M\Omega}(\mathbf{x})$	Amplified strain tensor
$\epsilon_{Mv}$	Volumetric strain in matrix
$\epsilon_o$	Farfield strain tensor
$\epsilon_p$	Plastic strain
$\epsilon_{shr}$	Shrinkage potential of the matrix
$\epsilon_M$	Matrix strain tensor
$\epsilon_\Omega$	Inclusion strain tensor
$\epsilon_{0d}$	Local directional strains when effectively fully micro-cracked
$\epsilon_{0h}$	Local strains when healed material is effectively fully micro-cracked
$\epsilon_{0vh}$	Local volumetric strains when healed material is effectively fully micro-cracked
$\epsilon_{0v}$	Local volumetric strains when effectively fully micro-cracked
$\epsilon_{s\Omega}$	Volumetric solidification strain in inclusion
$\epsilon_{shrM}$	Volumetric shrinkage strain in matrix
$\epsilon_{sM}$	Volumetric solidification strain in matrix
$\epsilon_s$	Solidification strain
$\epsilon_{td}$	Strain at first directional uniaxial micro-cracking
$\epsilon_{th}$	Strain at first volumetric uniaxial micro-cracking in healed material
$\epsilon_{tvh}$	Strain at first volumetric uniaxial micro-cracking in healed material
$\epsilon_{tv}$	Strain at first volumetric uniaxial micro-cracking
$\gamma$	As defined for equation (3.71)
$\Gamma_c$	Starting threshold degree of hydration
$\Gamma_r$	Relative degree of hydration
$\gamma_{xy}$	Shear strain x-y direction
$\delta_{ij}$	Kronecker delta
$\nu_\Omega$	Poisson's ratio for inclusion
$\nu_M$	Poisson's ratio for matrix
$\omega$	Micro-cracking parameter
$\omega_d$	Directional micro-cracking parameter
$\omega_h$	Healed material micro-cracking parameter
$\omega_{th}$	Micro-cracking parameter at time of healing
$\omega_v$	Volumetric micro-cracking parameter
$\psi$	Spherical coordinate reference angle
$\rho$	Relative distance from the centre of a spherical aggregate particle
$\bar{\sigma}$	Composite average stress tensor
$\Delta\sigma_a$	Stress path increment
$\Delta\sigma_{rc}$	Out of balance stress increment
$\sigma_\Omega$	Inclusion stress tensor
$\sigma_{M\Omega}$	Amplified stress adjacent to inclusion
$\sigma_{M\Omega}(\mathbf{x})$	Amplified stress tensor

$\sigma_M$	Matrix stress tensor
$\sigma_d$	Directional stress tensor
$\sigma_I$	Principal stress
$\sigma_{Mv}$	Volumetric matrix stress
$\sigma_m$	Volumetric stress
$\tau$	Hydration time parameter
$\tau_L$	As defined for equation (3.68)
$\theta$	Spherical coordinate reference angle
$\theta_H$	Change in slope of the beam
$\zeta$	Effective local strain parameter
$\zeta_d$	Directional effective local strain parameter
$\zeta_h$	Healed effective local strain parameter
$\zeta_v$	Volumetric effective local strain parameter
$\beta$	Subscript denoting volumetric ( <i>v</i> ) or directional ( <i>d</i> ) micro-cracking
<i>e</i>	Subscript denoting elastic
<i>f</i>	Subscript denoting final solidified value
<i>h, heal</i>	Subscript denoting healed
<i>M</i>	Subscript denoting matrix
<i>ns</i>	Subscript denoting specified number of steps
$\Omega$	Subscript denoting inclusion
<i>pr</i>	Subscript denoting previous time step
$\Delta v$	Subscript denoting solidification increment
<i>v, vol</i>	Subscript denotes volumetric



# Chapter 1

## Introduction

This introduction chapter sets the scene for the thesis by describing the significance of concrete, highlighting important design issues and discussing the potential role that self-healing can play in addressing these issues. The overall research objectives and aims are then set out alongside the author's publications to date and finally an outline of the thesis content is given.

### 1.1 Concrete, durability and the role of self-healing

Concrete is currently the most used man-made material in the world, with global production of cement being 4 billion tonnes in 2013 (USGS 2014). As such, concrete is used on many construction projects and it is being used in increasingly innovative design solutions expanding the known material capabilities. The history of concrete technology is well documented and it is widely recognised that the Ancient Romans first used a form of concrete over 2000 years ago (Neville & Brooks 2010). Concrete in its basic form is a composite material with coarse aggregate particles embedded homogeneously in a hard matrix material. Modern concrete comprises cement, sand, coarse aggregate, water and chemical admixtures. Cement is a hydraulic binder where the most well known is Portland cement which was first patented by Aspdin in 1824. Many other materials have hydraulic properties, such as, granulated blast furnace slag, natural pozzolana, fly ash and silica fume (BS EN 197-1 2011). When a hydraulic binder is mixed with water, the resulting paste reacts chemically during the hydration process, binding the sand and aggregate, setting hard to form a 'rock like' material.

Traditionally, strategies for designing concrete structures have involved damage prevention, that is, ensuring the materials used meet both serviceability and ultimate limit requirements of codes of practice such as (EN 1990 2002). Codes of practice provide basic design requirements taking account of design working life, durabil-

ity, reliability and quality. Balancing these various design elements whilst satisfying increasing sustainability requirements is becoming increasingly important. The current design practice is to limit damage in structures. One such example is to use partial factors for loads and materials to avoid excessive damage resulting in the need for larger structural elements and stronger materials. When damage does occur the re-active approach is employed where by maintenance and repair takes place. In 2014 repair and maintenance activity was £44.6 Billion which accounted for 39 % of the total UK construction and building work (ONS 2014).

An alternative approach, to creating stronger structures, is to pro-actively manage the damage by accepting that damage will occur in concrete and implementing strategies to managing this deterioration over time. This planned, pro-active form of maintenance and repair can lead to increased capital cost but would have low or negligible maintenance costs over the life of the structure (Van Breugel 2007). Inspiration is taken from living organisms, such as the bones and skin of the human body and plants, and their ability to detect damage and repair themselves. Biomimetic products are beginning to be used across the whole engineering industry. This thinking has created an opportunity for self-healing materials where by the material can regain a proportion of its performance after being damaged without intervention. These self-healing technologies appear promising when targeted at a specific application, but the technology is in its infancy and is yet to be proven at a large scale. Modelling self-healing concrete should lead to a better understanding of the mechanisms which govern its behaviour and thereby help transfer the technology from small scale laboratory experiments to large scale structural designs.

In the first International Conference on Self-Healing Materials, Van Breugel (2007) asked a valid question: it might be possible to create such materials but 'is there a market for self-healing materials?'. The article argues that this depends on being able to take these concepts forward to the design and building processes, to prevent rejection by the construction industry. The large number of papers and attendees at the fifth International Conference on Self-Healing Materials in the summer of 2013 is further proof that this exciting and rapidly evolving field is slowly being understood and will be the future of engineered materials.

Cracking can be considered one of the major causes of concrete degradation and is typically initiated by thermal effects, early age shrinkage, mechanical loading or a combination of these actions. These cracks can in turn lead to water and carbon dioxide ( $CO_2$ ) ingress causing damage to the cementitious material and corrosion of the reinforcement. Despite the fact that durability has for many years been an important aspect of reinforced concrete design, a significant proportion of these structures have had problems with durability in recent years (Richardson 2002). The development of cementitious materials that are capable of self-repairing any cracks that

form, and thereby addressing the problems of poor durability associated with cracking, would therefore be very advantageous. Enhanced crack healing can maintain the stringent tightness requirements of structural protective systems against extreme events (van Breugel 2011). Crack repair techniques built into the material system can be broadly grouped into two categories; the first takes advantage of the natural autogenous (or self) healing properties of cementitious materials and the second is artificial (or autonomic) healing typically making use of embedded adhesive repair agents (Dry 1994, Ghosh 2009, Joseph et al. 2010, Li et al. 1998).

The need to incorporate advanced self-healing materials into the design of sustainable structures has led the recent need for a greater understanding of the associated complex processes. According to the "Research direction in computational modelling report" computational modelling forms part of our everyday lives (Oden et al. 2003). Hence, computational modelling of these novel materials is required to allow engineers to make the most of the self-healing properties and thereby manage our infrastructure.

## **1.2 Overall objectives and aims**

The objectives of the main body of research work are listed below.

- Develop a full 3D micromechanical model with the ability to apply prescribed stress, anisotropic loading (or displacement), inelastic strains and hydration processes in cementitious materials.
- Simulate time dependent inelastic strains, such as shrinkage, creep, micro-cracking, differential thermal expansion or ageing.
- Understand the key experimental parameters which control or influence autogenous healing in cementitious materials.
- Quantify autogenous healing using mechanistic experiments to determine the mechanical properties.
- Validate and assess performance of any proposed numerical model solution by linking to an experimental study.
- Develop a mechanistic numerical model capable of direct application to real problems.
- Make positive steps towards achieving a fully coupled thermo-hygro-chemo-mechanical finite element model of concrete describing self-healing.

## 1.3 Publications

The author is named on the following publications

- Isaacs, B., Lark, R., Jefferson, T., Davies, R. & Dunn, S. (2013), ‘Crack healing of cementitious materials using shrinkable polymer tendons’, *Structural Concrete* **14**(2), 138–147.  
**URL:** <http://onlinelibrary.wiley.com/doi/10.1002/suco.201200013/abstract>
- Davies, R. E. & Jefferson, A. D. (2014), ‘The simulation of inelastic matrix strains in cementitious materials using micromechanical solutions’, *Engineering Fracture Mechanics*.  
**URL:** <http://www.sciencedirect.com/science/article/pii/S0013794414003324>  
(This paper covers the work detailed in Chapters 3 and 4)

The author is also named on the following conference proceedings and presented at the conferences as first author:

- Davies, R. E. & Jefferson, A. D. (2012), The simulation of time dependent behaviour of cement bound materials with a micromechanical model, *in* ‘1st International Conference on Numerical Modelling Strategies for Sustainable Concrete’, SSCS, Aix en Provence, France.
- Davies, R. E. & Jefferson, A. D. (2013), The simulation of inelastic strains and fracture in a two-phase composite using a micromechanical model, *in* ‘International Conference on Computational Mechanics (CM13)’, ACME, Durham, UK.

## 1.4 Outline of the thesis

This thesis reports on the research work undertaken in developing a micromechanical model for self-healing cementitious materials. The research work is mostly numerical in nature supported by investigative experimental findings.

Chapter 2 discusses the state of the art for micromechanical constitutive modelling. This chapter provides background to the modelling approach adopted. The micromechanical techniques that have been used to model the time dependent processes in cementitious materials are reviewed alongside key micro-cracking considerations. Finally, the state of the art for self-healing is presented, focusing on autogenous healing in cementitious materials. The first steps in being able to develop engineering solutions using self-healing materials is to bridge the gap between the experimental findings and numerical predictions.

A novel micromechanical model is developed in Chapter 3 which is capable of taking account of inelastic strains in the matrix. The constitutive model theory is presented before the effects of micro-cracking, micro-crack initiation criterion and its evolution with time are discussed. The numerical implementation of the model in a constitutive driver program is described.

This micromechanical model is then validated in Chapter 4. Results from a 3D finite element model of a two-phase composite are compared with the homogenised model solution without micro-cracking for a free shrinkage problem. The performance of the model is assessed using prescribed stress and strain paths to obtain characteristic responses. The model is then applied to the problem of autogenous shrinkage of a cementitious material. For this work, a specialised form of the model was developed which only employed volumetric components of the constitutive tensors.

Alongside developing a self-healing numerical model, an experimental study was carried out on autogenous cementitious healing and is presented in Chapter 5. The preliminary investigations, experimental procedures adopted and findings are presented and discussed.

The development of a novel self-healing micromechanical model is presented in Chapter 6. The rationale behind the two-phase composite constitutive model with micro-crack healing is given alongside the means used to simulate the solidification strain and continued damage of healed material. The numerical implementation and characteristic model performance are first described before a comparison with experimental data from Chapter 5 is presented.

Finally, Chapter 7 outlines the conclusions from each chapter, which are then placed in context with the overall objectives and aims alongside the recommendations for future study.



# Chapter 2

## Micromechanics State-of-the-art

This state-of-the-art review brings together the main topic areas which are required to appreciate and develop a self-healing concrete model. Chapter 1 provided the motivation for this research by giving the background to the problems facing some concrete structures and how self-healing could provide a step change in how we design with concrete in the future. The four topic areas presented within this chapter include defining a suitable numerical model framework, understanding the time dependent processes that occur in concrete, making an allowance for micro-cracking and exploring self-healing mechanisms.

Over the last century concrete has been studied in increasing detail as technology, experiments, modelling and understanding have developed. Concrete has been considered at different length scales, from bulk macro-scale strength down to nano-scale pores. The first section in this review, Section 2.1, provides a general background to the cementitious modelling framework that has been established, whilst examining the current processes, techniques and theories. It is favourable to adopt approaches that allow individual properties and processes to be modelled at the scale at which they occur. For concrete this scale is deemed to be at the micro-scale. Section 2.2 takes a closer look at how micromechanics is used to model key processes, such as shrinkage and creep, within cementitious materials at the micro-scale.

Ever since Coignet placed steel within the concrete in the mid-18th century, concrete has been used not only in structural elements subject to pure compression but also in structures subject to high tensile forces. In most case, cracks develop in the tension zone of reinforced structural members (Mosley et al. 2012). The presence of these cracks reduce the strength of concrete and its durability by allowing the ingress of water and other foreign agents. This significantly reduces the design life. Section 2.3 discussed how these micro-cracks are taken into account in a constitutive model at the micro-scale.

An example of self-healing in concrete is its natural ability to heal itself, sometimes termed ‘autogenous healing’. At present this mechanism is investigated empirically and has not been incorporated into design codes of practice such as EC2 (EN 1992 2008) or the CEB-FIP model code (fib 2013). Therefore, there is a need to better understand the healing processes, to accurately predict experimental behaviour and to determine how this impacts on the overall mechanical properties of concrete. The final Section 2.4 considers self-healing in concrete, focussing on the state-of-the-art for autogenous healing mechanisms, laboratory experiments and numerical modelling.

## **2.1 Modelling framework**

The main aspects of concrete behaviour are presented in Section 2.1.1 before moving on to give a brief history of concrete modelling in Section 2.1.2. The benefits of micromechanical numerical models along with justification for adopting this approach are discussed. The rationale behind and details of some of the relevant micromechanical elastic moduli composite solutions are given in Section 2.1.3. Finally, the modelling approaches considering time dependent inelastic strains are presented in Section 2.1.4. These have been shown to be particularly relevant to modelling cementitious materials.

### **2.1.1 General cementitious material properties**

The properties of a cementitious material can be described by considering two main aspects. The first is the basic nonlinear mechanical response, which includes cracking and crushing. The second is time dependent behaviour, which includes changing mechanical properties during hydration, shrinkage and creep. Each aspect can control the stress and strain response of the material which can be combined to provide an overall constitutive relationship.

Concrete is stronger in compression than in tension, with the uniaxial compressive strength of concrete being approximately ten times greater than the uniaxial tensile strength (Neville & Brooks 2010). Consequently, mechanical failure is often due to some form of cracking, initially micro and then macro-cracking. Materials are generally classified as fracturing in either brittle failure or ductile yielding. However, cementitious materials exhibit quasi-brittle behaviour characterised by a softening response (Ferretti 2004). Micro-cracking begins before the peak load is reached and is believed to contribute to the post-peak softening response as these cracks develop into macro-cracks alongside the effects of aggregate interlock and frictional slip (on fracture surface). Section 2.3 presents the micromechanical ap-

proaches to modelling micro-cracking in concrete.

The development of properties with time, such as hydration, ageing, shrinkage, creep and thermal behaviour (Bažant 2001), often lead to inelastic responses in concrete. These processes are often interdependent, for example, the ageing process is linked with the development of creep. The strains associated with these time dependent phenomena can be summed to give an overall response with time.

Total shrinkage in cementitious materials is known to be a sum of drying shrinkage and autogenous shrinkage (Neville et al. 1983). Drying shrinkage is caused by the evaporation of water from the surface of concrete. This process continues until the relative humidity inside the concrete reaches equilibrium with its environment. The loss of moisture and subsequent movement of water through the pore system of hardened cement paste (hcp) causes shrinkage strains throughout the material. The differential straining between the hcp and aggregate phases are associated with the build up of stresses. The moisture content and subsequent shrinkage strain has been simulated using water loss (Bažant 2001), relative humidity (Beltzung & Wittmann 2005) or pore pressure (Mainguy et al. 2001) as the moisture content variable. Autogenous shrinkage is attributed to chemical volume changes and self-desiccation in the cement paste (Hua et al. 1995). Consideration of total shrinkage, in isolation to all other time dependent mechanisms, can provide an insight into the development of micro-cracking associated with shrinkage cracking problems in concrete structures.

There are two types of creep commonly used to describe the behaviour of cementitious materials at ambient temperature; basic creep and drying creep (or the Pickett effect). The generally accepted theories that explain these creep responses are the solidification theory for short-term ageing (Bažant & Prasannan 1989) and microprestress of creep sites in cement gel microstructure causing the Pickett effect and long-term ageing (Bažant et al. 1997). These theories are combined in the B3 model (Bažant 1995) which has recently been advanced in terms of viscosity and reduced number of parameters (Jirásek & Havlásek 2014). The Pickett effect is typically referred to as the additional strain observed in a concrete specimen when loaded and subjected to a loss in moisture. It is accepted that micro-cracking does contribute to the Pickett effect, but does not fully explain the experimental results. A theory used to model the Pickett effect is stress-induced shrinkage (Bažant & Xi 1994).

An alternative theory to describe creep in cement paste is given by Thomas & Jennings (2006). The Calcium Silica Hydrate (C-S-H) gel is assumed to be an aggregation of precipitated, colloidal-sized particles that undergo chemical ageing. Recent work by Vliet et al. (2013), extend this colloidal gel interpretation and, using models hypothesis and experiments, show that drying shrinkage and creep can

be explained by the role of water in the cement paste pore system. Indentation experiments at the nano-scale have been able to show the effects of relative humidity on creep (Ulm et al. 2013).

These time dependent phenomena of shrinkage and creep, described by micromechanical models, are discussed further in Section 2.2.

### 2.1.2 History of concrete modelling

This section provides a brief history of concrete modelling and is dependent on many previous review papers. The proposed micromechanical model is placed in the context of a large body of concrete modelling research work.

Concrete is traditionally modelled using continuum mechanics and since the late 1960s, the beginning of numerical research on concrete, there are two fundamentally different approaches to modelling damage in quasi-brittle materials such as concrete: the discrete approach (Ngo & Scordelis 1967) and smeared approach (Rashid 1968). The discrete approach is based on the principles of fracture mechanics and is ideal for solving localised failure problems. However, the need for re-meshing of the finite element (FE) mesh with progressive failure makes the approach both computationally inconvenient and expensive. In the smeared approach, on the other hand, cracking is simulated with the constitutive model. However, the smeared approach cannot be considered completely in isolation from the FE mesh due to scaling and size effects of the fracture (de Borst & Guitiérrez 1999, de Borst 2002, Jefferson 2010).

The difference between these techniques are discussed by Jendele et al. (2001) where, according to the authors' experience, the smeared approach remains the most widely used for practical structural FE analyses. This is due to the reasonably accurate results and lower computational cost. These trends continue to the present day and are echoed by Jefferson (2010). The smeared approach is also called the constitutive modelling approach, which can be further subdivided into two areas: plasticity theory and damage models.

Plasticity models describe nonlinear material behaviour in a material by using a yield function, flow rule and hardening/softening equation(s). This plasticity approach has been used to model concrete but fails to address the degradation of material stiffness due to micro-cracking. The flow rule controls the development of the inelastic strains when loading and a hardening rule controls the evolution of yield surface (or function). A yield function may be expressed in the form shown by equation (2.1),

$$f(\bar{\sigma}, k) = 0 \quad (2.1)$$

$\bar{\sigma}$  is the composite average stress tensor and  $k$  is the plastic variable. The model

behaves elastically if  $f < 0$  and plastically if  $f \geq 0$ . Important contributions to this field were made by Willam & Warnke (1975), Han & Chen (1985), Feenstra & de Borst (1995), Grassl et al. (2002) and more recently Chen (2007).

Damage models, on the other hand, are based on the concept of a scalar damage variable. This idea was first introduced by Kachanov (1999) in 1958. This approach can be shown by a relatively simple isotropic damage equation as shown in equation (2.2),

$$\bar{\sigma} = (1 - \omega) \mathbf{D}_{el} : \bar{\epsilon} \quad (2.2)$$

$\bar{\epsilon}$  is the composite average strain,  $\mathbf{D}_{el}$  is the elasticity tensor and  $\omega \in [0, 1]$  is the damage variable. 0 represents zero damage and 1 represents a fully damaged material. An example of such an isotropic damage model is given by Mazars (1986) and Giry et al. (2011). Anisotropic damage models have also been developed using this scalar damage variable in different directions. These anisotropic models are believed to better represent the damage pattern that occurs in concrete (Simo & Ju 1987, de Borst & Guitiérrez 1999, Desmorat et al. 2007). A comprehensive summary of macroscopic damage models are given in Krajcinovic (2000).

These two approaches have also been combined to create hybrid plastic-damage models where the positive aspects of each approach are employed. These have been able to simulate the behaviour exhibited by concrete, such as, permanent deformation, inelastic volume expansion in compression, crack opening/closure effects and stress relaxation due to micro-cracking (Simo & Ju 1987, Lee & Fenves 1998, Jefferson 2003, Grassl & Jirásek 2006, Nguyen & Korsunsky 2008, Taqieddin et al. 2012). The basic stress-strain relationship typically used in these models is shown in equation (2.3), where  $\epsilon_p$  is the plastic strain.

$$\bar{\sigma} = (1 - \omega) \mathbf{D}_{el} : (\bar{\epsilon} - \epsilon_p) \quad (2.3)$$

The microplane model, based on a slip theory developed by Taylor (1938), has elements of micromechanical, damage and plasticity theories, but is generally categorised separately because it doesn't use any of the formalism of any of these theories. The model has been developed over many years by Bazant and co-workers, from the M1 versions (Bažant & Oh 1985) to the most recent M7 version (Caner & Bažant 2013). The stress, strain and inelastic relations are defined on individual microplanes with different orientations. The effects from all directions are integrated around a hemisphere to provide an overall constitutive relationship. To solve the microplane model there is a need to fix and resolve the stress (static constraint) or strain (kinematic constraint) components in the microplane using the macroscopic tensors.

Constitutive models can be further classified as using either a phenomenologi-

cal or a mechanistic approach. Phenomenological models, often developed at the macro-scale, are typically formulated using the thermodynamics of irreversible processes. These thermodynamic potentials are based on internal variables such as plastic strain, damage parameters and plastic hardening variables (Zhu et al. 2011). These variables are derived by fitting models to experimental data which often use a large number of parameters that do not have a physical meaning and are not directly measurable. The microplane model is a phenomenological model (Caner & Bažant 2013). One disadvantage of these models, whilst being able to replicate experimental results, is that they have to be used within the limits of the experimental calibration and validation data. As such, greater care has to be taken when working at the limits or outside these bounds. Furthermore, these models become mathematically difficult when considering crack closure or crack interactions (Zhu et al. 2011).

The mechanistic approach, on the other hand, are micromechanical solutions based on the physical mechanisms that can be observed at the micro-scale. Concrete testing in the laboratory is undertaken at the macro-scale using typically beams, cylinders or cubes. However, the micro-cracking and inelastic deformation responsible for the material response occurs at the micro-scale. Research work has moved to working at this micro-scale, leading to ‘engineering concrete from the bottom up’ as coined by Jennings & Bullard (2011). Micromechanical models allow individual material properties, micro-cracking and inelastic behaviour to be modelled at the particle scale of a composite material. They also provide a means of linking the predicted behaviour to the macro-scale response through the homogenisation process. This micromechanical approach requires a relatively small number of real measurable material properties and can describe experimental observations such as material softening due to localization and coalescence of micro-cracks (Zhu et al. 2011).

These micromechanical composite solutions, applicable to most materials, are presented for the elastic case in Section 2.1.3 and for time dependent inelastic strains in Section 2.1.4. Micromechanical considerations specifically addressing cementitious materials and micro-cracking can be found in Sections 2.2 and 2.3 respectively.

### **2.1.3 Micromechanical elastic moduli composite solutions**

This section defines the micromechanical elastic composite, discusses modelling assumptions and various statistical, analytical and homogenisation methods. The macro-scale strength of a material is dependent on the strength of its microstructure. This strength is expressed in terms of compressive and tensile strength. The mi-

mechanical approach uses the constitutive response of the microstructure components to calculate the macro-scale constitutive response.

At the micro-scale, concrete has two distinct phases; aggregate particles and mortar. Figure 2.1 shows a representative volume element (RVE) of concrete at the micro-scale. The effective size of the concrete RVE, also known as the characteristic length, is typically 3 times the maximum aggregate particle diameter (Bazant & Pijaudier-Cabot 1989). Coarse aggregate particles for laboratory concrete are typically 10 mm in diameter and 20 mm for structural concrete. This size of RVE ensures that the homogenized properties are independent of the micro-structural variations but small enough to ensure separation of scales. The inclusion volume percentage for concrete is typically 30 %.

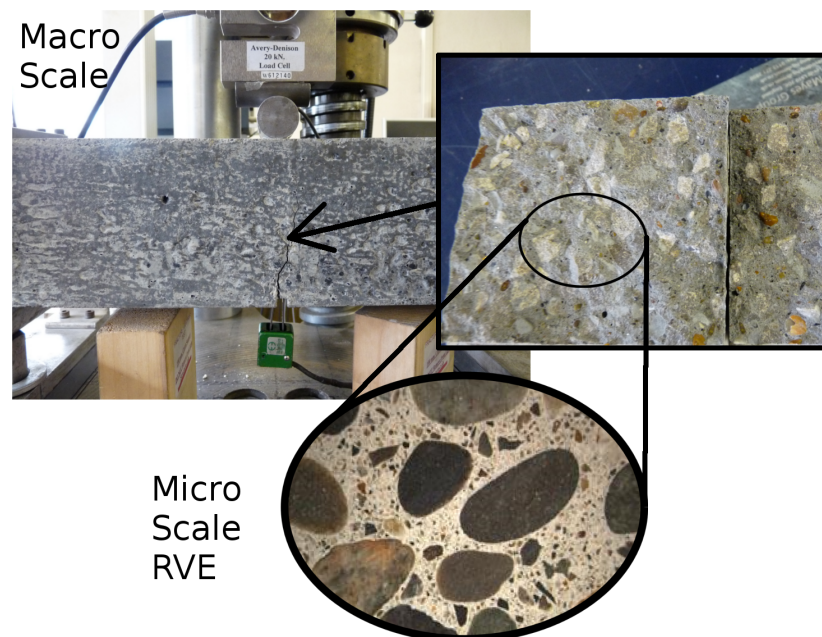


Figure 2.1: RVE of concrete

The heterogeneous nature of cementitious materials and resulting homogenised behaviour mean that they can be idealised as being statistically isotropic or quasi-isotropic (Bohm 1998). For concrete, aggregate particles are idealised as spherical inclusions ( $\Omega$ ) and the mortar is taken to be a single matrix ( $M$ ) phase material. The bond between the inclusion and matrix for numerical modelling is assumed to be perfect and continuous. A solution based on a single inclusion within a matrix subject to farfield strains in which particle interactions are ignored, is termed the dilute case, as shown in Figure 2.2a. A non-dilute formulation is one in which interactions between multiple inclusions within a matrix are taken into account, as shown in Figure 2.2b.

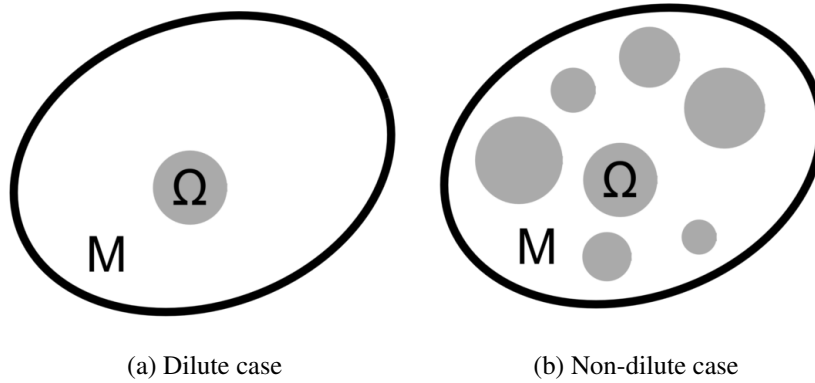


Figure 2.2: Idealisation of a homogeneous concrete material

The statistical analytical methods for evaluating the average elastic moduli of composite materials include Voigt, Reuss, Hashin-Shtrikman bounds, Hill's theory, Eshelby method, Self Consistent Scheme and Mori-Tanaka methods (Mura 1987).

The Voigt and Reuss methods are defined by the rule of mixtures for stiffness and compliance components respectively. The strains are constant in the composite for the Voigt method and the stresses remain constant for the Reuss method. Hashin-Shtrikman bounds' variational principle (Hashin & Shtrikman 1963) takes the average elastic moduli from the Voigt and Reuss methods. Hill (1963) related these phase averaged strains and stresses to the overall strains and stresses by using phase strains and stress concentration tensors. The effective elasticity and compliance tensors for a composite can be obtained from the material properties and the concentration tensors.

The Eshelby (1957) method determines the stress field within the composite. This approach adopts a single ellipsoidal inclusion within a matrix (dilute approach) which undergoes a farfield stress. The state of stress in the ellipsoidal sub-region was proven to be uniform and this finding is often referred to as the most important aspect of Eshelby's work because it results in relatively straight forward calculations (Mura 1987). The extension to this analysis considers the stress field outside of the ellipsoid sub-region, this is called the exterior point analysis (Eshelby 1959). A detailed description of the Eshelby method is included in the derivation of the basic two-phase composite equation set-up in Chapter 3 and Section 3.1.1.

The self-consistent scheme is a homogenisation theory (also called effective medium or particle interaction theory) based on the Eshelby method and is suitable for the situation with non-dilute inclusion idealisation. This effective medium theory calculates the average macro-scale properties based on the relative properties of its constituent components. The boundary value problem must first be solved before calculating the interaction between the components. Voids, cracking or damage have an impact on the average properties of the material, as such the self-consistent

scheme is less suitable for nonlinear problems such as quasi-brittle fracture in concrete.

The Mori-Tanaka method is also a homogenisation theory based on the Eshelby method (Mori & Tanaka 1973, Benveniste 1987). This method allows micro-scale models to be used as a basis for macro-scale simulations. The Mori-Tanaka method allows the average inclusion strains to be related to the average matrix strain, instead of being related to the farfield strain. This approach applies to the non-dilute inclusion idealisation. The approximate nature of the theory means that the effective field theory cannot then be transferred to shorter length scales. However, the method is efficient and sufficiently accurate. This approach has also been shown to be applicable to viscoelastic composites (Brinson & Lin 1998) and therefore can be extended for use in inelastic strains, as shown in Section 2.1.4.

These basic homogenisation procedures have been developed to include many other facets of material properties, such as unilateral effects, different shape inclusions and micro-crack interactions. Castaneda & Willis (1995) proposed a rigorous homogenisation procedure which takes account of inclusion interactions through their shape and spatial distribution. The Castaneda & Willis (1995) approach is used to overcome the limitations of the crack interaction in the work of Zhu et al. (2008). Subsequent micromechanical models have been developed to include inelastic response and micro-cracking, and Section 2.2 particularly focuses on the application of models to cementitious materials.

#### **2.1.4 Time dependent inelastic strains**

Inelastic strains are considered to include all strains that do not have an elastic response. Inelastic strains may derive from shrinkage, creep, micro-cracking, differential thermal expansion or ageing. Many of these are time dependent phenomena and are particularly important when simulating cementitious composite materials such as concrete. In cementitious composites, time-dependent inelastic strains are believed to originate in the matrix phase (or matrix-inclusion interface)(van Mier 1997) and thus it advantageous to be able to explicitly model inelastic behaviour in the separate phases of a composite at the micro-scale.

Inelastic strains in inclusions are readily considered with the standard Eshelby (1957) approach and such strains may be added to the eigenstrains arising from a mismatch of elastic properties (Mura 1987, Weng 1988, Nemat-Nasser & Hori 1999). However, if the elastic properties and strains change with time due, for example, to hydration and/or micro-cracking, then methods which consider the non-linear behaviour of the phases are needed.

A general approach for including inelastic strains in one (or more) of the phases

of a composite is to linearise the nonlinear constitutive equations. Models based on this approach have used incremental tangent moduli (Hill 1965), secant moduli (Tandon & Weng 1988, Dunn & Ledbetter 1997) and second order moduli estimates of the phase constitutive equations (Castaneda 1996). Ju & Sun (2001) presented a model for simulating the inelastic behaviour of metal matrix composites in which an effective yield function was derived using a statistical distribution of inclusions.

The method described as ‘Transformed Field analysis’ (TFA) was conceived by Laws (1973) and further developed by Dvorak (1992*a,b*) and Chaboche et al. (2001). This method allows the simulation of generally anisotropic behaviour in the phases of a composite at the expense of solving a local nonlinear system. Recently Monchiet et al. (2012) presented a closed form solution for an orthotropic medium containing arbitrarily orientated cracks.

## **2.2 Micromechanical modelling of cementitious materials**

Micromechanical models have been developed for cementitious materials which take account of inelastic strains. These models have a number of material phases and are considered at various length scales. These length scales are separated by at least one order of magnitude. Firstly, single phase materials will be discussed followed by two-phase and three-phase materials. Multi-scale models are then discussed which consider chemical shrinkage, autogenous shrinkage and basic creep. The transformation techniques required to convert the nonlinear viscoelastic models into linear solutions are then discussed before describing how cement hydration, and the associated strength development, is simulated with multi-scale models. Finally, micromechanical models considering multiple-phases at the same length scale and the introduction of other materials, such as fibres, into the concrete mix are discussed.

A single phase, two-scale micromechanical model taking account of shrinkage, creep and damage was presented by Benboudjema et al. (2001). This work was developed into a hydro-mechanical orthotropic elasto-plastic damage model (Benboudjema et al. 2005) where the model produces a pure viscous response for creep and does not include the Pickett effect. The single phase nature of the model means that free shrinkage cannot be simulated. A two-phase model with shrinkage strain in the matrix could generate stresses in the matrix due to the elastic inclusions and thus would be advantageous.

Neville et al. (1983) reviewed a number of two-phase models for creep and shrinkage of concrete, including those of Hirsch (1962), Counto (1964) and England

(1965), in which the behaviour of the composite was derived from the properties of the aggregate and cement paste phases. A number of more recent models are based on multi-scale schemes in which macro-scale stresses and strains are derived by up-scaling the behaviour from the micro-scale and below. Xi & Jennings (1997) presented a multi-scale model for shrinkage in cement paste that considered the behaviour from the nano-scale up to the meso-scale. The effective bulk modulus and effective shrinkage strains were calculated from the displacement of the phase in the radial direction. Their three-phase model predicts the shrinkage of cement paste at the millimetre level based on the parameters at the micrometre level.

Bernard et al. (2003) described the inelastic strains from chemical shrinkage in cementitious composites with a multi-scale model and Pichler, Lackner & Mang (2007), also using a multi-scale scheme, simulated early age autogenous shrinkage for the same type of cement based material. These multi-scale microstructure models have four levels, namely Calcium Silicate Hydrates (C-S-H)/anhydrous cement, cement paste, mortar and concrete. Chemical shrinkage effects are incorporated at the cement paste scale as part of the hydration reactions (Bernard et al. 2003). The shrinkage eigenstrains are homogenised from the cement paste scale, where the shrinkage eigenstrains rely on the porous C-S-H scale below (Pichler, Lackner & Mang 2007). These shrinkage strains provide linear isotropic stresses within the matrix at the scale of the mortar.

In the work of Bernard et al. (2003), the localisation tensor for each material phase, within each scale, uses the Eshelby inclusion method. The Mori-Tanaka homogenisation scheme is adopted for all levels apart from the cement paste scale, where the self-consistent scheme is adopted because it best suits the percolation theory. Pichler, Lackner & Mang (2007) took the shrinkage eigenstrains from the cement paste scale by using a strain localisation tensor, Eshelby tensor and repeated use of the Hill's Lemma. Hill's Lemma use a condition such that the local average equilibrated stress and local compatible strain field can be related to the macroscopic stress and strain (Zaoui 2002).

These multi-scale approaches have many benefits. The macroscopic material can be related to the intrinsic properties of its constituents and to the mixture composition. A link can also be established between the material components and cement chemistry (Pichler, Lackner & Mang 2007). In addition to shrinkage, creep deformations can also be included at the macroscopic concrete scale (Pichler, Lackner & Mang 2007) or included in the up-scaling process (Pichler & Lackner 2008, 2009).

A three-scale multi-staged model was presented by Scheiner et al. (2009) describing basic creep in early age concrete. The first homogenisation occurs with a two-phase composite model, consisting of cement paste and aggregate, where only

the cement paste exhibits the creep properties. The cement paste properties are obtained by homogenising the components of cement, water, hydrates and air. The viscoelastic behaviour is deemed to only appear in the cement hydrates which are approximated by a Burgers creep model. Laplace-Carson transformations allows homogenisation of viscoelastic properties to be related to the elastic properties. These are then back-transformed into the time domain using a Gaver-Wynn-Rho algorithm.

The viscoelastic creep of composite materials is discussed in the early works of Laws & McLaughlin (1978). They transformed the viscoelasticity problem into a "quasi-elastic" problem and made comparisons with a number of materials. Viscoelastic constitutive equations are also used in a micromechanical context by Barbero & Luciano (1995) who use the Laplace transform technique. It is noted that the correspondence principle used in Barbero and Luciano's work cannot be applied to nonlinear models. A simplified linear version of a power law is required to write the creep compliance. However, the authors state that there is a good correlation with experimental data for materials with transversely isotropic fibres.

The effect of creep in the cement paste has been studied by Sanahuja & Dormieux (2010) using a micromechanical model. Their approach applies the Eshelby principle to the ratio of pores to the matrix material and homogenises this two-phase material using a self-consistent scheme. The effective creep functions for short and long term are obtained. The non-ageing linear viscoelastic problem is transformed into to a linear elastic problem by the means of the Laplace-Carson transform. It is noted that a recent approach by Sanahuja (2013) negates the need to invert the Laplace Carson transformation by using a Volterra integral which is evaluated numerically and validated using convergence analysis.

Multi-scale models are particularly successful at simulating the development of strength during cement hydration. Sanahuja et al. (2007) simulated the increasing stiffness of cement paste during hydration using a micromechanical model. For a degree of hydration greater than 50 %, the modelling agrees with the experimental results even without the consideration of creep processes. This model considered the creep and hydration processes at the scale of the cement paste. The model, presented by Pichler & Hellmich (2011), has recently been employed in a combined experimental-numerical investigation of the micro-structure of hcp which explored the importance of the gel-space ratio and the role of unhydrated clinker on hardened mechanical properties of the paste (Pichler et al. 2013). Zhang et al. (2012) developed an effective micromechanical model for simulating shrinkage in isolation. This model uses the internal relative humidity (RH), related to the associated capillary pressure, as the driving parameter for shrinkage predictions. Zhang et al. (2013) applied this type of multi-scale model, in a thermo-hygro-chemo-mechanical

framework, to the analysis of early-age concrete and used the model to explore the influence of the ‘age of shutter stripping’ on the quality of the near-surface concrete. Chen et al. (2013) used a micromechanical model for mortar in which the sand particles were treated as elastic inclusions and the hcp matrix was assumed to be elasto-plastic. The authors used this model to explore the effect of changing moisture content on the constitutive behaviour of mortar specimens.

When considering a multi-scale approach there is also the opportunity to work with many phases at the same length scale. Pichler et al. (2010) considered a number of material phases within a RVE. There are three governing conditions presented by Pichler et al. (2010) which are taken from Dvorak (1992a): strain compatibility, stress admissibility and the elastic reciprocal theorem. The Eshelby matrix-inclusion scheme has been used and developed for each phase in the composite. The TFA (Dvorak 1992a) is extended to consider arbitrarily many Hill’s tensors. The authors derive a Hill tensor relationship for all of the phases by introducing ‘auxiliary matrix eigenstresses’ to account for the multiple phase eigenstress interaction. This model has been applied at the cement paste scale.

Finally, this micromechanical approach has been extended to include fibres in the concrete (Dutra et al. 2010). This work is carried out on two levels, in which concrete at micro-scale and the steel fibres are treated as being separate. At this scale, the concrete consists of aggregate particles and mortar which is assumed to be an homogenised matrix containing micro-cracks. The authors show that model becomes less accurate as the fibre volume increases. A significant restriction of this model is that it does not allow for anisotropic loading behaviour.

Micromechanical models have successfully been developed for cementitious materials taking account of inelastic strains. However, to date, there is no single model that is capable of describing all relevant inelastic processes (Section 2.1.1). A concrete material model, in its basic form at the micro-scale, should contain aggregate particles embedded in a mortar matrix represented by a two-phase model. Introducing many phases and multiple scales, as well as being more complex, introduces additional assumptions, material parameters and increases computational cost. Using a relatively simple two-phase micromechanical model based on a limited number of physical mechanisms and a limited number of assumptions, in the author’s opinion, provides the right balance between accuracy and complexity.

## **2.3 Micro-cracking considerations in concrete**

A number of different cementitious material models were briefly discussed in Section 2.1.1. In this section the dominant role of micro-cracking in governing the non-linear behaviour of these materials was discussed. This micro-cracking is thought

to occur initially in the matrix material, at matrix-inclusion interfaces, where the highest stresses are reached (Prado & Van Mier 2003).

There are two particular requirements when describing micro-cracks in concrete. The first is to estimate the effective elastic properties of a micro-cracked media and the second is to determine the micro-crack initiation and evolution law. Micro-cracks are typically idealised as either penny-shaped, slit like or flat ellipsoidal voids (Mura 1987). Complex phenomena such as interacting micro-cracks, micro-cracking recovery and micro-cracking closure effects can also be described at the micro-scale. The directional dependent crack density parameter of Budiansky & O'Connell (1976) can be regarded as a damage variable (Jefferson & Bennett 2007) for brittle materials which indirectly links the penny-shaped crack volume fraction to directional damage degree and micro-crack distribution.

The effective elastic properties of the micro-cracked media are generally evaluated using one of two approaches. In the direct method the micro-cracks or fracture strains are added to the elastic homogenised macro-strain. In the homogenised method, the micro-cracks are included in the homogenisation procedure.

The direct approach to determining the effective elastic properties has been given by many authors (Mura 1987, Nemat-Nasser & Hori 1999, Krajcinovic 2000, Voyiadjis & Kattan 2006). An example of the direct approach specifically used in micromechanical models, is given by the work of Pensée et al. (2002). A full 3D anisotropic damage model for brittle materials was developed using an elastic solid combined with penny-shaped open and closed micro-cracks. The additional fracture strain is provided by adding the contributions from a set of penny-shaped micro-cracks evaluated using Eshelby theory (Nemat-Nasser & Hori 1999, Mura 1987). This fracture strain was added to the strain contribution for the elastic solution. A similar approach was employed by Jefferson & Bennett (2007) and Jefferson & Bennett (2010). Pensée & Kondo (2003) found that strain based formulations, taking account of moderate crack density, are preferred to stress based formulations, having non-interacting cracks, for brittle anisotropic damage with unilateral micro-cracking effects.

The alternative approach to determining the effective elastic properties of concrete is the homogenised method which is typically based on the standard Eshelby homogenisation procedure. A composite with micro-crack inclusions in the matrix are up-scaled (Eshelby 1957, Mura 1987). However, in these basic models, crack interaction is not taken into account. Lee & Ju (2007) analysed the stress within an infinite solid containing both a penny-shaped micro-crack and a spherical inclusion. A two step superposition scheme was used to obtain a stress field over the crack site. This was interpreted in terms of the stress intensity factor for a penny-shaped crack.

Both the direct and homogenised approaches are compared by Zhu et al. (2008).

The direct approach used is from Pensée et al. (2002) and the homogenisation schemes include Mori & Tanaka (1973) and Castaneda & Willis (1995). It was found that only Castaneda & Willis (1995) can take account of the spacial distribution of frictional micro-cracks (Zhu et al. 2009). This work was developed further to included tensile and compressive tests (Zhu et al. 2011). Their formulation, that combines micro-cracking and frictional sliding, led to a hybrid mechanistic-phenomenological model. Another example of such an approach was given by Brencich & Gambarotta (2001) where a plane crack model was simplified to an isotropic damage model with frictional sliding for closed cracks under compression. Isotropic versions of this model were validated with experimental data. In later works (Gambarotta 2004) developed this model into an anisotropic version and applied it to a biaxial stress state problem.

Jefferson & Bennett (2007) looked to retain a mechanistic approach throughout their derivation of a micromechanical model for concrete by introducing a rough crack closure model alongside penny-shaped micro-cracks. This contact model was based on the Craft concrete model which simulated rough crack contact behaviour (Jefferson 2003).

Pichler, Hellmich & A. Mang (2007) studied the fracture process zone ahead of a main macro-crack and developed a model where the penny-shaped micro-cracks were treated as void inclusions using the classical Eshelby (1957) procedure. The penny-shaped voids were specialised for sharp open cracks to simplify the approach. This included the void having zero stiffness, a volume fraction linked to the Budiansky crack density parameter and where the height of micro-crack tends towards zero. Micromechanics and fracture energy theories were combined successfully although they showed that the approach led to an overly brittle post peak solution, thought to be due to the model not accounting for crack arresting due to the presence of aggregate particles or large voids. This initial work was later developed to study the cracking risk of partially saturated porous geomaterials in a thermodynamically based microporoelasticity model (Pichler & Dormieux 2010a). Spherical micropores at the micro-scale were homogenised and up-scaled to form the matrix which included penny-shaped micro-cracks. This was further extended and applied to a drying shrinkage case (Pichler & Dormieux 2010b). One of the difficulties in simulating anisotropic cracking using a void is that, upon first cracking, the once isotropic medium turns into an anisotropic medium and the standard Eshelby tensors are no longer applicable.

Having addressed the effective elastic properties of a cracked media, attention is now briefly given to damage initiation and evolution laws. Pioneering work of Kachanov (1982) incorporated the initiation and propagation of micro-cracks in the theoretical framework of fracture mechanics. Many researchers have dedicated time

to dealing with issues of how these cracks are incorporated and homogenised with the elastic components. Alongside each of these developments an initiation criterion and continuing yield conditions are been proposed. A few of the significant contributions included in the review above are the energy-based yield criterion with a general elastic predictor and damage corrector scheme (Pensée et al. 2002) and a criterion based on a combination of friction and damage limit states (Gambrotta 2004). However a strain based damage rule with an experimentally derived exponential equation has been shown to be particularly effective (Jefferson & Bennett 2007, 2010, Mihai & Jefferson 2011). This damage initiation and evolution is presented in Chapter 3, Section 3.3.

Avoiding the need for a numerical solution to evaluate the Eshelby tensor for a changing generally anisotropic matrix material has great advantages (Desrumaux et al. 2001). It is apparent that a combination of volumetric cracking built into the homogenisation equations, added strains to allow for directional cracking and allowing for progression from micro-cracks to macro-cracks would be very useful for describing a 3D cementitious material. Having a void as inclusions built into the modelling framework provides an opportunity to bring in self-healing through filling of these voids. Utilising these micromechanical frameworks, self-healing mechanisms are discussed in Section 2.4 and in Chapter 6.

## **2.4 Self-healing cementitious composites**

Research into healing of cementitious materials remains a prominent topic, despite autogenous healing first being recognised by the French Academy of Science in 1835 (Hearn 1998). The early work of the last century investigated this new phenomena with particular interest in the long term exposure to the environment and the water permeability of concrete structures (Abrams 1925, Glanville 1931). Various researcher have looked to capitalise on these early findings by taking advantage of this healing concept. Section 2.4.1 provides standard definitions, categorises the different type of healing and intervention mechanisms. These general descriptions can be applied to many material types.

The breadth and depth of current knowledge in cementitious materials is shown by the comprehensive ‘State-of-the-Art Report of RILEM Technical Committee 221-SHC: Self-Healing phenomena in Cement-based materials’ by de Rooij et al. (2013). The focus of this review will remain within the field of cementitious materials and in particular on autogenous self-healing. The mechanisms believed to be responsible for this autogenous healing are described in Section 2.4.2. Experimental evidence for this healing is presented in Section 2.4.3 and finally, in Section 2.4.4, general self-healing modelling is discussed.

## 2.4.1 What is self-healing?

“*Self-healing*: Any process by the material itself involving the recovery and hence improvement of a performance after an earlier action that had reduced the performance of the material.”

This general description is provided by de Rooij et al. (2013). However, self-healing materials can be classified further into categories. de Rooij et al. (2013) describes self-healing as either autogenic or autonomic as shown in the following definitions.

“*Autogenic*: The self-healing process is autogenic when the recovery process uses materials components that could otherwise also be present when not specifically designed for self-healing (own generic materials).”

“*Autonomic*: The self-healing process is autonomic when the recovery process uses materials components that would otherwise not be found in the material (engineered additions).”

A Venn diagram, as shown in Figure 2.3, from JCI TC-075B (Igarashi et al. 2009) by the Japanese Concrete Institute diagram further captures the terminology used when classifying self-healing materials.

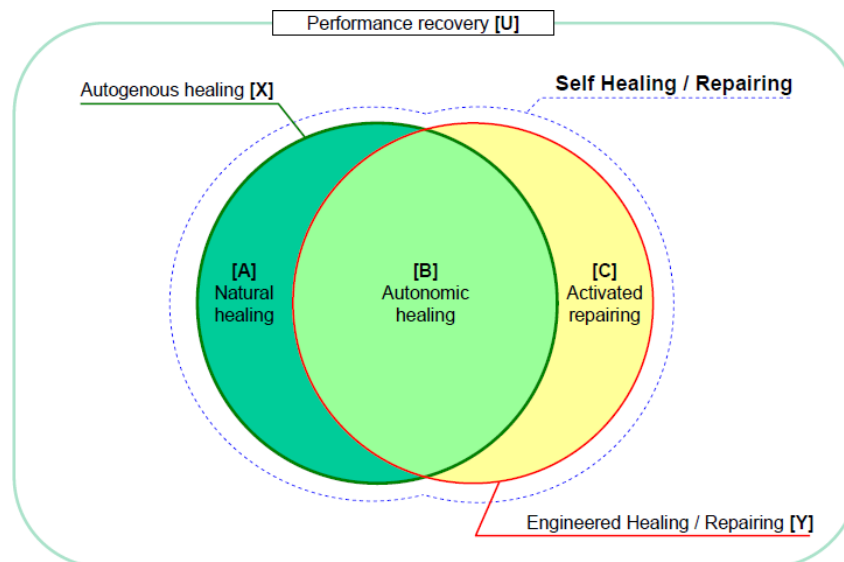


Figure 2.3: Venn diagram to explain terminology of self-healing according to JCI TC-075B

The healing intervention mechanism can be either passive or active. The report by de Rooij et al. (2013) also consider active healing materials to have a level of intelligence. Furthermore, the concept of performance recovery by a healing function

is important. This performance recovery is often presented as two distinct self-healing mechanisms focusing on regaining environmental properties or mechanical properties. Examples for improvement in environmental properties of concrete include water tightness and durability linked to limiting crack widths, prevention of carbonation and corrosion by filling up the cracks. The possibilities for improving mechanical properties following damage include strength, toughness and stiffness recovery.

Autogenic, or also termed autogenous, healing materials have the intrinsic ability to heal themselves. Cementitious materials possess this quality which is examined in further detail in the next three Sections 2.4.2, 2.4.3 and 2.4.4.

Passive autonomic healing within a polymer material was described in the landmark paper by White et al. (2001) in the Nature journal. This work involves repairing damage in structural polymer composites. Micro-capsules containing healing agents were embedded into the composite, where upon cracking, the healing agent was released into the crack. Polymerisation of the healing agent occurs on contact with a catalyst embedded in the composite in which up to 75 % of the toughness was recovered.

More specifically for autonomic self-healing in cementitious materials, various techniques have been investigated. An early example of active autonomic healing was the timed release of chemicals from fibres into cement matrices (Dry 1994). A summary list of autonomic healing solutions is provided here along with significant contributions from research groups.

- Hollow fibres (Dry 2000, Joseph et al. 2010)
- Micro-encapsulation (Boh & Sumiga 2008)
- Expansive agents and mineral admixtures (Ahn & Kishi 2010)
- Bacteria (Jonkers et al. 2010, Van Tittelboom et al. 2010)
- Shape memory materials (Saiidi et al. 2007, Jefferson et al. 2010)
- Super absorbent polymers (Snoeck et al. 2012)
- Cement replacement materials (Van Tittelboom et al. 2012)
- Engineered Cementitious Composite (ECC) (Li et al. 1998, Li & Yang 2008)

Detailed discussion and analysis of each technique is beyond the scope of this review. Interested readers are directed to the works of Wu et al. (2012) and Van Tittelboom & De Belie (2013) where detailed comparative studies have been undertaken. Many of these systems rely on the intrinsic properties of cementitious materials which are linked to the availability of unhydrated cement and its ability to

provide calcium ions. This gives further weighting to the need to fully understand autogenous healing first.

## 2.4.2 Cementitious autogenous self-healing mechanisms

Autogenous healing in a cementitious material is a complex chemo-physio-mechanical phenomenon. Figure 2.4 from de Rooij et al. (2013), based on the original work by Edvardsen (1999), shows the different causes of autogenous healing; these being physical, chemical and mechanical causes.

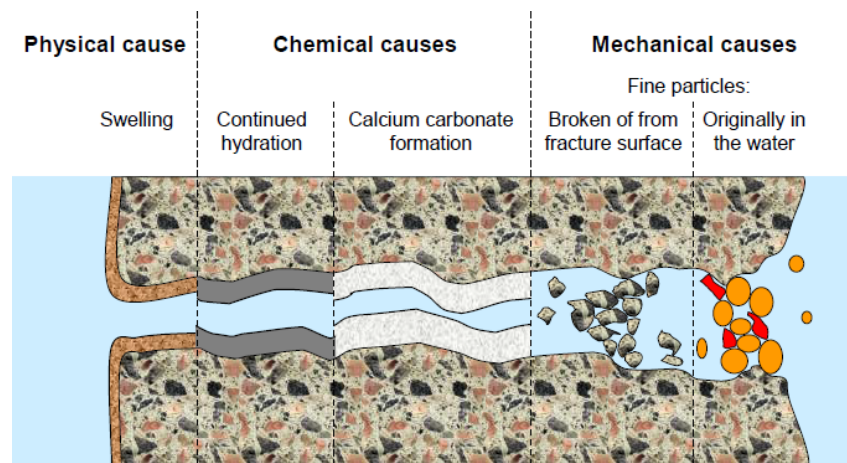


Figure 2.4: Different causes that can lead to autogenic self-healing

Physical causes are linked to swelling of concrete in the presence of water (Hearn 1998). This swelling can be enhanced with expansive agents and geomaterials. One such material is montmorillonite, a swelling clay mineral, these do not improve the mechanical strength, only durability (Ahn & Kishi 2010).

Mechanical causes are linked to fine particles blocking the flow paths through the crack. These particles can be present due to impurities in the water or movement of fragments of concrete mobilised during the cracking process. Another mechanism linked to the movement of particles is the self-sealing (or leaching) effect. These were observed whilst measuring self-healing using water permeability tests. Various minerals and hydrates present in cement paste dissolve in water and are then deposited when the physical or chemical conditions change (Hearn 1998).

Chemical causes are believed to be the main contributor to self-healing in cementitious materials. Numerous postulations, often contradictory, have been made over the years as to what chemical processes are linked to autogenous healing in concrete. Early works suggested that continuing hydration of un-reacted cement particles lead to build up of hydration products which eventually bridge the cracks (Soroker & Denson 1926, Brandeis 1937). Indeed, rehydration products found in small cracks (1-10 $\mu$ m) due to the freeze thaw cycle have been shown to be mainly

C-S-H, the main component of reacted cement paste (Jacobsen et al. 1995). Recent mechanical characterisation by comparing re-loading specimens after curing under water and air, shows an initial stiffness gain in specimens cured in water coincident with new hydrates being formed (Granger et al. 2005).

Others, more recently attribute the whole of self-healing to carbonation, which is the precipitation or build-up of calcium carbonate ( $CaCO_3$ ) on crack surfaces (Clear 1985, Hearn 1998, Edvardsen 1999). This  $CaCO_3$  is often seen as a white crystalline substance. This  $CaCO_3$  is formed when the calcium hydroxide ( $Ca(OH)_2$ ) in concrete reacts with the carbonic acid ( $H_2CO_3$ ) formed from carbon dioxide ( $CO_2$ ) dissolved in water or moisture. This is the reverse chemical process of calcination of lime in the cement kiln. Carbonation is often an unwanted reaction in reinforced concrete, since it decreases the alkalinity on and below the surface of concrete. A high alkaline environment is required to pacify the steel reinforcement and prevent corrosion (Neville & Brooks 2010). The self-healing carbonation process which deposits  $CaCO_3$  within crack eventually block the cracks, reducing the migration paths and therefore reducing the risk of concrete degradation through chloride or sulphate attack. Continued hydration is linked to early age cracks where there is a surplus of unhydrated cement. Conversely, calcium carbonate formation is associated with healing in older concrete once the hydration process has largely been completed. Therefore the type of self-healing that occurs depends very much on the environment and age of the concrete.

### **2.4.3 Autogenous self-healing experiments**

There are two distinct investigative approaches that are typically used when investigating self-healing: qualitative observation and quantitative assessment of healing. Autogenous healing in cementitious materials has been investigated using visual techniques, by changing the environmental conditions, measuring permeability and examining the mechanical properties.

The advancement of new material testing techniques over the last 50 years, such as acoustic emissions examining (to measure the Kaiser effect), x-ray diffraction (XRD) (to discover the chemical composition) and scanning electron microscope (SEM), all help to provide greater visual detail and insight into the self-healing phenomenon (Mor et al. 1989, Jacobsen et al. 1995). Healing can be observed in surface cracks using microscopes. However, the latest visual techniques can provide both qualitative and quantitative data. Microstructure and fracture in three dimensions (3D) have been investigated using a high resolution 3D scanning technique called X-ray microtomography (CT) (Landis et al. 2003). The microstructure formation process of cement paste is examined by using a combination of techniques

such as ultrasonic pulse velocity (UPV), non-contact electrical resistivity (NER) and X-ray computed tomography (CT) (Jiang et al. 2012). In this work the development of cement paste properties during hydration was tracked by calculating the solid volume fraction change with age. This recent work has potential to be applied to formation/precipitation of healing products inside a crack. Indeed, Fan & Li (2013) present two samples characterising the self-healing response within the micro-cracks using time dependent 3D micro-CT. This appears to be a promising technique which could lead to further understanding of healing in concrete at the micro-scale.

Environmental recovery has been traditionally quantified by measuring the permeability of water through a crack or observing crack closure on the surface of concrete. A comprehensive list of state-of-the-art techniques are given in de Rooij et al. (2013). The techniques outside the scope of this review are capillary water absorption, resonant frequency analysis, ultrasonic measurements, electrochemical impedance measurements and resistance against corrosion. It is clear that different environmental control conditions have been used to examine the various mechanisms that impact on autogenous healing in concrete. For example, the presence of water, initial size of crack, curing temperature, compression and the age of material, all have an effect on autogenous healing.

Experimental observations have been made on the importance of water in the self-healing process (Hannant & Keer 1983). Water is an essential factor in enabling self-healing. The traditional approach to determine the degree of self-healing is to measure the water permeability through cracks and inspect the surface crack (Clear 1985, Ahn & Kishi 2010). These techniques provide an indirect measurement of regained durability properties.

An example experiment showing self-healing in concrete is given by Edvardsen (1999) where a 0.2 mm width crack in a 400 mm thick concrete sample is subjected to 2.5 m head of water. The initial flow rate was 30 litre/hour through the crack. This flow rate reduced gradually to almost zero after 400 hours (Edvardsen 1999). Using water to measure the healing is a problem, since water reacts with the products in the concrete and is itself fundamental to the chemical healing processes. Furthermore, the permeability of the concrete matrix is dependent on the moisture content which changes as water migrates through the sample. Other experiments identifying the effect of self-healing include isolating cracks from the carbonation, using different chemical compositions of water (Parks et al. 2010) and having still or flowing water (Clear 1985).

All experiments show that the smaller the crack size the higher the degree of self-healing. This is believed to be due to less build-up of material being required to bridge the cracks. Particles are also more likely to get trapped in smaller cracks

increasing the sealing effects. Crack widths of less than 0.3 mm are typically investigated for autogenous healing to satisfy maximum tolerable crack widths for serviceability limit state design (EN 1992 2008). Some studies have shown that there is little likelihood of autogenously healing cracks wider than 0.1 mm (Reinhardt & Jooss 2003). However, other studies show that 0.2 mm can heal completely with 0.3 mm healing sufficiently to limit the permeability (de Rooij et al. 2013). However, more recent work with the expansive and self-healing agents have shown cracks up to 0.22 mm completely healing over a period of 33 days (Ahn & Kishi 2010).

A higher temperature has been shown to favour a faster self-healing process in cracks measured by water permeability (Reinhardt & Jooss 2003). Furthermore, it has been demonstrated that natural self-healing is significantly enhanced if a crack is subject to compression (Ter Heide & Schlangen 2007). The amount of compression has been shown not to impact on the degree of healing. Sufficient compression is only required to bring the two crack faces into contact or to close sufficiently for healing to take place. The younger the concrete the greater the potential for autogenous healing, likely to be due to there being more un-hydrated cement available (Ter Heide & Schlangen 2007). The potential for healing is also higher during first exposure to water curing where there is an increased water leakage rate (3 to 5 days) (Edvardsen 1999) and is more likely to occur in younger concrete specimens (de Rooij et al. 2013). Even with considerably older samples (3 months to 1 year) research on freeze/thaw cycles showed that self-healing remained a possibility with recovery of 4-5 % compressive strength (Jacobsen & Sellevold 1996).

Studies quantifying self-healing through regained mechanical properties to date have mainly been focused at the macro-scale. Examples include impact on compressive strength, fatigue resistance, tensile strength of flexure and splitting tests through modulus of rupture tests. Granger et al. (2007a) compared the mechanical recovery of samples aged in water and air using three point bending and acoustic emission apparatus. Micro-cracking within a material was detected from the acoustic emission response before any cracking was visible. Zhong & Yao (2008) used an ultrasonic pulse velocity measurement of concrete cubes to obtain the degree of damage in a specimen before and after autogenous healing. This reading was compared against the ratio of compressive strength recovery of samples. They found that there was an optimum degree damage, which gave the highest ratio of strength increase. Van Tittelboom et al. (2011) compared the healing efficiency of cementitious materials with manual healing against autonomous healing. The autonomic healed beams had tubular capsules containing a healing agent that was release upon cracking. The efficiency was measured using peak strength, stiffness and permeability. All three measurements showed an improvement in the autonomous samples.

The measurement of strength recovery, from the macro-scale experiments, is a direct measurement of healing performance. The strength recovery ratio depends on a peak load (or stress), a measurement of the remaining strength (load or stress) at the time of healing is initiated and the strength (load or stress) after healing has occurred. This is represented by  $c$  in equation 2.4 and is illustrated in Figure 2.5 (Homma et al. 2009).

$$c_{\gamma} = \frac{\sigma_2 - \sigma_0}{\sigma_1 - \sigma_0} * 100 \quad (2.4)$$

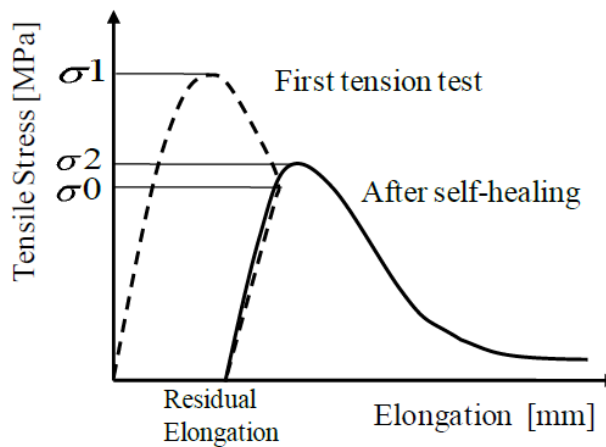


Figure 2.5: Schematic of the relationship between tensile stress and tensile elongation of FRCC

In situ non-destructive tests are also used to determine the mechanical properties of concrete. Some of these tests make use of indentation techniques in which the material response is related indirectly to determine the strength properties. These have been applied at the macro, micro- and nano-scale and a comprehensive review is given in Section 5.1.1.

The mechanical properties of self-healed cementitious materials are required to enable any micromechanical modelling to be calibrated and verified. The availability of mechanical properties for self-healed materials is limited, in particular, when considering the micro-scale and its application in micromechanical computational models.

#### 2.4.4 Self-healing modelling review

Numerical research seeks to explain and simulate experimental findings and as such its progress tends to follow experimental discoveries. Self-healing materials also follow this trend, evident at the Fourth International Conference on Self-Healing Materials 2013, where approximately 10 % of contributions addressed numerical or analytical modelling. The wide range of materials mean that numerical models

for self-healing processes should concentrate on the most promising technologies and on understanding the associated healing mechanisms. These can be individual component mechanisms or contributions from any of the thermo-hygro-chemo-mechanical processes. This section reviews a range of these modelling techniques and considers how they could be applicable to autogenous healing of cementitious materials.

When visualising healing within a crack, initial thoughts turn to discrete crack modelling. Recent work by Perelmuter (2013) looked to explicitly describe the effects of healing on discrete cracks by using a crack bridging approach. Even though this approach is promising, there is very limited research work on healing in the discrete crack field. Most of the healing models have been developed around the relatively simple smeared crack approach. Traditionally these smeared models have irreversible damage and it would seem important to maintain this quality. Recent developments in micromechanical modelling have shown a tendency to move away from being phenomenologically based, as already mentioned in Section 2.1.2. Mechanistic models have the advantage of being less dependent on individual experimental results and rely on a limited number of easily measurable material properties. Understanding the essential healing components is key to deriving realistic dependable self-healing models, as is the measurement and quantification of self-healing properties.

A multiple phase self-healing model was developed by Remmers & de Borst (2008). Their model simulated three distinct stages in the healing process: fracture, transport of fluid to the healing location and mechanical recovery. This healing is simulated by re-bonding the crack surfaces with increased stiffness in the cohesive constitutive relationship controlling the crack opening (Schimmel & Remmers 2006). This interface element is described by the traction relationship shown in equation (2.5).

$$\bar{\sigma} = (1 - \omega)Ku + \omega_{th}f(t - t_{th})(1 - \omega_h)K(u - u_{th}) \quad (2.5)$$

The stiffness of the undamaged material is given by  $K$  and the opening of the crack is given by  $u$ .  $\omega$  is the damage parameter of the original material and  $\omega_h$  is the damage parameter of the healed material. Both parameters are functions of the opening.  $u_{th}$  and  $\omega_{th}$  are the crack opening and damage at the time of healing. The new material is undamaged at the time of healing and develops its strength in relation to a given time function ( $f(t - t_{th})$ ). This approach is at the macro-scale and working with a micromechanical model could provide further insight into the mechanical response of the healing.

The quantity and properties of the healing agent in a damaged location is re-

quired to be able to model self-healing. This necessitates the use of a hydro-chemical transportation model. In many healing processes, the active chemical species are transported through the pore fluid via advective, diffusive and dispersive fluxes (Gawin et al. 2008, Baroghel-Bouny et al. 2011). In other cases, such as the polymer work of White et al. (2001), the healing agent is transported through the macro-cracks by capillary flow. The factors governing the capillary flow of healing agents through macro-cracks in cementitious materials have recently been investigated by Gardner et al. (2014).

Another healing mechanism is presented by Mergheim & Steinmann (2013a). The thermodynamically consistent self-healing thermoset polymer model is derived at the macro-scale using an isotropic scalar damage model (Mergheim & Steinmann 2013b). The healing component is added into the strain-energy density, which leads to the constitutive relationship shown in equation (2.6).

$$\bar{\boldsymbol{\sigma}} = (1 - \omega) \mathbf{D}_{el} : \bar{\boldsymbol{\varepsilon}} + (1 - \omega_h) \boldsymbol{\sigma}^h \quad (2.6)$$

The contribution of healing stress ( $\boldsymbol{\sigma}^h$ ) is defined by equation 2.7.

$$\dot{\boldsymbol{\sigma}}^h(t) = h(t) \mathbf{D}_{el} : \dot{\boldsymbol{\varepsilon}} \quad (2.7)$$

$\omega$  is the original material damage variable and  $\omega_h$  is the healed material damage variable.  $\mathbf{D}_{el}$  denotes the elasticity tensor and  $\mathbf{D}_{el} : \boldsymbol{\varepsilon}$  represents the effective stress of the original material. This rate equation ensures that when the strain rate is zero, only the stiffness, not the stress, is increased during healing. Mergheim & Steinmann (2013b) use a 1D example to illustrate the model response with healing for after load removal, partial damage and constant strain cases.

Traditionally damage that occurs in continuum damage mechanics is irreversible. However, a team of researchers in Texas, targeting healing in asphalt, assumed that this recovery can occur by applying a healing factor (Abu Al-Rub et al. 2010). Equation (2.8) shows how the composite average stress ( $\bar{\boldsymbol{\sigma}}$ ) is related to the composite elastic stress ( $\bar{\boldsymbol{\sigma}}_e$ ).

$$\bar{\boldsymbol{\sigma}} = (1 - \omega(1 - h)) \bar{\boldsymbol{\sigma}}_e \quad (2.8)$$

$\omega$  is the irreversible original damage parameter and  $h$  is healed fraction of the damaged area. This micro-damage healing model integrates non-linear viscoelastic, viscoplastic and viscodamage constitutive models with application focused on asphalt and fatigue response. A phenomenological healing evolution function is used where the rate of healing is dependent on two material constants and healing viscosity, which itself is a function of temperature. Three continuum damage mechanics transformation approaches using the strain, elastic strain energy and power equiv-

alence hypotheses are related to this healing mechanism by Darabi et al. (2012). This micro-damage healing model and power-correlating transformation hypothesis were incorporated into a general thermodynamic framework for a healing constitutive model Abu Al-Rub & Darabi (2012), Darabi et al. (2013). This enhanced approach splits the forces into energetic and dissipative components, ensuring that the positive-definite rate of dissipation is maintained, thus ensuring that the model obeys the laws of thermodynamics. Even though these models aim to simulate healing at the micro-scale they do not explicitly take account of the different material phases.

Other authors who have developed micro-damage healing models within a thermodynamic framework are Miao et al. (1995), Alfredsson & Stigh (2004) and Barbero et al. (2005). Miao et al. (1995) presented one of the first thermodynamically based healing models where an experimentally derived rate of healing function is derived for crushed rock salt. Alfredsson & Stigh (2004) used a strain equivalence hypothesis where the damage variable is increased for continued damage and decreased to represent healing. Barbero et al. (2005) developed an elastoplastic-damage-healing constitutive model for fibre reinforced polymer-matrix composites. This work was extended by Voyiadjis et al. (2011) to deal with healing in shape memory polymers by using elastic strain energy equivalence hypothesis to obtain a new damage-healing effect tensor. These works do not decompose the damage and micro-damage healing forces into energetic and dissipative components.

Many of the constitutive models presented are not specific to a material type and depend on strength properties and damage relationships. An area of research that specifically addresses cementitious materials is one that takes account of the hydration process. Furthermore, simulating the hydration process in a cementitious material, based on continued hydration, has direct application to autogenous healing. Schlangen et al. (2006) tested this approach for early age crack healing in concrete using a 2D FE model with developing material properties. Once a specimen has been cracked, the healing process was simulated as having the same developing properties as the original concrete but with a time delay. Developing properties included maturity, degree of hydration, temperature and moisture potential. The example chosen was a beam cracked one day after casting and then immersed in water for 14 days to allow healing to take place. The specimen was then tested at 15 days and it was found that the tensile strength of this healed beam on day 15 was equal to the tensile strength gain of the main uncracked concrete at 14 days. The study therefore showed that an increase in flexural stress was achieved in the cracked beam. The authors postulated that this was due to the unhydrated cement in the crack being able to fully hydrate in the presence of additional water and thus achieve a higher strength. The authors acknowledge that their model predictions

do not exactly match the experimental data but that the model is able to simulate the healing mechanism. Further detailed studies considering the chemical composition and the effect of continued hydration on the self-healing potentials have been investigated using water transport, ion diffusion and thermodynamic theory (Ye & van Breugel 2007, Huang & Ye 2012). Unhydrated cement particles were simulated using HYMOSTRUC3D, a cement hydration microstructure model. The amount of water from broken capsules to promote self-healing could be optimised. This study did not consider the healing impact on mechanical strength.

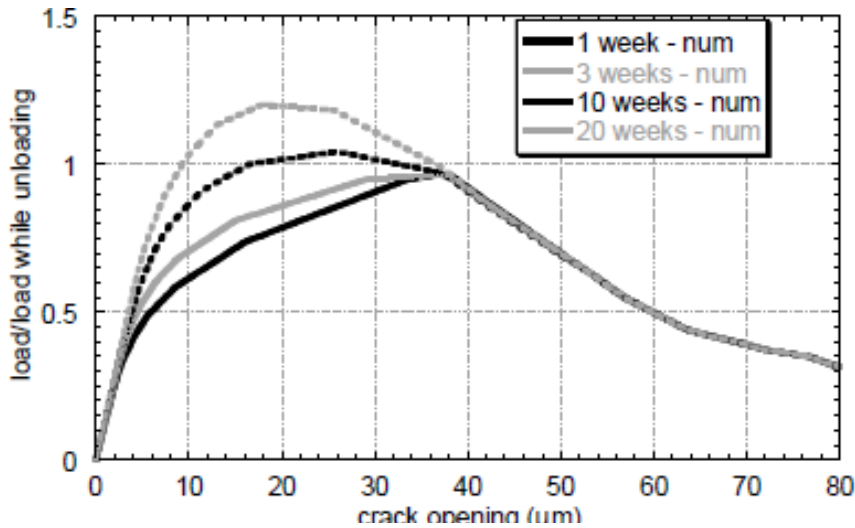
The hydration processes and elastic damage models have been combined in a dual coupled approach within a thermodynamic framework by Granger et al. (2007b). The healing behaviour in their model is simulated by introducing new mechanical properties into the damaged layers within a layered finite beam element model using a thermodynamic potential. The resulting constitutive relationship is shown in equation (2.9).

$$\bar{\sigma} = E [(1 - \omega) + (1 - \omega_h) g(x, \omega)] \bar{\epsilon} \quad (2.9)$$

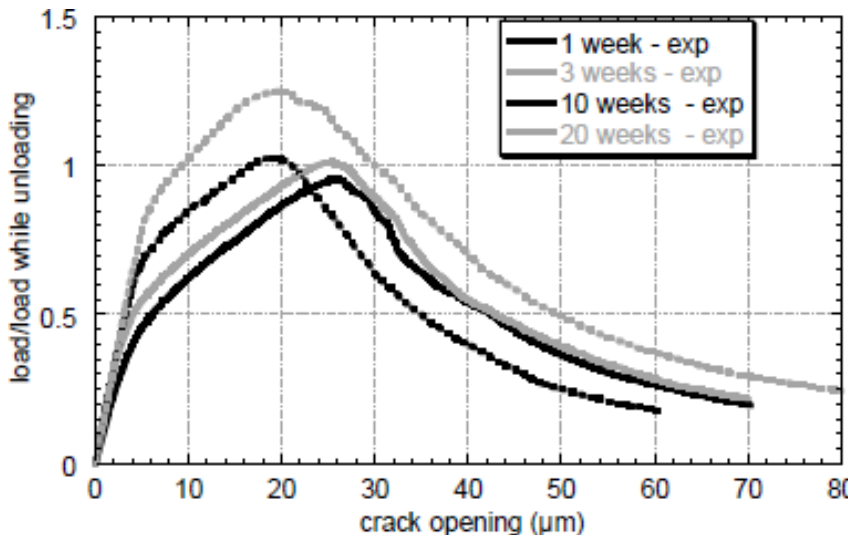
$E$  is the Young's modulus,  $\omega$  and  $\omega_h$  are the damage variables of the original and healed materials.  $g$  is a scalar function dependent on the evolution of healing linked to the continued hydration of cement ( $x$ ), and the degree of damage at time of healing. The evolution of damage in the newly healed material, represented by  $\omega_h$  takes precedence over the primary damage ( $\omega$ ) which continues when  $\omega_h$  has reached unity. Figures 2.6 show how the numerical and experimental results compare.

The numerical solution does show an increase in strength during the re-loading phase due to healing, similar to that seen in the three point bending experiments. However, the distinctive two gradient pre-peak slope apparent in the experimental curves is not evident in the numerical responses. This model by Granger et al. (2007b) is at the macro-scale which allows for easy comparison with experimental results.

The same research group extended this coupled model by using a hydro-chemo-mechanical model for autogenous healing (Hilloulin et al. 2013). A macro-scale 1D damage model is used where total and plastic strain are related to an isotropic scalar damage variable. The authors describe how ingress of water through a crack changes the water concentration which in turn triggers the hydration. This continued hydration causes a volume build-up of new material within the crack affecting the overall mechanical properties by increasing the stiffness. The numerical results are compared to an experimental plot from Granger et al. (2007b) and is shown in Figure 2.7. The general characteristic response is represented by the numerical model. The authors suggest investigating the elastic properties in order to obtain



(a) Numerical simulations



(b) Experimental results

Figure 2.6: Comparison of numerical and experimental bending test on healed concrete specimens (Granger et al. 2007b)

the distinctive dual gradient in the re-loading phase.

A comparison can be made between the self-healing processes and other phenomena, such as mechanical recovery in cracks and precipitation of materials within metals. The mechanical recovery of cementitious materials when unloading has been shown to occur during experiments. This response has been described using contact theory; one such approach is the rough crack closure mechanism using contact theory at the macro and micro-scales (Jefferson 2003, Jefferson & Bennett 2007). This recovered stress is built into the local stress model, dependent on the crack contact state, which increases the local compliance. There are similarities between self-healing cementitious materials and self-healing in metallic composites where materials precipitate within voids. Precipitation of austenite in stainless

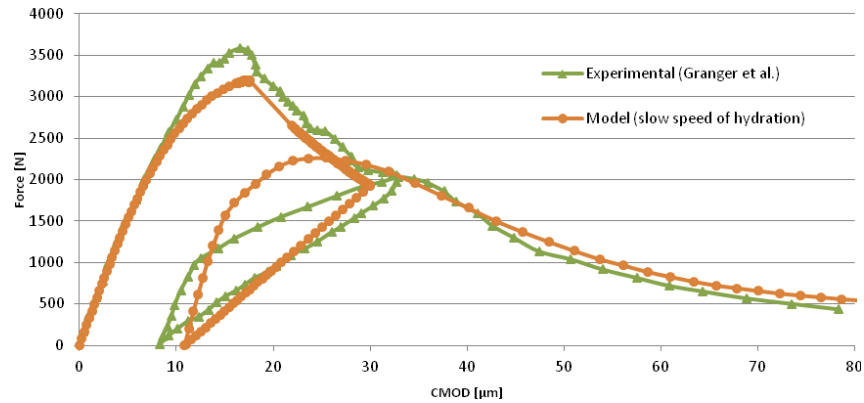


Figure 2.7: Comparison of Hilloulin et al. (2013) numerical self-healing model with experimental data

steel is one such example (Karpov et al. 2012). This was modelled by considering the volume diffusion, precipitation and creep mechanisms using random sampling (Monte-Carlo) at an atomic level within a system of lattices which was solved using a FE technique.

Considering the broader field of cementitious materials, a lattice approach similar to Karpov's work was used to model autonomic healing at the macro-scale. A discrete lattice beam method has been used to describe the impact of adhesive solidifying in a crack (Joseph 2008). This 2D model characterised the mechanical response captured during experiments of mortar beams that were healed through external supply of a healing agent through glass capillary tubes. The experiments showed that the cyanoacrylate adhesive, upon release, solidified within seconds within the crack. As such, the healing is modelled as taking place instantaneously. The mechanical recovery of the healed state is considered by making a composite beam with part mortar and part adhesive. At the time of healing the adhesive had zero stress and was included in the model by adjusting the nodal displacements.

A similar approach could be developed for the autogenous healing where the healed portions of the lattice take the properties of newly healed or formed cementitious material. This approach has the advantage of modelling at the same scale as the experimental work. However, the early stages of micro-cracking and the extent of damage in the fracture process zone around a macro-crack are difficult to capture at this scale. Working at the micro-scale allows the non-linear effects present within the various materials to be captured.

None of the micromechanical (or macro) models developed to date can capture all observed self-healing behaviour in cementitious materials. To develop such a model requires the mechanical properties of the constitutive components of concrete, including the healed components, at the micro-scale.

## Conclusions

It would be desirable to have a full 3D micromechanical model with the ability to apply prescribed anisotropic loading or displacement, inelastic strains and hydration processes in cementitious materials for all eventualities. However, to date, no single model is capable of describing all of the processes and phenomenon exhibited in concrete experiments. Micromechanics has shown to be a suitable tool and a scale at which to model concrete. This technique takes advantage of the individual properties and different processes that occur at this length scale during the life cycle of the material. Time dependent inelastic strains from shrinkage, creep, micro-cracking, differential thermal expansion or ageing, particularly within the matrix phase, are important when simulating behaviour in cementitious composites materials. Considering shrinkage in isolation at the micro-scale can provide an insight into shrinkage cracking problems.

A micro-scale mechanistic based damage or hybrid constitutive modelling approach with inputs from easily measurable mechanical properties is preferred. This reduces dependence on phenomenological relationships and the need to have extensive experimental research programme for new materials. The two-phase composite micromechanical model, based on Eshelby (1957) and Mori & Tanaka (1973) framework containing penny-shaped micro-cracks in the form shown by Budiansky & O'Connell (1976), provides an excellent starting point from which to develop such a model. This two-scale approach can potentially simulate a free shrinkage problem and has a good balance between accuracy and simplicity. Inelastic strains can be readily considered using the Eshelby and Mori-Tanaka based approaches. A combination of volumetric micro-cracking and added directional micro-cracks, whilst also considering the inelastic strains in the matrix, would be an useful contribution to the literature. A novel approach to incorporating all inelastic strains at the micromechanical level is presented in Chapter 3 with the model validation, performance and application are encountered in Chapter 4.

Autogenous self-healing is an important phenomenon known to take place in cementitious materials. However, this aspect is often overlooked when designing structures and a better understanding of the processes could lead to more sustainable concrete structures, with increased durability, that have the ability to recover from damage. The main healing mechanism in cementitious materials during early age is continued hydration whereas carbonation is the dominant mechanism in older specimens. The performance recovery of the autogenous healing is either measured by the regained durability properties and/or mechanical properties. It is these mechanical properties that are important to validate a numerical self-healing model. These minimal experimental requirements for enabling a mechanistic autogenous

self-healed model are explored in Chapter 5. A micro-scale micromechanical model capable of explaining autogenous self-healing in cementitious materials whilst retaining the irreversible damage components and having the capability to be coupled with the hydration process would be an interesting contribution. A novel micromechanical self-healing model is presented in Chapter 6.



# Chapter 3

## Inelastic Strain Modelling

Micromechanical models allow individual material properties, inelastic behaviour and micro-cracking to be modelled at the particle scale of a composite material. They also provide a means of linking the predicted behaviour to the macro-scale response. This chapter describes a new two-phase composite micromechanical material model having a matrix phase, inclusions, inelastic strains in the matrix and micro-cracking. The state-of-the-art is presented in the previous chapter, Sections 2.2 and 2.3.

The constitutive model theory for a basic elastic two-phase composite is presented for dilute and non-dilute inclusions. Particular focus is given to simulating inelastic behaviour in the matrix phase alone. The material remains generic for the purpose of this chapter and the inelastic strains may derive from shrinkage, creep, micro-cracking, differential thermal expansion or ageing. These time dependent phenomena are particularly important when simulating cementitious composite materials such as concrete, examples of which are given in the next chapter.

Two forms of micro-cracking are introduced into the model, namely volumetric and directional micro-cracking. Early age volumetric matrix changes cause volumetric strains which lead to isotropic micro-cracking. Directional, or anisotropic, micro-cracking strains are added to the isotropically micro-cracked composite upon loading. Furthermore, exterior point Eshelby theory is used to allow for the amplification in stress and strain at the matrix/inclusion interface. The micro-crack criterion and evolution for both forms of micro-cracking are described before showing how the micromechanical model is implemented numerically through a constitutive driver algorithm.

## 3.1 Constitutive model theory

The two-phase composite average stress ( $\bar{\sigma}$ ) and strain ( $\bar{\epsilon}$ ) tensors are defined by the summations in equations (3.1) and (3.2),

$$\bar{\sigma} = f_{\Omega}\sigma_{\Omega} + f_M\sigma_M \quad (3.1)$$

$$\bar{\epsilon} = f_{\Omega}\epsilon_{\Omega} + f_M\epsilon_M \quad (3.2)$$

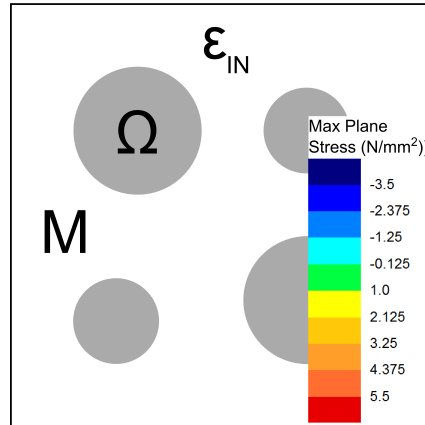
in which the subscripts  $\Omega$  and  $M$  denote the inclusion and matrix phases respectively. The sum of the volume fractions ( $f_{\Omega}$  and  $f_M$ ) is unity. The right handed system of rectangular Cartesian coordinates, 3D micromechanical model and direct tensor notation are used throughout this thesis, unless otherwise specified. A summary of the notation used is given in Appendix A.

A diagram illustrating the principles of the proposed constitutive model is shown in Figure 3.1. Figure 3.1a shows an idealised two-phase composite with a matrix phase ( $M$ ) containing spherical inclusions ( $\Omega$ ) and inelastic strains ( $\epsilon_{IN}$ ). For concrete, the matrix material represents the mortar and spherical inclusions represent the coarse aggregate particles. Volumetric inelastic strains cause micro-cracks quasi-isotropic in nature as shown in Figure 3.1b. Applying uniaxial strain to the isotropically micro-cracked composite results in directional, or anisotropic, micro-cracking strains as shown in Figure 3.1c. The stress gradients were created using the LUSAS (2012) finite element software, whereby 2D elastic composite solution has been subjected a shrinkage strain (Figure 3.1b) and then a far-field tensile strain (Figure 3.1c). It is noted that the cracks have been drawn onto the diagrams in the regions with highest stress.

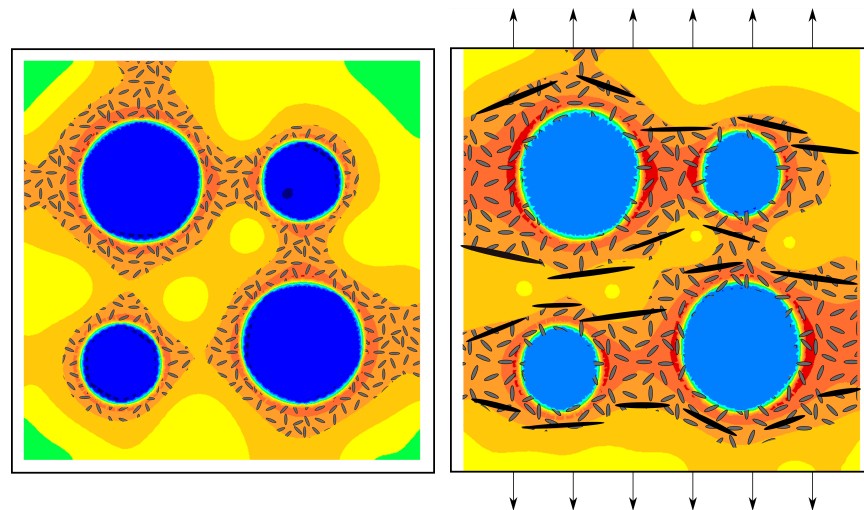
### 3.1.1 Elastic two-phase composite

The elastic properties of the two-phase composite are computed using the classical Eshelby (1957) solution and the Mori-Tanaka homogenisation scheme for non-dilute inclusions (Mori & Tanaka 1973, Benveniste 1987).

Eshelby (1957) considered the transformation of a single ellipsoidal elastic inclusion embedded in an infinite elastic body. The ‘free’ transformation of this inclusion when undergoing a transformation is restricted by the surrounding matrix material. Using a “simple set of imaginary cutting, straining and welding operations” a closed form solution to the problem was developed (Eshelby 1957). These transformation strains ( $\epsilon_i$ ) (also called eigenstrains) (Mura 1987) are produced without external forces, such as thermal expansion, a change in shape or in size, and produce a self-equilibrated stress field within the inclusion and matrix called ‘eigenstress’.



(a) Idealised two-phase composite with a matrix phase (M) containing spherical inclusions ( $\Omega$ ) and inelastic strain ( $\epsilon_{IN}$ )



(b) Isotropic inelastic shrinkage strain applied in the matrix only, causing overall shrinkage and higher stress levels around the inclusions. Note. The volumetric micro-cracks have been drawn in the regions of high stress

(c) Isotropic inelastic shrinkage strain applied in the matrix together with a tensile uniaxial farfield strain. Note. The directional micro-cracks have also been drawn on in the higher stress regions

Figure 3.1: Two-phase composite with illustrative rationale

Eshelby found that the strain and stress field inside an inclusion remained uniform irrespective of material type and initial transformation strain. The disturbance field inside the inclusion can be related to this transformation strain using a fourth order tensor called the interior point Eshelby tensor.

Many composite materials have elastic inclusions, such as the sand particles in mortar, that have different material properties to the host matrix. When this occurs the inclusion is called an inhomogeneity or inhomogeneous inclusion. Eshelby's relationship is also used to solve the problem of different material properties. By

replacing the elastic properties of the inhomogeneous inclusion with elastic properties of the matrix, an equivalent homogeneous inclusion is created. The difference in the material properties is accounted for through a transformation eigenstrain ( $\boldsymbol{\varepsilon}_\tau$ ) included in the equivalent homogeneous inclusion. Equating the stress in the inhomogeneous inclusion and the stress in the equivalent homogeneous inclusion, allows this transformation eigenstrain to be determined. This is called the consistency condition (Nemat-Nasser & Hori 1999) and is shown in equation (3.3). The disturbance (or constrained) strain ( $\boldsymbol{\varepsilon}_c$ ) is shown in equation (3.4).

$$\mathbf{D}_\Omega : (\boldsymbol{\varepsilon}_o + \boldsymbol{\varepsilon}_c) = \mathbf{D}_M : (\boldsymbol{\varepsilon}_o + \boldsymbol{\varepsilon}_c - \boldsymbol{\varepsilon}_\tau) \quad (3.3)$$

$$\boldsymbol{\varepsilon}_c = \mathbf{S} : \boldsymbol{\varepsilon}_\tau \quad (3.4)$$

in which  $\boldsymbol{\varepsilon}_o$  is the farfield strain tensor.  $\mathbf{D}_\Omega$  and  $\mathbf{D}_M$  are the elastic tensors for the inclusion and matrix phases respectively.  $\mathbf{S}$  is the interior point fourth order Eshelby tensor (Nemat-Nasser & Hori 1999) for an ellipsoidal inclusion. The standard solution for spherical inclusions is shown in equation (3.5) using the summation convention for compact representation.

$$\mathbf{S} = \frac{5\nu_m - 1}{15(1 - \nu_m)} \delta_{ij} \delta_{kl} + \frac{4 - 5\nu_m}{15(1 - \nu_m)} (\delta_{ik} \delta_{jl} + \delta_{il} \delta_{jk}) \quad (3.5)$$

$\nu_m$  is Poisson's ratio of the matrix and  $\delta_{ij}$  is the Kronecker delta with  $\delta_{ij} = 1$  when  $i = j$  otherwise  $\delta_{ij} = 0$ .

Substituting equation (3.4) into equation (3.3) and rearranging yields a relationship for the  $\boldsymbol{\varepsilon}_\tau$  shown in equation (3.6).

$$\boldsymbol{\varepsilon}_\tau = \mathbf{A}_\Omega : \boldsymbol{\varepsilon}_o \quad (3.6)$$

where

$$\mathbf{A}_\Omega = [(\mathbf{D}_\Omega - \mathbf{D}_M) \cdot \mathbf{S} + \mathbf{D}_M]^{-1} \cdot (\mathbf{D}_M - \mathbf{D}_\Omega). \quad (3.7)$$

It is noted that these relationships are for a single inclusion in an infinite domain and these are readily applied to a composite with dilute inclusions. Mori & Tanaka (1973) proposed that for non-dilute inclusions the  $\boldsymbol{\varepsilon}_o$  can be replaced by the average matrix strain tensor ( $\boldsymbol{\varepsilon}_M$ ). Substituting equations (3.4) and (3.6) into the stress-strain relationships for the phases and applying the Mori-Tanaka theory leads to the standard constitutive relationship shown in equation (3.8).

$$\bar{\boldsymbol{\sigma}} = \mathbf{D}_{M\Omega} : \bar{\boldsymbol{\varepsilon}}_e \quad (3.8)$$

where

$$\mathbf{D}_{M\Omega} = (f_{\Omega}\mathbf{D}_{\Omega} \cdot \mathbf{T}_{\Omega} + f_M\mathbf{D}_M) \cdot (f_{\Omega}\mathbf{T}_{\Omega} + \mathbf{I}^{4s}f_M)^{-1} \quad (3.9)$$

and

$$\mathbf{T}_{\Omega} = \mathbf{I}^{4s} + \mathbf{S} \cdot \mathbf{A}_{\Omega}. \quad (3.10)$$

$\mathbf{I}^{4s}$  being the fourth order identity tensor and subscript  $e$  denotes elastic.

### 3.1.2 Inelastic strains in the matrix

Time dependent inelastic strains ( $\varepsilon_{IN}$ ) are incorporated in the matrix phase of the composite material using a new approach. The state-of-the-art review in Section 2.1.4 give an overview of the methods to incorporate time dependent inelastic strains. The Eshelby based micromechanical solutions are used here to defined a matrix restrained by a single inclusion. Multiple inclusions can be considered by applying the Mori-Tanaka averaging theory.

Firstly, each phase within the composite material is addressed by their individual constitutive equations. The stress in the matrix including the  $\varepsilon_{IN}$  is shown in equation (3.11) and the stress in the inclusion is shown in equation (3.12). Noting that the  $\varepsilon_{IN}$  appears in the matrix stress only.

$$\sigma_M = \mathbf{D}_M : (\varepsilon_M - \varepsilon_{IN}) = \mathbf{D}_M : (\varepsilon_o + \varepsilon_c - \varepsilon_{IN}) \quad (3.11)$$

$$\sigma_{\Omega} = \mathbf{D}_{\Omega} : \varepsilon_{\Omega} = \mathbf{D}_{\Omega} : (\varepsilon_o + \varepsilon_c) \quad (3.12)$$

Due to the inclusion stress being the same as for the elastic approach, the Eshelby's equivalent inclusion method sets up the same consistency equation as in the standard approach, shown in equation (3.3). However, the  $\varepsilon_c$  needs to consider the impact of matrix inelastic strain tensor on the inclusion.

Two specific examples having an elastic inclusion and plastic matrix are chosen from Weng (1988) for a comparison with the proposed approach: the 'secant moduli tensor' approach and the 'elastic constraint' approach. The consistency equation and associated  $\varepsilon_c$  for each approach are shown by equations (3.13) and (3.14) for the 'secant moduli tensor' and equations (3.15) and (3.16) for the 'elastic constraint' approach.

$$\mathbf{D}_{\Omega} : (\varepsilon_o + \varepsilon_c) = \mathbf{D}_{Sec} : (\varepsilon_o + \varepsilon_c - \varepsilon_{\tau}) \quad (3.13)$$

$$\varepsilon_c = \mathbf{S}_{Sec} : \varepsilon_{\tau} \quad (3.14)$$

$$\mathbf{D}_{\Omega} : (\varepsilon_o + \varepsilon_c + \varepsilon_{IN}) = \mathbf{D}_M : (\varepsilon_o + \varepsilon_c + \varepsilon_{IN} - \varepsilon_{\tau}) \quad (3.15)$$

$$\varepsilon_c = \mathbf{S} : (\varepsilon_{\tau} - \varepsilon_{IN}) \quad (3.16)$$

The restraining effect of the matrix on the inclusion reduces in the secant moduli tensor approach as the stiffness of the secant elastic tensor ( $\mathbf{D}_{Sec}$ ) reduces with damage. The inelastic shrinkage strain cannot be related directly to stress, and as such, this secant moduli tensor approach cannot be applied to inelastic shrinkage. In the elastic constraint approach, the plastic strain in the matrix is transferred to the inclusion using compatible deformations. Weng (1988) shows that the secant formulation provides a better estimation of stress when compared with experimental data and the elastic constraint method gives a stiffer response than the secant method.

### 3.1.3 First principle constrained strain with matrix inelastic strains

Consider a problem made from a single matrix material where an ellipsoid within the matrix undergoes an  $\epsilon_{IN}$ .

$$\sigma_M = \mathbf{D}_M (\epsilon_o + \epsilon_c) \quad (3.17)$$

and

$$\sigma_{M_{IN}} = \mathbf{D}_M (\epsilon_o + \epsilon_c - \epsilon_{IN}) \quad (3.18)$$

where

$$\epsilon_c = \mathbf{S} : \epsilon_{IN}. \quad (3.19)$$

$\sigma_{M_{IN}}$  in equation (3.18) is the stress inside the ellipsoid. Now, consider a matrix material which already has an inelastic strain in the matrix. This is shown by adding this to both the inside and outside of the ellipsoid.

$$\sigma_M = \mathbf{D}_M (\epsilon_o + \epsilon_c + \epsilon_{IN}) \quad (3.20)$$

and

$$\sigma_{M_{IN}} = \mathbf{D}_M (\epsilon_o + \epsilon_c - \epsilon_{IN} + \epsilon_{IN}) = \mathbf{D}_M (\epsilon_o + \epsilon_c) \quad (3.21)$$

where

$$\epsilon_c = \mathbf{S} : \epsilon_{IN}. \quad (3.22)$$

The addition of the matrix inelastic strain tensor in the  $\sigma_{M_{IN}}$  has the effect of cancelling the transformation strain tensor. Allowing the matrix and ellipsoid material to undergo a negative inelastic strain, the following equations may be derived.

$$\sigma_M = \mathbf{D}_M (\epsilon_o + \epsilon_c - \epsilon_{IN}) \quad (3.23)$$

and

$$\sigma_{M_{IN}} = \mathbf{D}_M (\epsilon_o + \epsilon_c) \quad (3.24)$$

where

$$\boldsymbol{\varepsilon}_c = -\mathbf{S} : \boldsymbol{\varepsilon}_{IN}. \quad (3.25)$$

Applying the same principle for a two material problem, the consistency condition for the inclusion is shown in equation (3.3) and the  $\boldsymbol{\varepsilon}_c$  is shown in equation (3.26) which includes the  $\boldsymbol{\varepsilon}_{IN}$  due to the inelastic strain and the  $\boldsymbol{\varepsilon}_\tau$  due to the material phase change.

$$\boldsymbol{\varepsilon}_c = \mathbf{S} : (\boldsymbol{\varepsilon}_\tau - \boldsymbol{\varepsilon}_{IN}) \quad (3.26)$$

### 3.1.4 Individual phase equations for single inclusion

Substituting equation (3.26) into equation (3.3) and rearranging yields the transformation eigenstrain equation (3.27) in terms of the farfield strain and inelastic strain.

$$\boldsymbol{\varepsilon}_\tau = \mathbf{A}_\Omega : (\boldsymbol{\varepsilon}_o - \mathbf{S} : \boldsymbol{\varepsilon}_{IN}) \quad (3.27)$$

Noting that the  $\mathbf{A}_\Omega$  term remains the same as for the standard elastic solution in equation (3.7). The relationship for the stress in the inclusion, shown in equation (3.12), can then be expressed by substituting in equations (3.26) and (3.27), as shown in equation (3.28).

$$\boldsymbol{\sigma}_\Omega = \mathbf{D}_\Omega : \boldsymbol{\varepsilon}_\Omega = \mathbf{D}_\Omega : (\boldsymbol{\varepsilon}_o + \mathbf{S} : (\mathbf{A}_\Omega : (\boldsymbol{\varepsilon}_o - \mathbf{S} : \boldsymbol{\varepsilon}_{IN}) - \boldsymbol{\varepsilon}_{IN})) \quad (3.28)$$

Collecting terms and making use of equation (3.10), equation (3.28) reduces to (3.29).

$$\boldsymbol{\sigma}_\Omega = \mathbf{T}_\Omega : (\boldsymbol{\varepsilon}_o - \mathbf{S} : \boldsymbol{\varepsilon}_{IN}) \quad (3.29)$$

This a solution for an infinite elastic matrix undergoing an inelastic strain and containing a single inclusion.

### 3.1.5 Individual phase equations for multiple inclusions

Multiple inclusions impact on each other and influence the surrounding stress fields. The disturbance strain tensor for non-dilute inclusion has been shown by Mori & Tanaka (1973) to be based on the average matrix strain tensor and not the farfield strain tensor. Applying this theory, where  $\boldsymbol{\varepsilon}_o = \boldsymbol{\varepsilon}_M$ , yields the relationship for the strain and stress tensors in the inclusion as shown in equations (3.30) and (3.31) and stress tensor in the matrix as shown in equation (3.32) for non-dilute inclusions.

$$\boldsymbol{\varepsilon}_\Omega = \mathbf{T}_\Omega : (\boldsymbol{\varepsilon}_M - \mathbf{S} : \boldsymbol{\varepsilon}_{IN}) \quad (3.30)$$

$$\boldsymbol{\sigma}_\Omega = \mathbf{D}_\Omega : \mathbf{T}_\Omega : (\boldsymbol{\varepsilon}_M - \mathbf{S} : \boldsymbol{\varepsilon}_{IN}) \quad (3.31)$$

$$\boldsymbol{\sigma}_M = \mathbf{D}_M : (\boldsymbol{\varepsilon}_M - \boldsymbol{\varepsilon}_{IN}) \quad (3.32)$$

### 3.1.6 Constitutive equation

The constitutive equation is constructed by eliminating the individual components of stresses or strains tensors from the homogenisation equations. Substituting the inclusion strain tensor equation (3.30) into the total strain tensor equation (3.2) and isolating the matrix strain tensor yields a relationship equation (3.33).

$$\boldsymbol{\varepsilon}_M = (f_\Omega \mathbf{T}_\Omega + f_M \mathbf{I}^{4s})^{-1} : (\bar{\boldsymbol{\varepsilon}} + f_\Omega \mathbf{T}_\Omega \cdot \mathbf{S} : \boldsymbol{\varepsilon}_{IN}) \quad (3.33)$$

Substituting in equations (3.31), (3.32) and (3.33) into equation (3.1), produces the overall constitutive equation relationship shown by equation (3.34),

$$\bar{\boldsymbol{\sigma}} = \mathbf{D}_{M\Omega} : (\bar{\boldsymbol{\varepsilon}} - \boldsymbol{\varepsilon}_{INEQ}) \quad (3.34)$$

where

$$\boldsymbol{\varepsilon}_{INEQ} = [\mathbf{D}_{M\Omega}^{-1} (f_\Omega \mathbf{D}_\Omega \cdot \mathbf{T}_\Omega \cdot \mathbf{S} + f_M \mathbf{D}_M) - f_\Omega \mathbf{T}_\Omega \cdot \mathbf{S}] : \boldsymbol{\varepsilon}_{IN}. \quad (3.35)$$

### 3.1.7 Exterior point Eshelby solution

The exterior point Eshelby solution gives the strain and stress amplification at any point in the matrix. This exterior point amplification is accounted for in equation (3.26) by replacing the interior point Eshelby tensor with the exterior point Eshelby tensor resulting in equation (3.36).

$$\boldsymbol{\varepsilon}_c = \mathbf{S}^E(\mathbf{x}) : (\boldsymbol{\varepsilon}_\tau - \boldsymbol{\varepsilon}_{IN}) \quad (3.36)$$

$\mathbf{S}^E(\mathbf{x})$  is the exterior point Eshelby tensor defined by Ju & Sun (1999) and particularised by Li et al. (2007) see also Mihai & Jefferson (2011). The  $\mathbf{S}^E(\mathbf{x})$  standard solution for a spherical inclusion in an elastic medium is given in equation (3.37). The summation convention is again used for compact representation.

$$\begin{aligned} \mathbf{S}_{ijmn}^E(\mathbf{x}) &= \frac{\rho^3}{30(1-\nu)} [(3\rho^2 + 10\nu - 5) \delta_{ij} \delta_{mn} + (3\rho^2 - 10\nu + 5) \\ &\cdot (\delta_{im} \delta_{jn} + \delta_{in} \delta_{jm}) + 15(1 - \rho^2) \cdot \delta_{ij} \bar{x}_m \bar{x}_n + 15(1 - 2\nu - \rho^2) \delta_{mn} \bar{x}_i \bar{x}_j \\ &+ 15(\nu - \rho^2) \cdot (\delta_{im} \bar{x}_j \bar{x}_n + \delta_{jm} \bar{x}_i \bar{x}_n + \delta_{in} \bar{x}_j \bar{x}_m + \delta_{jn} \bar{x}_i \bar{x}_m) \end{aligned}$$

$$+ 15 (7\rho^2 - 5) \cdot \bar{x}_i \bar{x}_j \bar{x}_m \bar{x}_n] \quad (3.37)$$

$\mathbf{x}$  is the position vector from the centre of a spherical aggregate particle,  $\rho = a/|\mathbf{x}|$  is the relative distance taken as 0.999,  $|\mathbf{x}| = \sqrt{x_i x_i}$  is the position vector and  $a$  is the radius of the spherical inclusion.

The transformation strain, from equation (3.27), retains the interior point Eshelby solution. Equations (3.36) and (3.27) are substituted into the inclusion constitutive equation (3.12) and then the Mori-Tanaka theory is applied. The exterior point Eshelby amplification for the strain tensor  $\varepsilon_{M\Omega}$  and stress tensor  $\sigma_{M\Omega}$  in the matrix are shown in equations (3.38) and (3.39) respectively.

$$\varepsilon_{M\Omega}(\mathbf{x}) = \mathbf{T}^E(\mathbf{x}) : \varepsilon_M - \mathbf{T}_\Omega \cdot \mathbf{S}^E(\mathbf{x}) : \varepsilon_{IN} \quad (3.38)$$

and

$$\sigma_{M\Omega}(\mathbf{x}) = \mathbf{D}_M : \varepsilon_{M\Omega}(\mathbf{x}) \quad (3.39)$$

where

$$\mathbf{T}^E(\mathbf{x}) = \mathbf{I}^{4s} + \mathbf{S}^E(\mathbf{x}) \cdot \mathbf{A}_\Omega. \quad (3.40)$$

Mihai & Jefferson (2011) showed that a solution based on this exterior point Eshelby approach can represent the mechanisms that occur within the interface transition zone (ITZ), between the two composite phases, without needing to explicitly define the ITZ properties. The coarse aggregate particles are also idealised as spherical particles in this micromechanical solution. In reality these particles can have a range of shapes and textures (see the particle shape classification in Neville & Brooks (2010)) which can impact on the material response. An icosahedron (polyhedron with 20 faces) or similar 3D shape could be used to represent the coarse aggregate shape. However, this option would necessitate a numerical solution to obtain the Eshelby tensor. This aspect was not pursued further in this study.

## 3.2 Micro-cracking

The inelastic micro-cracking strains arising from early-age volumetric time-dependent phenomena are generally quasi-isotropic in nature and distributed (Hearn 1999). The micro-cracking (and subsequent macro-cracking) resulting from mechanical loading and/or mechanical restraints are generally anisotropic in nature and arise once the hydration process is substantially complete, e.g. during initial mechanical loading. It is this separation in time scales and the different nature of these micro-cracking mechanisms that is exploited in the proposed model. Therefore, two sets of micro-cracking variables are introduced into the model, one of which represents distributed isotropic micro-cracking in the matrix and the other of which accounts

for anisotropic (or directional) cracking of the composite. The advantage of the proposed approach is that it avoids the need for a numerical solution to evaluate the Eshelby (or concentration) tensor for a changing generally anisotropic matrix material (Desrumaux et al. 2001). Furthermore, the ability to develop anisotropic micro-cracking means that the model is able to simulate multi-axial loading conditions such as occur in shear tension problems (Fichant et al. 1999).

Although the model presented in this paper does not use a volumetric-deviatoric separation of the stress/strain tensors, there are some similarities with approaches that do use such a separation (Carol et al. 2001, Leukart & Ramm 2003, 2006, Grassl & Jirásek 2006).

### 3.2.1 Volumetric matrix micro-cracking

The micro-cracking which arises from the volumetric changes in the matrix phase due to shrinkage and early age thermal effects for cementitious composites are considered to be effectively isotropic. Such micro-cracking can be simulated by replacing  $\mathbf{D}_M$  with  $\mathbf{D}_{M\omega_v}$ , where  $\mathbf{D}_{M\omega_v}$  is defined by,

$$\mathbf{D}_{M\omega_v} = (1 - \omega_v)\mathbf{D}_M \quad (3.41)$$

where the volumetric micro-cracking parameter is  $\omega_v \in [0, 1]$ . 0 is the undamaged state and 1 is the fully damaged state. The constitutive equation, equation (3.34), including volumetric matrix micro-cracking is shown in equation (3.42).

$$\bar{\boldsymbol{\sigma}} = \mathbf{D}_{M\Omega\omega_v} : (\bar{\boldsymbol{\varepsilon}} - \boldsymbol{\varepsilon}_{INEQ\omega_v}) \quad (3.42)$$

where

$$\boldsymbol{\varepsilon}_{INEQ\omega_v} = [\mathbf{D}_{M\Omega\omega_v}^{-1} (f_\Omega \mathbf{D}_\Omega \cdot \mathbf{T}_{\Omega\omega_v} \cdot \mathbf{S} + f_M \mathbf{D}_{M\omega_v}) - f_\Omega \mathbf{T}_{\Omega\omega_v} \cdot \mathbf{S}] : \boldsymbol{\varepsilon}_{IN}, \quad (3.43)$$

$$\mathbf{D}_{M\Omega\omega_v} = (f_\Omega \mathbf{D}_\Omega \cdot \mathbf{T}_{\Omega\omega_v} + f_M \mathbf{D}_{M\omega_v}) \cdot (f_\Omega \mathbf{T}_{\Omega\omega_v} + \mathbf{I}^{4s} f_M)^{-1}, \quad (3.44)$$

$$\mathbf{T}_{\Omega\omega_v} = \mathbf{I}^{4s} + \mathbf{S} \cdot \mathbf{A}_{\Omega\omega_v} \quad (3.45)$$

and

$$\mathbf{A}_{\Omega\omega_v} = [(\mathbf{D}_\Omega - \mathbf{D}_{M\omega_v}) \cdot \mathbf{S} + \mathbf{D}_{M\omega_v}]^{-1} \cdot [\mathbf{D}_{M\omega_v} - \mathbf{D}_\Omega]. \quad (3.46)$$

It is noted that the standard form of the Eshelby tensor remains valid with changing degrees of volumetric micro-cracking because  $\mathbf{D}_{M\omega_v}$  retains the isotropic form.

### 3.2.2 Directional micro-cracking from mechanical loading

Added mechanical loading (and structural restraints) often leads to the development of anisotropic micro-cracks which can develop into macro-cracks. Mihai & Jefferson (2011) employed the Budiansky & O'Connell (1976) solution to represent such micro-cracking but replaced the elastic properties of single phase material in the original paper with effective elastic properties of the composite material. This avoided the need for Eshelby tensors for generally anisotropically cracked media which (other than for specialised cases) require numerical evaluation.

The same approach is now adopted for the isotropically cracked composite. The resulting stress-strain relationship is given by equation (3.47),

$$\bar{\boldsymbol{\sigma}} = \mathbf{D}_{M\Omega\omega_v} : (\bar{\boldsymbol{\varepsilon}} - \boldsymbol{\varepsilon}_{INEQ\omega_v} - \boldsymbol{\varepsilon}_a) \quad (3.47)$$

in which the added strain ( $\boldsymbol{\varepsilon}_a$ ) is now relative to the isotropically micro-cracked composite. Nemat-Nasser & Hori (1999) describe the derivation of this micro-crack solution in detail. The additional strain for each micro-crack plane  $i$  is given by equation (3.48).

$$\boldsymbol{\varepsilon}_{addi} = \frac{1}{a_i^3} \int_{\mathbb{S}} \frac{1}{2} (ru_a^T + r^T u_a) d\mathbb{S} \quad (3.48)$$

$\mathbb{S}$  is the plane area of the crack,  $u$  is the displacement of the micro-crack and  $a$

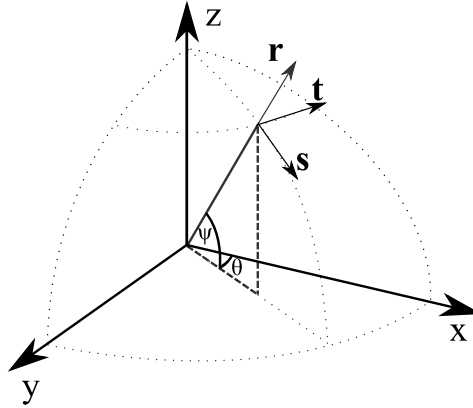


Figure 3.2: Reference system for crack planes

is the crack radius.  $r$ ,  $s$  and  $t$  define the unit local coordinate vectors as shown in Figure 3.2 for a single direction.  $r$  is the vector normal to the micro-crack surface. The non-zero additional strain components for a dilute series of circular (penny-shaped) cracks ( $\boldsymbol{\varepsilon}_\alpha$ ) is given by equation (3.49) (Budiansky & O'Connell 1976). The spherical coordinates reference angles ( $\psi, \theta$ ) for each direction have not explicitly

been written for the variables in the following equations.

$$\boldsymbol{\varepsilon}_\alpha = \begin{bmatrix} \varepsilon_{\alpha_{rr}} \\ \varepsilon_{\alpha_{rs}} \\ \varepsilon_{\alpha_{rt}} \end{bmatrix} = \mathbb{F} \frac{16(1-\nu_M^2)}{3E_M} \begin{bmatrix} s_{rr} \\ \frac{4}{2-\nu_M} s_{rs} \\ \frac{4}{2-\nu_M} s_{rt} \end{bmatrix} = \mathbb{F} \mathbf{C}_\alpha \mathbf{s} \quad (3.49)$$

$\nu_M$  and  $E_M$  are Poisson's ratio and Young's modulus of the matrix material.  $\mathbb{F}$  is the crack density parameter, originally given by Budiansky & O'Connell (1976) as  $\mathbb{F} = N_c a_o^3$ , for circular (penny-shaped) cracks, where  $N_c$  is the number of cracks per unit volume and  $a_o$  is a single crack radius.  $\mathbf{C}_\alpha$  contains the elastic compliance terms and  $\mathbf{s}$  is the local stress vector. This solution is independent of the crack radius.

Micro-cracks typically occur in more than one direction and by summing the contribution of the directional cracks the total additional strain can be calculated. The total additional strains for  $n_i$  discrete directions and a continuous distribution of micro-cracks are shown in equations (3.50) and (3.51) respectively.

$$\boldsymbol{\varepsilon}_a = \sum_{n_i} \mathbf{N}_\varepsilon \boldsymbol{\varepsilon}_{\alpha_i} \quad (3.50)$$

$$\boldsymbol{\varepsilon}_a = \frac{1}{2\pi} \int_{2\pi} \int_{\frac{\pi}{2}} \mathbf{N}_\varepsilon \boldsymbol{\varepsilon}_\alpha \sin(\psi) d\psi d\theta \quad (3.51)$$

$\mathbb{F}$  can also be expressed in terms of a directional micro-crack variable  $\omega_d \in [0, 1]$  (Jefferson & Bennett 2007), as shown in equation (3.52).

$$\mathbb{F} = \frac{3}{16(1-\nu_M^2)} \left( \frac{\omega_d}{1-\omega_d} \right) \quad (3.52)$$

which means that equation (3.49) may now be written as follows

$$\boldsymbol{\varepsilon}_\alpha = \mathbb{F} \mathbf{C}_\alpha \mathbf{s} = \left( \frac{\omega_d}{1-\omega_d} \right) \mathbf{C}_L : \mathbf{s} \quad (3.53)$$

where

$$\mathbf{s} = \begin{bmatrix} s_{rr} & s_{rs} & s_{rt} \end{bmatrix}^T = \mathbf{N} \cdot \bar{\boldsymbol{\sigma}} \quad (3.54)$$

The local stress vector is related to the average composite stress ( $\bar{\boldsymbol{\sigma}}$ ) using the stress transformation tensor ( $\mathbf{N}$ ). Similarly, the strain transformation tensor ( $\mathbf{N}_\varepsilon$ ) relates the local strain to the composite average strain ( $\bar{\boldsymbol{\varepsilon}}$ ).  $\mathbf{N}$  and  $\mathbf{N}_\varepsilon$  are the transformation tensors given by Jefferson (2003).  $\mathbf{C}_L$  is the elastic compliance (Nemat-Nasser &

Hori 1999) as shown in equation (3.55).

$$\mathbf{C}_L = \mathbf{D}_L^{-1} = \frac{1}{E_M} \begin{bmatrix} 1 & 0 & 0 \\ 0 & \frac{4}{2-\nu_M} & 0 \\ 0 & 0 & \frac{4}{2-\nu_M} \end{bmatrix} \quad (3.55)$$

Integrating contributions from all directions around a hemisphere gives the total added strain  $\epsilon_a$  equation as shown in equation (3.56). McLaren's integration rule with 50 sample directions, which reduces to 29 sample directions in a hemisphere, is used to evaluate this integration numerically (Stroud 1972).

$$\epsilon_a = \left( \frac{1}{2\pi} \int_{2\pi} \int_{\frac{\pi}{2}} \mathbf{N}_\epsilon \cdot \mathbf{C}_L \cdot \mathbf{N} \cdot \frac{\omega_d(\psi, \theta)}{1 - \omega_d(\psi, \theta)} \sin(\psi) d\psi d\theta \right) : \bar{\sigma} \quad (3.56)$$

These relationships can be used in equation (3.47) to yield the overall constitutive equation (3.57),

$$\bar{\sigma} = (\mathbf{I}^{4s} + \mathbf{D}_{M\Omega\omega_v} \cdot \mathbf{C}_{add})^{-1} \mathbf{D}_{M\Omega\omega_v} : (\bar{\epsilon} - \epsilon_{INEQ\omega_v}) \quad (3.57)$$

where

$$\mathbf{C}_{add} = \left( \frac{1}{2\pi} \int_{2\pi} \int_{\frac{\pi}{2}} \mathbf{N}_\epsilon \cdot \mathbf{C}_L \cdot \mathbf{N} \cdot \frac{\omega_d(\theta, \psi)}{1 - \omega_d(\theta, \psi)} \sin(\psi) d\psi d\theta \right) \quad (3.58)$$

$\mathbf{C}_{add}$  is the added local compliance term. This solution considers a dilute distribution of micro-cracks which means that the crack interactions are ignored.

### 3.2.3 Decomposition of equations into phases

In order to examine the matrix and inclusion phases the final constitutive equation, equation (3.57), is decomposed by grouping all accessible volume fractions terms. The stress in the matrix is shown in equation (3.59) and the stress in the inclusion is shown by equation (3.60).

$$\begin{aligned} \sigma_M &= (\mathbf{I}^{4s} + \mathbf{D}_{M\Omega\omega_v} \cdot \mathbf{C}_{add})^{-1} (f_M \mathbf{D}_{M\omega_v}) \cdot (f_\Omega \mathbf{T}_{\Omega\omega_v} + \mathbf{I}^{4s} f_M)^{-1} \\ &: (\bar{\epsilon} - [\mathbf{D}_{M\Omega\omega_v}^{-1} (f_M \mathbf{D}_{M\omega_v})] : \epsilon_{IN}) \end{aligned} \quad (3.59)$$

$$\begin{aligned} \sigma_\Omega &= (\mathbf{I}^{4s} + \mathbf{D}_{M\Omega\omega_v} \cdot \mathbf{C}_{add})^{-1} (f_\Omega \mathbf{D}_\Omega \cdot \mathbf{T}_{\Omega\omega_v}) \cdot (f_\Omega \mathbf{T}_{\Omega\omega_v} + \mathbf{I}^{4s} f_M)^{-1} \\ &: (\bar{\epsilon} - [\mathbf{D}_{M\Omega\omega_v}^{-1} (f_\Omega \mathbf{D}_\Omega \cdot \mathbf{T}_{\Omega\omega_v} \cdot \mathbf{S}) - f_\Omega \mathbf{T}_{\Omega\omega_v} \cdot \mathbf{S}] : \epsilon_{IN}) \end{aligned} \quad (3.60)$$

### 3.2.4 Exterior point Eshelby stress with micro-cracking

The volumetric damage in the matrix is accounted for when using the exterior point Eshelby solution, as shown in Section 3.1.7. The strain and stress amplification at any point in the matrix with volumetric damage is shown in equations (3.61) and (3.62) respectively. The stress tensor in the matrix on each local plane is given by equation (3.63).

$$\boldsymbol{\varepsilon}_{M\Omega}(\mathbf{x}) = \mathbf{T}_{\omega_v}^E(\mathbf{x}) : \boldsymbol{\varepsilon}_M - \mathbf{T}_{\Omega\omega_v} \cdot \mathbf{S}^E(\mathbf{x}) : \boldsymbol{\varepsilon}_{IN}, \quad (3.61)$$

$$\boldsymbol{\sigma}_{M\Omega}(\mathbf{x}) = \mathbf{D}_{M\omega_v} : \boldsymbol{\varepsilon}_{M\Omega}(\mathbf{x}) \quad (3.62)$$

and

$$\mathbf{s}_{M\Omega}(\mathbf{x}) = \mathbf{N} \cdot \boldsymbol{\sigma}_{M\Omega}(\mathbf{x}) \quad (3.63)$$

where

$$\mathbf{T}_{\omega_v}^E(\mathbf{x}) = \mathbf{I}^{4s} + \mathbf{S}^E(\mathbf{x}) \cdot \mathbf{A}_{\Omega\omega_v}. \quad (3.64)$$

$\mathbf{S}^E(\mathbf{x})$ ,  $\mathbf{T}_{\Omega\omega_v}$  and  $\mathbf{A}_{\Omega\omega_v}$  are given in equations (3.37), (3.45) and (3.46) respectively.  $s_{M\Omega}$  is the transformed amplified stress adjacent to an inclusion (Mihai & Jefferson 2011).

## 3.3 Micro-crack criterion and evolution

The proposed model requires two micro-crack evolution equations for (i) volumetric micro-cracks which are considered to be controlled by the coarse aggregate particles and (ii) directional micro-cracks (and eventually macro-cracks) which are considered to extend over the coarse aggregate particles.

The measurement of post-peak volumetric tensile behaviour of concrete at low strains is difficult and there is little experimental data upon which to base the evolution function directly. However, a volumetric softening function may be chosen by making the following assumptions:

1. The start of micro-cracking is associated with pre-peak non-linearity in uniaxial tension, which typically occurs at approximately 70 % of the peak tensile load (van Mier 1997),
2. the relative displacement at full softening, in any direction under volumetric loading, is governed by the coarse aggregate particles and
3. this relative displacement is of similar magnitude to that for directional loading.

The above assumptions allow the same function form to be used for both volumetric and directional micro-crack evolution. The equation selected is based on a standard form which was adopted by Mihai & Jefferson (2011), as follows

$$\sigma_{\beta} = f_{t\beta} e^{-c_{\beta} \frac{u_{\beta} - u_{t\beta}}{u_{0\beta} - u_{t\beta}}} \quad (3.65)$$

in which subscript  $\beta$  denotes volumetric ( $v$ ) or directional ( $d$ ) micro-cracking,  $c_{\beta}$  is a constant taken to be 5, which is appropriate for this type of evolution,  $f_{t\beta}$  is a local tensile strength at the aggregate/cement paste interface and  $u_{\beta}$ ,  $u_{t\beta}$  and  $u_{0\beta}$  are the relative displacements across a zone of material.

The strain at first uniaxial micro-cracking ( $\epsilon_{t\beta}$ ) is taken as

$$\epsilon_{t\beta} = \frac{f_{t\beta}}{E_{\beta}} \quad (3.66)$$

in which  $E_v$  is Young's modulus of the matrix and  $E_d$  is Young's modulus of the composite. The local strains in the effectively fully micro-cracked ( $\epsilon_{0\beta}$ ) state are assumed to be related to the relative displacements by

$$\epsilon_{0\beta} = \frac{u_{0\beta}}{h_{\beta}} \quad (3.67)$$

in which  $h_v$  is the size of a coarse aggregate particle and  $h_d$  is assumed to be 3 times the size of a coarse aggregate particle. Coarse aggregate particles are typically 10 mm in diameter for laboratory concrete and 20 mm for structural concrete. The relative displacement at the fully micro-cracked state for  $u_{0v}$  is taken as 0.1 mm whereas  $u_{0d}$  is taken as 0.2 mm (Walraven & Reinhardt 1981).

The function described by equation (3.65), for both the volumetric and directional micro-cracking cases, is illustrated in Figure 3.3.

The onset of micro-cracking is controlled by the elastic stress field. The micro-cracking initiation criterion for the volumetric component is reached when the mean matrix stress reaches the tensile strength of the matrix. The micro-cracking initiation criterion for the directional component is reached when the local principal stress ( $s_I$ ), given by equation (3.68), exceeds the initial interface tensile strength ( $f_{td}$ ).

$$s_I = s_{rr} \left( \frac{1 + \alpha_L}{2} \right) + \sqrt{s_{rr}^2 \left( \frac{1 - \alpha_L}{2} \right)^2 + \tau_L^2} \quad (3.68)$$

where  $\alpha_L = \left( \frac{v_M}{1 - v_M} \right)$  and  $\tau_L = \sqrt{s_{rs}^2 + s_{rt}^2}$ , in which  $s = s_{M\Omega}$  as defined in equations (3.54) and (3.63).

Once formed, the extent of micro-cracking is expressed in terms of the parame-

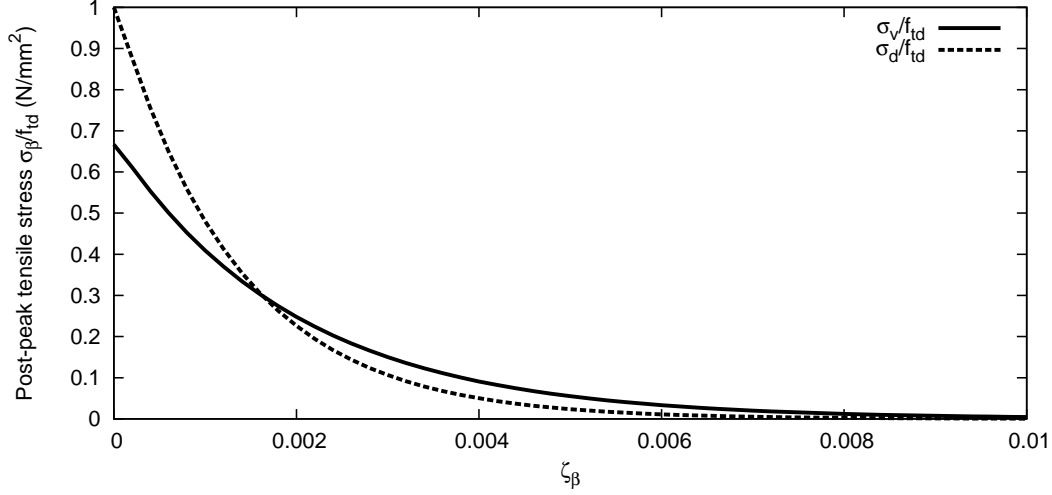


Figure 3.3: Volumetric and directional tensile softening functions

ters ( $\omega_{\beta}$ ), which are given by

$$\omega_{\beta} = 1 - \frac{\varepsilon_{t\beta}}{\zeta_{\beta}} e^{-c_{\beta} \left( \frac{\zeta_{\beta} - \varepsilon_{t\beta}}{\varepsilon_{0\beta} - \varepsilon_{t\beta}} \right)} \quad (3.69)$$

this depends on the effective local strain parameters  $\zeta_v$  and  $\zeta_d$ , the former of which is governed by the following volumetric micro-cracking function equation (3.70) and the latter by the directional micro-cracking function equation (3.71).

$$F_{\zeta_v}(\varepsilon_{Mv}, \varepsilon_{IN}, \zeta_v) = \frac{\varepsilon_{Mv} - \varepsilon_{IN}}{3} - \zeta_v \quad (3.70)$$

$$F_{\zeta_d}(\varepsilon_L, \zeta_d) = \varepsilon_{Lrr} \left( \frac{1 + \alpha_L}{2} \right) + \sqrt{\varepsilon_{Lrr}^2 \left( \frac{1 - \alpha_L}{2} \right)^2 + r_{\zeta}^2 \gamma^2} - \zeta_d \quad (3.71)$$

where  $\gamma = \sqrt{\varepsilon_{Lrs}^2 + \varepsilon_{Lrt}^2}$  and  $r_{\zeta_d} = \left( \frac{\nu_M - 1/2}{\nu_M - 1} \right)$ .

The functions are subject to the standard loading/unloading conditions as follows;

$$F_{\zeta_{\beta}} \leq 0, \quad \dot{\zeta}_{\beta} \geq 0 \text{ and } F_{\zeta_{\beta}} \dot{\zeta}_{\beta} = 0. \quad (3.72)$$

The micro-cracking evolution for the volumetric component is always controlled by the mean local matrix strains, shown in volumetric terms by  $\varepsilon_{Mv}$ . The directional local strain component ( $\varepsilon_L$ ) is assumed equal to the sum of the peak elastic strain in the matrix phase ( $\varepsilon_{LMe}$ ), based on  $s_{M\Omega}$  and the local micro-cracking strain ( $\varepsilon_{\alpha}$ ) (Mihai & Jefferson 2011), as shown in equation (3.73).

$$\varepsilon_L = \varepsilon_{LMe} + \varepsilon_{\alpha} \quad (3.73)$$

where

$$\varepsilon_{LMe} = (1 - \omega_d) \mathbf{C}_L : s_{M\Omega} \quad (3.74)$$

and

$$\varepsilon_\alpha = \omega_d \mathbf{N}_\varepsilon \cdot \bar{\varepsilon}_e = \omega_d \mathbf{N}_\varepsilon \cdot (\bar{\varepsilon} - \varepsilon_{INEQ\omega_v}). \quad (3.75)$$

### 3.4 Numerical implementation

The constitutive model, including micro-cracking, presented in this chapter has been implemented in a Mathcad (2010) sheet using a constitutive driver algorithm. This model can be driven by total stress ( $\bar{\sigma}$ ), total strain ( $\bar{\epsilon}$ ) or the shrinkage potential of the matrix ( $\epsilon_{shr}$ ). Material data and initial conditions are read along with initial stress and strain parameters. The integral presented in equation (3.58) cannot easily be solved analytically and as such is evaluated numerically with the weighted summations over a finite number of directions. The accuracy of this rule is deemed sufficient for this study.

A general constitutive driver algorithm is shown in Table 3.1 showing the essential steps required for a specified stress path increment ( $\Delta\sigma_a$ ) or strain path increment ( $\Delta\epsilon_a$ ). Once these updated stresses and strains are found, the degree of micro-cracking is determined using a local micro-cracking solution.

Table 3.1: Constitutive driver algorithm

Read in title, control data and material data	
Read in initial conditions	Initialise the stress and strain
Read in the applied $\Delta\sigma_a$ and/or $\Delta\epsilon_a$	
For $i = 1$ to $n$	Loop over stress/strain increments
$\bar{\sigma} = \bar{\sigma} + \Delta\sigma_{a_i}$	Update total stresses
$\Delta\sigma = \Delta\sigma_{a_i}$	Set initial value of out-of-balance stresses for this increment
For $j = 1$ to $m$	Loop over iterations
Compute $\mathbf{D}_{Sec}$	Compute secant stiffness ( $\mathbf{D}_{Sec}$ ) using previous total added compliance ( $C_{add}$ )
$\Delta\sigma = \mathbf{D}_{Sec}\Delta\epsilon$ , extract $\Delta\sigma_{rc}$	Compute strain increment ( $\Delta\epsilon$ ) from out of balance stress and secant stiffness matrix and extract 'reaction' stress ( $\Delta\sigma_{rc}$ ) using Gaussian elimination algorithm capable of solving for fixed stresses, strains or a mixture
$\bar{\epsilon} = \bar{\epsilon} + \Delta\epsilon$ and $\bar{\sigma} = \bar{\sigma} + \Delta\sigma_{rc}$	Update strains and add reaction stress components to total stresses
$\sigma_{ex} = \mathbf{D}_{Sec} : \bar{\epsilon}$	Use iterative local micro-cracking algorithm to update the stress. See Table 3.2.
$\Delta\sigma = \bar{\sigma} - \sigma_{ex}$	Compute existing stresses
If $ \Delta\sigma  < tol$	Compute the out of balance stress
End $j$ Loop	If converged, exit iteration loop
$\epsilon_M, \epsilon_\Omega, \sigma_M, \sigma_\Omega$	
Output results for increment	Decompose component strains and stresses
End $i$ Loop	
Finish	

Table 3.2 shows the essential steps of the computational algorithm with a specified stress path increment ( $\Delta\sigma_a$ ) and applied shrinkage strain increment ( $\Delta\varepsilon_{shr}$ ) in the matrix only. The detailed steps for the local micro-cracking solution using volumetric and directional cracking is shown.

Table 3.2: Computational algorithm for specified stress path with matrix shrinkage

Enter with $\bar{\varepsilon}_{pr}, \zeta_{vpr}, \zeta_{dpr}, \Delta\varepsilon_{shr}$	Enter with strains and previous ( $pr$ ) equivalent strain parameters
$\Delta\sigma = \Delta\sigma_a - \mathbf{D}_{Sec}\Delta\varepsilon_{shr}$	Compute out of balance stresses
$\bar{\varepsilon} = \bar{\varepsilon} + \Delta\varepsilon, \quad \bar{\sigma} = \bar{\sigma} + \Delta\sigma_{rc}$	Update strains and stresses
Volumetric micro-crack component	
If $\sigma_{Mv} \leq f_{tv}$ then $\omega_v = 0$	Micro-crack initiation condition
Else	Volumetric micro-crack evolution
$\zeta_v = \frac{(\varepsilon_{Mv} - \varepsilon_{shr})}{3}$ if $\zeta_v > \zeta_{vpr}$	Update strain parameter if it exceeds previous maximum
Update $\omega_v$	Update damage parameter
End	
Directional micro-crack components	
For $i = 1$ to $n_i$	Loop over integ. dir. (i)
$\varepsilon_{M\Omega} = \mathbf{T}_{\omega_v}^E(\mathbf{x}) : \varepsilon_M - \mathbf{T}_{\Omega\omega_v} \cdot \mathbf{S}^E(\mathbf{x}) : \varepsilon_{shr}$	Compute average matrix stress at peak position (EPE)
$s_{M\Omega} = \mathbf{N}_i \cdot \mathbf{D}_{M\omega_v} : (\varepsilon_{M\Omega} - \varepsilon_{shr})$	Compute local cracking stress at peak position
If $s_I(s_{M\Omega})_{max} \leq f_{td}$ then $\omega_{d_i} = 0$	Micro-crack initiation criterion
Else	Directional micro-crack evolution
$\varepsilon_{L_i} = (1 - \omega_{d_i})\mathbf{C}_{LM} : s_{M\Omega} + \omega_{d_i}\mathbf{N}_{\varepsilon_i} \cdot \bar{\varepsilon}$	Evaluate local strain vector
$\zeta_i = F_{\zeta_d}(\varepsilon_{L_i})$ if $\varepsilon_{L_i} > \zeta_{pr_i}$	Update strain parameter if exceeds previous max
Update $\omega_{d_i}$	Update damage parameter
End	
$\mathbf{C}_{add} = \sum_{i=1}^{n_i} \mathbf{N}_{\varepsilon_i} \cdot \mathbf{C}_L \cdot \mathbf{N}_i \cdot \frac{\omega_{d_i}}{1 - \omega_{d_i}} w_i$	Evaluate total added compliance
$\mathbf{D}_{Sec} = (\mathbf{I}^{4s} + \mathbf{D}_{M\Omega\omega_v} \cdot \mathbf{C}_{add})^{-1} \cdot \mathbf{D}_{M\Omega\omega_v}$	Form secant constitutive matrix
$\bar{\sigma} = \mathbf{D}_{Sec} : (\bar{\varepsilon} - \varepsilon_{INEQ\omega_v})$	Compute stresses

In the next chapter, in Section 4.2, a selected set of stress/strain paths are used to present the characteristic response of the model using the algorithms shown in Tables 3.1 and 3.2.

## Conclusions

A new constitutive model was presented in this chapter that describes a two-phase composite micromechanical material model with inelastic strains in the matrix. The basic elastic two-phase composite, the derivation of the inelastic strains in the matrix and solutions for dilute and non-dilute inclusions were given. The inelastic strains allow time-dependent behaviour to be considered within a two-phase composite.

A novel micro-cracking approach was used where two sets of micro-cracking variables were introduced into the model, namely for volumetric and directional (anisotropic) micro-cracking parameters. Volumetric isotropic micro-cracking represents the response due to volumetric shrinkage strains in the matrix. Directional, or anisotropic, micro-cracking strains can be added to the isotropically micro-cracked composite to respond to applied loadings. The combination of model components for isotropic matrix micro-cracking and directional micro-cracking in the composite material allows early age volumetric and mechanically induced directional micro-cracking to be simulated in a computationally convenient manner.

The constitutive model theory for a basic elastic two-phase composite with micro-cracking is presented for dilute and non-dilute inclusions. Furthermore, the exterior point Eshelby theory was used to allow for the amplification in stress and strain at the matrix/inclusion interface for both the elastic case and when considering micro-cracking.

Even though the material properties remains generic with non-specific inelastic strains applied in the matrix, the micro-crack criterion and evolution, presented focuses on application to cementitious materials for both forms of micro-cracking. A description of how the micromechanical model is implemented numerically is given for a constitutive driver algorithm and specified shrinkage stress path.

Chapter 4 validates the model presented here through 3D Finite Element simulations, demonstrating the performance of the model through illustrative stress and strain paths, and applying the theory to a cementitious composite with autogenous shrinkage in the matrix.

# Chapter 4

## Model Validation, Performance and Application

The solutions presented in Chapter 3 are developed further in this chapter. The accuracy of the homogenisation solutions are assessed using a series of three dimensional finite element analyses. Single and multiple inclusion models are presented in Section 4.1 showing the finite element model details, sections and stress distributions. Four illustrative stress/strain paths are then used to demonstrate the performance and capability of the model. These are shown in Section 4.2.

This model is also applied to a real problem where autogenous shrinkage occurs in a cementitious composite. A free shrinkage problem is simulated using a volumetric solution where a hydration model (Section 4.3.2) and associated solidified volume (Section 4.3.1) is used to evaluate the degree of hydration and elastic modulus of the matrix over time. Volumetric micro-cracking is also built into the model.

This autogenous shrinkage model predictions are compared with two experimental results found in the literature, see Section 4.3.3. The effect of including micro-cracking in a simulation of a matrix shrinkage problem is evaluated by comparing results with a solution in which micro-cracking was not considered. A parametric study has been undertaken on the model parameters (Section 4.3.4) where consideration has been given to using this approach a design tool.

### 4.1 FE Validation of homogenised solution

In this section, the accuracy of the proposed approach adopted for homogenisation and stress concentrations is assessed using two 3D Finite Element (FE) simulations. These models simulate the free shrinkage of the composite and were carried out using the LUSAS (2012) finite element software. Sun et al. (2007) compared the upper

and lower bound of elastic properties using random unit cell finite element models for accuracy against an analytical solution and experimental results for varying inclusion volume fractions. Here the effect of including the exterior point Eshelby amplification for a perfect interface bond is examined. The material properties, chosen to represent a typical cementitious composite, used for both analyses are given in Table 4.1 Neville & Brooks (2010). Young's modulus and Poisson's ratio are shown for a concrete where subscripts  $M$  and  $\Omega$  denote the cement paste matrix and coarse aggregate particle inclusion phases respectively. A minimum set of restraints were applied to the model to prevent free body displacements and rotations, but these did not provide any restraint against overall shrinkage of the model.

Table 4.1: Material properties used for the FE validation

$E_M$ ( $N/mm^2$ )	$\nu_M$	$E_\Omega$ ( $N/mm^2$ )	$\nu_\Omega$
24000	0.15	55000	0.25

The first model simulated a spherical inclusion within a matrix where the volumetric shrinkage potential (strain) of 0.0003 was applied to the matrix only. A 3D mesh was built using quadratic tetrahedral stress elements. Multiple meshes were employed in this study and the mesh converged solution had 54000 elements for the single inclusion model. The matrix cube boundary lines were split into 10 elements and each quarter circumference of the inclusion sphere was also divided into 10 elements. Figure 4.1 compares the numerical and analytical major principal stresses along section A-A. These major principal stresses compare favourably.

The second model contains multiple inclusions to simulate a homogenised composite material. 64 spherical inclusions were placed within a cube of matrix material. Again, multiple meshes were employed in the study. In total there were 93000 quadratic tetrahedral stress elements in the model. The Mori-Tanaka homogenisation scheme and exterior point Eshelby solution were used in the micromechanical solution. Figure 4.2 compares the numerical and analytical major principal stresses along section B-B. Again, the principal stresses recorded for both the micromechanical model and FE model compare favourably. Complete mesh convergence was not reached, however, these micromechanical and FE comparisons are sufficiently close to provide confidence in the homogenisation scheme for the present work.

The time taken for this linear 3D finite element solution was approximately half an hour on a modest laptop computer. The computations were carried out using a single one core of an Intel i3 CPU M350 2:27 GHz processor. The linear single and linear multi-inclusion FE analysis took 18 min 24 s and 30 min 11 s respectively, whereas the analytical solution only took 0.007 s for both the single inclusion and

the Mori-Tanaka homogenisation. These computational differences are comparable to the findings of Sanahuja (2013).

A detailed FE mesh sensitivity and convergence study has not been undertaken. If a full 3D non-linear solution had been attempted for multiple time steps the solution time is expected to be at least two orders of magnitude greater. Comparing these solution times the overall benefit of employing this type of non-linear micromechanical to simulate complex micro and meso material behaviour becomes evident.

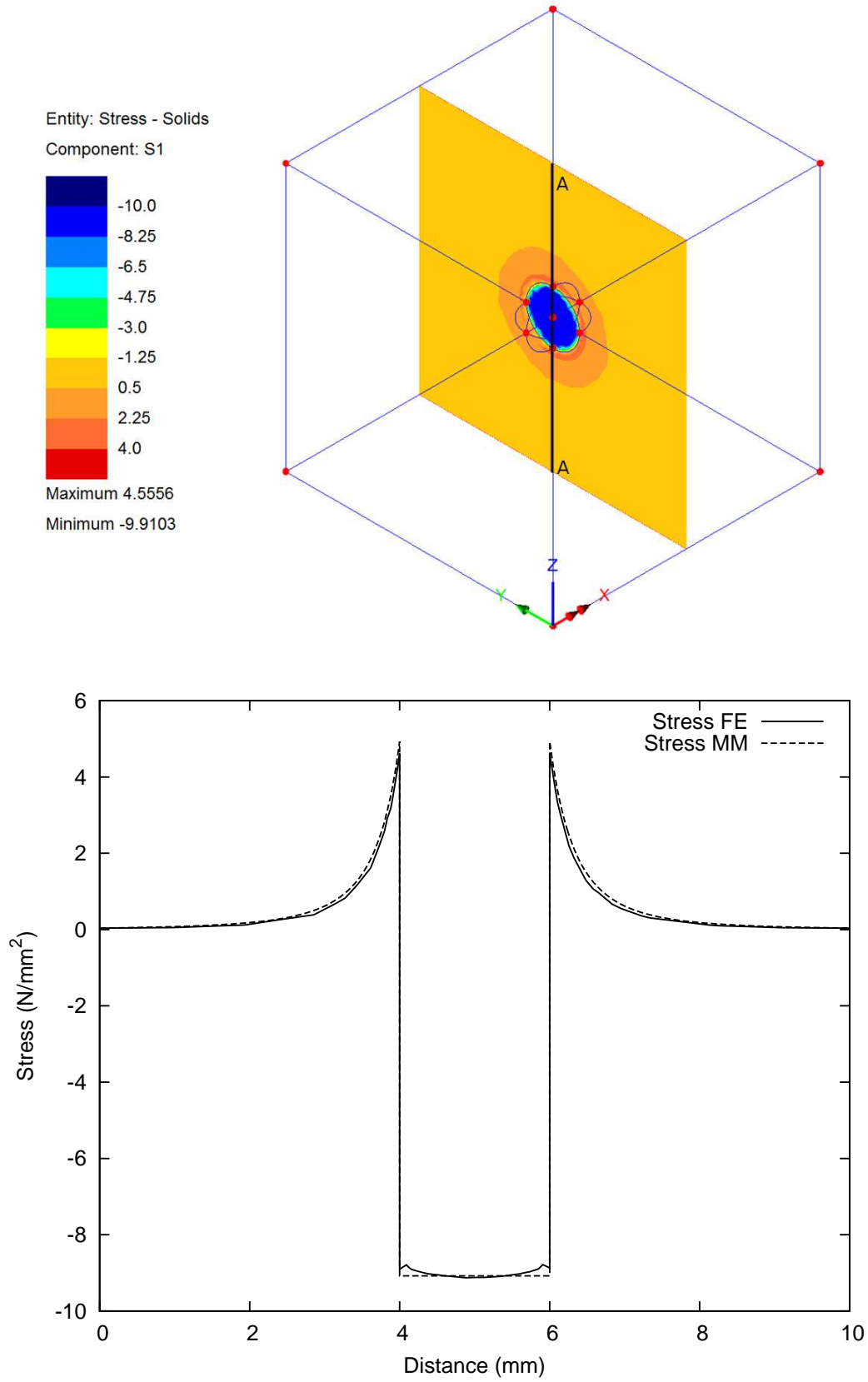


Figure 4.1: 3D FE plot and stress spatial distribution plot for one inclusion

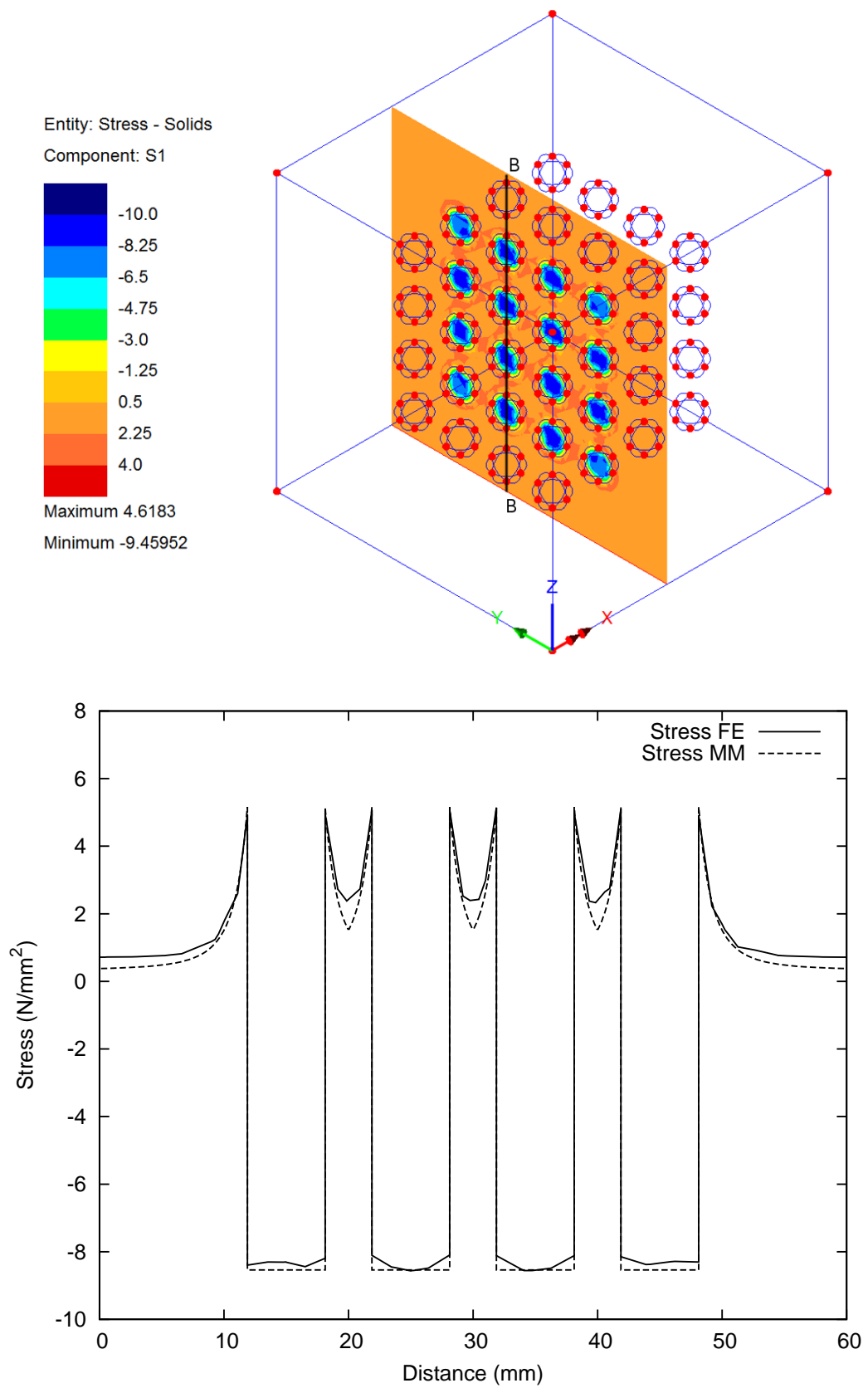


Figure 4.2: 3D FE plot and stress spatial distribution plot for multi-inclusion

## 4.2 Characteristic model predictions

A series of stress-strain paths are used to illustrate the characteristic response of the model. The paths selected are as follows;

1. Time dependent matrix shrinkage with and without associated matrix micro-cracking.
2. Matrix shrinkage restrained uniaxially with and without micro-cracking.
3. A uniaxial tensile strain path with and without matrix shrinkage.
4. Matrix shrinkage during the Willam et al. (1989) strain path which involves micro-crack formation under uniaxial tension followed by a rotating principal strain path.

The material properties are presented in Table 4.2 and are typical for a standard strength concrete. The inelastic strain applied in the matrix in all of the stress-strain paths is derived from the drying shrinkage strain from the EC2 code of practice (EN 1992 2008). The results are presented in graphical form showing the response for each path in terms of composite average stress and strain components.

Table 4.2: Typical cementitious composite material properties

$f_M$	$E_M$ ( $N/mm^2$ )	$\nu_M$	$f_\Omega$	$E_\Omega$ ( $N/mm^2$ )	$\nu_\Omega$	$\epsilon_{0v}$	$f_{tv}$ ( $N/mm^2$ )	$\epsilon_{0d}$	$f_{td}$ ( $N/mm^2$ )
0.3	20000	0.15	0.7	55000	0.25	0.01	1.33	0.0067	2

Path 1 simulates free shrinkage of the composite, for which the mean composite stress remains null. The results for simulations with and without micro-cracking (denoted MC and NMC respectively) are given in Figures 4.3b and 4.3c. These graphs provide the separate responses of the phases and show that the inclusion of micro-cracking in the model has a very significant effect on the stresses within the phases.

Path 2 simulates the behaviour in a restrained structural component. In this path, the composite xx strain component is fixed at zero and all other composite strain components are unrestrained. The results are given in Figures 4.4a to 4.4c and again illustrate the importance of micro-cracking on the response of the phases.

Path 3 shows an uniaxial strain path with shrinkage strain (SS) in the matrix and an uniaxial strain path without shrinkage strain (NSS) in the matrix. Figures 4.5a and 4.6a show the control data and strain loading paths. The stress results in Figure 4.6b show that the peak stress in the SS case is 7 % greater than in the NSS, for this particular loading case. This is because the shrinkage strain in the matrix opposes

the uniaxial force in the composite x direction. This results in xx-stress component, for the SS case, being less than for the NSS case, thus leading to reduced damage. It is noted that the inclusion stress is higher than the matrix up to  $2 N/mm^2$  for the SS case. The difference between the magnitude of the uniaxial strain and the shrinkage strain determines the Path 3 response.

In Paths 1 and 2 only the  $\omega_v$  micro-cracking parameter increases with time whilst  $\omega_d$  remains null. However, in Path 3 both parameters increase with time. Figures 4.7b and 4.7a show the volumetric micro-cracking parameter along with the directional micro-cracking parameters in six selected directions (See Figure 4.5b), for cases with and without matrix shrinkage respectively.  $\omega_{d_1}$  (parallel to the loading direction) exhibits the most micro-cracking and  $\omega_{d_2}$  (perpendicular to the loading direction) shows the least. As might be expected, matrix shrinkage increases the volumetric micro-cracking variable  $\omega_v$ .

Figures 4.8a to 4.8c illustrate the input for Path 4. The stress plots in Figure 4.9a compare the rotating stress (RS) response with the uniaxial stress (US) response without any rotation strains and correctly shows degradation of strength in the lateral direction with rotation. Figure 4.9b shows that the major principal stress decreases as the shear strain ( $\gamma_{xy}$ ) increases, as is desirable (Willam et al. 1989).

These paths illustrate the response of the model for a range of paths with and without micro-cracking and matrix shrinkage. The responses are all considered to be reasonable and to show that the two micro-cracking model components work together seamlessly.

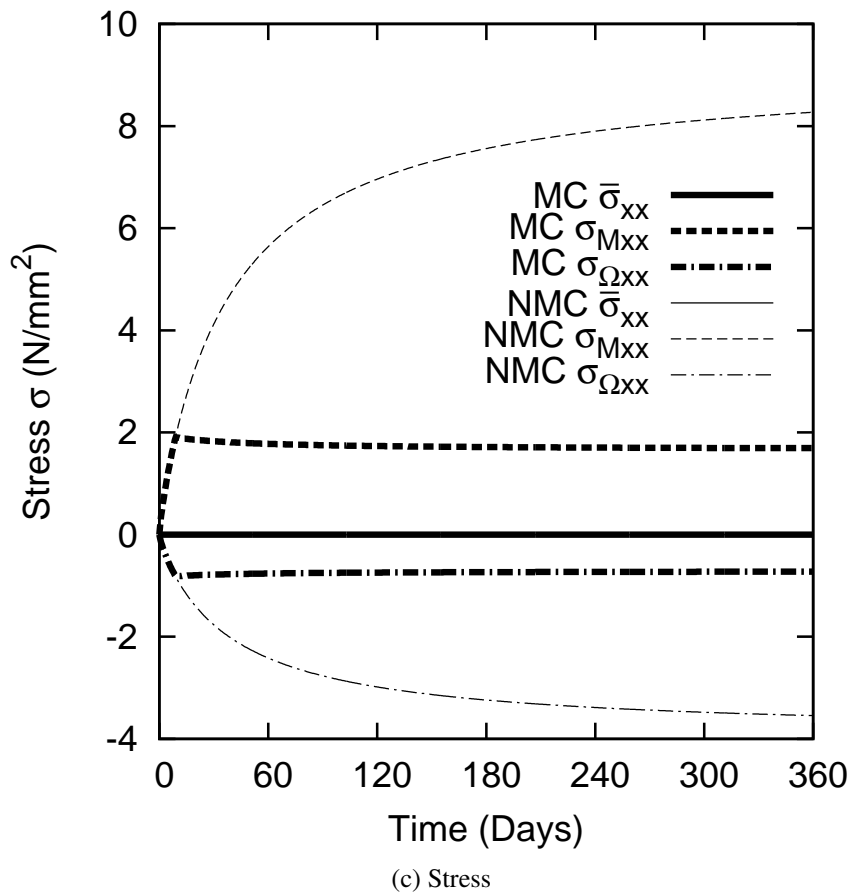
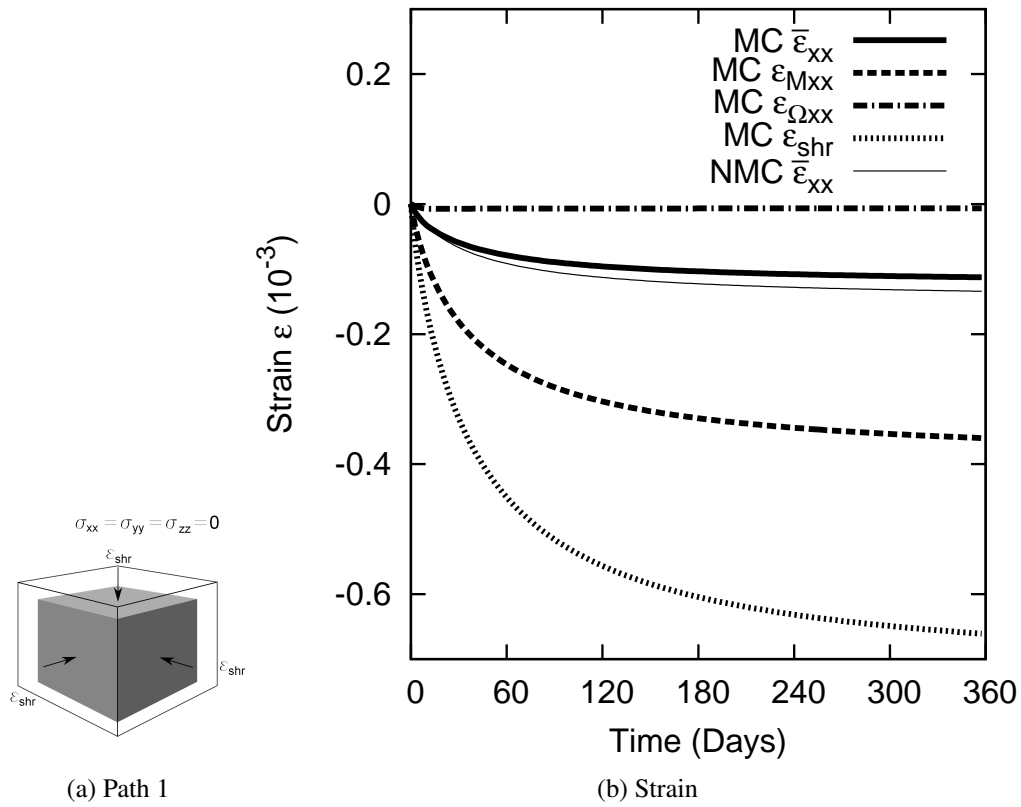


Figure 4.3: Time dependent matrix shrinkage with associated matrix micro-cracking (MC) and without matrix micro-cracking (NMC)

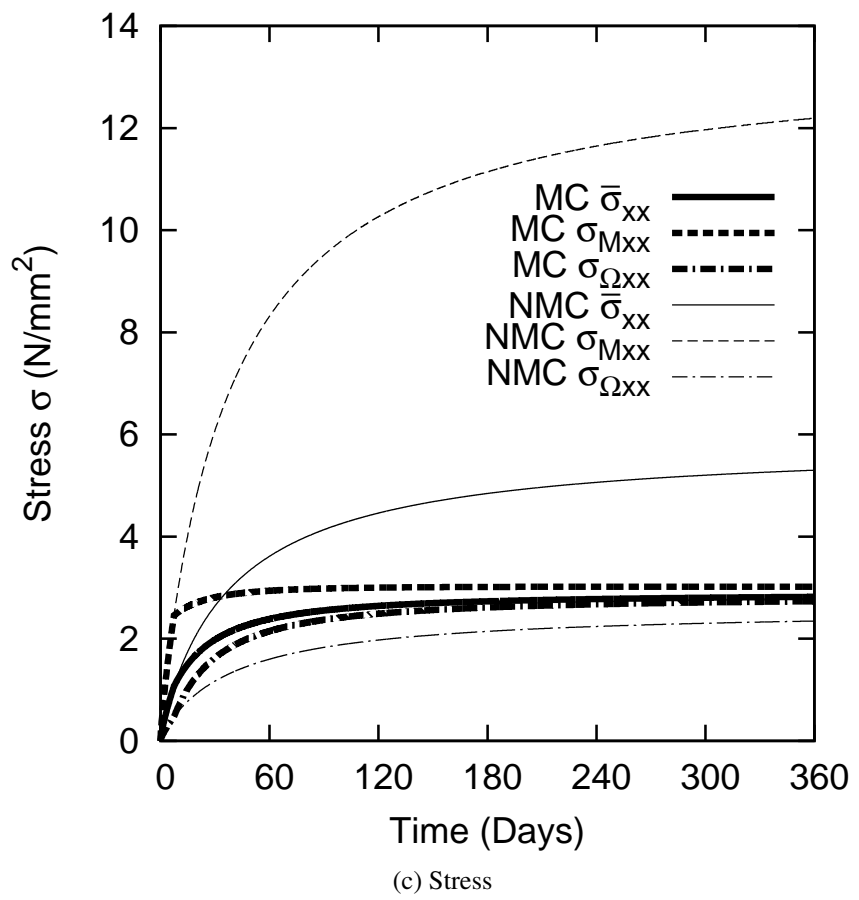
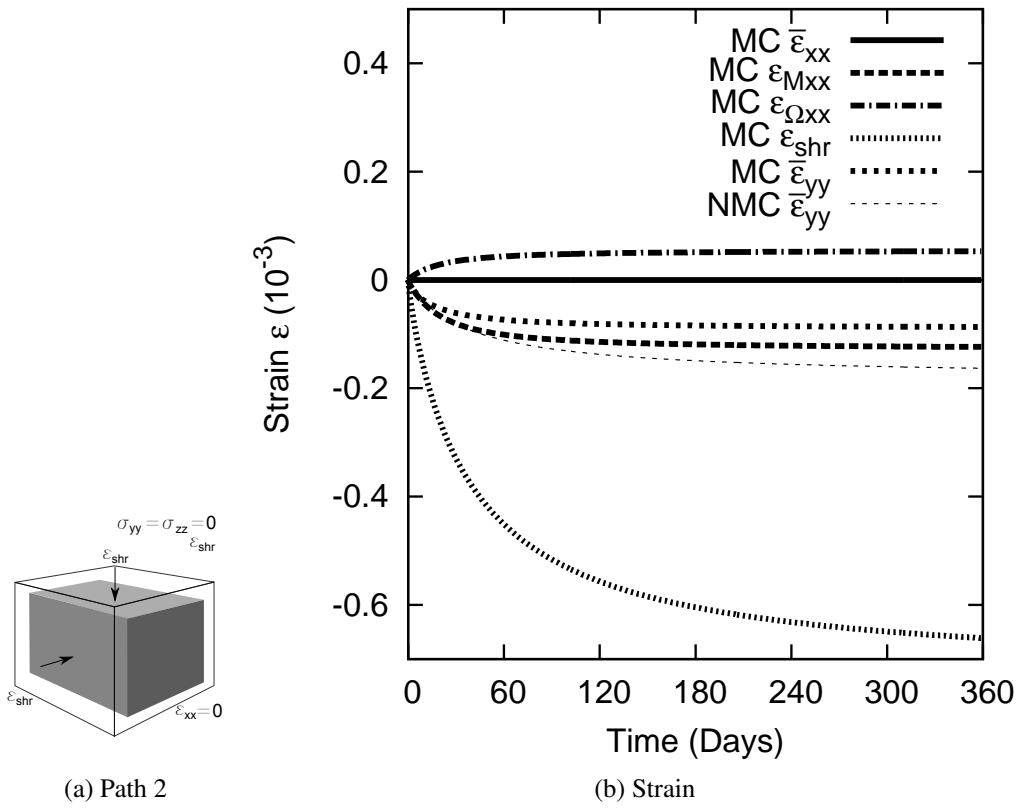
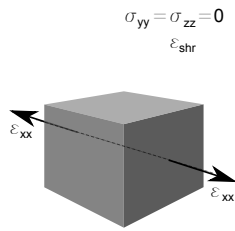
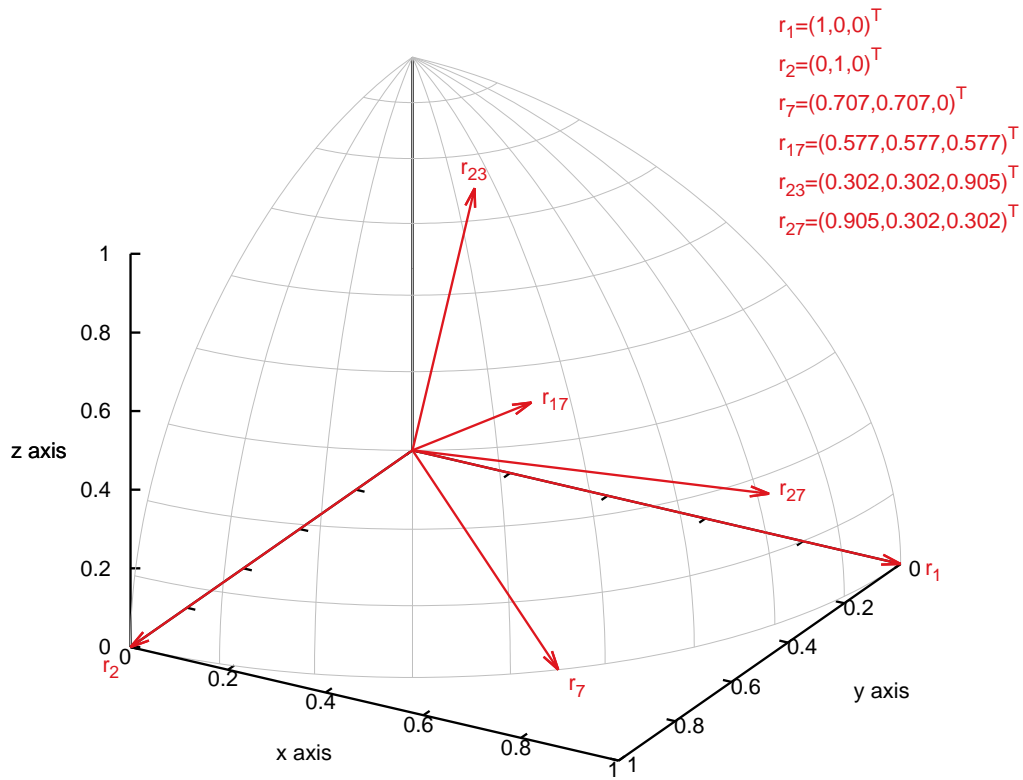


Figure 4.4: Matrix shrinkage restrained uniaxially with micro-cracking (MC) and without micro-cracking (NMC)

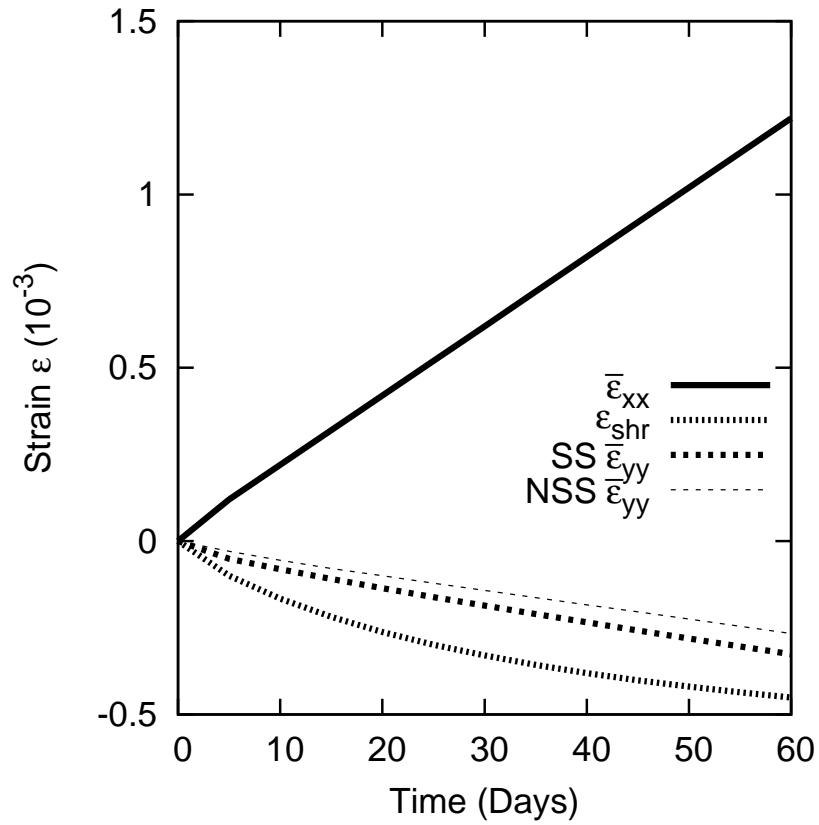


(a) Path 3

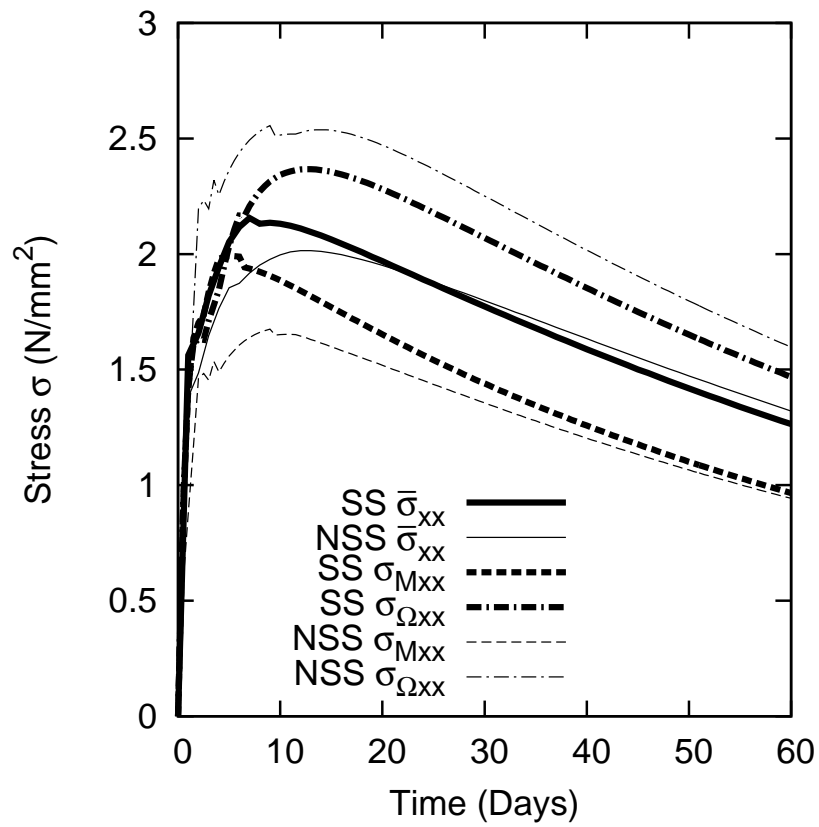


(b) Six selected directions

Figure 4.5: An uniaxial tensile strain path and selected micro-cracking directions

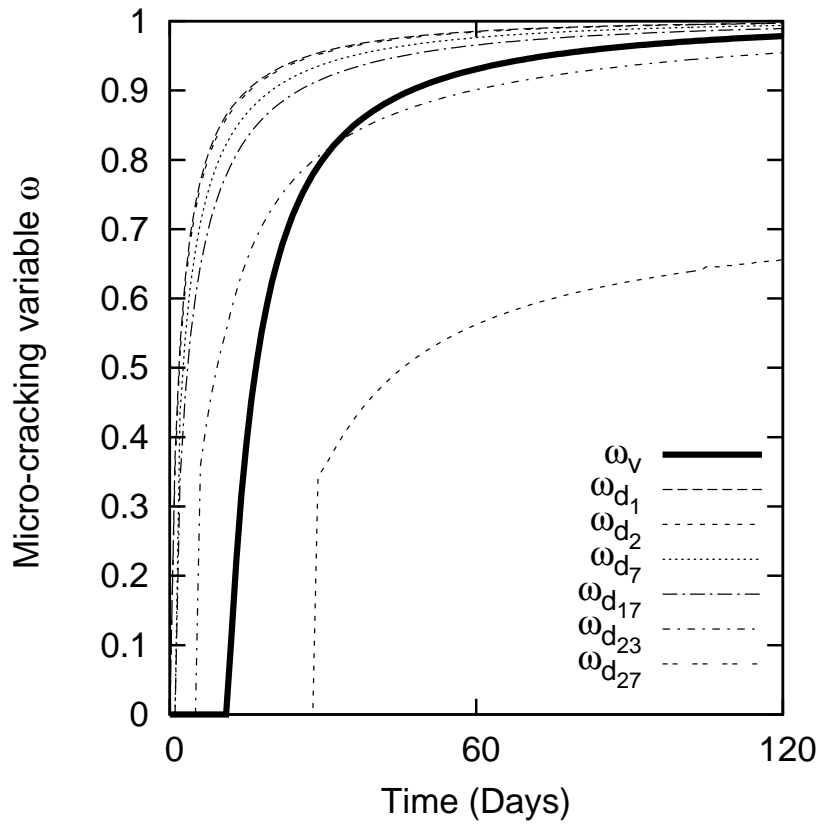


(a) Strain

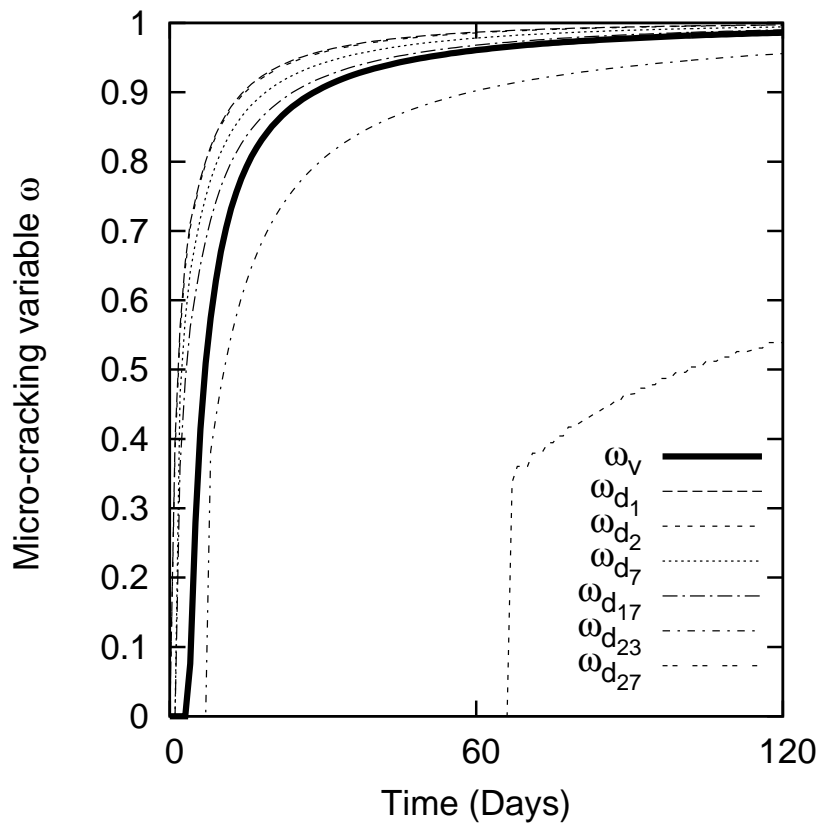


(b) Stress

Figure 4.6: An uniaxial tensile strain path with matrix shrinkage strain (SS) and without matrix shrinkage strain (NSS)

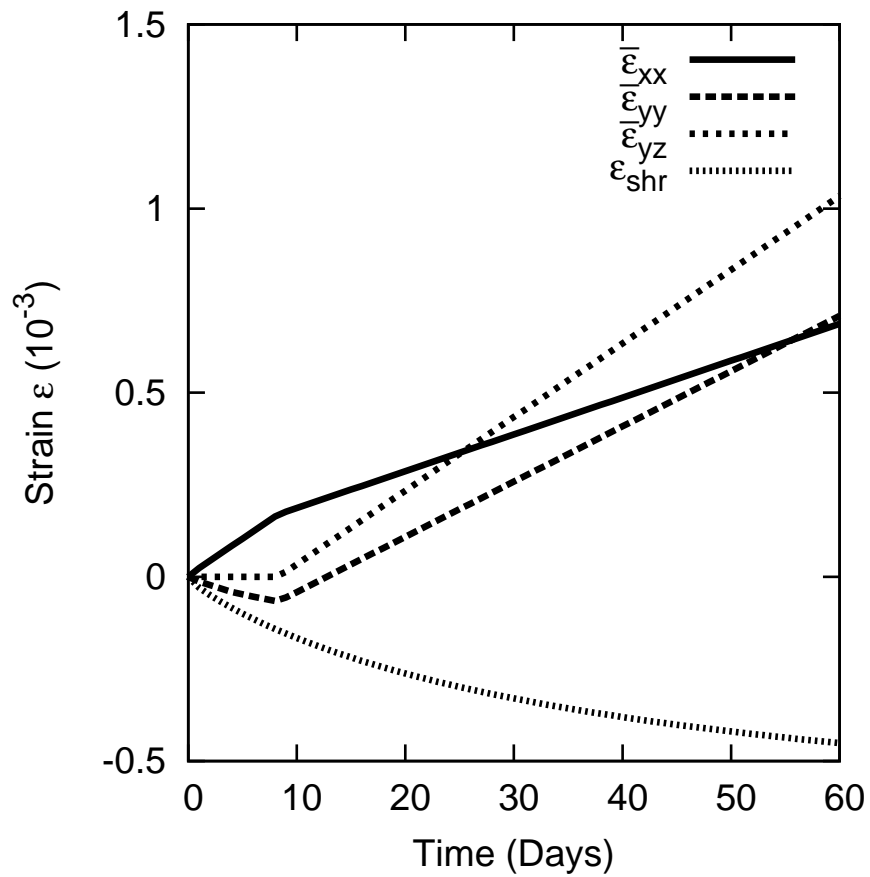
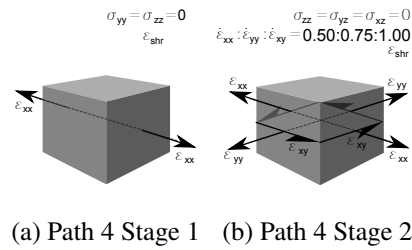


(a) Without matrix shrinkage



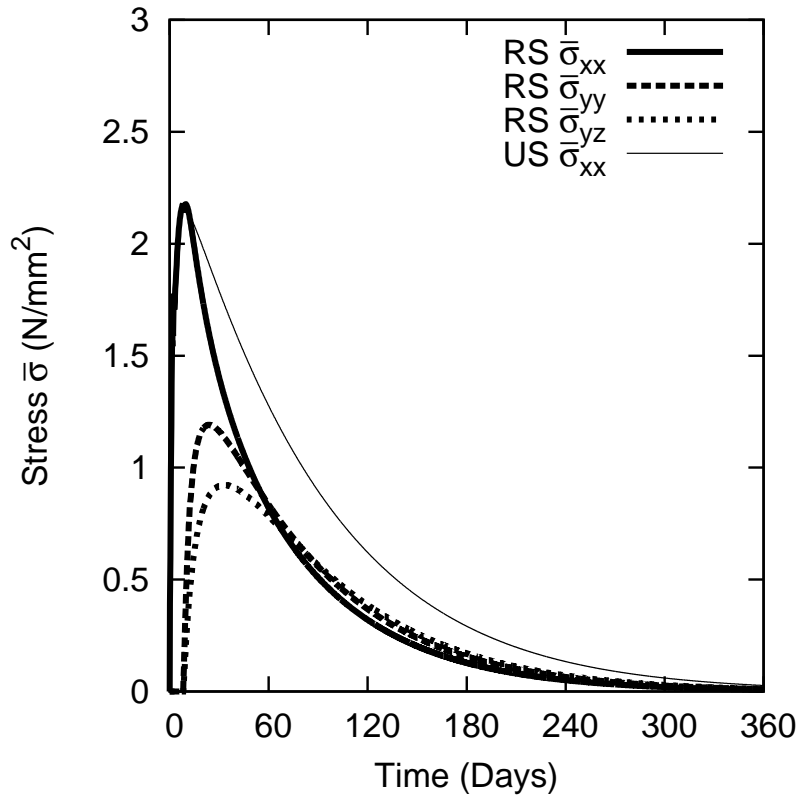
(b) With matrix shrinkage

Figure 4.7: Micro-cracking parameter response with/without matrix shrinkage

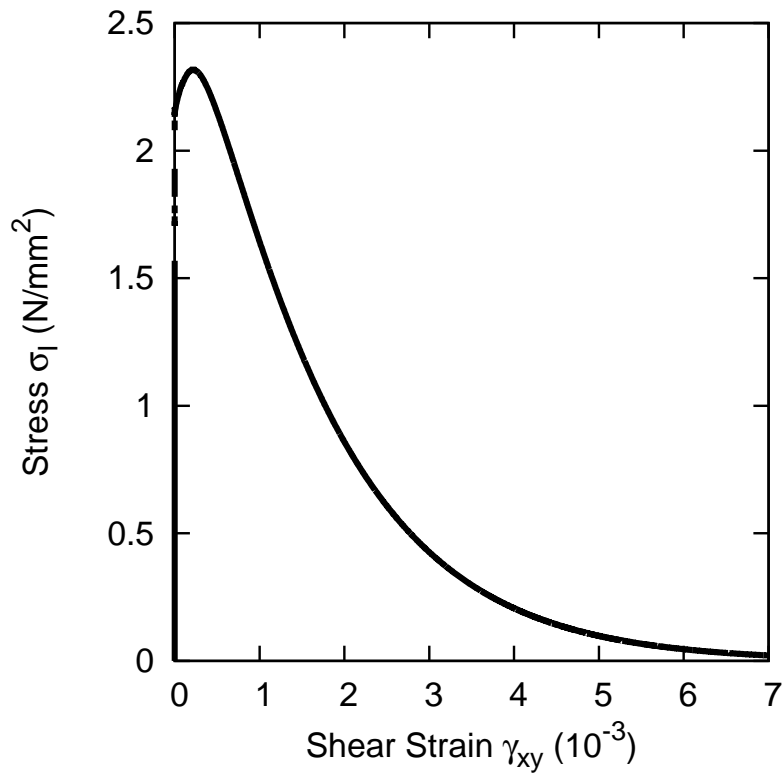


(c) Strain

Figure 4.8: Matrix shrinkage during the Willam et al. (1989) strain path which involves micro-crack formation under uniaxial tension followed by a rotating principal strain path



(a) Stress plot where the rotating stress (RS) response is compared to the uniaxial stress (US) response



(b) Principal stress and shear strain

Figure 4.9: Matrix shrinkage during the Willam et al. (1989) strain path results of the stress, principal stress and shear strain

## 4.3 Autogenous shrinkage during curing

In a cementitious composite material during curing, creep and shrinkage occur mainly in the matrix phase whilst the aggregate phase tends to restrain matrix movements. Most constitutive models for concrete creep and shrinkage consider the material as a whole e.g. (Neville et al. 1983, Bažant 1995, Benboudjema et al. 2001, 2005, EN 1992 2008) and do not explicitly consider the separate behaviour of the phases. This means that material parameters for these empirically derived models must be generated for each mix. In this section an alternative approach is explored in which the model described in Chapter 3 is applied to the problem of autogenous shrinkage of a cementitious composite. The aim is not to derive a comprehensive two-phase time dependent model for composite materials but rather to illustrate the benefits of applying the present model to such a problem. There have been a number of two-phase models for creep and shrinkage in concrete, for example Hirsch (1962), Counto (1964), England (1965) and Scheiner et al. (2009), see also Neville et al. (1983), but these do not explicitly consider the effects of micro-cracking. The present model is intermediate in complexity between the 4 level model of Pichler, Lackner & Mang (2007) and a single phase empirically based model, such as Bažant's B3 model (1995), although it is noted that the former model does not explicitly allow for the evolution of micro-cracks.

The objective of the following derivation is to produce a single shrinkage strain expression for a composite, given the properties of the matrix and inclusions as well as a shrinkage response for the matrix alone. To allow comparison with experimental results, an autogenous free shrinkage problem is simulated using a volumetric solution for a two-phase solidification model based on the solidifying material forming in a stress free state (Bažant & Prasanna 1989), shown in Section 4.3.1, which is implemented with a hydration model (Schindler & Folliard 2005) shown in Section 4.3.2). The relationship between the degree of hydration and the elastic modulus is established using the work of De Schutter (2002).

### 4.3.1 Solidification model

The solidified volume ( $v$ ) of material is related to the degree of hydration according to equation (4.29) shown and explained in Section 4.3.2. Working in volumetric terms the bulk modulus of the inclusion ( $K_{\Omega}$ ) retains its elastic value, whereas the bulk modulus of the matrix ( $K_M$ ) includes volumetric micro-cracking and solidification as shown in equation (4.1).

$$K_{Mv} = (1 - \omega_v) \cdot v \cdot K_M \quad (4.1)$$

The notation referring to micro-cracking in the matrix is omitted for clarity. If the volume of solidified material increases by  $\Delta v$  the damaged bulk modulus of the matrix becomes

$$K_{M(v+\Delta v)} = (1 - \omega_v) \cdot (v + \Delta v) \cdot K_M = K_{Mv} + K_{M\Delta v} \quad (4.2)$$

$\omega_v$  is the volumetric micro-cracking parameter as used Section 3.2.1.

Solidification strains ( $\epsilon_s$ ) are evaluated explicitly and these are defined as the inelastic strains necessary to ensure that solidified material first forms in a stress-free state. These strains are evaluated for each phase of the composite material by summing the increments associated with a change of solidified volume ( $\Delta v$ ) that occurs over a step interval ( $\Delta t$ ). The derivation and final expressions for the volumetric solidified strain increments for the matrix and inclusion phases are given below.

### Solidification in the matrix

The stress in the matrix material before solidification is

$$\sigma_M = K_{Mv} (\epsilon_M - \epsilon_{shrM} - \epsilon_{sM}) \quad (4.3)$$

where  $\epsilon_{shrM}$  is the matrix shrinkage strain and  $\epsilon_{sM}$  is the solidification strain in the matrix. Bažant's solidification theory states that material should form in a stress free state, thus there should be no change of stress due to an increment of solidification alone i.e.  $\Delta\sigma_{M\Delta v} = 0$ .

$$\sigma_M + \Delta\sigma_{M\Delta v} = K_{M(v+\Delta v)} (\epsilon_M - \epsilon_{shrM} - \epsilon_{sM} - \Delta\epsilon_{sM}) \quad (4.4)$$

Therefore,

$$\Delta\sigma_{M\Delta v} = -K_{Mv}\Delta\epsilon_{sM} + K_{M\Delta v} (\epsilon_M - \epsilon_{shrM} - \epsilon_{sM} - \Delta\epsilon_{sM}) = 0 \quad (4.5)$$

which can be rearranged to provide the change in solidification strain in the matrix ( $\Delta\epsilon_{sM}$ ).

$$\Delta\epsilon_{sM} = (v + \Delta v)^{-1} \Delta v (\epsilon_M - \epsilon_{shrM} - \epsilon_{sM}) \quad (4.6)$$

### Solidification impact on the inclusion

Similarly, the stress in the inclusion during solidification of the matrix is given by,

$$\sigma_\Omega = K_\Omega T_{\Omega v} (\epsilon_M - S_v (\epsilon_{shrM} + \epsilon_{s\Omega})) \quad (4.7)$$

where  $\epsilon_{s\Omega}$  is the solidification strain in the inclusion. It is noted that the terms  $T_{\Omega_v}$ ,  $S_v$  and  $A_{\Omega_v}$  are volumetric and as such are reduced to scalars as shown in the following equations.

$$T_{\Omega_v} = (1 + S_v \cdot A_{\Omega_v}) \quad (4.8)$$

$$S_v = \frac{1}{3} \cdot \frac{(v_M + 1)}{(1 - v_M)} \quad (4.9)$$

$$A_{\Omega_v} = [(K_{\Omega} - K_{M_v}) \cdot S_v + K_{M_v}]^{-1} \cdot (K_{M_v} - K_{\Omega}) \quad (4.10)$$

Upon solidification there is no change in stress in the inclusion i.e.  $\Delta\sigma_{\Omega\Delta v} = 0$ .

$$\sigma_{\Omega} + \Delta\sigma_{\Omega\Delta v} = K_{\Omega} T_{\Omega_{(v+\Delta v)}} (\epsilon_M - S_v (\epsilon_{shrM} + \epsilon_{s\Omega} + \Delta\epsilon_{s\Omega})) \quad (4.11)$$

Therefore,

$$\Delta\sigma_{\Omega\Delta v} = -K_{\Omega} T_{\Omega_v} S_v \Delta\epsilon_{s\Omega} + K_{\Omega} T_{\Omega_{\Delta v}} (\epsilon_M - S_v (\epsilon_{shrM} + \epsilon_{s\Omega} + \Delta\epsilon_{s\Omega})) = 0 \quad (4.12)$$

which can be rearranged to provide the change in solidification strain in the inclusion.

$$\Delta\epsilon_{s\Omega} = (T_{\Omega_v} S_v + T_{\Omega_{\Delta v}} S_v)^{-1} T_{\Omega_{\Delta v}} \cdot (\epsilon_M - S_v (\epsilon_{shrM} + \epsilon_{s\Omega})) \quad (4.13)$$

Where

$$T_{\Omega_{(v+\Delta v)}} = (1 + S_v \cdot A_{\Omega_{(v+\Delta v)}}) \quad (4.14)$$

and

$$A_{\Omega_{(v+\Delta v)}} = [(K_{\Omega} - K_{M_{(v+\Delta v)}}) \cdot S_v + K_{M_{(v+\Delta v)}}]^{-1} \cdot (K_{M_{(v+\Delta v)}} - K_{\Omega}). \quad (4.15)$$

Noting that  $T_{\Omega_{\Delta v}} = T_{\Omega_{(v+\Delta v)}} - T_{\Omega_v}$  is calculated explicitly.

### Solidification in a composite

The average stress upon solidification is,

$$\bar{\sigma} = f_M \cdot (\sigma_M + \Delta\sigma_M) + f_{\Omega} \cdot (\sigma_{\Omega} + \Delta\sigma_{\Omega}) \quad (4.16)$$

which upon substitution becomes,

$$\begin{aligned} \bar{\sigma} = & f_M K_{M_{(v+\Delta v)}} (\epsilon_M - \epsilon_{shrM} - \epsilon_{sM} - \Delta\epsilon_{sM}) + \\ & f_{\Omega} K_{\Omega} T_{\Omega_{(v+\Delta v)}} (\epsilon_M - S_v (\epsilon_{shrM} + \epsilon_{s\Omega} + \Delta\epsilon_{s\Omega})) \end{aligned} \quad (4.17)$$

The total strain upon solidification is,

$$\bar{\varepsilon} = f_{\Omega} \cdot T_{\Omega(v+\Delta v)} (\varepsilon_M - S_v (\varepsilon_{shrM} + \varepsilon_{s\Omega} + \Delta\varepsilon_{s\Omega})) + f_M \cdot \varepsilon_M \quad (4.18)$$

The overall constitutive relationship is therefore given by equation 4.19.

$$\bar{\sigma} = K_{M\Omega(v+\Delta v)} \cdot (\bar{\varepsilon} - \varepsilon_{INEQ_{v+\Delta v}}) \quad (4.19)$$

where

$$K_{M\Omega(v+\Delta v)} = \left( f_M K_{M(v+\Delta v)} + K_{\Omega} T_{\Omega(v+\Delta v)} \right) \left( f_{\Omega} T_{\Omega(v+\Delta v)} + f_M \right)^{-1} \quad (4.20)$$

and

$$\begin{aligned} \varepsilon_{INEQ_{v+\Delta v}} = & -f_{\Omega} T_{\Omega(v+\Delta v)} S_v (\varepsilon_{shrM} + \varepsilon_{s\Omega} + \Delta\varepsilon_{s\Omega}) + \\ & K_{M\Omega(v+\Delta v)}^{-1} f_M K_{M(v+\Delta v)} (\varepsilon_{shrM} + \varepsilon_{sM} + \Delta\varepsilon_{sM}) + \\ & K_{M\Omega(v+\Delta v)}^{-1} f_{\Omega} K_{\Omega} T_{\Omega(v+\Delta v)} S_v (\varepsilon_{shrM} + \varepsilon_{s\Omega} + \Delta\varepsilon_{s\Omega}) \end{aligned} \quad (4.21)$$

The mean composite stress in the material for a free shrinkage case is zero which results in  $\bar{\varepsilon} = \varepsilon_{INEQ_{v+\Delta v}}$ . The relationship between the total shrinkage in the composite and the shrinkage in the cement paste is given in equation (4.22). The separate components of the solidification strains are accumulated over time and thus remain explicit in the expression for the current time step.

$$\bar{\varepsilon} = -f_{\Omega} T_{\Omega v} S_v (\varepsilon_{shrM} + \varepsilon_{s\Omega}) + \quad (4.22)$$

$$\begin{aligned} & K_{M\Omega v}^{-1} f_M K_{Mv} (\varepsilon_{shrM} + \varepsilon_{sM}) + \\ & K_{M\Omega v}^{-1} f_{\Omega} K_{\Omega} T_{\Omega v} S_v (\varepsilon_{shrM} + \varepsilon_{s\Omega}) \end{aligned}$$

where  $K_{M\Omega v}$  is volumetric and as such are reduced to a scalar as follows.

$$K_{M\Omega v} = (f_M K_{Mv} + K_{\Omega} T_{\Omega v}) (f_{\Omega} T_{\Omega v} + f_M)^{-1} \quad (4.23)$$

Scalar equations for  $T_{\Omega v}$ ,  $S_v$  and  $A_{\Omega v}$  are already given in equations 4.8,4.9 and 4.10.

### 4.3.2 Hydration model

The relative degree of hydration of the cement with time is based on the work of Schindler & Folliard (2005). The total heat of hydration ( $H_{cem}$  in J/g) for cement is calculated using the fraction by weight ( $p_i$ ) for the different cement components of the total cement ( $p_{cem}$ ).

$$H_{cem} = 500p_{C_3S} + 260p_{C_2S} + 866p_{C_3A} + 420p_{C_4AF} + 624p_{SO_3} \quad (4.24)$$

$$+ 1186p_{FreeCaO} + 850p_{MgO}$$

The total heat of hydration ( $H_u$ ) is calculated taking account of all the cementitious materials: cement (*cem*), slag (*slag*), fly ash (*FA*).

$$H_u = H_{cem} \cdot p_{cem} + H_{slag} \cdot p_{slag} + H_{FA} \cdot p_{FA} \quad (4.25)$$

where,  $H_{slag}$  and  $H_{FA}$  are the heat of hydration of slag and fly ash respectively. The ultimate heat of hydration is calculated from

$$H_{uls} = H_u \cdot C_{cem} \quad (4.26)$$

where  $C_{cem}$  is the cementitious materials content. The relative degree of hydration ( $\Gamma_r$ ) is given by equation (4.27).

$$\Gamma_r = \exp\left(1 - \left(\frac{\tau}{t_e}\right)^{\beta_h}\right) \quad (4.27)$$

Where,  $\tau$  is hydration time parameter and  $\beta_h$  is a hydration shape factor.  $t_e$  is the equivalent maturity or age and defined as follows.

$$t_e = \sum_0^t \exp\left(\frac{A_E}{R} \left(\frac{1}{T_r} - \frac{1}{T_c}\right)\right) \cdot \Delta t \quad (4.28)$$

Where  $A_E$  is the activation energy,  $R$  is the universal gas constant,  $T_r$  and  $T_c$  are the reference and current temperatures respectively. The rate of heat generation is also given by Schindler & Folliard (2005) but not used in this work. The expressions proposed in this hydration model are therefore;

$$v = \Gamma_r^{c_E} \quad (4.29)$$

$$E(\Gamma_r) = \Gamma_r^{c_E} \cdot E_f = v \cdot E_f \quad (4.30)$$

$$f_c(\Gamma_r) = \Gamma_r^{c_{fc}} \cdot f_{cf} \quad (4.31)$$

$$f_t(\Gamma_r) = \Gamma_r^{c_{ft}} \cdot f_{tf} \quad (4.32)$$

with  $c_E$  taken as 0.7 from De Schutter (2002) also implemented in the solidification theory.  $c_{fc}$  and  $c_{ft}$  are taken as 1.5 and 1.0, matching data from Yi et al. (2003). The definition of  $\Gamma_r$  is different from that employed by De Schutter, in that

the present expression does not include a percolation threshold value of  $\Gamma$ . The approach taken is to assume that the stress is zero up to a certain degree of hydration ( $\Gamma_c$ ), which is typically taken to be 0.35, with the zero stress state being maintained via solidification strains.

### 4.3.3 Comparison with experimental results

Two examples are now used to illustrate the model performance with and without micro-cracking; (i) considers the experimental data of Pickett (1956) where the shrinkage of concrete with different volumetric proportions of aggregate were tested and (ii) compares model results with shrinkage test data from Baroghel-Bouny (1994). In both cases, the cement paste shrinkage experimental results have been used to drive the volumetric free shrinkage for the concrete model. Key model parameters used are shown in Tables 4.3 and 4.5. For the Pickett (1956) data, Ottawa sand, type 1 cement and 0.35 W/C ratio were used. The model results are compared to the experimental results with micro-cracking (MC) and without micro-cracking (NMC). The data used in the hydration model to simulate the data of Pickett (1956) and Baroghel-Bouny (1994) are shown in Tables 4.4 and 4.6 respectively.

Table 4.3: Typical cementitious composite material properties Pickett (1956)

$f_M$	$E_M$ ( $N/mm^2$ )	$v_M$	$f_\Omega$	$E_\Omega$ ( $N/mm^2$ )	$v_\Omega$	$E$	$\epsilon_{0v}$	$f_{tv}$ ( $N/mm^2$ )
0.338	12600	0.2	0.662	60000	0.25	28600	0.0375	1.0

Table 4.4: Hydration model parameters used for Pickett (1956)

$p_{C_3S}$	$p_{C_2S}$	$p_{C_3A}$	$p_{C_4AF}$	$p_{SO_3}$	$p_{FreeCaO}$	$p_{MgO}$	$p_{cem}$	Blaine ( $m^2/kg$ )	$C_{cem}$ ( $kg/m^3$ )
0.565	0.140	0.100	0.080	0.035	0.029	0.013	1	350	400

Table 4.5: Typical cementitious composite material properties Baroghel-Bouny (1994)

$f_M$	$E_M$ ( $N/mm^2$ )	$v_M$	$f_\Omega$	$E_\Omega$ ( $N/mm^2$ )	$v_\Omega$	$E$	$\epsilon_{0v}$	$f_{tv}$ ( $N/mm^2$ )
0.213	25500	0.25	0.787	55000	0.3	48707	0.0563	0.67

Figure 4.10 and 4.11 show results without micro-cracking and with volumetric micro-cracking. It can be seen, in both cases, micro-cracking brings the strain results closer to the experimental findings. The difference between the computational

Table 4.6: Hydration model parameters used for Baroghel-Bouny (1994)

$PC_3S$	$PC_2S$	$PC_3A$	$PC_4AF$	$PSO_3$	$PFreeCaO$	$PMgO$	$p_{cem}$	Blaine ( $m^2/kg$ )	$C_{cem}$ ( $kg/m^3$ )
0.573	0.240	0.030	0.076	0.020	0.053	0.008	1	312	400

solution and the experimental results without micro-cracking is 8.3 % for Pickett (1956) and 18.0 % for Baroghel-Bouny (1994). With micro-cracking the difference is 2.6 % for Pickett (1956) and 4.4 % for Baroghel-Bouny (1994).

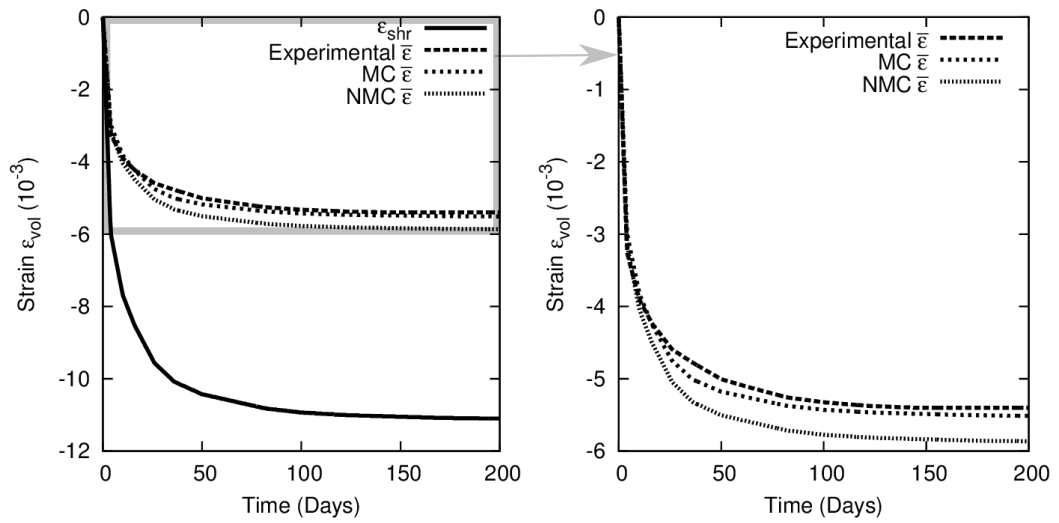


Figure 4.10: Pickett (1956) experimental results compared to model with/without micro-cracking

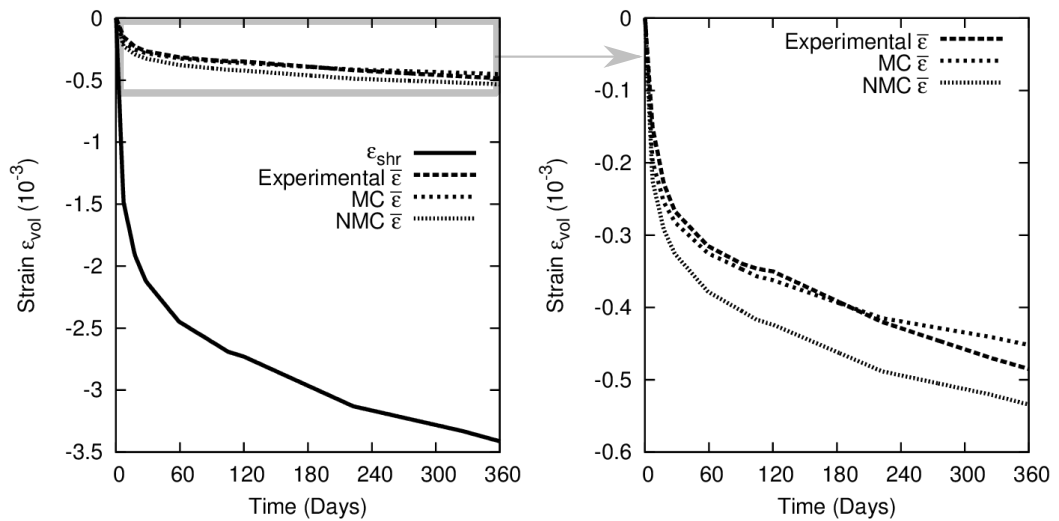


Figure 4.11: Baroghel-Bouny (1994) experimental results compared to model with/without micro-cracking

### 4.3.4 Parametric study for design

In addition to comparing with experimental results, this volumetric model has been subjected to a parametric study. The hydration model is based on a type *II* cement with shrinkage strain taken from EC2 code of practice (EN 1992 2008) and with fixed micro-cracking parameters. The composition (volume fraction of aggregate  $f_{\Omega}$ ) and elastic modulus have been varied, and cases with and without micro-cracking considered as shown in Figure 4.12. As may be seen, micro-cracking is most pronounced when the matrix and inclusion volume fractions are equal. These plots suggest that the model could be used as a concrete design tool.

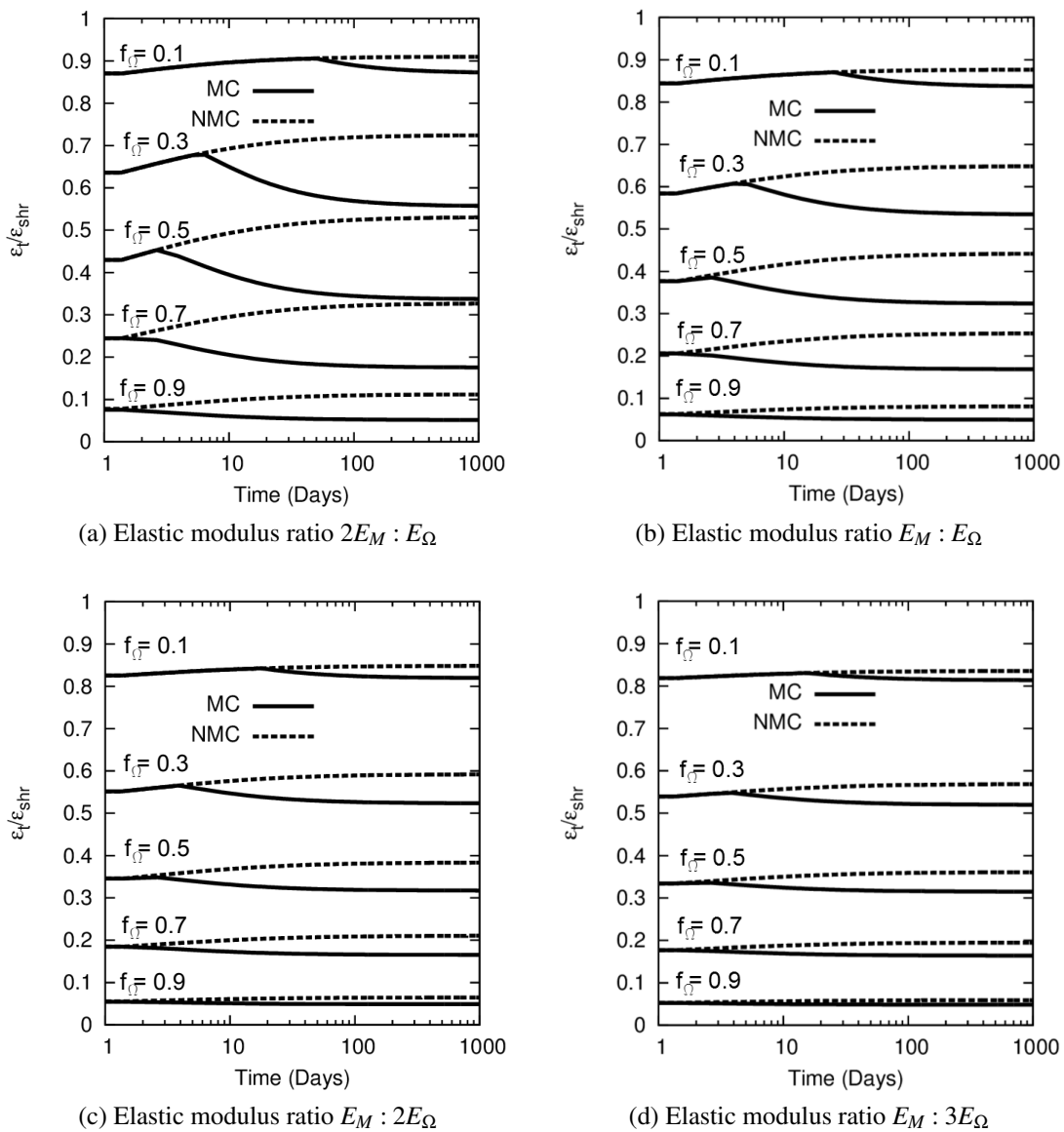


Figure 4.12: Parametric study of total shrinkage/matrix shrinkage with/without micro-cracking

## Conclusions

This chapter has shown a range of applications for the micromechanical theory developed in Chapter 3. The ability to simulate inelastic strains in the matrix only for a two-phase composite is an important step towards creating a comprehensive micromechanical model for cementitious materials. In particular, when considering that the solution is generic and can use inelastic strains derived from shrinkage, creep, micro-cracking, differential thermal expansion or ageing. The model solves these time dependent inelastic processes in a computationally convenient manner.

A 3D FE validation of the homogenisation scheme, including the exterior point Eshelby solution for matrix shrinkage problem, showed that the solution has satisfactory accuracy for the cementitious composite considered. The shrinkage of the matrix constrained by inclusions, during the 3D FE validation, clearly illustrated the importance of using the EPE solution when choosing realistic micro-cracking initiation criterion and evolution parameters. The amplified stresses in the matrix in the inclusion/matrix interface zone show where the micro-cracking will begin. The computational time saved in using the non-linear micromechanical solution compared to the FE solution shows how beneficial this micromechanical approach can be in simulating complex micro and meso material behaviours.

The combination of model components for isotropic matrix micro-cracking and directional (anisotropic) micro-cracking in the composite material allows early age volumetric and mechanically induced directional micro-cracking to be simulated in a computationally convenient manner. The characteristic model predictions using the stress/strain paths clearly showed this separation between the isotropic and directional micro-cracking components. In particular, this can be seen when comparing the difference between the free shrinkage and uniaxial tensile strain path examples, where the micro-cracking variables are shown graphically. The final stress strain path chosen, being the Willam et al. (1989) strain path, involved micro-crack formation under uniaxial tension followed by a rotating principal strain path. The reasonable response of the model showed that the two micro-cracking model components work together seamlessly and that the model is capable of representing the shear softening response, which is important for future application in fracture propagation problems in FE simulations.

The inelastic behaviour of concrete subject to autogenous drying is successfully simulated. The volumetric solidification and hydration model provides an accurate means for simulating the inelastic behaviour of concrete subject to autogenous drying and is capable of quantifying the effects of micro-cracking. The model results compare favourably with experimental data and show the importance of including the effects of micro-cracking during the drying process.



# Chapter 5

## Experimental Study on Autogenous Cementitious Healing

The aim of this experimental study was to determine the mechanical properties of an autogenous self-healing cementitious material which could then be used to verify a numerical study of the self-healing process. The material stiffness development with time was sought for a healed specimen at the macro- and micro-scale. Firstly, techniques that are capable of measuring autogenous healing as well as the findings from preliminary investigations into suitable experiments are discussed. The experimental set-up, programme of study, specimen preparation and testing procedure are then described. Finally, the qualitative and quantitative results are presented and discussed.

### 5.1 Preliminary investigations

It was initially envisaged that in order to determine the autogenous crack healing material properties, they should be isolated from those of the bulk material. However, this proved difficult since the amount of autogenous material produced in a healed crack was very small in comparison with the original cementitious material and was difficult to identify. During the preliminary investigations a range of techniques were reviewed and investigated to establish those that were most appropriate to be taken forward to the main investigation programme.

An overview of the experimental techniques used in the literature to examine various forms of self-healing in cementitious materials has already been presented in Chapter 2.4 Section 2.4.4. The preliminary investigations focused on standard techniques used to examine material strength.

### 5.1.1 Review of indentation techniques

Indentation tests, also known as hardness tests, have been widely applied across many material types to indirectly determine their strength properties. Similar to many techniques, indentation tests can be applied at the macro-, micro- and nano-scales. The general principle of indentation testing is relatively simple. A known load is applied through a known shaped indenter onto the surface of the material for a single loading - unloading cycle. The indentation depth is measured and converted to a relative material property, for example, compressive strength, tensile strength or effective yield strength.

In situ non-destructive tests to obtain mechanical properties of concrete are widely available at the macro-scale. Impact tests on concrete include the Schmidt hammer test (or rebound hammer test), in which a relationship between rebound distance and hardness is used to determine an estimate of the compressive strength (BS EN 12504-2 2012). Schmidt's invention in the 1950s standardised the in situ test to determine concrete compressive strength. The hammer measures the rebound amount of a spring loaded mass impacting against the surface. Windsor probes (or penetration resistance), measure the hardness of concrete below the surface (Neville & Brooks 2010). The forces involved in both the Schmidt hammer and Windsor probes are too large to be applied at the micro-scale. The Schmidt hammer, for example, applies a significant force over an approximately  $1\text{cm}^2$  area resulting in high impact energy (typically greater than 0.735 Nm). This would be too much impact energy for small, early age samples and would not be sufficiently sensitive to consider autogenous healing deposits.

At the other end of the physical scale are nano indentation techniques, commonly called Atomic Force Microscopy (AFM). These have also been applied to determine the properties of cementitious materials (Mondal 2008). This involves measuring the movements and force applied to a mechanical probe when moving over the surface of a material. One of the downsides associated with this approach is that it is difficult to attribute the local mechanical properties measured to the matrix or individual micro-structure elements in the cement paste. A variation on this AFM approach is the Hysitron Triboindenter, where a scanning probe microscopy imaging facility, was used to determine the mechanical properties of hardened cement paste and cement paste at the early age (Mondal et al. 2007). The image resolution of a Triboindenter is not as high as a conventional AFM, and consequently, it overcomes the ambiguity of assigning properties to these individual material phases.

The AFM technique has been applied to many other materials. The properties of glass coatings, for example, were investigated by Malzbender et al. (2002). The key difference between these glass coatings and concrete is the uniform nature of

the surface at the nano-scale. The issues of surface roughness and contact with the smooth probe on concrete are discussed in detail by Mondal (2008). Another relevant application of AFM is in the observation of the carbonation process on the surface of calcium hydroxide crystals in hardened cement paste (Yang et al. 2003). Again, at the nano-scale another technique used is the scratch test. The effect of friction on scratch adhesion testing can be examined using bespoke apparatus, such as the one used by Blees et al. (2000). These nano indentation techniques cannot be ruled out altogether, although they require considerable specialist knowledge and apparatus to use and apply the results objectively.

Micro-scale tests, lying in between the macro- and nano-scale, are ideally suited to obtaining mechanical properties of the individual components identified in the micromechanical two-phase models developed in Chapters 3 and 6. At this micro-scale, hardness testing is widely used to determine metal properties, where empirical relationships are made between hardness, yield strength and tensile strength (Pavlina & Van Tyne 2008).

Brinell, Vickers, Knoop and Rockwell are examples of such superficial hardness tests (BS EN 843-4 2005). These are suited to metals and ceramics with smooth surfaces. The Vickers test uses a square pyramid and the Knoop test uses an extended pyramid shaped indenter. They both rely on measuring the width at the top of an imprint given by a known load on the indenter. The difficulty in applying these techniques to non-reflective materials, such as concrete, is that the imprint cannot be seen which leads to the requirement of further processing using another optical techniques, such as Scanning Electron Microscope (SEM), to accurately measure the imprint.

The Rockwell hardness test is more suited to ceramics and other non-reflective materials since the technique does not rely on seeing the imprint left by the indenter. The Rockwell test applies a minor and major load through a penetrator and measure the deformation in the surface upon removal of the major load. This test has been used for concrete samples (Windslow 1981). In these experiments the testing surface was polished to obtain a smooth surface. An advantage of the test is that is very rapid and is applied using a manually operated unit and the hardness number can be correlated against tensile strength. The Windslow (1981) experiments showed that there was only a small variation in Rockwell number even for a rough sawn sample. The thickness of the material impacted by the major load has shown to be typically 10 times the depth of the indenter (Wilson Instruments 2004, Low 2001) which is an important consideration when interpreting the Rockwell test results.

## 5.1.2 Preliminary investigation

Preliminary investigations were undertaken to establish suitable experimental procedures and configurations. This involved the selection of the curing, size of beams, data to measure and how to create cracks. The results of these investigations are not explicitly reported here, but the lessons learnt feed directly into the main experimental programme.

It was found, consistent with many other studies, that curing samples completely in water produced much better self-healing results compared to tests in which the specimens were air cured, partially immersed in water or exposing only the crack face to water. It was difficult to distinguish the results of self-healing over short time periods. Using periods of weeks rather than days was therefore deemed suitable for these experiments.

Larger 500 mm x 100 mm x 100 mm beams were initially tested but it was found that smaller samples, 255 mm x 75 mm x 75 mm, provided very similar results but had the advantage of being easier to handle. A few trials were carried out to determine whether or not to include steel as conventional reinforcement or as a hinge mechanism at the top of the beam. It was decided not to include any reinforcement since the higher loads to fracture the samples were avoided. The difficulty of removing the proportion of load carried by the reinforcement was also saved, thus giving the pure concrete response leading to transparent results.

The deflection in some specimens was measured using a Linear Variable Differential Transducer (LVDT) gauge. This LVDT gauge was held in place by a custom made aluminium arm that was connected to one side of the specimen. The purpose of this was to avoid bedding in effects of the sample in the test rig when measuring central displacement. However, it was decided that detailed information on displacement was not required and that deflection data from the testing rig ram would suffice. This meant that there was no need to drill holes into the concrete before testing, thus minimising disturbance to the samples.

Self-healing tests were initially carried out on beams where a crack was formed in the sample through loading using a three point bending test arrangement to produce natural cracks in the beam at a notch position. The best self-healing results occurred when the initial stage of testing of the beam took place as soon as possible after casting and de-moulding the samples, this being at an age of 24 hours. The details are not reported here but confirm investigations carried out by Ter Heide (2005). The greatest difficulty with this approach was the adhesion of the knife edge spacers to the 'green' concrete for the Crack Mouth Opening Displacement (CMOD) clip gauge. The young age and low strength of the samples meant that the gauge exerted forces that were sometimes higher than the knife edge bond to the

concrete.

Being able to control the crack width during the healing or curing phase of the experiments was an important aspect of the study. The natural cracks widths were varied by wedging open the cracks using different thickness steel fibres. However, creating a preformed narrow notch in the sample has the distinct advantage of having an uniform width. This simulated an idealised crack, in which the deposition and build up of autogenous healing material was obtained. This method had the added advantage of giving a clear distinction between the original material and any new material deposited. Trials were carried out to determine how best to create these preformed narrow notches. Different materials, such as metals, plastic and cardboard were tested, creating different uniform cracks width and different notch depth. It was found that having a metal plate (brass or steel shim) 0.1 mm, 0.2 mm and 0.3 mm thick to half the depth of the beam gave the best results. Figures 5.1 and 5.2, in the next section, give a visual interpretation of this experimental set-up.

To prevent bonding, this metal plate was removed from the sample approximately 6 hours after casting. This was an optimum time where the cement paste had stiffened sufficiently, to prevent plastic deformation and keep the crack open, yet remained easy to remove. The metal plates were specifically not coated with mould release oil in order to prevent a change in the nature of the artificial crack surface. A much thinner copper foil at 0.045 mm thick was used to simulate an unhealed crack by Ter Heide (2005). Two beams had the foil removed and then healed in water for two weeks. The mechanical strength under three point bending was compared to beams with the foil left inside. There was no difference in the mechanical response of these beams and the authors concluded that no healing had taken place.

For the control beams, where the plates were to be left in, it was found beneficial to surround the metal plates with a plastic wrap (cling film) to remove the effects of any bond between the concrete and the plate. Samples were also examined where they were completely cracked in two and where a full depth plate meant that two pieces could be put back together to form a beam. These were cured by standing the samples vertically in water, using self-weight and loading with 20 kg weights to force the two halves together. In all cases the beam samples failed whilst attempting to place them in the three point bending rig.

## **5.2 Experimental procedure**

As a result of the preliminary investigations, a programme of study was planned to investigate autogenous self-healing in cementitious materials. The procedure described below was deemed to be the most suitable and practical for obtaining

the required experimental data to support the numerical models in this thesis. The investigative nature of the experimental work and interesting results led to further work examining in greater detail the properties of the preformed narrow notch.

### 5.2.1 Programme of study and specimen preparation

Sets 1 to 3 were experiments carried out on rectangular concrete beams where natural cracks were induced. Sets 4 to 6 were experiments again on rectangular concrete beams but had preformed narrow notches. Set 7 and set 8 samples were also rectangular beams but this time made from mortar. These mortar beam tests focused on tracking the development of healing with time for the preformed narrow notches. A summary of these experiments are shown in Table 5.2.

The primary focus of these experiments was to quantify and obtain the mechanical properties of cementitious materials that are associated with autogenous healing. Permeability test were not used as an indirect method to determine the amount of healing, which meant that self-healing is isolated from self-sealing, as discussed in Section 2.4.2, Chapter 2. The preliminary investigations showed that the maximum potential for self-healing occurred when the specimen was damaged as soon as possible after casting. The healing process began when the samples were submerged under water in the concrete curing tanks. The crack width to be healed and length of time of self-healing were the main variables.

Figure 5.1 shows the general arrangement that was used throughout this programme of study. The samples were small scale laboratory specimens; with the dimensions being height ( $h_b$ ) = 75 mm, width ( $b_b$ ) = 75 mm, length between supports ( $L$ ) = 200 mm and full length ( $L_1$ ) = 255 mm. The concrete composition, for both concrete and mortar, is shown in Table 5.1 for mass per cubic metre and mass proportion to cement.

Table 5.1: Composition of concrete and mortar beams

Material	Concrete ( $kg/m^3$ )	Mass proportion (to cement)	Mortar ( $kg/m^3$ )	Mass proportion (to cement)
Cement	396.7	1	533.3	1
Water	178.5	0.45	266.7	0.5
Coarse aggregate	1110.7	2.8	-	-
Sand	714.0	1.8	1600.0	3

The aggregate used was 10 mm crushed limestone and the sand was natural dredged sand sieved to obtain 2 mm size and smaller. The cement used was general purpose CEM II/B-V 32.5R Portland composite cement complying with BS EN 197-1. This contained 65-79 % of clinker, 21-35 % siliceous fly ash and up to 5 %

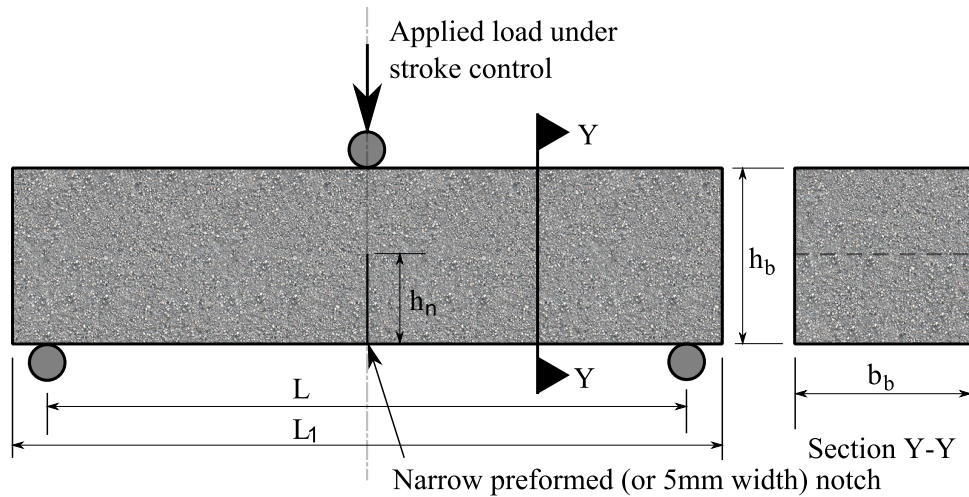


Figure 5.1: Specimen general arrangement

minor additional constituents.

Natural cracks were created using a three point flexural bending test, where the crack width was varied by limiting the degree to which the crack closed upon unloading. Crack widths of zero (where the crack was allowed to close under self-weight), 0.18 mm and 0.3 mm were examined. These were achieved by placing steel fibres into the opened crack on the underside of the beam whilst under load, effectively wedging the crack open. Removal of the load resulted in maintaining the crack widths at the bottom of the beam whilst gradually reducing the crack width to zero at the top of the beam.

A preformed narrow notch (or ideal crack) with uniform width was achieved by casting a metal plate into the mix to half the depth of the beam ( $h_n=37.5$  mm) and removing 6 hours after casting. The resulting narrow notch was prevented from drying out by covering the beam samples with wet hessian sacks. This was done to preserve the surfaces within the notch and prevent any changes that could occur due to drying. Three different metal plates with uniform thickness were used; 0.1 mm, 0.2 mm and 0.3mm. Figure 5.2 shows the plate configuration before casting the concrete mix. Two control samples were also set-up; one in which the plate was left in simulating zero healing and a plain beam with no plates which provides results for an uncracked beam.

All samples were de-moulded 24 hours after casting and then cured under water at 20 °C. The length of curing for the samples varied between 7 and 56 days. A 5 mm wide and deep notch was sawn across the mid-point on the underside of the samples to form a crack initiator before testing.



Figure 5.2: Plate configuration before casting shown with twin moulds

The material strength tests undertaken included:

- Flexural strength using a three point bending test (BS EN 12390-5 2009).
- Compressive strength ( $f_c$ ) - 100 mm cube were tested in compression (BS EN 12390-3 2009) carried out on the same day as the flexural test.
- Specific fracture energy ( $G_f$ ) was calculated indirectly from the load-CMOD results following Brokenshire (1995) which is based on work from the RILEM Committee FMC-50.
- Rockwell hardness test on newly deposited material (Wilson Instruments 2004, BS EN 843-4 2005).

Material property tests were also carried out in addition to visual observations, which included single samples run through SEM and X-ray diffraction (XRD). Table 5.2 shows the summary of the specimen programme configuration, the material strength and property tests carried out for each set.

Table 5.2: Summary of experimental study

Label	Set 1	Set 2	Set 3	Set 4	Set 5	Set 6	Set 7	Set 8
Material	Concrete	Concrete	Concrete	Concrete	Concrete	Concrete	Mortar	Mortar
Crack Type	Natural	Natural	Natural	Narrow notch	Narrow notch	Narrow notch	Narrow notch	Narrow notch
Maximum crack width (mm)	0	0.18	0.3	0.1	0.2	0.3	0.2	0.3
SH samples	9	9	9	4	9	9	8	8
Control beams (No.)	6	6	6	4	6	6	8	8
Zero healing beams (No.)	-	-	-	4	6	6	8	8
Age at first test (hours)	24	24	24	-	-	-	-	-
Length of SH (days)	6, 13, 27	13, 27, 41	13, 27, 44	13, 27	13, 27, 35	13, 27, 41	13, 27, 41, 55	13, 27, 41, 55
Flexural strength test	Yes	Yes	Yes	Yes	Yes	Yes	Yes	Yes
Cube strength test	Yes	Yes	Yes	Yes	Yes	Yes	Yes	Yes
Specific fracture energy	-	-	-	-	-	-	Yes	Yes
Rockwell test	-	-	-	-	-	-	Yes	-
Material prop. SEM	-	-	-	-	-	-	Yes	Yes
Material prop. XRD	-	-	-	-	-	-	Yes	Yes
5 mm deep notch	Yes	Yes	Yes	Control only	Control only	Control only	Control only	Control only

## 5.2.2 Testing procedure

A three point bending test was used for the flexural strength test as shown in Figure 5.3. This was a closed loop hydraulic machine (Avery Denison 7152) with a maximum load of 600 kN and a digital control system (Dartec 9600) fitted with a 20 kN load cell. The smaller load cell was used to provide greater level of detail at the lower loads encountered for the unreinforced beams. The span of the beam between the support ( $L$ ) was 200 mm and a point load was applied at the centre of the beam. The load was controlled by the CMOD rate through a CMOD clip gauge. This was placed between two knife edges fixed to the underside of the sample either side of the notch.

Deflection measurements were taken at the midspan of the beam between the sample and the loading plate. It is noted that this was the deflection of the loading ram and not the true deflection of the beam. For sets 1 to 3, the first stage of testing, the samples were limited to a CMOD of 0.4 mm or until the cracks were large enough to easily insert the steel fibre spacers, before then unloading. For all remaining tests to failure, the process was continued until the load on the softening curve had reduced to 1 % of the peak or the sample fractured completely.

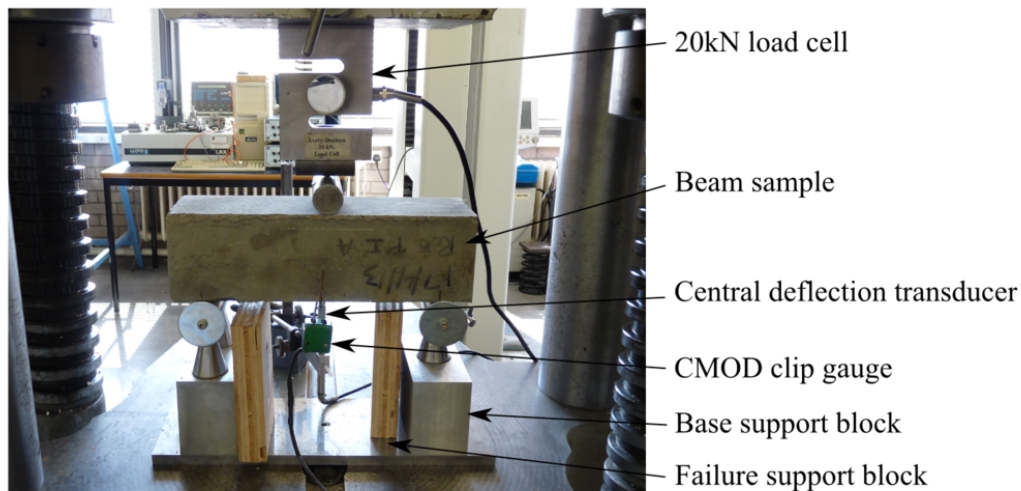


Figure 5.3: Flexural test arrangement

Set 7 and set 8 samples also underwent SEM, XRD and Rockwell Hardness testing. The deposited material on the flat surface of the narrow notch was scraped off and collected for XRD testing. The flat surface ensured that a minimum amount of the original material was collected, this isolating only the deposited material. The XRD required a minimum weight of 2 g, as such, all 4 healing duration deposits were combined together for a single test. It was considered that the healing time-scale of the samples were within the same range and thus would be of the same type. An alternative method would be to have a much larger number of samples

to obtain the required weight for a single time period. The specimens required for the Rockwell hardness test were sawn 20 mm either side of the fracture surface for loading into the Rockwell hardness test. A single sample, Set 7 beam A, was sawn further into quarters to obtain a specimen small enough for the SEM. No treatment or polishing was undertaken on the sample surface.

The SEM observations were carried out on a 1540XB Carl Zeiss apparatus. The sample was coated with a thin film of gold (80 %) and palladium (20 %) using a sputter coater. The XRD was carried out on a Phillips PW3830 X-ray generator apparatus and the set up parameters used are shown in Table B.1 in Appendix B.

A Wilson Rockwell hardness tester JR model was used for the hardness test as shown in Figure 5.4. This apparatus was operated following the procedure described in the instruction manual P/N T582-277. A Rockwell test type C with a brale penetrator was used with a minor load of 10 kg and major load of 150 kg.

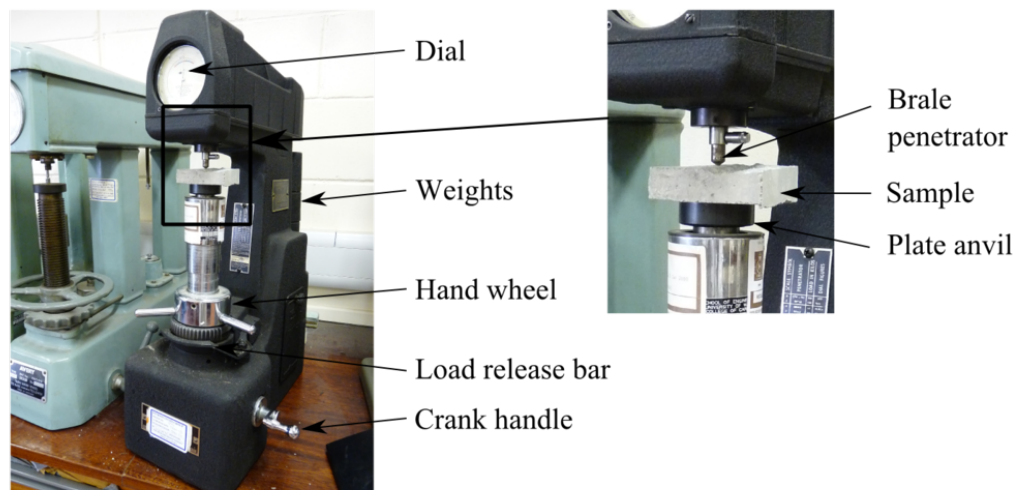


Figure 5.4: Rockwell hardness test arrangement

Figure 5.5 from Low (2001) shows the mechanics of the procedure and the required testing cycles in terms of the force against time. After the minor load was applied the displacement gauge dial was reset. The major load was applied and held until the dial stopped moving or for a recovery dwell time of 20 seconds. The difference in indenter depth measurements is taken as  $h$  shown in Figure 5.5 which is read from the dial as a Rockwell hardness number. The accuracy of the tester was checked against a calibrated test block each day. Due to the random nature of the material on the surface, the penetrator was not deliberately targeted at deposited material, rather randomly positioned in 5 places across the width of the sample in three regions. Region one being at the top of the notch and region three at the bottom of the notch, nearest to the underside of the beam as shown by Figure 5.6. It is recognised that the size of the indenter and depth of major penetration were too

large for the thin layer of deposited material. In order to achieve an accurate reading for a material layer, its thickness is required to be typically 10 times the depth of the indenter (Wilson Instruments 2004, Low 2001). For these samples the underlying material would also be measured but this approach provides an useful starting point.

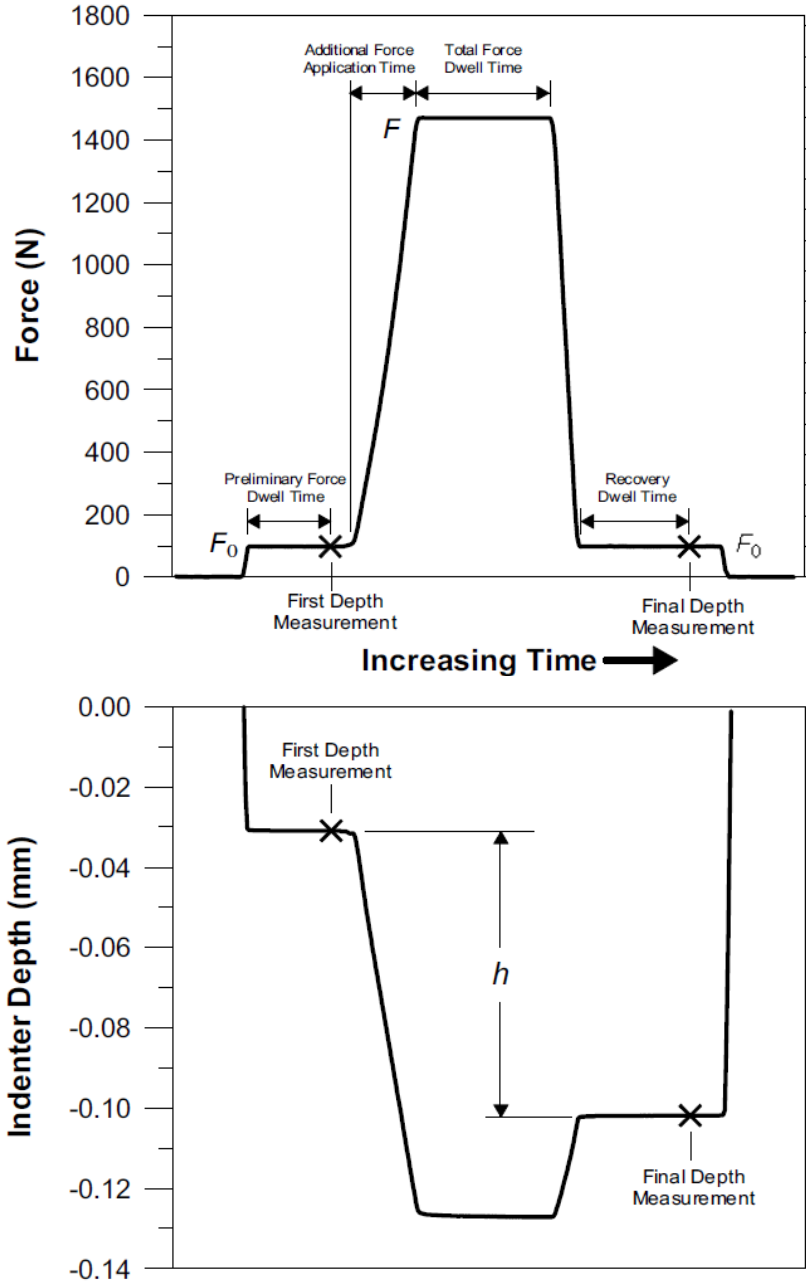


Figure 5.5: Plots of force against time and indenter-depth against time (Low 2001)

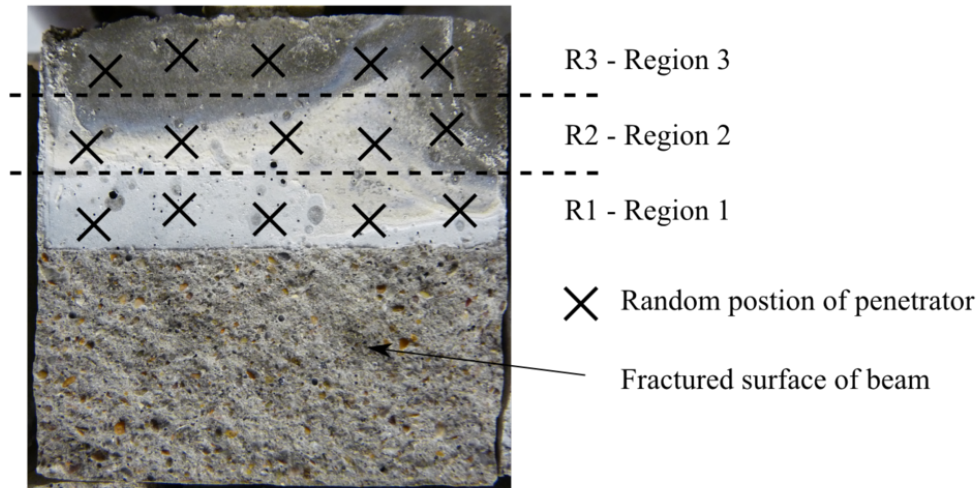


Figure 5.6: Hardness test indenter position within sample region

## 5.3 Results and discussions

The results and discussions from this experimental study have been divided in to qualitative observations and quantitative results in Sections 5.3.1 and 5.3.2 respectively. Visual evidence is examined on the external surfaces, on the cracked surface, under an SEM and development with time. The identification of this material is made through examine its structure under a microscope and using crystallography. The typical mechanical response of a sample is examined using flexural strength, peak loading, fracture energy and using a hardness test. These observations and results have been able to guide the numerical modelling in Chapter 6.

### 5.3.1 Qualitative observations

#### Visual evidence on external surface

The mechanisms for autogenous self-healing in cementitious materials are presented in Section 2.4.2 of Chapter 2. Both continued hydration and precipitation of calcium carbonate healing mechanisms are believed to occur in young cementitious samples. A white crystalline substance can be seen on the boundary of the fracture on the outer surfaces of these cementitious samples. This is evidence for the precipitation of calcium carbonate. Figures 5.7a and 5.7b show a natural cracked sample with the white crystalline substance, which was also evident on the pre-formed narrow notched samples, see Figures 5.7c and 5.7d.

In many studies, the amount of self-healing is measured by the amount of crack width reduction from the outside of the sample. This may also be directly linked to the permeability through the crack and hence the increase in durability due to self-healing. The presence of this material was a good indicator that healing had taken

place within the crack. However, it was found that measuring this crack reduction was not a reliable way of achieving repeatable experimental observations.

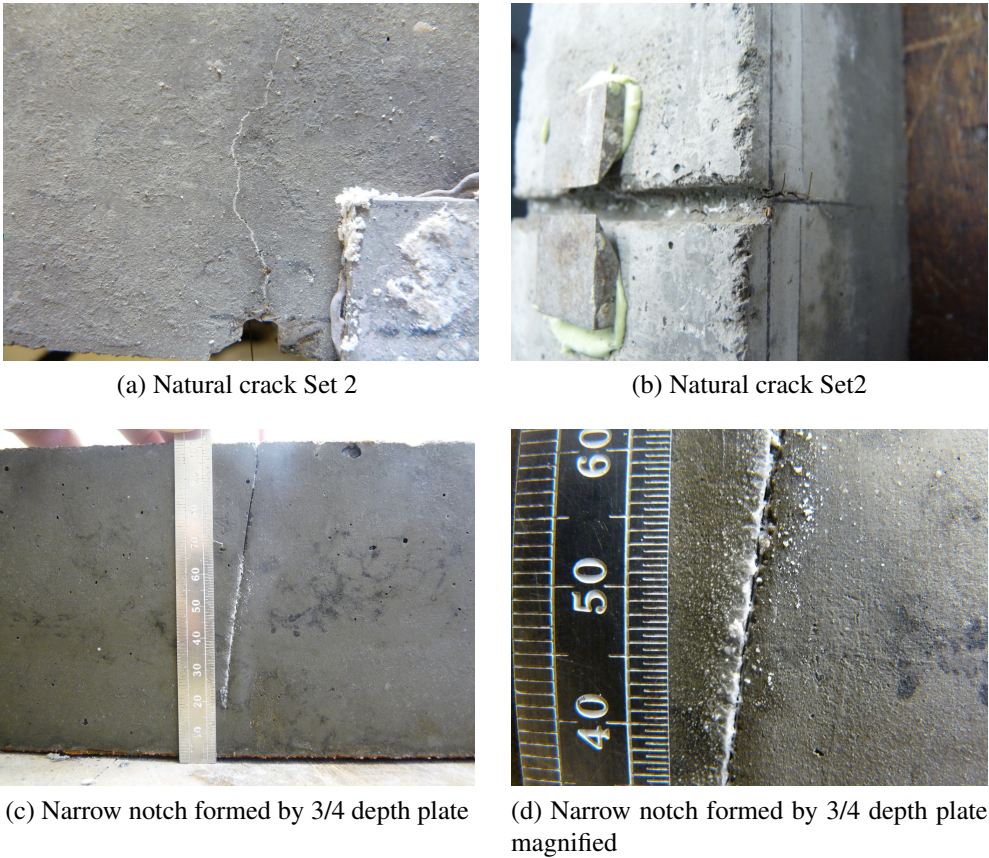


Figure 5.7: Selection of self-healing evidence on external surfaces

**Visual evidence on crack surface**

Without the latest micro-CT techniques, the only way of looking for visual evidence of autogenous healing on the cracked surface was to break open the sample and examine the material deposited. For a natural crack surface it is difficult to distinguish between the existing material and new deposited material, due to the nature of the tortuous surface.

A benefit of using a narrow notch is that any new material deposits within the crack can clearly be seen, as shown in Figure 5.8a. In many of the samples a ridge of material build up was seen near to the external surface of the sample. The proximity of this ridge to the external surface could indicate that this is the boundary between the environmental conditions within the crack and outside of the sample. This build up of material is the same colour as the bulk sample.

Another observation can be made with respect to the location of white crystalline material, believed to be calcium carbonate, on the surface of the concrete. A

distinctive pattern of this build up can often be seen, as in Figure 5.8b. The beam was placed in the curing tank in the same orientation as the figure. It is thought that this pattern is linked to the capillary rise of water within the crack. It was established that there was insufficient calcium carbonate in the water to create these deposits.

It was noticed that an increasing whitening of the surface occurred with time once the fractured surface of the narrow notch was exposed to the air. Figures 5.8c and 5.8d show the difference in sample surface after 1 hour of drying at room temperature. The complete series of time-lapse photography images are shown in Figure B.12 in Appendix B.

Visual build up of material can be linked to the increased durability of a reinforced concrete structure. The flow paths for contaminants through the material is made more difficult by having to navigate through a more tortuous route, smaller crack widths and some completely sealed areas.

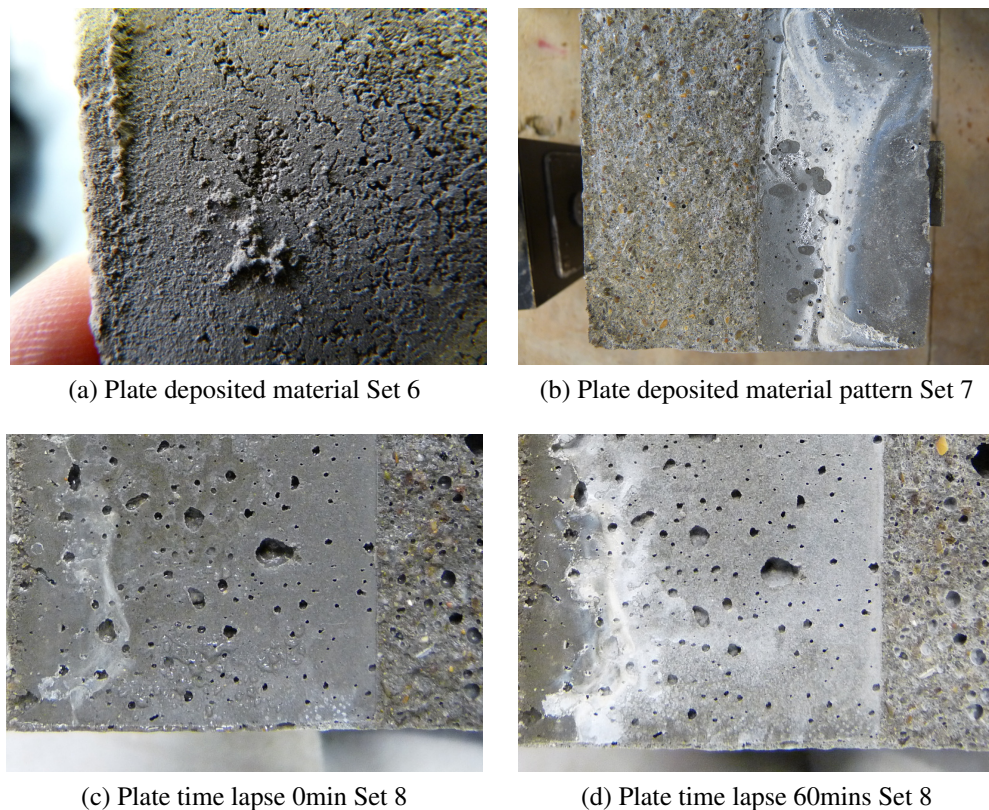


Figure 5.8: Selection of self-healing evidence on internal surfaces

### Scanning Electron Microscope (SEM)

Scanning electron microscope was used, as mentioned in Section 5.2.2, to examine the differences between a flat surface and where there was deposited material.

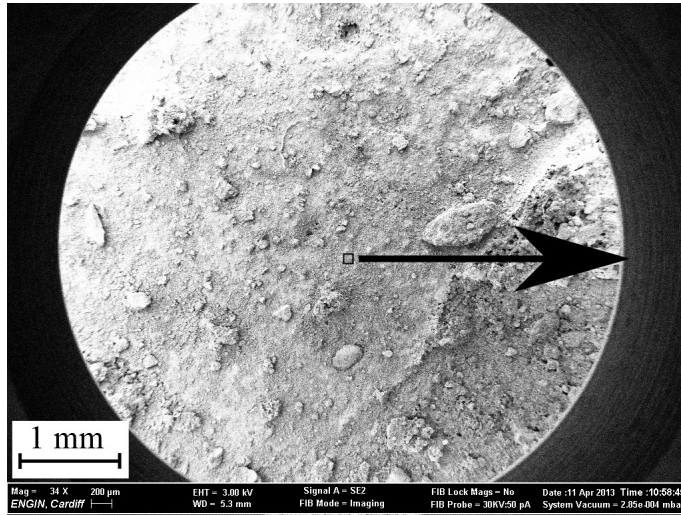
Figure 5.8a shows a typical flat surface where 2 zones of deposited self-healing material can be identified by the naked eye. Figures 5.9a and 5.9c show the sample at 34 times magnification for the flat surface and self-healed deposited material respectively. Figures 5.9b and 5.9d show the sample at 2030 times magnification. Figure B.11 in Appendix B shows a range of magnifications from 34 to 54.14 K which relate to scales between 200  $\mu\text{m}$  and 200  $\text{nm}$ . Stutzman (2000) used an SEM to identify hardened cement paste constituents. The terminology and rationale describing images used here are the same as that used by Stutzman (2000).

The flat surface has a nondescript micro-structure which results from the hardened cement paste maturing and the build up of crystals in the voids. At 2030 times magnification (or 10 $\mu\text{m}$  scale) in Figure 5.9b, the different forms of the cement structure can be seen. For this flat surface, sparsely distributed plates and blocky crystals can be seen on the surface, these are assumed to be calcium hydroxide crystals. This layer of plate-like and foil-like appearance substance can be seen, which takes the typical form of calcium silicate hydrate gel (C-S-H) Type II.

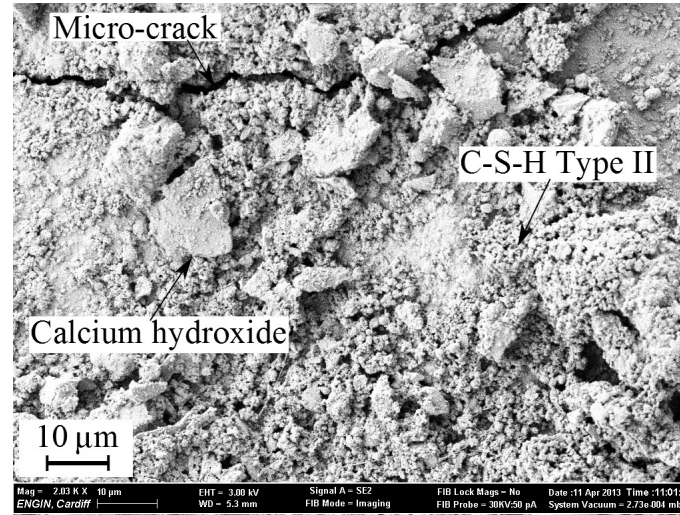
For the self-healed sample it can be seen that many layers of material have been deposited. The plates and blocky crystals, again assumed to be calcium hydroxide, can be seen throughout the sample in Figure 5.9d. There are needle crystal structures visible in the voids consistent with the description for ettringite. Shorter needles, typical of C-S-H Type I, appear in fine bundles mixed in with the plate-like and foil-like appearance typical of C-S-H Type II. It is this C-S-H Type II is dominant in the structure. The presence of these compounds shows that continued hydration is likely to be the main source of the deposited material.

The traditional carbonation attack would be identified under a microscope by the presence of calcite crystals and distinct absence of calcium hydroxide, ettringite and un-hydrated cement grains (Siddiqi 2009). The trigonal-rhombohedral, obtuse rhombohedra, and prisms of calcite crystals are not visible in the SEM images.

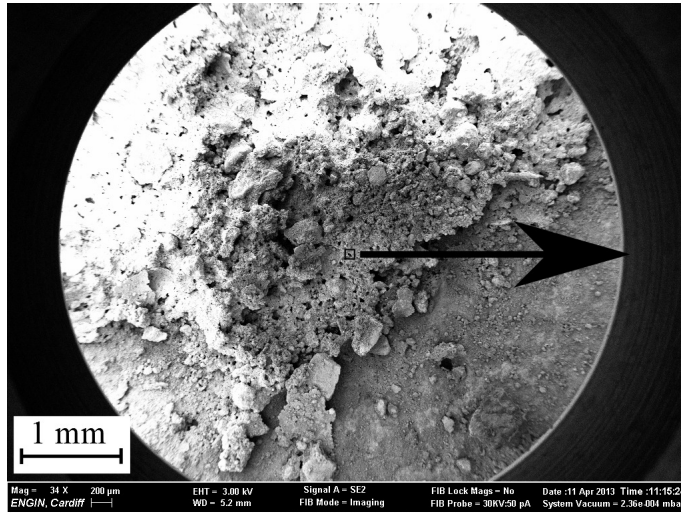
A micro-crack can clearly be seen on the flat surface in Figure 5.9b with a crack width of approximately 2  $\mu\text{m}$ . Due to the flexural strength test set-up, loading would not have been concentrated in this region. It is likely that this micro-crack is due to the shrinkage of the cementitious material in the mortar beam. At the maximum magnification, the crystalline grains can be seen to be smaller than 0.2  $\mu\text{m}$  and the growth of these within the micro-crack could lead to full healing.



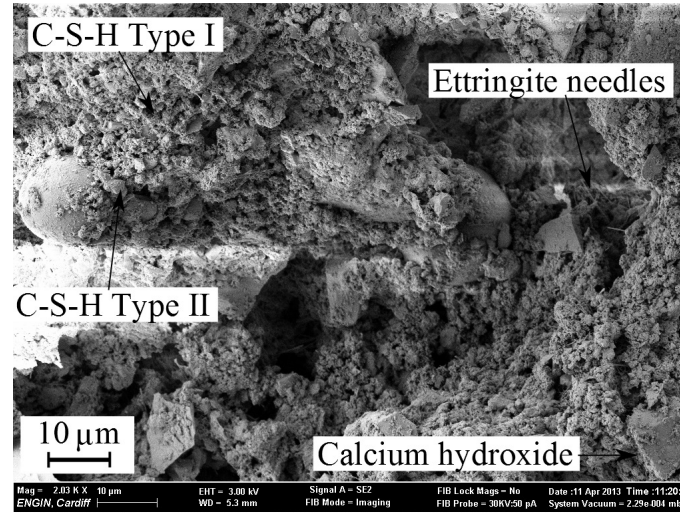
(a) Flat surface 34x mag



(b) Flat surface 2.03Kx mag



(c) SH surface 34x mag



(d) SH surface 2.03Kx mag

Figure 5.9: Selected SEM images Set 7 Beam A

**Self healing development with time**

The narrow pre-formed notch experiments, undertaken in Set 7 and 8, were tested at two week intervals. Figure 5.10 shows photographs of the 0.2 mm narrow notched surface upon complete failure of the beam at increasing length of healing duration.



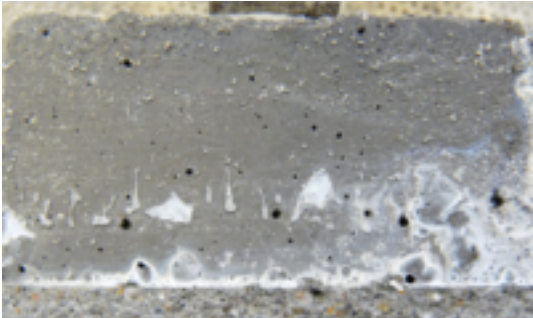
(a) 14 day sample 13 days SH 0.2 mm B



(b) 28 day sample 27 days SH 0.2 mm A



(c) 28 day sample 27 days SH 0.2 mm B



(d) 42 day sample 41 days SH 0.2 mm C



(e) 42 day sample 41 days SH 0.2 mm D



(f) 56 day sample 55 days SH 0.2 mm C



(g) 56 day sample 55 days SH 0.2 mm D

Figure 5.10: Photographs of self-healing development with time for Set 7

## Material identification

The collected deposited material on the narrow notched surface, from Set 7, was placed in an XRD scanner. Details of the apparatus were given in Section 5.2.2 and the set-up parameters are shown in Table B.1 in Appendix B. The ‘XPert Highscore’ software program from the ‘PANalytical’ suite was used to analyse the results. The accuracy of the results obtained from the XRD analysis was dependent on experienced laboratory technicians.

The purpose of the material identification process in this study was to supplement the SEM image assessment by determining the mineral composition of the deposited material. The XRD apparatus counts the reflection of X-rays that rebound from the lattice structure of the crystalline materials. The sample response is compared to the database containing characterised materials. It is noted that one of the main products of hydration, C-S-H, is amorphous. The lack of lattice planes means that it is difficult to identify C-S-H using XRD. Notwithstanding these factors the XRD can provide an insight into the composition and healing mechanism.

The computed diffractogram for the sample is shown in Figure 5.11, where the intensity (or count) is plotted against the angle of diffraction ( $2\theta^\circ$ ). Comparisons were made between the diffractogram and the cement and hydration product subset database. The three most suitable matches were Calcite ( $CaCO_3$ ), Silica ( $SiO_2$ ) and Portlandite ( $Ca(OH)_2$ ). The details of the identified patterns are shown in Table 5.3 and the plot of identified samples are shown in Figure 5.12. The small ‘y’ symbol on top of the diffractogram plots show that these peaks are not matched by the three above, however the residual intensities of these two peaks are small. The software also determines the approximate percentage volume of each material in the crystalline sample. These are also given in Table 5.3 where Calcite is shown to make up two thirds of the crystalline materials.

Table 5.3: Identified patterns list

Ref. Code	Score	Compound Name	Disp. ( $2\theta^\circ$ )	Scale Factor	Chemical Formula	Volume (%)
00-005-0586	67	Calcite	-0.195	0.769	$CaCO_3$	67
00-046-1045	42	Quartz	-0.196	0.615	$SiO_2$	31
00-004-0733	6	Portlandite	-0.051	0.014	$Ca(OH)_2$	2

Calcite is the most stable polymorph of Calcium Carbonate. Silica is either a trace picked up from quartz sand or the crystalline structure of the S component of C-S-H. Portlandite is the typical terminology for calcium hydroxide in cement notation form. The other cement notation in terms of standard chemical composition are  $C = CaO$ ,  $S = SiO_2$  and  $H = H_2O$ .

During the hydration process the two main calcium silicates, Dicalcium Silicate ( $C_2S$ ) and Tricalcium Silicate ( $C_3S$ ), are converted into C-S-H and calcium hydroxide ( $Ca(OH)_2$ ) in cement paste (Neville & Brooks 2010). This calcium hydroxide can react with carbonic acid from carbon dioxide ( $CO_2$ ) dissolved in water or moisture, to form calcium carbonate ( $CaCO_3$ ). The high volume of calcite shown in the XRD analysis suggests that the newly formed hydration products deposited in the crack, as seen in the SEM, undergo carbonation once they have been collected and waiting for the test to be undertaken. This carbonation is the same reaction that typically leads to a reduction in durability of reinforced concrete over years. However, this traditional carbonation attack penetrating the concrete material has been shown not to occur at extreme humidity values as found in fully submerged samples in water (Neville & Brooks 2010). Carbonation in its traditional sense is unlikely to be occurring. The evidence gathered from the SEM and XRD suggests that the continued hydration is the dominant process taking place in the narrow notched cracks.

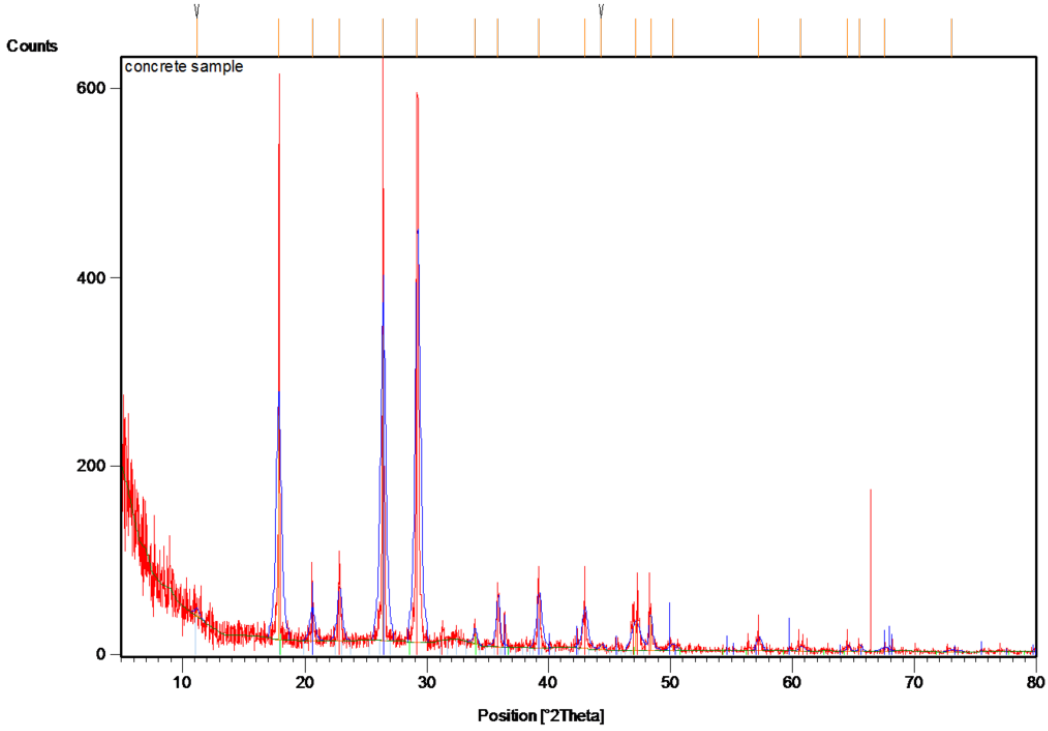


Figure 5.11: Plot of computed diffractogram Set 7

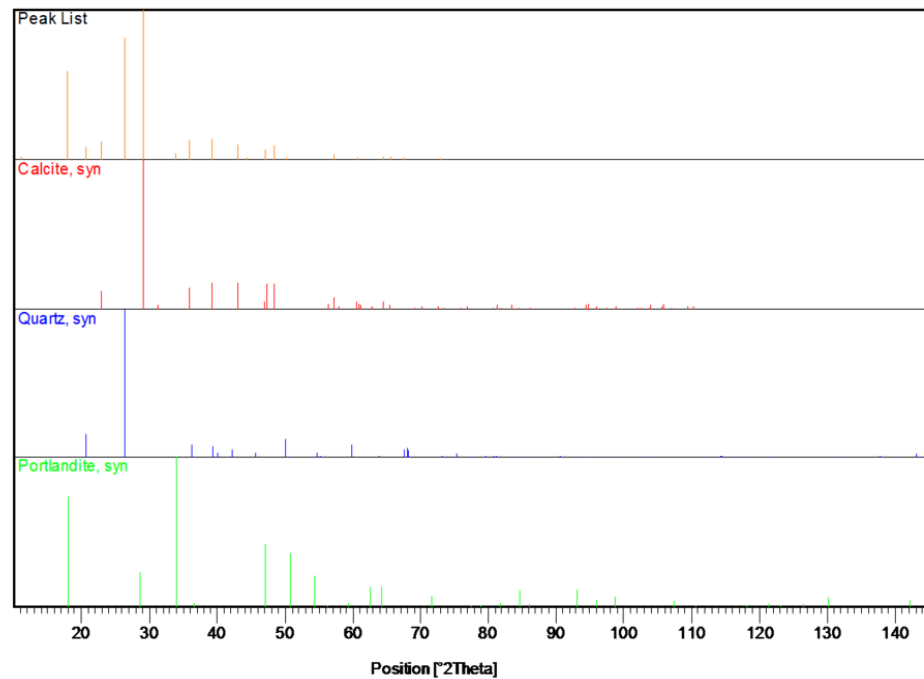


Figure 5.12: Plot of identified samples Set 7

### 5.3.2 Quantitative results

Only a selection of typical results are plotted and discussed in the following section. The source of the peak results along with a complete Load-CMOD plots, SEM and time lapse images for all Sets can be found in Appendix B.

#### Typical mechanical response

The mechanical response of the beam under a three point bending test can be shown by plotting the load-CMOD graph. The classical concrete softening curve is observed for all samples. A linear elastic response is typically shown up to 70 % of the peak load. There is then a non-linear response up-to and beyond the peak load, and this can be attributed to micro-cracking. This non-linear response continues by following the softening curve until failure.

For the natural crack case, Set 1 to 3, the typical load-CMOD response is shown in Figure 5.13. This figure shows the initial fracture stage of testing at one day, subsequent re-loading after curing for 28 days and comparison with a control sample. The gradient of the initial loading curve for the first fracture is relatively straight up to 70 % of the peak load. The CMOD was 0.01 mm at the peak load. A similar response is achieved for the control sample where the CMOD was 0.02 mm at the peak load. The control sample shown in the figure has a peak load 3.2 times greater

than the first stage of testing, which is to be expected, as the sample continued to cure and gain strength over 28 days.

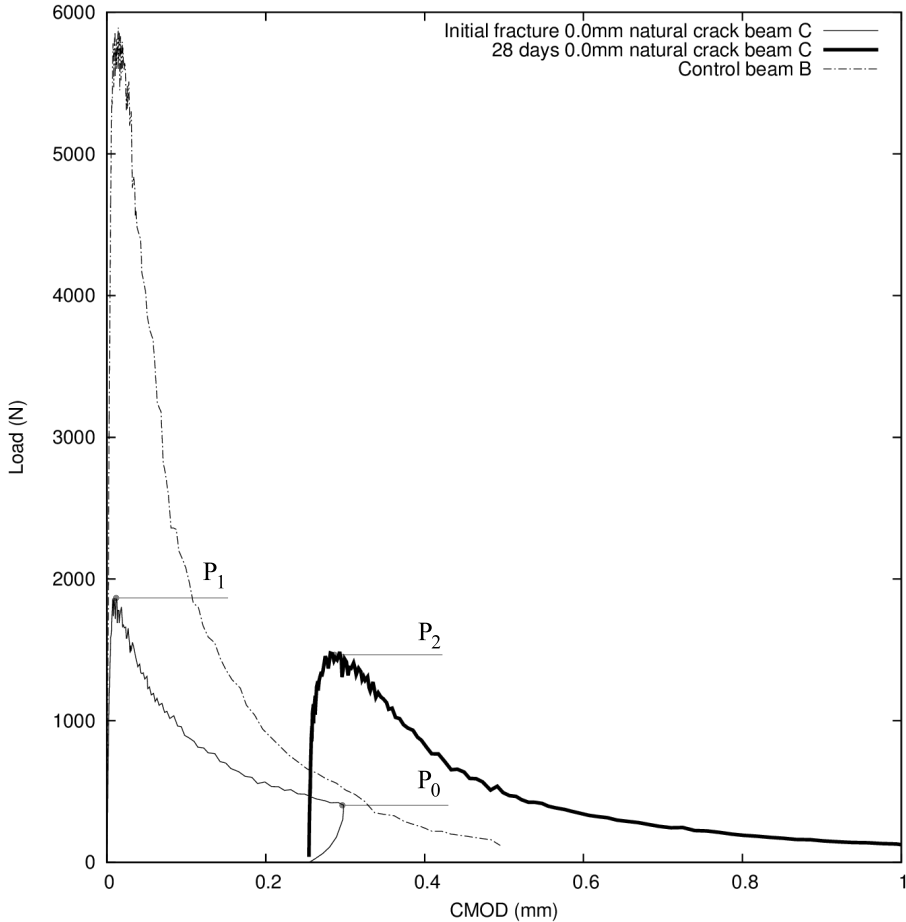


Figure 5.13: Typical response 28 days autogenous healing Set 1 Beam C

The peak load, on the first stage of testing, reached 1900 N at a CMOD width of 0.05 mm and was unloaded when the CMOD reached 0.3 mm for which the corresponding load was 400 N. The CMOD measurement on completion of unloading was 0.25 mm, where the only load on the sample was its self-weight. Resting this sample on a flat surface meant that the effect of its self-weight was removed which allowed the crack to close. The crack line was visible but was not able to be measured and for the purpose of this experiment it was classed as having a zero crack width.

The load-CMOD response for the second stage of testing is plotted on the same graph with the CMOD measurement continued from the unloading point. This is done to illustrate the response of the sample and to clearly show the strength gain.

For the second stage of testing, the positive gradient loading section of the graph has two distinct regions. This response was also exhibited by the work of Ter Heide (2005). A linear region up to 60 % of the peak load and then another region with a shallower gradient up to the peak. It is postulated that the initial linear section is due

to the original material increasing in strength due to curing and the elastic region of the healed material. The second region has a shallower gradient which is attributed to the micro-cracking in the self-healed material. The peak load of the second stage of testing results from a combination of the amount of crack healing, the strength of this newly deposited healed material and the strength of the interface between the new and old materials. This response is consistent with the experimental results of Granger et al. (2007a).

The post-peak load-CMOD curve for the second stage of testing has a shallower gradient than the first stage and control beam. The load-CMOD peak width is also significantly larger than for the first test and control. This indicates that the sample is less brittle and that some of the micro-cracks are already present in the material and are simply re-opened during loading.

For the narrow notched cases, Sets 4 to 8, the typical load-CMOD response is shown in Figure 5.14. The figure shows the results for Set 5, 36 day sample with a narrow notch 0.2 mm wide. The length of water curing or self-healing duration is 35 days. The gradient of the initial loading curve for the control sample with zero healing (plate remaining) is shallowest, then the narrow notch specimens exhibit a steeper gradient and finally the control sample has the steepest initial gradient. The gradient is reflective of the stiffness of the material and directly related to the Young's modulus. The peak load for the narrow notched sample reached 2560 N, compared to 1960 N and 7890N for the zero healing beams (plate remaining) and control samples, with CMOD measurements at the peak load of 0.02 mm, 0.02 mm and 0.04 mm respectively. The load-CMOD peak widths for the zero healing and narrow notched samples were comparable.

The measurement of strength recovery ( $c_\gamma$ ) is calculated from equation (5.1). This equation is of the same form as that presented by Homma et al. (2009) and reported in Section 2.4.3, but with load (P) replacing stress. Although the same equation is used for all samples, the position of the load values used varies dependent on the test. For the natural crack case, Set 1 to 3, as shown in Figure 5.13, the strength recovery is denoted as  $c_1$  and all three loads are taken from the same sample.  $P_0$  is at the unloading point of first stage of testing,  $P_1$  is the peak load of the first stage of testing and  $P_2$  is the peak load of the second stage of testing. For the preformed narrow notch, Sets 4 to 8 as shown in Figure 5.14, the strength recovery, denoted as  $c_2$ , uses three loads from three different samples.  $P_0$  is the peak load for the zero healing control beam,  $P_1$  is the peak load of the healed sample and  $P_2$  is the peak load of the solid control beam. The position of these loads are shown on the typical Figures 5.13 and 5.14.

$$c_\gamma = \frac{P_2 - P_0}{P_1 - P_0} * 100\% \quad (5.1)$$

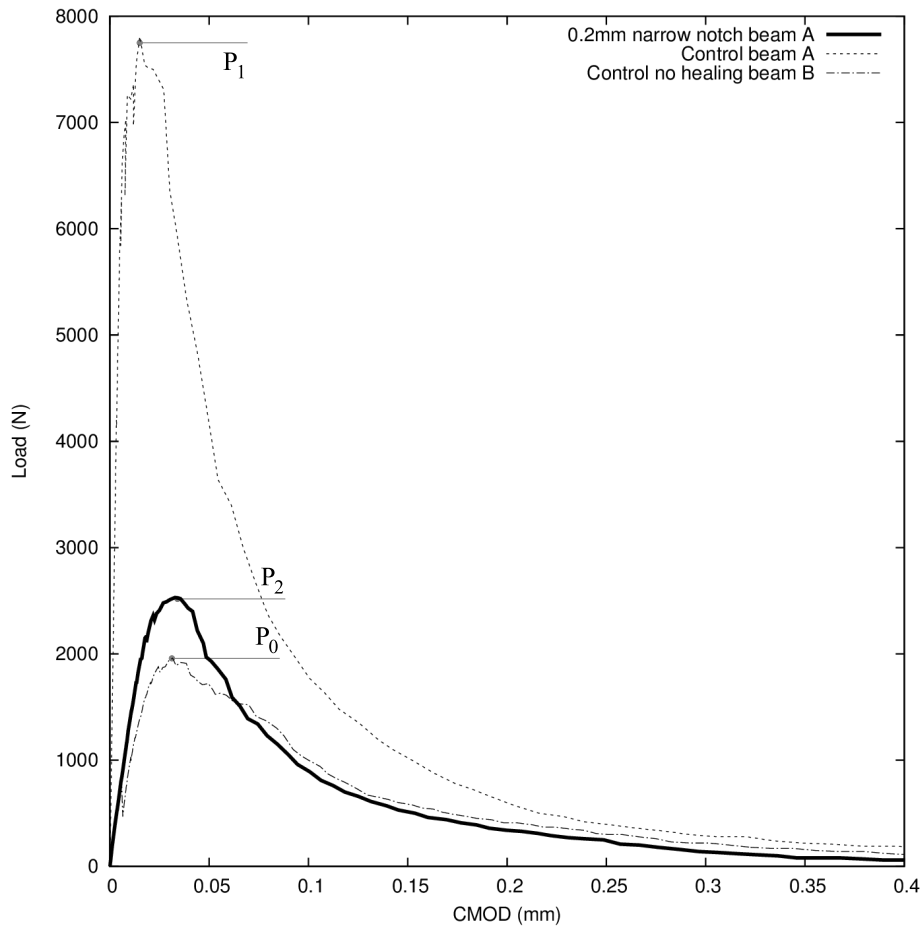


Figure 5.14: Typical response 35 days self-healing 0.2 mm half depth plate Set 5 Beam A

The natural cracked samples the strength recovery ( $c_1$ ), shown in Figure 5.13, is 72 % and the preformed narrow notch sample the strength recovery ( $c_2$ ), shown in Figure 5.14, is 7.6 %. The large difference in the reported strength recovery is due to the fact that  $c_1$  is being compared to the strength of the sample at first testing (24 hour maturity) whereas  $c_2$  makes a comparison with concrete having the same maturity as the time of healing. The benefit of the latter is that the measured strength increase is directly as a result of the new material deposited within the narrow notch. The effect of continued hydration and ageing on the uncracked ligament for the natural cracked samples is examined using the layered beam model in Chapter 6, Section 6.4.3.

### Flexural strength

The flexural strength development over time for different natural cracks is shown in Figure 5.15. The crack widths shown are 0 mm, 0.18 mm and 0.3 mm, from Sets 1, 2 and 3 respectively. This crack width is the maximum opening at the base of the beams when unloaded. The individual results and average values for each crack

width are shown for three healing time periods. The 0 mm and 0.18 mm crack width samples show an increase in strength recovery with time. It is noted that this recovery increases with the inverse of the age of the sample at first fracture. The 0 mm crack width sample shows an average strength recovery of 77 % at 28 days with the highest recovery being 93 %. The 0.3 mm crack width sample shows a variable strength recovery with minimum recovery of 11 % and maximum 25 % over 44 days.

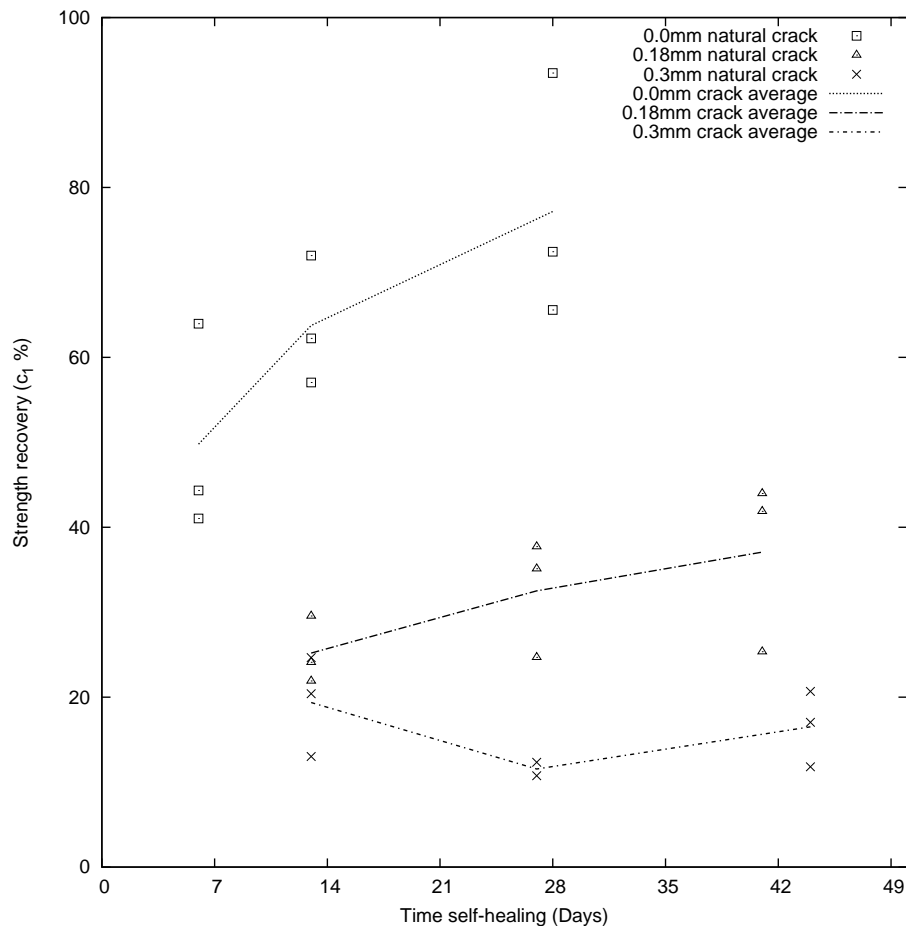


Figure 5.15: SH strength recovery of samples with different natural cracks

The flexural strength development over time and for different narrow notch widths are shown in Figure 5.16 from Sets 4, 5 and 6 for concrete and Figure 5.17 from Sets 7 and 8 for mortar. The individual results and average values for each narrow notch are shown for different healing time periods.

In Figure 5.16 the increase in strength measurement ( $c_2$ ) on the whole remains between 0 and 10 %. There are a few anomalous results, in particularly linked to the 0.3 mm thickness plate. There is one result with an abnormally high  $c_2$  ratio at 13 days self-healing for the 0.3 mm thick plate. The negative strength recovery results, show that sample which retained the plate had a higher peak load than when the plate was removed. This can be partially explained by the amount of healing

in the 0.3 mm narrow notch, linked to the strength increase being small compared to the bond strength between the plates and the concrete. This interface effect was eliminated from set 7 and set 8 results by using a plastic wrap separating the metal plate and mortar. However, considering the general trends of the 0.1 mm and 0.2 mm narrow notched samples, the strength increase measurement  $c_2$  appears to decrease gradually but remain above zero. There are only two results for the 0.1 mm thickness plate due to difficulties encountered in removing the plate in concrete due to excessive deformation of the concrete increasing the crack width.

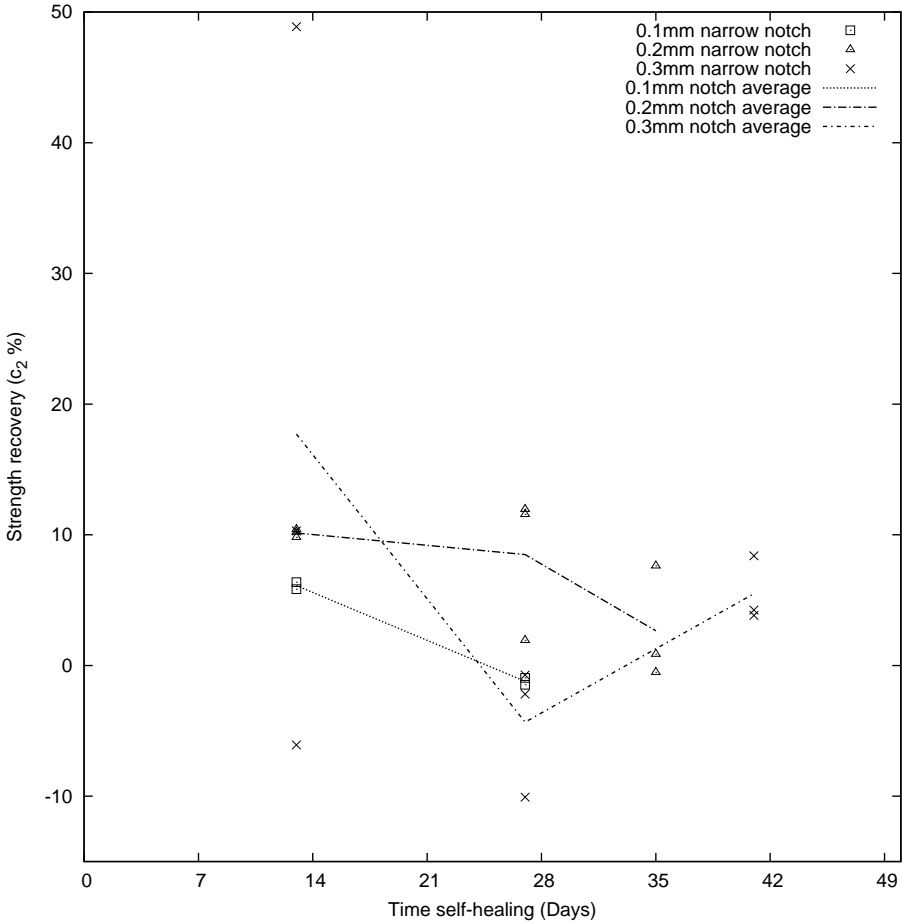


Figure 5.16: SH strength recovery of samples with different narrow notches Sets 4, 5 and 6

In Figure 5.17, for set 7 and set 8 using mortar beams, the increase in strength measurement ( $c_2$ ) can be seen with time of self-healing for 0.2 mm and 0.3 mm narrow notches. Both narrow notches showed a general increase in strength with time, apart from the 55 days healing samples. The 0.3 mm samples did not show positive strength recovery with only the 41 day self-healing time samples showing an increase in strength recovery. The average strength recovery in the 0.2 mm samples was 2 % higher than that measured for the 0.3 mm samples. This supports the findings of other autogenous healing experiments investigating permeability that

0.3 mm crack does not heal as discussed in Section 2.4.3. The 55 day self-healing results for both 0.2 mm and 0.3 mm narrow notches appear to be significant lower than the other results. The mortar was cast in two batches, with the 55 day samples coming from the same mortar batch as the 27 day healing. It can be seen that the highest results from the 55 days sample is directly comparable to the lowest results from the 27 days samples. Due to the relatively small differences in strength measurement and the limited number of samples is it believed the results obtained are within the variability expected from such a heterogeneous sample of mortar. Due to the sensitive nature of the response a number of other factors could have made a difference to the results, such as placement position in the curing tank, humidity of sample upon testing and variability in key sample dimensions measurements.

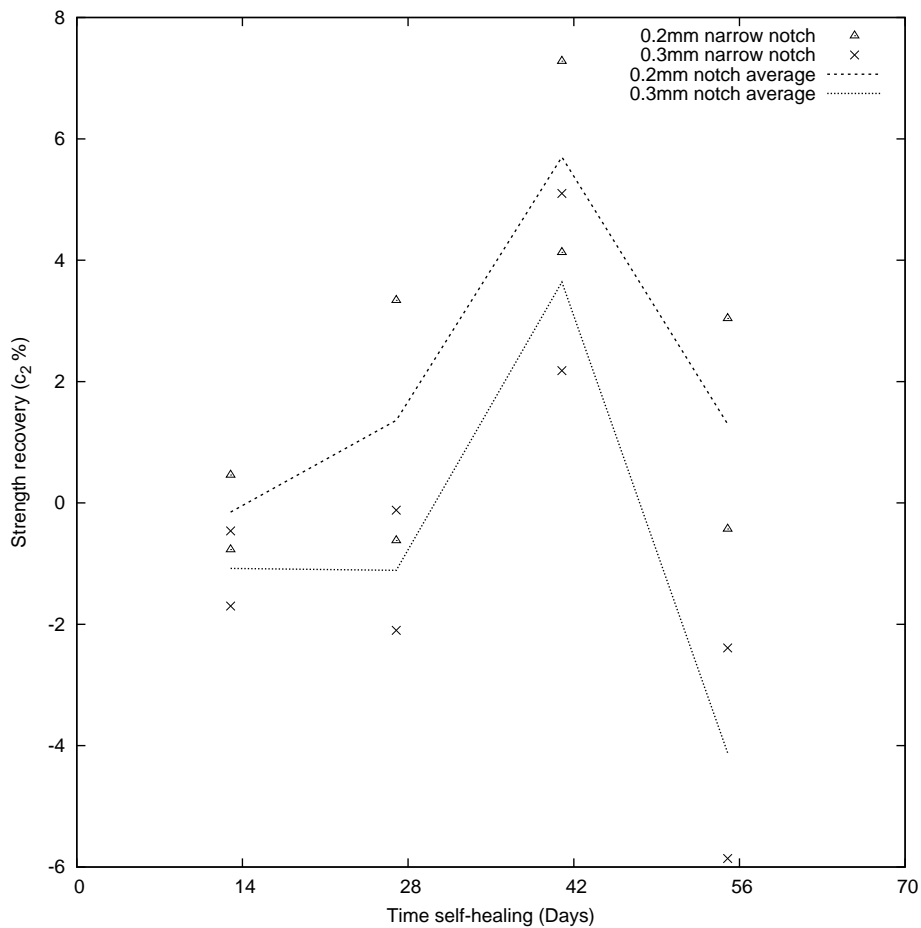


Figure 5.17: Self-healing strength recovery of samples with different narrow notches with time set 7 and set 8

These results show that although there is a strength recovery present, in both natural crack and narrow notches, due to autogenous healing this small amount of strength recovery means that full recovery of mechanical strength is limited. It can be seen that if the self-healing is used to target durability, then the reinforcement in the tension section of beam can be protected if the cracks are small enough to allow

autogenous healing to take place and prevent the ingress of water.

**Peak loads and fracture energy**

The peak load and fracture energy changes with time are now explored in set 7 and set 8. Figure 5.18 compares the peak loading for both 0.2 mm and 0.3 mm narrow notch samples with time. Figure 5.18a shows all the results including control samples, whereas Figure 5.18b show the magnified response of the self-healing and zero-healing samples. Again the 0.2 mm narrow notch samples show on average a higher response than the 0.3 mm, leading to the conclusion that the narrower the crack width the better the self-healing. The 41 day peak loads are lower than the 27 day peak loads. The 13 and 41 day samples are from the same mortar batch and the 27 and 55 day samples from the same mortar batch. Within the same batch the peak loads are higher the longer the time of self-healing. Even though the batches contain the same ratios by weight, the results remain within typical variability expected from mortar or concrete.

The fracture energy results calculated from the CMOD are shown in 5.19. These results almost directly reflect the peak loads results.

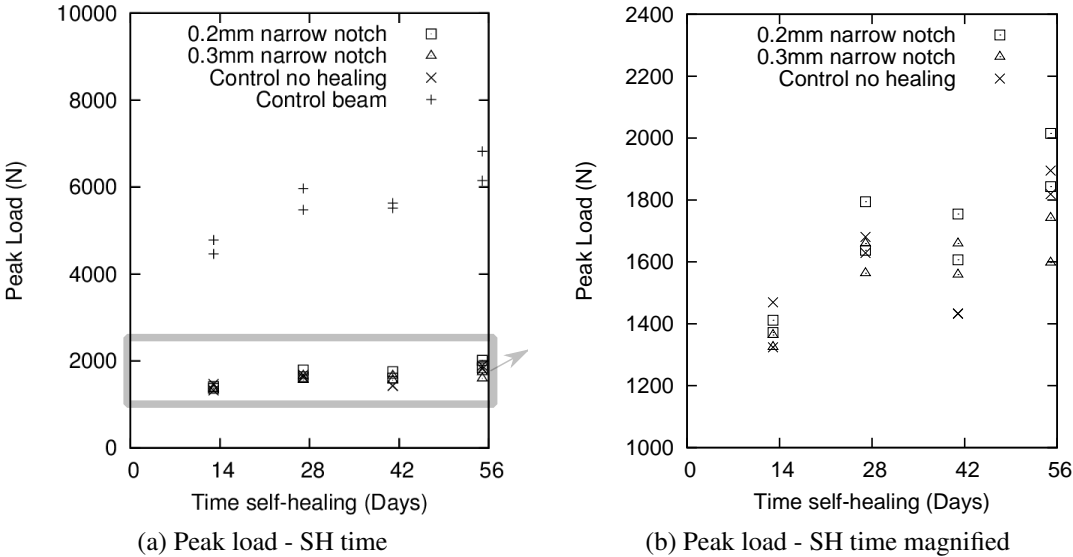


Figure 5.18: Peak load against Self-healing time for Set 7 and 8

**Rockwell hardness test**

The Rockwell hardness test was carried out on the 0.2 mm narrow notched samples from Set 7. Figure 5.20 shows the Rockwell hardness number plotted against time of self-healing. The results from the tests on the three regions 1-3 (defined in Figure 5.6 ) are plotted in groups above the time axes, for example, regions 1, 2

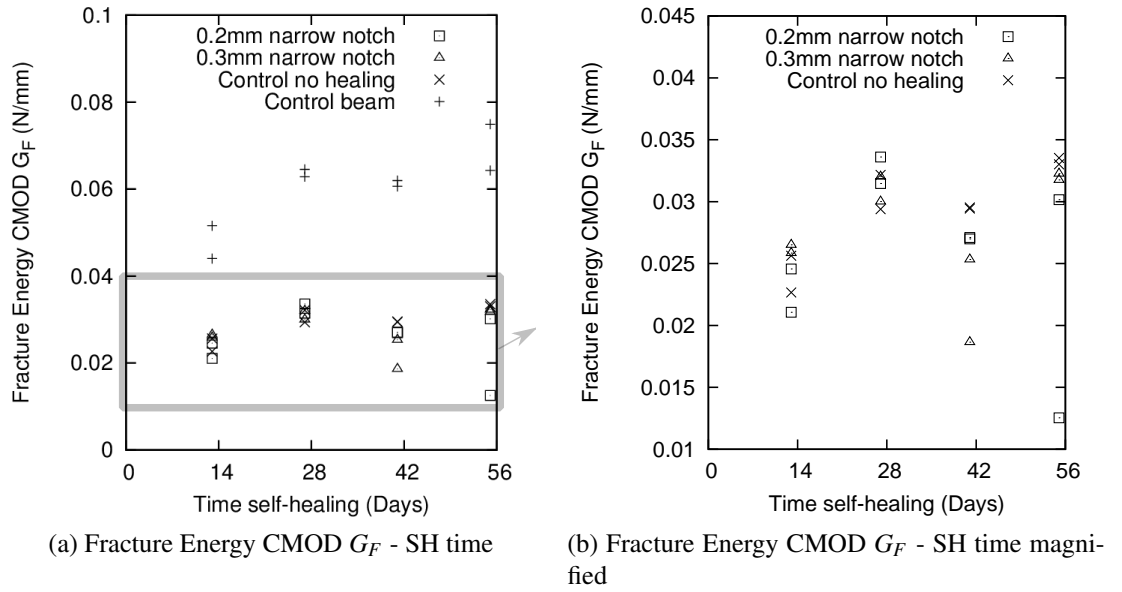


Figure 5.19: Fracture Energy CMOD against Self-healing time for Set 7 and 8

and 3 results were carried out on 13 day self-healing samples on the same day. The individual results showing the spread and average for each region are plotted on the figure. Table 5.4 shows the mean, standard deviation and coefficient of variance for each region and sample as a whole and how they vary with time and compressive strength. There is wide range of results from these Rockwell hardness tests, with the values ranging between 20 and 65. The widest range was shown by the samples after 41 days of self-healing and could be linked to the higher number of tests carried out.

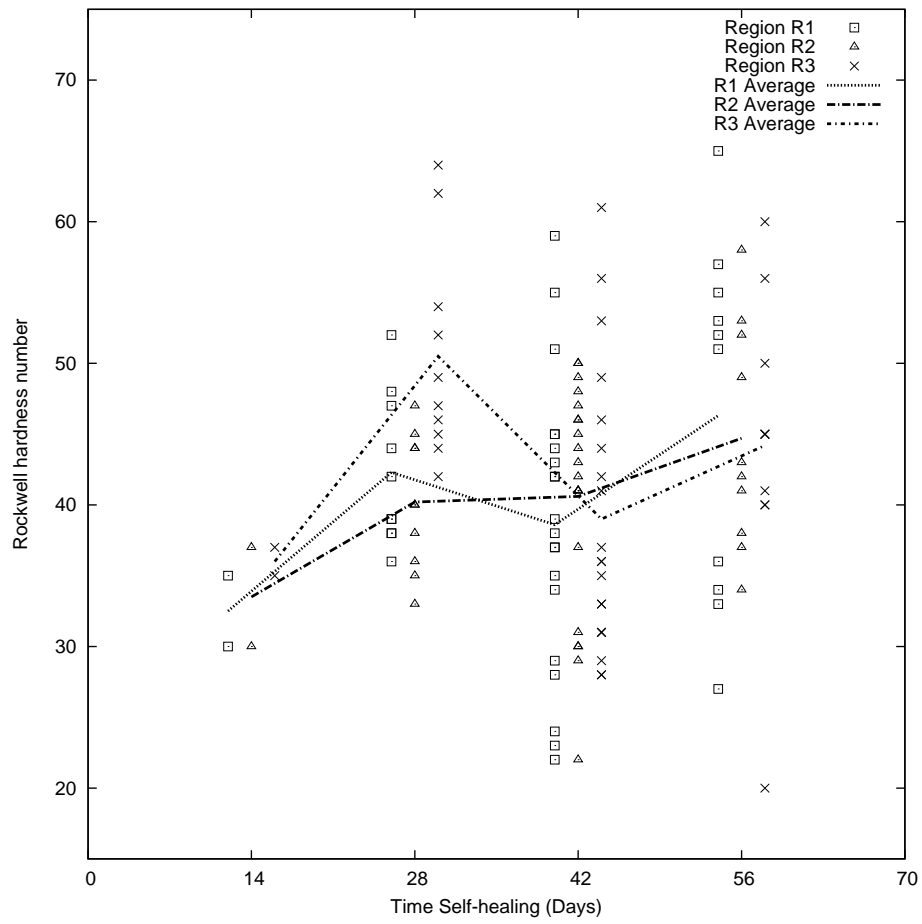


Figure 5.20: Rockwell Hardness test individual and average results Set 7

Table 5.4: Summary of Rockwell hardness number experimental results

Self-healing time (days)	Compressive strength ( $N/mm^2$ )	Strength Recovery (%)	Rockwell number											
			Region R1			Region R1			Region R1			All		
			Mean	SD	CV (%)	Mean	SD	CV (%)	Mean	SD	CV (%)	Mean	SD	CV (%)
13	35.0	-0.15	32.5	3.5	10.9	33.5	4.9	14.8	36.0	1.4	3.9	34.0	3.2	9.5
27	49.4	1.36	42.3	5.3	12.5	40.2	4.7	11.7	50.5	7.5	14.9	44.3	7.3	16.5
42	45.6	5.70	38.6	10.2	26.4	40.6	8.1	20.0	39.0	9.7	25.0	39.4	9.3	23.5
55	57.7	1.30	46.3	12.7	27.4	44.7	7.9	17.6	44.2	10.8	24.5	45.1	10.3	22.9

The general trend in the results show that the Rockwell hardness number increases gradually with time. The Rockwell hardness number for metals, and in particular steel, is typically correlated against tensile strength. Figure 5.21 plots the compressive strength of the mortar cubes against the average Rockwell hardness number with the associated standard deviation error (SD). There is a clear trend shown in that as the compressive strength of the sample increases so does the Rockwell hardness number. The standard deviation and coefficient of variance (CoV) increases with increasing compressive strength. There is also an increase in variability with increasing compressive strength. This is in contrast to the experiments of Windslow (1981) where the CV reduced from 20 % to 5 % as the concrete matured. One explanation for this observation is that the number of tests on young specimens (14 and 28 days) are too few to provide a reliable measure of their variability. Overall, it is noted that there were too few tests carried out to make detailed statistical interpretations.

There is no particular trend when considering the percentage strength recovery. This would suggest that the increase in Rockwell number is linked to the underlying material rather than the deposited healed material. Rockwell hardness tests carried out on the mortar alone (side of the sample) showed that there was little difference between the mortar and healed material. The variability of, even mortar, for such a hardness test at the micro-scale depends on the exact positioning of the penetrator. The presence of aggregate particles, air pockets and weaker material can alter the results significantly (Windslow 1981).

Even with further numerous repeated experiments it is difficult to envisage that the properties of self-healing cementitious materials can be reliably determined from the hardness tests. These preliminary results show that this technique cannot be relied upon alone to determine mechanical properties. Factors such as moisture content of test samples, surface roughness, effects of fine and coarse, aggregate type, zone of influence below indenter and statistical considerations all have an influence on the results.

The disadvantage of this technique is that to be able to perform a subjective, even comparative study, the surface of the samples need to be relatively flat, ideally polished. The flat surface provided by casting a plate into the samples and then removing it, did provide a good reference starting point. However, the build up of deposited or formed material was of neither sufficient thickness nor with a smooth surface. If the samples were to be polished to obtain a smooth flat surface this process would result in removing the material that is wanted for measurement. No attempt is made in this study to define the zone of influence under the tested region.

The latest techniques of measuring a dynamic hardness test could provide more useful results. This would involve recording the load and penetration depth accu-

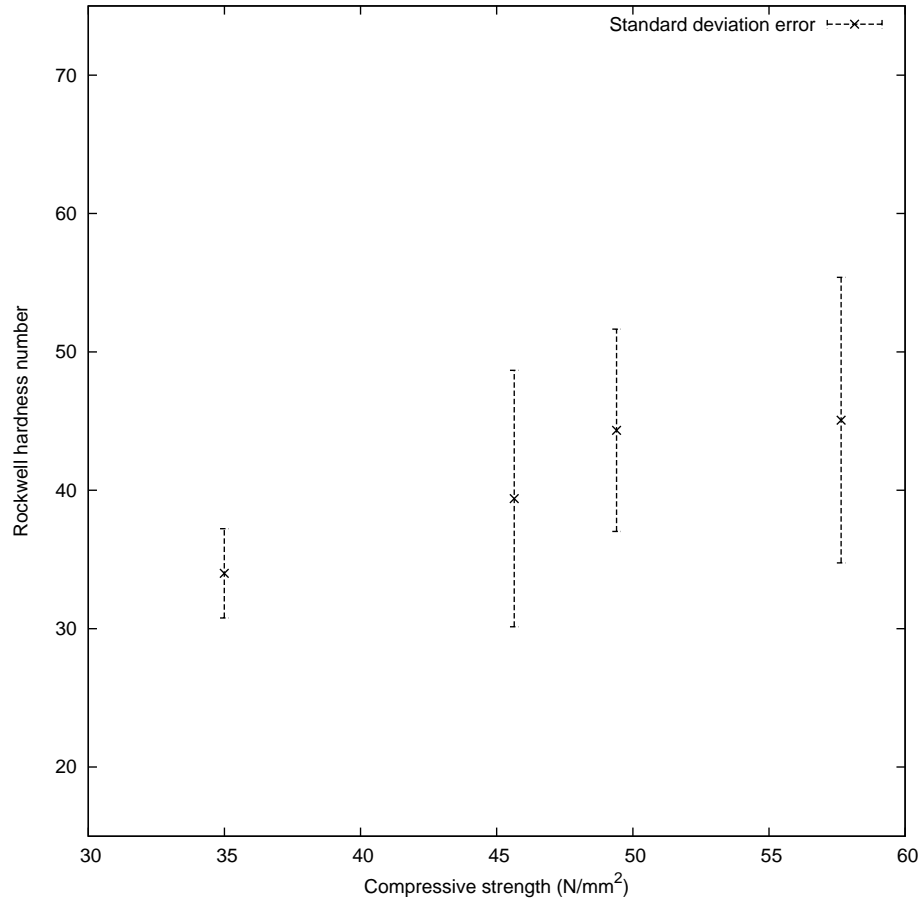


Figure 5.21: Rockwell Hardness test plotted against compressive strength Set 7

rately as the sample is loaded, obtaining a load against displacement curve. The effect of the underlying material could be examined using this technique. However, the apparatus required to carry out such dynamic tests are relatively new on the market and were not available in the University at the time of this study.

## Conclusions

These series of experiments carried out on concrete and mortar samples showed that autogenous healing does readily occur under laboratory conditions. The evidence gathered through qualitative observations and quantitative mechanical strength results provide an insight into the development of autogenous healing material with cracks of different widths over time. The natural crack, closed after loading, showed the greatest degree of autogenous self-healing and mechanical strength recovery. The smaller the crack width the greater the strength recovery and it was found that increasing healing time led to increased recovery levels.

It should be noted that autogenous healing, evident in these experimental results, occurred for newly cast concrete or mortar where the healing process began within

24 hours in the presence of water. There was evidence of precipitation of calcium carbonate on the boundary of the fracture on the outer surfaces. However, inside the crack the dominant process was found to be continued hydration. Upon fracture and exposure to the air the calcium hydroxide from the continued hydration turned into calcium carbonate. The hardness tests performed at the micro-scale did not provide valuable information for quantifying autogenous healing in cementitious materials owing to the inherently high variation and idealisation of the sample to obtain a flat reference surface and small thickness of material build up.

The recovery percentage shown by the natural cracks, in particular the closed crack, provide confidence that the increase in strength could be significant and legitimately form part of a system for managing the strength and durability of structures post-damage. The mechanical response of a concrete beam with a natural crack healed in water over 28 days (Set 1) is taken forward to the next Chapter 6, where the self-healing cementitious materials will be modelled using micromechanics.

# Chapter 6

## Self-healing Micromechanical Model

A novel self-healing micromechanical model for cementitious materials is presented in this chapter building upon the micromechanical work described in Chapter 3. A state-of-the-art review of a wide range of materials including autogenous cementitious healing is given in Chapter 2, Section 2.4.4. This included a review of a range of numerical models for cementitious materials as well as a number of models that simulate self-healing processes. One group of models use a staged approach to the simulation of self-healing, and it is these which are particularly relevant to the present work. Chapter 4 showed how this approach, considering solidification and continued hydration, can be applied to a micromechanical model. The development of a self-healing micromechanical model in this chapter will focus only on mechanical strength regain.

Early phenomenological based models have given way to more mechanistic models. The mechanistic nature and scale of applicability of micromechanical models means that they are ideally suited to considering material constituent properties and their interaction. The micromechanical model presented in Chapter 3 is considered to be a suitable point for developing a self-healing model. This 3D two-phase elastic model with micro-cracking has the ability to describe a range of applied stresses and strains whilst remaining simple enough to visualise the various mechanisms.

This chapter firstly describes the rationale behind the two-phase composite model, its individual components and healing mechanisms, before combining each component to form a new constitutive model. The introduction of a solidification strain together with its derivation is also presented along with allowance for continued damage of the healed material. Secondly, the numerical implementation of the model is presented and then the performance of the model is illustrated with a series of theoretical examples. Finally, comparisons are made with experimental results from Chapter 5 and examples from literature.

## 6.1 Micro-crack healing in a two-phase composite

### 6.1.1 Rationale of the model

The basic two-phase composite with elastic properties to account for healing is based on the classical Eshelby (1957) solution and the Mori & Tanaka (1973) homogenisation approach. The anisotropic micro-cracking is taken into account by summing the additional strain developed from the Budiansky & O'Connell (1976) circular micro-cracks. Combining these approaches leads to the following form of constitutive equation (6.1), similar to that shown in equation (3.47).

$$\bar{\sigma} = \mathbf{D}_{M\Omega} : (\bar{\epsilon} - \epsilon_a) \quad (6.1)$$

$\epsilon_a$  is the total added strain and  $\mathbf{D}_{M\Omega}$  is the composite elasticity tensor, equation (3.9), derived in Section 3.1.1.

Autogenous healing in a cementitious materials does not occur instantaneously, in contrast to autonomic healing with some adhesives, which can produce effectively instantaneous healing (Joseph 2008). The continued hydration or precipitation of calcium carbonate takes place over a period of days or weeks. However, as far as the mechanical strength recovery is concerned, for simplicity and comparison with experiments, the healing is considered to take place instantaneously.

Healing for this micromechanical model is taken to mean an increase in mechanical strength. This is represented as the healed material being able to carry an additional stress over and above the original micro-cracked material. The micromechanical model uses the (micro) crack-plane relationship given in equation (6.2). Healing is added to this as shown in equation (6.3).

$$s_L = (1 - \omega) \mathbf{D}_L : \epsilon_L \quad (6.2)$$

$$s_{Lh} = (1 - \omega) \mathbf{D}_L \epsilon_{Lh} + h \omega_{th} \mathbf{D}_{Lh} (\epsilon_{Lh} - \epsilon_s) \quad (6.3)$$

The healed material present in the micro-cracks on this local plane will be able to carry stress. It is proposed that the equivalent local stress in each direction now comprises two components; original intact material and the healed micro-cracks that have regained strength.  $s_L$  is the equivalent local stress and  $\epsilon_L$  is the equivalent local strain. Subscript  $h$  refers to the stress or strain after healing has occurred.  $\mathbf{D}_L$  and  $\mathbf{D}_{Lh}$  are the local stiffness of the original and healed material respectively.

The healing proportion is defined by the parameter  $h$ .  $h = 0$  means that there is no healing and  $h = 1$  means that the material would be fully recovered, assuming that the healed material is the same strength as the original.  $h$  can be interpreted as

the healed volume of micro-cracks and micro-voids per unit volume of micro-cracks and micro-voids. Greater than 100 % healing can be achieved if the combination of healing ratio and material strength is greater than the original material strength.  $\omega_{th}$  is the micro-cracking parameter at the time of healing and  $\epsilon_s$  is the solidification strain.  $\epsilon_s$  ensures that the healing material solidifies in a stress free state, that is, upon healing the new material does not instantaneously change the stress state of the overall material.

Strength recovery will be used to measure and quantify the amount of self-healing that occurs using equation (2.4). The stresses used in this equation are shown in from Figure 2.5.

### 6.1.2 Constitutive model

The constitutive equation requires the local equivalent stress in terms of total added strain. To obtain this total added strain, equation (6.3) is rearranged to obtain the local equivalent stress ( $\epsilon_{Lh}$ ) shown in equation (6.4).

$$\epsilon_{Lh} = [(1 - \omega) + h\omega_{th}B]^{-1} \mathbf{C}_L (s_{Lh} + h\omega_{th}B\mathbf{D}_L\epsilon_s) \quad (6.4)$$

where,

$$\mathbf{D}_{Lh} = B \cdot \mathbf{D}_L \quad (6.5)$$

$B$  is therefore the ratio between the healed and original isotropic stiffness tensor.  $\mathbf{D}_L = \mathbf{C}_L^{-1}$ , where  $\mathbf{C}_L$  is the local elastic compliance shown previously in equation (3.55).

The equivalent local strain is the sum of the added local strain ( $\epsilon_{\alpha h}$ ) and the elastic strain ( $\epsilon_{Le}$ ). This relationship is the same as derived in the micro-crack criterion and evolution, Section 3.3 shown in equation (3.73). Rearranging this equation yields the added local strain with healing as shown in equation (6.6).

$$\epsilon_{\alpha h} = \epsilon_{Lh} - \epsilon_{Le} \quad (6.6)$$

Substituting equation (6.4) and  $\epsilon_{Le}$  into equation (6.6) yields equation (6.7).

$$\epsilon_{\alpha h} = [(1 - \omega) + h\omega_{th}B]^{-1} \mathbf{C}_L (s_{Lh} + h\omega_{th}B\mathbf{D}_L\epsilon_s) - \mathbf{C}_L : s_{Lh} \quad (6.7)$$

Simplifying and grouping terms leads to the added local strain with healing as shown by equation 6.8.

$$\epsilon_{\alpha h} = \left( \frac{\omega - h\omega_{th}B}{1 - \omega + h\omega_{th}B} \right) \mathbf{C}_L s_{Lh} + \left( \frac{h\omega_{th}B}{1 - \omega + h\omega_{th}B} \right) \epsilon_s \quad (6.8)$$

The total added strains for a discrete number of cracks and a continuously distributed series of cracks were given in equations (3.50) and (3.51) respectively in Section 3.2.2. The Budiansky & O'Connell (1976) crack density parameter was equated to the conventional directional damage parameter ( $\omega$ ). The added strains for a standard micro-cracking case, without healing, is given in equation (3.53) in Section 3.2.2. For the healed case, the equivalent relationship when substituting equation (6.8) into equation (3.53) is as follows,

$$\boldsymbol{\varepsilon}_{\alpha h} = \mathbb{F}\mathbf{C}_{\alpha} : s_{Lh} = \left( \frac{\omega - h\omega_{th}B}{1 - \omega + h\omega_{th}B} \right) \mathbf{C}_L s_{Lh} + \left( \frac{h\omega_{th}B}{1 - \omega + h\omega_{th}B} \right) \boldsymbol{\varepsilon}_s \quad (6.9)$$

Where  $\mathbf{C}_L$  remains the same as in equation (3.55).

The added local strain with healing, shown in equation (6.9), has two parts; the stress carried by the material and the compensating solidification strain. This summation can also be applied to the total added strain with healing, as shown in equation (6.10).

$$\boldsymbol{\varepsilon}_{ah} = \boldsymbol{\varepsilon}_{ac} + \boldsymbol{\varepsilon}_{as} \quad (6.10)$$

where the total added strain in the new material ( $\boldsymbol{\varepsilon}_{ac}$ ) is

$$\boldsymbol{\varepsilon}_{ac} = \left[ \frac{1}{2\pi} \int_{2\pi} \int_{\frac{\pi}{2}} \mathbf{N}_{\boldsymbol{\varepsilon}} : \mathbf{C}_L : \mathbf{N} \left( \frac{\omega - h\omega_{th}B}{1 - \omega + h\omega_{th}B} \right) \sin(\psi) d\psi d\theta \right] : \bar{\boldsymbol{\sigma}} \quad (6.11)$$

which can be simplified to

$$\boldsymbol{\varepsilon}_{ac} = \mathbf{C}_{addh} : \bar{\boldsymbol{\sigma}} \quad (6.12)$$

where

$$\mathbf{C}_{addh} = \frac{1}{2\pi} \int_{2\pi} \int_{\frac{\pi}{2}} \mathbf{N}_{\boldsymbol{\varepsilon}} : \mathbf{C}_L : \mathbf{N} \left( \frac{\omega - h\omega_{th}B}{1 - \omega + h\omega_{th}B} \right) \sin(\psi) d\psi d\theta \quad (6.13)$$

The total added strain contribution from solidification strain component ( $\boldsymbol{\varepsilon}_{as}$ ) is

$$\boldsymbol{\varepsilon}_{as} = \left[ \frac{1}{2\pi} \int_{2\pi} \int_{\frac{\pi}{2}} \mathbf{N}_{\boldsymbol{\varepsilon}} : \left( \frac{h\omega_{th}B}{1 - \omega + h\omega_{th}B} \right) \sin(\psi) d\psi d\theta \right] \boldsymbol{\varepsilon}_s \quad (6.14)$$

Noting that  $\mathbf{N}$ ,  $\mathbf{N}_{\boldsymbol{\varepsilon}}$  and  $\omega$  are functions of the spherical coordinate angles ( $\theta, \psi$ ).

Substituting the total added strain component contributions from equation (6.12) and (6.14) into the constitutive equation (6.1) leads to equation (6.15), which can be rearranged into the standard constitutive relationship as shown by (6.16).

$$\bar{\boldsymbol{\sigma}} = \mathbf{D}_{M\Omega} : (\bar{\boldsymbol{\varepsilon}} - \mathbf{C}_{addh} : \bar{\boldsymbol{\sigma}} - \boldsymbol{\varepsilon}_{as}) \quad (6.15)$$

$$\bar{\boldsymbol{\sigma}} = (\mathbf{I}^{4s} + \mathbf{D}_{M\Omega} \mathbf{C}_{addh})^{-1} \mathbf{D}_{M\Omega} : (\bar{\boldsymbol{\varepsilon}} - \boldsymbol{\varepsilon}_{as}) \quad (6.16)$$

### 6.1.3 Determining solidification strain

The deposition of the healed material is assumed to take place in a stress free state. The solidification approach is used where the stress for the overall composite does not change upon healing (Bažant & Prasanna 1989). In a single direction and when considering the isotropic loading case, the local solidification strain equals the local strain at the time of healing. However, when considering the composite material as a whole, this approach requires both the static and kinematic constraints to be met. To ensure that the average stress does not change upon solidification, the total added strain for the original material and healed material must be the same at the point of healing. Hence  $\epsilon_\alpha = \epsilon_{ah}$ , or similarly on a local plane  $\epsilon_\alpha = \epsilon_{\alpha h}$ , thus equating the added strain pre-healing and post-healing leads to equation (6.17) which can be rearranged to find the solidification strain in equation (6.18).

$$\left(\frac{\omega}{1-\omega}\right) \mathbf{C}_L : s_L = \left(\frac{\omega - h\omega_{th}B}{1-\omega + h\omega_{th}B}\right) \mathbf{C}_L : s_{Lh} + \left(\frac{h\omega_{th}B}{1-\omega + h\omega_{th}B}\right) : \epsilon_s \quad (6.17)$$

$$\epsilon_s = \left[\frac{h\omega_{th}B}{1-\omega + h\omega_{th}B}\right]^{-1} \left[\left(\frac{\omega}{1-\omega}\right) \mathbf{C}_L : s_L - \left(\frac{\omega - h\omega_{th}B}{1-\omega + h\omega_{th}B}\right) \mathbf{C}_L : s_{Lh}\right] \quad (6.18)$$

Noting that at the time of healing  $\omega = \omega_{th}$  and  $s_L = s_{Lh} = s_{Lth}$ . Simplifying equation (6.18) leads to a reduced form,

$$\epsilon_s = \left(\frac{1}{1-\omega_{th}}\right) \mathbf{C}_L : s_{Lth} \quad (6.19)$$

where  $\omega_{th}$  is the micro-cracking damage parameter at the time of healing,  $s_{Lth}$  is the local stress at the time of healing and  $\mathbf{C}_L$  remains the local compliance tensor of the original material.

### 6.1.4 Continuing damage of healed material

This new healed composite material will also be subjected to further stress or strain which would mean that the healed material will also eventually micro-crack. Without micro-cracking the healed portion of the composite would remain elastic and eventually dominate the response. A micro-cracking parameter can be applied to this healed portion of the local stress equation. The  $h\omega_{th}B\mathbf{D}_L$  term from equation (6.3) is replaced by  $(1-\omega_h)h\omega_{th}B\mathbf{D}_L$ . The local stress with continued damage is shown in equation (6.20).

$$s_{Lh} = (1-\omega) \mathbf{D}_L \epsilon_{Lh} + (1-\omega_h) h\omega_{th} B \mathbf{D}_L (\epsilon_{Lh} - \epsilon_s) \quad (6.20)$$

Where  $\omega$  remains the micro-cracking parameter of the original material and  $\omega_h$  is the micro-cracking parameter of the healed material. This set-up allows the micro-cracking criterion and evolution in both the original and healed material to be controlled independently. Working through the derivation again with this micro-cracking in the healed material leads to equation (6.21) for the added local strain.

$$\epsilon_{\alpha h} = \left( \frac{\omega - (1 - \omega_h) h \omega_{th} B}{1 - \omega + (1 - \omega_h) h \omega_{th} B} \right) \mathbf{C}_{LSLh} + \left( \frac{(1 - \omega_h) h \omega_{th} B}{1 - \omega + (1 - \omega_h) h \omega_{th} B} \right) \epsilon_s \quad (6.21)$$

The resulting component total added strain in the new material and total contribution from solidification strain then becomes,

$$\epsilon_{ac} = \left[ \frac{1}{2\pi} \int_{2\pi} \int_{\frac{\pi}{2}} \mathbf{N}_\epsilon : \mathbf{C}_L : N \left( \frac{\omega - (1 - \omega_h) h \omega_{th} B}{1 - \omega + (1 - \omega_h) h \omega_{th} B} \right) \sin(\psi) d\psi d\theta \right] : \bar{\sigma} \quad (6.22)$$

and

$$\epsilon_{as} = \frac{1}{2\pi} \int_{2\pi} \int_{\frac{\pi}{2}} \mathbf{N}_\epsilon : \left( \frac{(1 - \omega_h) h \omega_{th} B}{1 - \omega + (1 - \omega_h) h \omega_{th} B} \right) \epsilon_s \sin(\psi) d\psi d\theta \quad (6.23)$$

These equations are then substituted into equation (6.10) and upon following the original derivation steps, leads to the final constitutive relationship shown in equation (6.16) which includes continuing damage of the healed material.

### 6.1.5 Micro-crack criterion and evolution

The original and healed micro-cracking initiation and evolution criterion are based on the standard form as shown by equation (3.65) as described in Section 3.3. The effective local strain parameters  $\zeta$  and  $\zeta_h$  are governed by the directional micro-cracking function. The original material micro-cracking function is based on  $\epsilon_L$  whereas the healed material micro-cracking function is based on  $\epsilon_L - \epsilon_s$  which takes account of the solidification strain. This is illustrated by the volumetric model in section 6.3.1.

The strain at first uniaxial micro-cracking for the healed material ( $\epsilon_{th}$ ) is taken as

$$\epsilon_{th} = \frac{f_{th}}{B \cdot E_M} \quad (6.24)$$

where  $f_{th}$  is a local tensile strength at the aggregate/cement paste interface for the healed material. The local strains in the effectively fully micro-cracked ( $\epsilon_{0h}$ ) state are assumed to be related to the relative displacements by

$$\epsilon_{0h} = \frac{u_{0h}}{h_h} \quad (6.25)$$

in which  $h_h$  can be related to the size of the coarse aggregate.

Similar to the formulation in Section 3.3, where volumetric and direction crack-  
ing softening functions are described, the onset of original and healed material  
micro-cracking is controlled by the peak elastic stress in the matrix. The micro-  
cracking initiation criterion is reached when the local principal stress ( $s_{hl}$ ) exceeds  
the initial interface tensile strength ( $f_{th}$ ), using equation (3.68).

The exterior point Eshelby (*EPE*) solution (Ju & Sun 1999) is used to give the  
strain and stress amplification at any point in the matrix as shown in equations (3.38)  
and (3.39) in Section 3.1.7. The stress tensor in the matrix on each local plane is  
given by equation (6.26) for the healed material. The stress in the healed material  
is directly related to the ratio  $B$ .

$$s_{M\Omega h}(\mathbf{x}) = \mathbf{N} \cdot B \cdot \mathbf{D}_M : \varepsilon_{M\Omega}(\mathbf{x}) \quad (6.26)$$

For the autogenous healing case, the healed material is likely to be weaker than  
the original material as shown in Chapter 5. The introduction of this weaker ma-  
terial into the micro-cracks will have little effect on the original material stiffness  
because the volume of the healed material is very small in comparison with the  
total material volume. The effects of micro-cracking healing are explored using  
illustrative examples in Section 6.3.2.

## 6.2 Numerical implementation

The self-healing constitutive model presented in the previous section has been implemented in a Mathcad (2010) sheet using the algorithm shown in Figure 6.1. Pseudo-time  $t = 1$  to  $t_{heal}$  shows how the model behaves for the original material before healing, time  $t = t_{heal}$  is at the time of healing and time  $t = t_{heal}$  to  $t_{ns}$  are the time-steps post-healing to the end of the specified steps ( $ns$ ). This constitutive model can be driven by total stress ( $\bar{\sigma}$ ) or total strain ( $\bar{\epsilon}$ ). The constitutive driver algorithm is given in Table 3.1, where the essential steps of the computational algorithm for a specified stress path increment ( $\Delta\sigma_a$ ) or strain path increment ( $\Delta\epsilon_a$ ) are shown. Table 6.1 shows the computational algorithm for the pre-healed stress update and Table 6.2 shows the computational algorithm for the post-healed stress update.

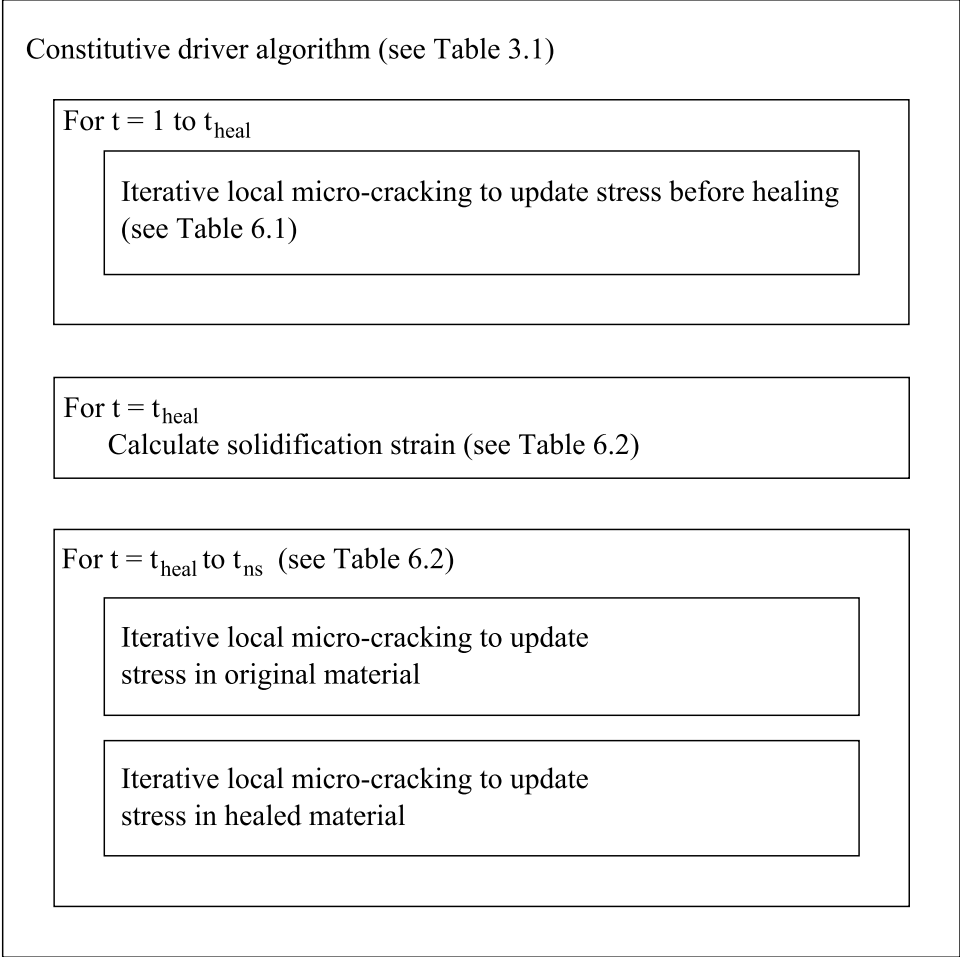


Figure 6.1: Self-healing algorithm

Table 6.1: Computational algorithm for iterative local micro-cracking to update stress before healing

Enter with $\bar{\epsilon}, \bar{\epsilon}_{prv}, \Delta \epsilon_a, \zeta_{Mprv}, \zeta_{prv}$	Enter with strains and previous equivalent strain parameters
For $t = 1$ to $t_{heal}$	Pre-healing
For $i = 1$ to $n_i$	Loop over integration directions
$\epsilon_{M\Omega} = \mathbf{T}^E(\mathbf{x}) : \epsilon_M$	Compute matrix stress (EPE)
$s_{M\Omega} = \mathbf{N}_i \cdot \mathbf{D}_M : \epsilon_{M\Omega}$	Compute local cracking stress at peak
If $s_I(s_{M\Omega})_{max} \leq f_t$ then $\omega_i = 0$	Micro-crack initiation criterion
Else	Micro-crack evolution
$\epsilon_{L_i} = (1 - \omega_i) \mathbf{C}_{LM} : s_{M\Omega} + \omega_i \mathbf{N}_{\epsilon_i} \cdot \bar{\epsilon}$	Evaluate local strain vector
$\zeta_i = f_d(\epsilon_{L_i})$ if $\epsilon_{L_i} > \zeta_{prv_i}$	Update strain parameter if exceeds previous max
Update $\omega_i$	Update damage parameter
End	
$\mathbf{C}_{add} = \sum_{i=1}^{n_i} \mathbf{N}_{\epsilon_i} \cdot \mathbf{C}_{LM\Omega} \cdot \mathbf{N}_i \cdot \frac{\omega_i}{1 - \omega_i} w_i$	Evaluate total added compliance
$\mathbf{D}_{Sec} = (\mathbf{I}^{4s} + \mathbf{D}_{M\Omega} \cdot \mathbf{C}_{add})^{-1} \cdot \mathbf{D}_{M\Omega}$	Form secant constitutive matrix
$\bar{\sigma} = \mathbf{D}_{Sec} : \bar{\epsilon}$	Compute stresses

Table 6.2: Computational algorithm for iterative local micro-cracking to update stress after healing

Enter with $\bar{\epsilon}$ , $\bar{\epsilon}_{prv}$ , $\Delta\epsilon_a$ , $\zeta_{Mprv}$ , $\zeta_{prv}$	Enter with strains and previous equivalent strain parameters
For $t = t_{heal}$ to $ns$	Time of healing
If $Healed = false$	Loop over integration directions
For $i = 1$ to $n_i$	Evaluate local solidification strain vector
$\epsilon_{Ls_i} = (1 - \omega_{ht_i})^{-1} \mathbf{C}_{LM\Omega} \mathbf{N}_i \cdot \bar{\sigma}$	
$Healed = true$	
End if	
If $Healed = true$	Post-healing
For $i = 1$ to $n_i$	Loop over integration directions
$\epsilon_{M\Omega} = \mathbf{T}^E(\mathbf{x}) : \epsilon_M$	Compute matrix stress (EPE)
$s_{M\Omega} = \mathbf{N}_i \cdot \mathbf{D}_M : \epsilon_{M\Omega}$	Compute local cracking stress original material
If $s_I(s_{M\Omega})_{max} \leq f_t$ then $\omega_i = 0$	Micro-crack initiation criterion
Else	Micro-crack evolution
$\epsilon_{L_i} = (1 - \omega_i) \mathbf{C}_{LM} : s_{M\Omega} + \omega_i \mathbf{N}_{\epsilon_i} \cdot \bar{\epsilon}$	Evaluate local strain vector
$\zeta_i = f_d(\epsilon_{L_i})$ if $\zeta_i > \zeta_{prv_i}$	Update strain parameter original material if exceeds previous max
Update $\omega_i$	Update damage parameter
End if	
$s_{M\Omega h} = \mathbf{N}_i \cdot \mathbf{B} \cdot \mathbf{D}_M : \epsilon_{M\Omega}$	Compute local cracking stress healed material
If $s_{hI}(s_{M\Omega h})_{max} \leq f_{th}$ then $\omega_{h_i} = 0$	Micro-crack initiation criterion
Else	Micro-crack evolution
$\epsilon_{L_{h_i}} = (1 - \omega_{h_i}) \mathbf{B}^{-1} \mathbf{C}_{LM} : s_{M\Omega h} + \omega_{h_i} \mathbf{N}_{\epsilon_i} \cdot \bar{\epsilon}$	Evaluate local strain vector
$\zeta_{h_i} = f_{dh}(\epsilon_{L_{h_i}} - \epsilon_{L_{s_i}})$ if $\zeta_{h_i} > \zeta_{prv_i}$	Update strain parameter healed material if exceeds previous max
Update $\omega_{h_i}$	Update damage parameter
End if	
End if	
$\mathbf{C}_{addh} = \sum_{i=1}^{n_i} \mathbf{N}_{\epsilon_i} \mathbf{C}_{LM\Omega} \mathbf{N}_i \frac{\omega_i - (1 - \omega_{h_i}) h \omega_{ht_i} B}{1 - \omega_i + (1 - \omega_{h_i}) h \omega_{ht_i} B} \mathbf{w}_i$	Evaluate total added compliance
$\epsilon_{as} = \sum_{i=1}^{n_i} \mathbf{C}_{LM\Omega} \mathbf{N}_i \frac{(1 - \omega_{h_i}) h \omega_{ht_i} B}{1 - \omega_i + (1 - \omega_{h_i}) h \omega_{ht_i} B} \mathbf{w}_i \epsilon_{L_{h_i}}$	Evaluate total solidification strain contribution
$\mathbf{D}_{Sech} = (\mathbf{I}^{4s} + \mathbf{D}_{M\Omega} \cdot \mathbf{C}_{addh})^{-1} \cdot \mathbf{D}_{M\Omega}$	Form secant constitutive matrix
$\bar{\sigma} = \mathbf{D}_{Sech} : (\bar{\epsilon} - \epsilon_{as})$	Compute stresses

## 6.3 Illustrative model performance

The model performance is tested by varying the different parameters that control the model response. A volumetric isotropic model is first used to give an insight into how the model performs. The full micromechanical model is then subjected to a parametric study. The micro-cracking initiation and subsequent evolution for both original and healed materials are observed. The four main parameters tested are the healed tensile strength at the aggregate/cement paste interface, the local strains in the effectively fully micro-cracked state, healing efficiency and strength of the healed material. The model response to healing whilst subjected to a load is also considered showing the impact of the solidification strain component.

### 6.3.1 Volumetric response

The single phase volumetric constitutive relationship is shown in equation (6.27), which has the basic form as that given in equation (6.20).

$$\sigma = (1 - \omega) K_M \varepsilon + (1 - \omega_h) h \omega_{th} B \cdot K_M (\varepsilon - \varepsilon_s) \quad (6.27)$$

$K_M$  is the bulk modulus of the material and all other terms remain as previously defined. The micro-cracking parameters are  $\omega$  for the original material,  $\omega_{th}$  for the original material at the time of healing and  $\omega_h$  for the healed material. Both  $h$  and  $B$  are taken to be 0.5 in this case and the other material properties used are shown in Table 6.3.

This model is subjected to a volumetric strain increment where both micro-cracking parameters are calculated directly. The volumetric strain is incremented until the original material reaches a point on the load-displacement (stress-strain) softening curve equal to half the peak stress, after which the strain is returned to zero. This strain response is shown in Figure 6.2a.

The healing here is assumed to take place when the sample is unloaded which occurs when there is zero stress and zero strain. For the time strain plot shown in Figure 6.2a, this unloading point occurs at a pseudo-time  $t = 1000(s)$ . At this point the  $\varepsilon_s$  is zero and the  $\omega_{th}$  is fixed. The new material incorporating the healing is then subjected to further strain increments up to and beyond the initial peak strain, until the strain is four times the original unloading strain.

Figure 6.2b shows the stress strain response of the volumetric healed model. The first loading phase, up to  $t = 1000(s)$ , can be seen where the stress returns along a linear line to zero. The second loading phase shows a bi-linear line returning to the softening curve (in stress-time space) of the healed material. This increase in stress directly relates to the healed material. The first steep gradient is due to the

Table 6.3: Material properties for volumetric model response

$E_M$ ( $N/mm^2$ )	$\nu_M$	$K_M$ ( $N/mm^2$ )	$f_{tv}$ ( $N/mm^2$ )	$\epsilon_{tv}$	$\epsilon_{tvh}$	$\epsilon_{0v}$	$\epsilon_{0vh}$
24000	0.15	11429	1	$4.17 \times 10^{-5}$	$8.33 \times 10^{-5}$	$6.67 \times 10^{-3}$	$6.67 \times 10^{-3}$

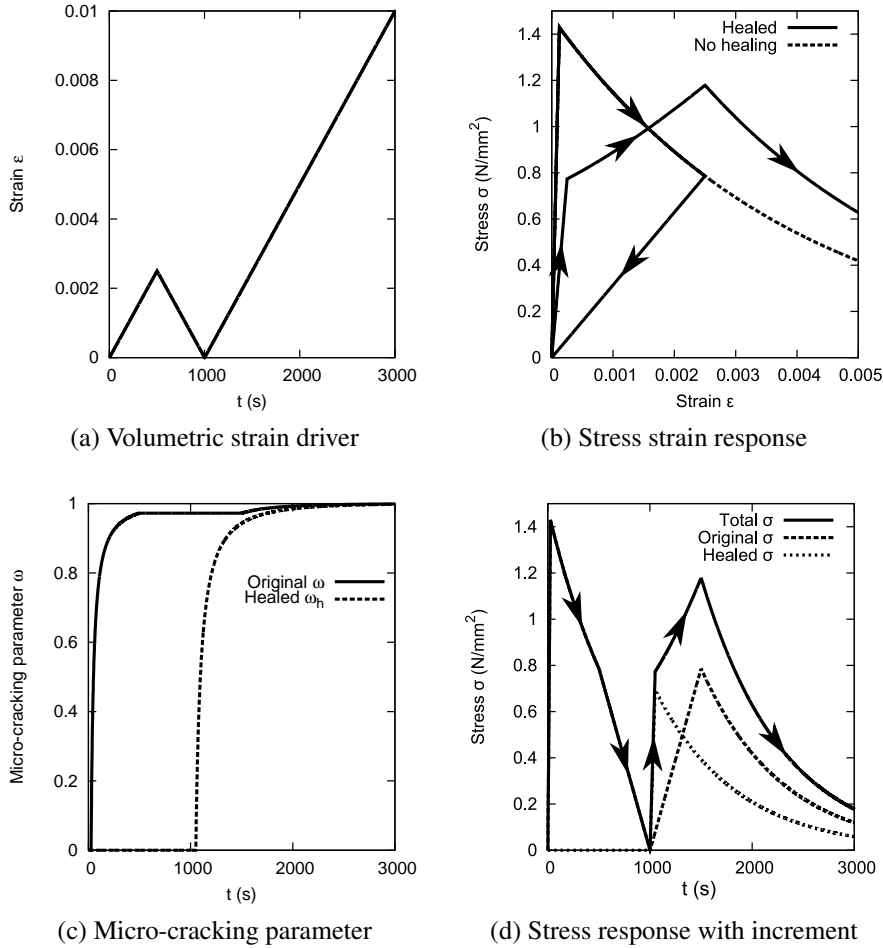


Figure 6.2: Typical volumetric healing response

elastic response of the healed material and the second flatter gradient is the sum of stresses in both materials. The peak stress after healing is reached at the same strain at which the model was first unloaded, this being  $t = 1500(s)$ . The softening curve for the case where no healing occurs is also shown on Figure 6.2b as a dotted line.

The original and healed material damage independently as illustrated by Figure 6.2c. During the strain unloading, between  $t = 500(s)$  and  $1000(s)$ , the degree of micro-cracking in the original material remains unchanged. Micro-cracking in the healed material starts soon after reloading commences. The original material continues to micro-crack only when the strain reaches the first unloading strain. Figure 6.2d has been included to show how the stress responds with time step increments for the original, healed and combined materials. The summation of individual com-

ponents show how they affect the model response.

When the healing is fully recovered, that is when  $h$  and  $B$  are unity, the first gradient upon reloading matches the original loading as expected. However, after this initial peak, the stresses are summed and, depending on the point of unloading, the stresses achieved in the material can be higher than the original peak. This volumetric example is useful in illustrating the mechanisms that occur during the damage and healing processes.

### 6.3.2 Parametric study of model performance

This parametric study will consider the response of the healing efficiency ( $h$ ) and relative strength of the healed material ( $B$ ) on the model performance. The same micro-cracking function is used for both original and healed material. The material properties fixed during this parametric study are shown in Table 6.4 and the material properties before being varied are shown in Table 6.5.

Table 6.4: Material properties fixed for parametric study

$f_M$	$E_M$ ( $N/mm^2$ )	$\nu_M$	$f_\Omega$	$E_\Omega$ ( $N/mm^2$ )	$\nu_\Omega$
0.3	20000	0.15	0.7	55000	0.25

Table 6.5: Material properties varied for parametric study

$f_t$ ( $N/mm^2$ )	$\epsilon_t$	$\epsilon_0$	$f_{th}$ ( $N/mm^2$ )	$\epsilon_{th}$	$\epsilon_{0h}$	B	h
1	$5 \times 10^{-5}$	0.0067	1	$1 \times 10^{-4}$	0.0067	0.5	0.5

The response of the benchmark model, using unchanged material properties, is shown in Figure 6.3. The model is subjected to a uniaxial tensile strain path, shown in Figure 6.3a, and the resulting stress strain response is shown in Figure 6.3b. Only one loading case is shown here, but it is noted that the model is capable of representing multi-directional 3D applied stress or strain increments. The strain upon first loading is increased linearly until the stress is approximately half the peak value and half way down the softening curve. Upon unloading, the stress and strain return to zero as would be expected in a model that does not include any plasticity. The model also does not simulate the hysteresis that can be seen during the unloading phase of the three point bending experimental test, as seen in Figure 5.13. The stress difference between the linear unloading curve and reloading strain is a measure of the amount of healing that takes place. For this benchmark model the strength recovery ( $c$ ) is 38 %.

In this example, the healing takes place when the strain is zero. This represents the experimental procedure in Chapter 5 where the unloaded fractured samples are allowed to heal in a curing tank before reloading. The strain is increased linearly (with respect to time) during the reloading phase where the stress response is shown to have two distinct gradients up to the peak healed stress. The initial steep gradient reflects the healed material stiffness and the next flatter gradient section results from a combination of the new healed material micro-cracking and the original material taking stress without further micro-cracking. As in the volumetric model example, the damage in the original material remains constant during the unloading phase. The micro-cracking parameter response is shown against pseudo-time ( $t$ ) in Figure 6.4. The healed material damages first during the reloading phase and only when the strain exceeds the previous maximum does the original material continue to damage. Only two of the 29 directional micro-cracking parameters are shown here,  $r_1$  and  $r_{17}$ , shown on Figure 4.5b in Chapter 4. The right hand figure shows the micro-cracking parameters magnified for 0.9 to 1.

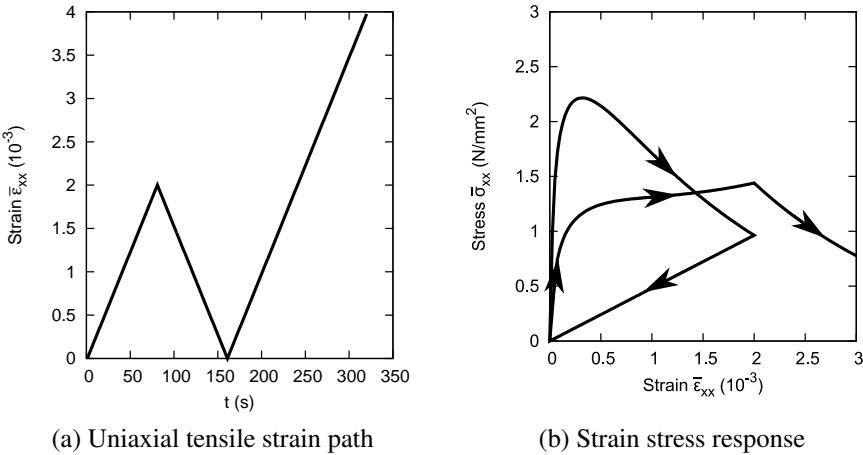


Figure 6.3: Model response with standard material properties

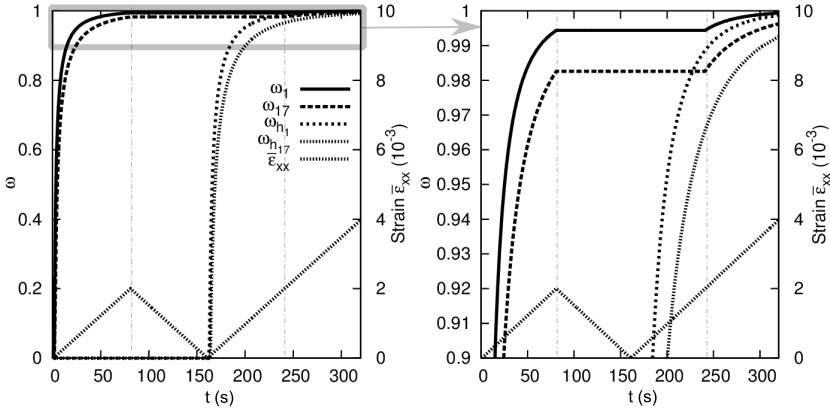


Figure 6.4: Micro-cracking parameter response

The four parameters varied include the local tensile strength ( $f_{th}$ ) at the aggregate/cement paste interface, the local strains ( $\epsilon_{0h}$ ) in the effectively fully micro-cracked state, healing efficiency ( $h$ ) and strength of the healed material ( $B$ ). The results of the parametric study are shown in Figure 6.5.

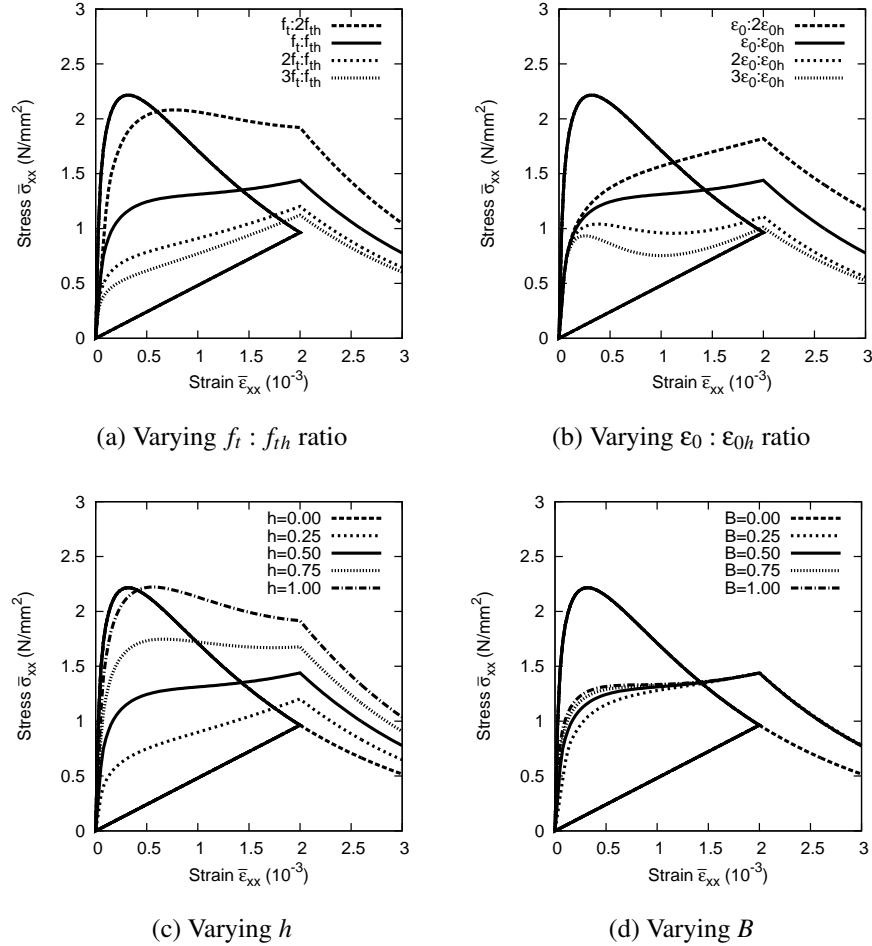


Figure 6.5: Parametric study of model performance

Figure 6.5a shows the influence of changing the ratio between  $f_t$  and  $f_{th}$  on the stress-strain response. This ratio controls the stress of the first portion of the post-healing linear reloading phase linked to the initial micro-cracking of the new material. This ratio also controls the peak reloading stress of the healing recovery (c).

Figure 6.5b shows how the fully micro-cracked local strain of the healed material influences the material response. The larger the  $\epsilon_{0h}$  value the less the healed material micro-cracks. It can be seen that for a smaller  $\epsilon_{0h}$  the new healed material is almost fully micro-cracked by the time the composite reaches the original unloading strain, as shown by the plot of  $3\epsilon_{0h} : \epsilon_{0h}$  resulting in negligible changes to the healing recovery .

Figure 6.5c shows how the healing efficiency ( $h$ ) influences the response of the

material. The initial change in gradient during reloading and the healing efficiency are both affected linearly with the change in  $h$ . The model is very sensitive to the change in  $h$ . Conversely, it appears that changing the relative stiffness of the healed material, within certain limits, has minimal impact on the response of the model, as shown in Figure 6.5d. This is because the stiffness of the healed micro-crack is a small proportion of the total stiffness of the material. The relative simplicity of this micromechanical healing model combined with the fact that it requires a small number of physically meaningful parameters suggest that it is suitable for simulating a wide range of two-phase cementitious materials.

The parametric study showed healing taking place when there is zero applied load and strain. This means that the  $\epsilon_s$ , from equation (6.19), was zero and  $\epsilon_{as}$  from equation (6.14) also remained zero. Real structures are likely to undergo healing whilst being subjected to self-weight and some serviceability loading. Therefore, it is considered important to also examine the predicted healing response of the model in which healing takes place under loaded conditions.

A series of paths have been chosen whereby the healing takes place at different strains during the unloading phase. Figure 6.6a shows 5 paths with uniaxial strain applied in the x-x direction. 100 % unloading takes place in Path 1 (similar to the parametric study) and the degree of unloading is reduced in Paths 2 to 4, eventually showing no unloading in Path 5. The composite is strained to a fixed value in Path 5 where healing takes place instantaneously before then continuing the uniaxial strain at the same initial rate. All other parameters are kept the same as in Tables 6.4 and 6.5. The stress-strain response of the model for these different paths are shown in Figure 6.6b.

An interesting response can be seen when plotting all of the strain paths. The peak stress reached during the reloading phase reaches a maximum between Paths 3 and 4, having 50 % and 25 % unloading respectively. Going from Paths 1 to 3, the height of the initial steeper gradient during the re-loading phase increases and the length of the second flatter gradient becomes shorter. The less unloading that takes place, the less opportunity there is for the new material to micro-crack before the original material continues to micro-crack. Paths 4 and 5 show the influence of this continued micro-cracking in the original material on the stress-strain response. This phenomenon is examined further by using the simplified volumetric model.

The results of the volumetric model are shown in Figure 6.7 for a path in which healing occurs under loaded conditions. The impact of the healed material on the stress-strain response can be seen by setting the fully micro-cracked local strain of the healed material  $\epsilon_{0h}$  to an infinitely large number. This has the effect of simulating a perfectly ductile healed material. This ductile material is compared to the original in Figure 6.7a. Whichever unloading percentage is chosen, the stress fol-

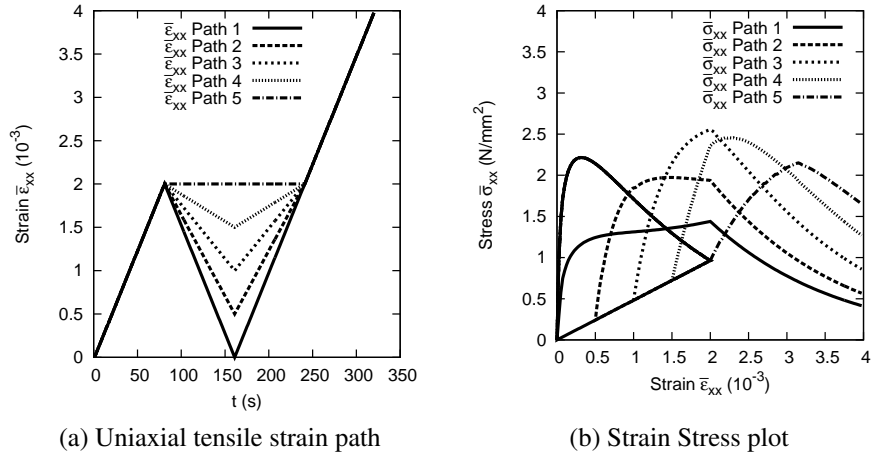


Figure 6.6: Healing under load

allows a maximum envelope. The peak response drawn by the envelope lines up with the original unloading strain position also reflected in Figure 6.6b.

The volumetric model allows the total stress and its constitutive contributions from the original and healed material to be plotted individually against time. Figures 6.7b, 6.7c and 6.7d plot the individual components for Paths 1, 3 and 5 respectively. Examining Figure 6.7d at the point of reloading, after healing, allows the phenomenon above to be explained. At this strain the original material continues to damage, whereas the healed material behaves elastically before micro-cracking. When the healed material reaches its peak stress the original material has already lost some stress carrying capacity, resulting in a reduced overall stress. The peak stress occurs when the healed material peak stress coincides with the point at which damage recommences in the original material.

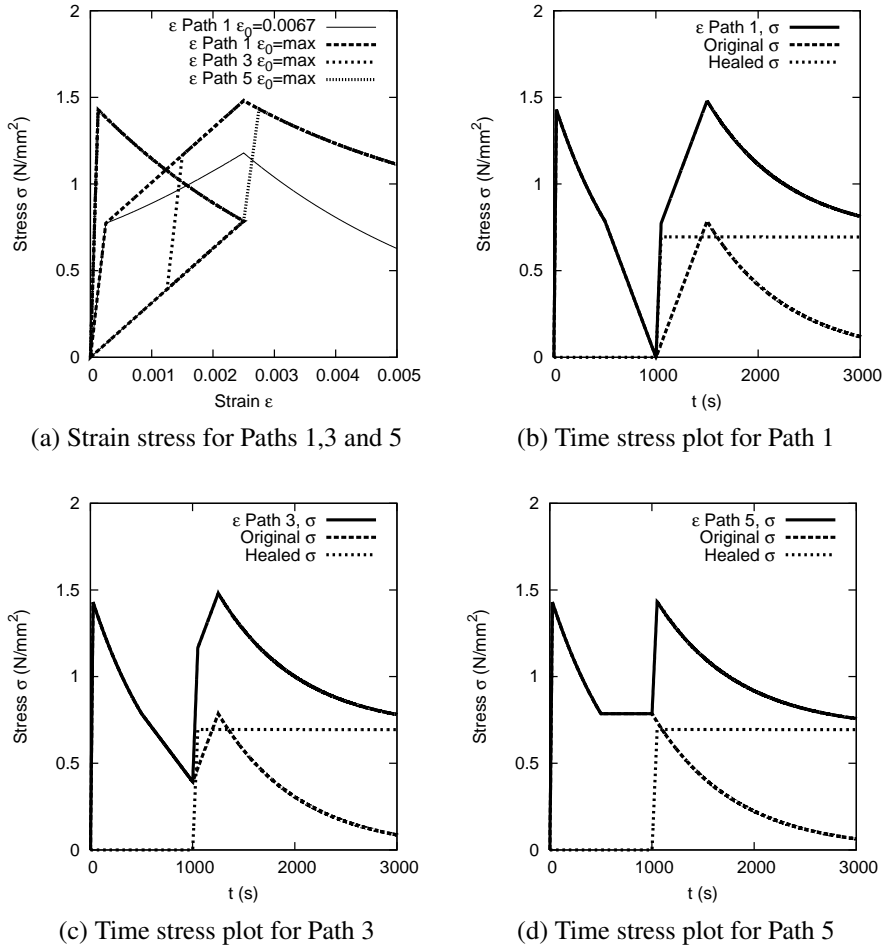


Figure 6.7: Volumetric healing under load

## 6.4 Comparison with experimental data

Examples are now used to illustrate the performance of the healing model by comparing it to experiments. The experimental data obtained in Chapter 5 for natural cracks in concrete healed under water for a period of 28 days, Set 1, are considered and compared to the micromechanical model. The experimental and modelling data from Granger et al. (2007b) are also compared, where standard strength concrete and ultra high performance cements are healed under water for 20 weeks. In all cases, beams have been tested under three point flexural bending and results given in terms of load and CMOD.

The micromechanical model described earlier in this Chapter produces a constitutive model response for a range of stress and strain loading conditions. However, the micromechanical model can not be compared directly to the experimental results. The load against CMOD results can be translated to average macro-scale stress and strain response for the beam but this would be one length scale higher than the micromechanical model. A model that is capable of describing the three

point flexural bending test uses a beam hinge approach that incorporates a central non-linear fracture process zone (FPZ). This beam hinge model can be implemented within a layered beam framework, where the beam is divided into layers having individual constitutive responses. The relationship between the load at mid-point and CMOD can be described by taking account of the micro-scale constitutive response at each layer. This is accomplished by using the micromechanical model to provide the constitutive relationship required for each layer of the beam model.

### 6.4.1 Layered beam model

The layered beam model consist of two elastic sections ( $L_e$ ) with a central FPZ section ( $w_c$ ) as shown on the schematic in Figure 6.8. The location of the cracking is controlled by the notch. This approach means that each layer is calculated individually and able to capture the response to deflection in each layer. This detailed information would not be available for a smeared crack approach. The FPZ damage would normally be controlled by a simple 1D strain based micro-cracking criterion and evolution similar to equation (3.65) as described in Section 3.3. However, this resulting constitutive relationship can be replaced by the constitutive relationship from a micromechanical model with uniaxial loading. The layered beam model response can therefore be controlled by a micromechanical constitutive model without deriving a special 1D case. The layered beam approach has the additional advantage of being able to examine the stress and strain at any specific location within the beam.

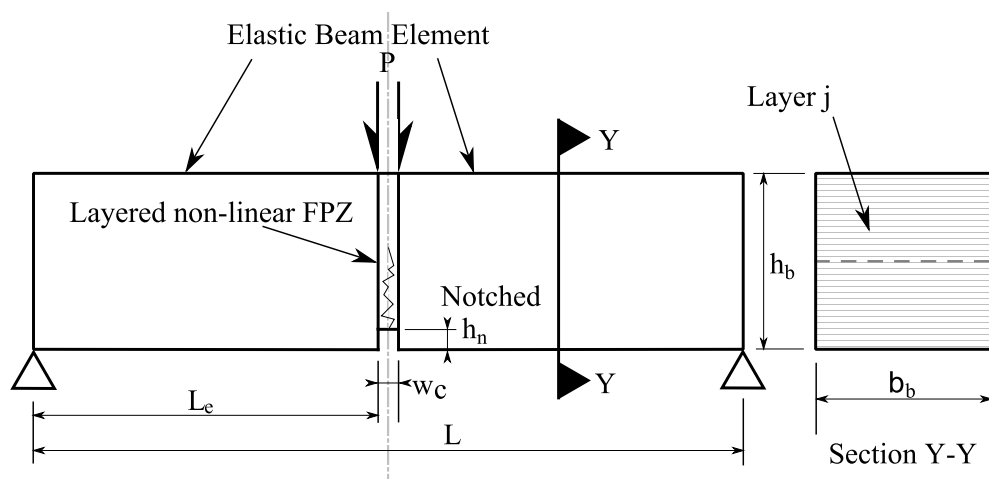


Figure 6.8: Layered beam model schematic

This layered beam model is relatively simple and implemented in a Mathcad (2010) sheet. The current model is driven by the change in slope of the beam ( $\theta_H$ ).

A similar layered beam model was used by Dunn (2011) when examining the pre-strain effects of an embedded polymer. A comprehensive derivation of the beam hinge element development is provided by Dunn (2011). A simplified representation of the beam is presented in Figure 6.9 and the key equations used for this comparison are given below.

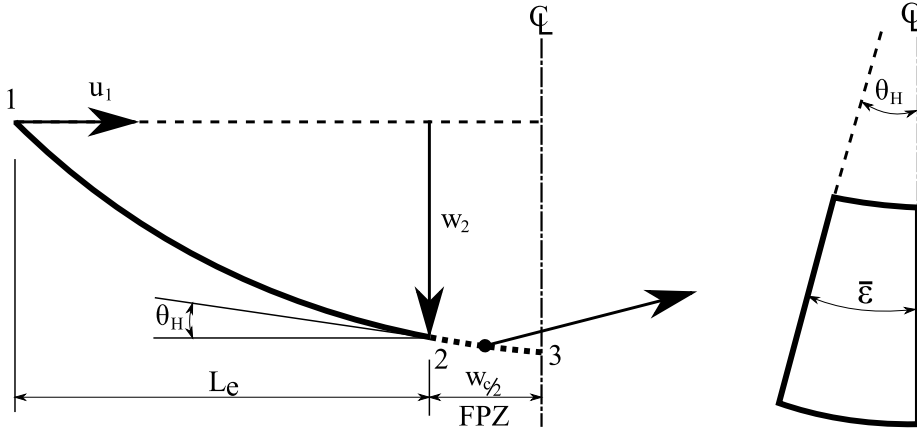


Figure 6.9: Simplified representation of beam

The strain ( $\epsilon$ ) in each layer ( $j$ ) is given by

$$\epsilon_j = \bar{\epsilon} - \frac{2 \cdot \theta_H}{w_c} \cdot z_j \quad (6.28)$$

where  $\bar{\epsilon}$  is the average strain at the neutral axis and  $z$  is the layer depth. The axial force ( $N$ ) in the beam hinge is given by equation (6.29) and the moment ( $M$ ) in the beam hinge is given by equation (6.30).

$$N = b_b \int_{-h_b/2}^{+h_b/2} \sigma dz \quad (6.29)$$

$$M = b_b \int_{-h_b/2}^{+h_b/2} \sigma \cdot z dz \quad (6.30)$$

where the stress in each layer is given by,

$$\sigma = (1 - \omega)E \cdot \epsilon = E_s \cdot \epsilon \quad (6.31)$$

$b_b$  is the width of the beam,  $h_b$  is the height of the beam and  $E_s$  is the secant Young's modulus term in each layer.

The overall relationship between the axial load, moment, strain and rotation

components are given by equation (6.32).

$$\begin{Bmatrix} N \\ M \end{Bmatrix} = \begin{bmatrix} \sum_{j=1}^{nlay} E_{s_j} \cdot b_{b_j} \cdot \Delta z_j & \frac{-2}{w_c} \sum_{j=1}^{nlay} E_{s_j} \cdot b_{b_j} \cdot z_j \cdot \Delta z_j \\ \sum_{j=1}^{nlay} E_{s_j} \cdot b_{b_j} \cdot z_j \cdot \Delta z_j & \frac{-2}{w_c} \sum_{j=1}^{nlay} E_{s_j} \cdot b_{b_j} \cdot z_j^2 \Delta z_j \end{bmatrix} \cdot \begin{Bmatrix} \bar{\epsilon} \\ \theta_H \end{Bmatrix} \quad (6.32)$$

The secant Young's Modulus is obtained from the micromechanical model, see equation (6.16). The load ( $P$ ) and CMOD responses are finally calculated using equations (6.33) and (6.34) respectively.

$$P = M \frac{2}{L_e} \quad (6.33)$$

$$CMOD = \bar{\epsilon} w_c + 2\theta_H \frac{h_b}{2} \quad (6.34)$$

The combined micromechanical and layered beam model is implemented in a Mathcad (2010) sheet. Figure 6.10 illustrates how both models interact. For each step angle ( $\theta_H$ ) the micromechanical provides the layered beam model with the constitutive response to allow the stress and strain in each layer to be calculated along with the overall load and CMOD.

A convergence study was completed where 100 layers, having reduced thickness towards the top of the beam, was found to be sufficient for comparison with the experiments. It should be noted that this approach is limited to a three point flexural test with a single central crack.

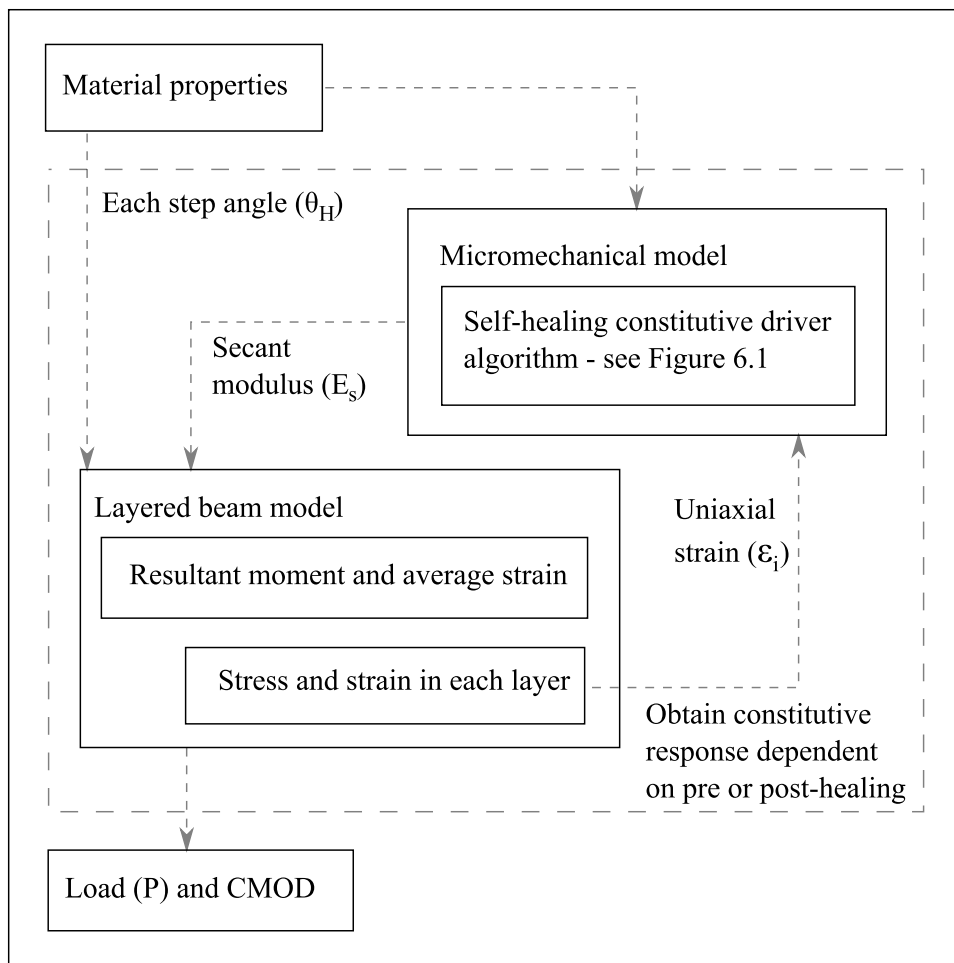


Figure 6.10: Self-healing micromechanical and layered beam model interaction

#### 6.4.2 Results of comparison with experimental data

Autogenous cementitious healing experiments are compared to the micromechanical healing model in this section. An example from the Chapter 5 is chosen alongside two further examples given by Granger et al. (2007b).

The example taken from Chapter 5 is Set 1 Beam C which represents a typical 28 days autogenous healing response. The experimental details are given in Section 5.2 and results shown on Figure 5.13. This beam had a natural crack which was loaded until the CMOD reached 0.3mm, before unloading and healing in water. This experiment is simulated using two different material data sets, one that was determined using realistic material strength properties (Parameters A) and the second set ascertained by inverse parameter identification (Parameters B).

The two Granger et al. (2007b) examples chosen are the standard strength concrete (SSC) and ultra high performance concrete (UHPC) samples subjected to autogenous healing in water. The CMOD, upon loading, was restricted to 0.028 mm

and then healed in water for 20 weeks. The specific example chosen for the standard concrete is beam number 4 sample 1 which had a w/c ratio of 0.48. The UHPC used by Granger et al. (2007b) is based on the concept of reactive powder concrete. The mass proportion of UHPC composition is not given and a typical UHPC composition was chosen for the numerical model (Mounanga et al. 2012) which assumed that there was no coarse aggregate present in the mix. The composition of both the SSC and UHPC mixes are given in Table 6.6. All of the model parameters used in each comparison, including beam and notch dimensions, material composition and material strengths, are shown in Table 6.7.

Table 6.6: Composition of SSC (Granger et al. 2007b) and UHPC (Mounanga et al. 2012)

Material	SSC ( $kg/m^3$ )	Mass proportion (to cement)	UHPC ( $kg/m^3$ )	Mass proportion (to cement)
Cement (CEM1 52.5N)	366.2	1	1003.6	1
Coarse aggregate	1051.3	2.87	-	-
Sand	722.7	1.97	1104.0	1.1
Water	174.1	0.48	160.6	0.16
Micro-silica fume	36.6	0.10	188.2	0.25 x 3/4
Crushed quartz	-	-	62.7	0.25 x 1/4
Superplasticiser	2.0	0.005	5.0	0.005

Table 6.7: Model material properties for experimental comparison study

Model	$L$ (mm)	$h$ (mm)	$b$ (mm)	Beam length (mm)	$nlay$ (mm)	$h_n$ (mm)	$w_c$
Parameters A	200	75	75	255	100	5	5
Parameters B	200	75	75	255	100	5	5
SSC	400	100	50	500	100	20	5
UHPC	400	100	50	500	100	20	5
Model	$f_M$	$E_M$ (N/mm <sup>2</sup> )	$\nu_M$	$f_\Omega$	$E_\Omega$ (N/mm <sup>2</sup> )	$\nu_\Omega$	$f_t$ (N/mm <sup>2</sup> )
Parameters A	0.463	20000	0.15	0.537	55000	0.25	0.475
Parameters B	0.463	20000	0.15	0.537	55000	0.25	0.475
SSC	0.553	7500	0.15	0.447	45000	0.25	8.0
UHPC	0.583	8000	0.15	0.417	19000	0.25	10.0
Model	$\epsilon_t$	$\epsilon_0$	$f_{th}$ (N/mm <sup>2</sup> )	$\epsilon_{th}$	$\epsilon_{0h}$	B	h
Parameters A	$1.22 \times 10^{-5}$	0.035	0.475	$2.45 \times 10^{-5}$	0.035	0.5	0.8
Parameters B	$2.38 \times 10^{-5}$	0.033	0.475	$1.59 \times 10^{-3}$	0.027	0.025	0.5
SSC	$1.07 \times 10^{-3}$	0.020	2.4	$4.27 \times 10^{-4}$	0.010	0.75	0.4
UHPC	$1.25 \times 10^{-3}$	0.031	8.0	$1.18 \times 10^{-3}$	0.031	0.85	0.2

Figure 6.11 presents the four comparisons made between the numerical and the experimental results. The experimental pre-healing (Exp. Pre-H) and post-healing (Exp. Post-H) results are compared with the micromechanical model pre-healing (Mod. Pre-H) and post-healing (Mod. Post-H) results.

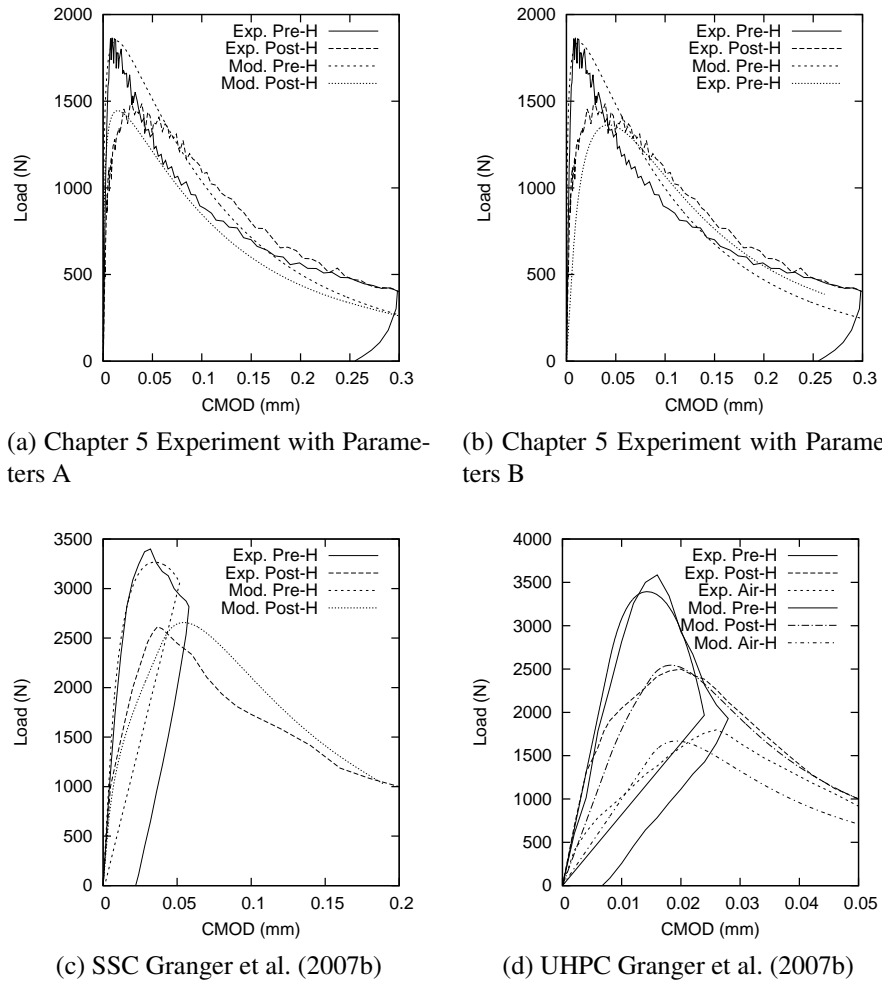


Figure 6.11: Load CMOD plots for micromechanical model and experimental data

Figure 6.11a shows the load CMOD comparisons between experimental and model results using initially selected strength parameters. It can be seen that the initial gradient of the predicted post-healing curve is steeper than that from the experiment. The post-healing experimental data also shows a more rounded response adjacent to the load peak. This suggests that the load carried by the experimental healed material was higher than the original material between 0.05 mm CMOD and 0.3 mm CMOD. For example, load carried by the healed sample at CMOD 0.1 mm was approximately 25 % higher than the original material. The numerical solution does not reflect these characteristics.

During the inverse parameter identification exercise, the two main parameters adjusted were the local strains ( $\epsilon_{th}$ ) during initial micro-cracking, which was in-

crease by two orders of magnitude, and the strength of the healed material ( $B$ ) reduced by 95 %. The impact of these changes are illustrated in Figure 6.11b.

Figures 6.11c and 6.11d show the results of the comparison between the numerical model and results for SSC and UHPC respectively. The post-healing experimental loading curve displays two straight gradient sections which are reflected in the model responses. For the UHPC case, the ‘healing in air’ results are also presented (Exp. Air-H and Mod. Air-H). The numerical model assumes that no healing takes place for the sample left in air hence the straight line to the peak load. However, the experimental data for this case does show a small amount of healing taking place by the slight change in gradient on the reloading section. These comparisons with experimental data suggest that the model can be used for a range of cementitious materials with minimal parameter fitting.

One drawback of this model is that it is assumed that healing takes place instantaneously, the time taken to heal is not being considered. A hygro-thermo-chemo diffusion model would provide the basis for predicting when and how much healing material arrives in the micro-cracks. Once this healed material has arrived, the material would have to cure and then describe the mechanical response of this new composite material. Many of the real structures made from cementitious materials would have healing taking place simultaneously with micro-cracking, such as early age loading, where hydration would continue to take place. To model this response there would be a need to simultaneously consider the healing and micro-cracking processes.

### 6.4.3 Effect of ageing material properties

The experiments undertaken in Chapter 5, in particular as shown in Figure 5.13, were initially fractured 24 hours after casting and subsequently re-tested after 28 days curing in water. The re-gain in peak strength of the beam was compared against the load at the unloading point of first fracture to obtain a measurement of strength recovery, see equation (5.1). This approach assumes that the residual strength in the beam does not change with time. However, the uncracked ligament will increase in strength with curing, as shown by the peak loads of the control beams. This section considers the effect of the ageing material properties on the strength increase in this uncracked ligament and examines the impact of this increase on the measurement of strength recovery.

The layered beam model developed in Section 6.4.1 is used to investigate the effect of ageing material properties. Beam C from Set 1, presented in Chapter 5, is again used as the sample for the comparison with the numerical model. The model material properties used in the comparison are shown in Table 6.8. The hydration

model, described in Section 4.3.2, was used to obtain the development of Young's Modulus ( $E$ ) with time using equation (4.30). The hydration model parameters are given in Table 6.9. The micro-crack criterion and evolution functions are based on the work described in Section 3.3. The  $f_t$  and  $\epsilon_0$  values were back calculated to fit the experimental load vs CMOD response for both the initial fracture tests at 1 day and the control beam at 29 days. Figures 6.12a and 6.12b show the load plotted against CMOD for the layered beam model and the experiment for the beams at 1 day and 29 days respectively.

Table 6.8: Model material properties when examining effect of ageing

Age	$L$ (mm)	$h$ (mm)	$b$ (mm)	$nlay$ (mm)	$h_n$ (mm)
Day 1	200	75	75	100	5
Day 28	200	75	75	100	5
Age	$w_c$	$E$ (N/mm <sup>2</sup> )	$f_t$ (N/mm <sup>2</sup> )	$\epsilon_t$	$\epsilon_0$
Day 1	5	16707	0.6	$3.591 \times 10^{-5}$	0.06
Day 28	5	27853	2.15	$7.719 \times 10^{-5}$	0.034

Table 6.9: Hydration model parameters

$PC_3S$	$PC_2S$	$PC_3A$	$PC_4AF$	$PSO_3$	$PFreeCaO$	$PMgO$	$p_{cem}$	Blaine (m <sup>2</sup> /kg)	$C_{cem}$ (kg/m <sup>3</sup> )
0.51	0.240	0.053	0.166	0.025	0.004	0.009	1	310	396

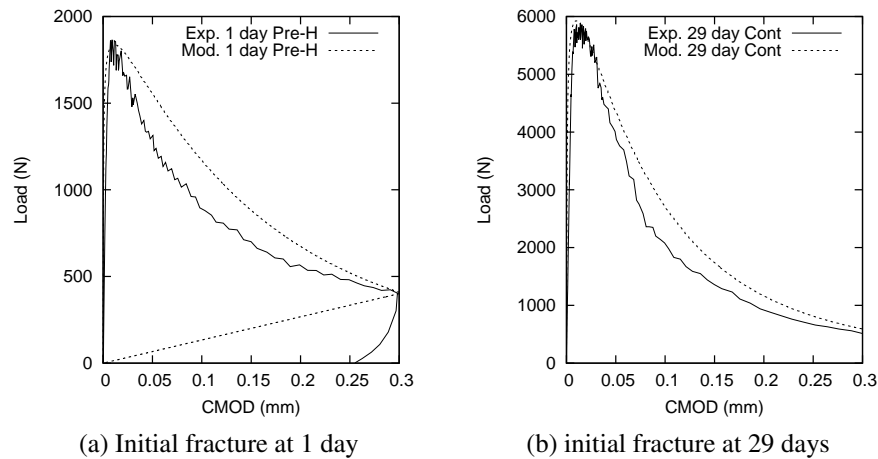


Figure 6.12: Load CMOD plots comparison of model and experimental results

The maximum micro-cracking parameter ( $\omega$ ), for each layer of the numerical model, can be extracted from the model following the initial fracture. This maxi-

imum occurs at the unloading point, which is at a CMOD of 0.3mm for this case in Figure 6.12a. The micro-cracking parameter will remain unchanged for the cured beam if no healing occurs. The micro-cracking parameter for the example presented here is shown in Figure 6.13a. The micro-cracking parameter development in each layer of the numerical model is controlled by the material properties and the effective strain parameter ( $\zeta$ ) in each layer. Translating the micro-cracking parameter from the initial model to the cured material model requires the effective strain parameter, in the cured model, to be adjusted to account for the change in material properties.

Equating the two micro-cracking damage parameters for 1 and 29 days, as shown in equation (6.35), and substituting in the material properties gives equation (6.36).

$$\omega_1 = \omega_{29} \quad (6.35)$$

$$1 - \frac{\epsilon_{t1}}{\zeta_1} e^{-c_1 \left( \frac{\zeta_1 - \epsilon_{t1}}{\epsilon_{01} - \epsilon_{t1}} \right)} = 1 - \frac{\epsilon_{t29}}{\zeta_{29}} e^{-c_{29} \left( \frac{\zeta_{29} - \epsilon_{t29}}{\epsilon_{029} - \epsilon_{t29}} \right)} \quad (6.36)$$

Solving equation (6.36) for the only unknown,  $\zeta_{29}$ , gives the starting effective strain parameter for the aged material properties model. The effective strain parameter in each layer can be seen in Figure 6.13b.

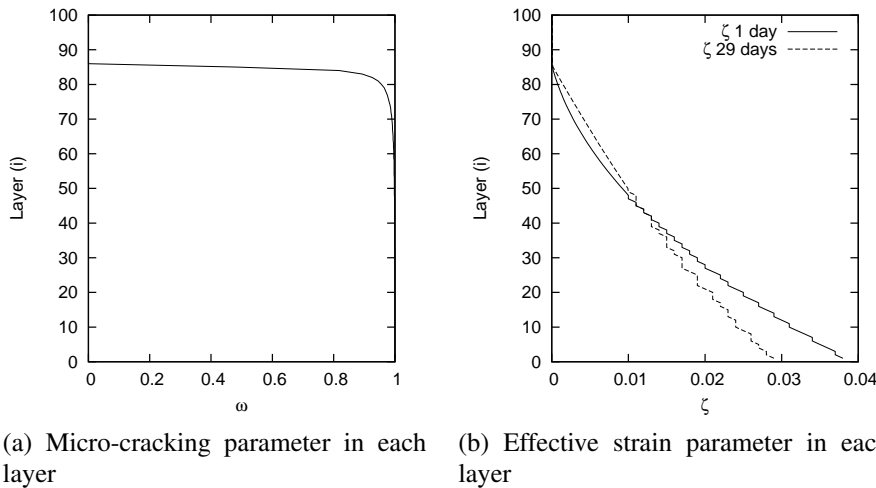


Figure 6.13: Micro-cracking parameter and effective strain parameter distribution through beam section

Figure 6.14 shows the effect of the ageing material properties on the strength increase in the uncracked ligament. Table 6.10 shows peak loads at the various positions as shown on Figure 6.14. The peak load with ageing material properties ( $P_{0(29day)}$ ) is approximately 35 % higher than the original ( $P_{0(1day)}$ ). However, the impact of this increase in peak load on the measurement of strength recovery is minimal. For this natural cracked sample the strength recovery ( $c_1$ ), using the model

results as calculated using equation (5.1), is 77% and using the updated peak load taking account of ageing material properties gives a strength recovery of 74%. This means that the ageing material properties and ongoing hydration in the uncracked beam do not contribute significantly to the increase in strength for this degree of damage, since there is very little residual strength in the beam when unloaded. The hydration that takes place within the crack remains the main factor for increasing the strength and therefore healing the beam. It should be noted that if the control sample at 29 days is taken as the reference load ( $P_{2(29day)}$ ), the strength recovery without aged material and with aged material properties is taken to be significant lower at 20 % and 18 % respectively.

This assessment was undertaken using the layered beam model and illustrated the process required to take account of ageing material properties. The same principles could be applied to the micro-mechanical model developed in Section 6.1.

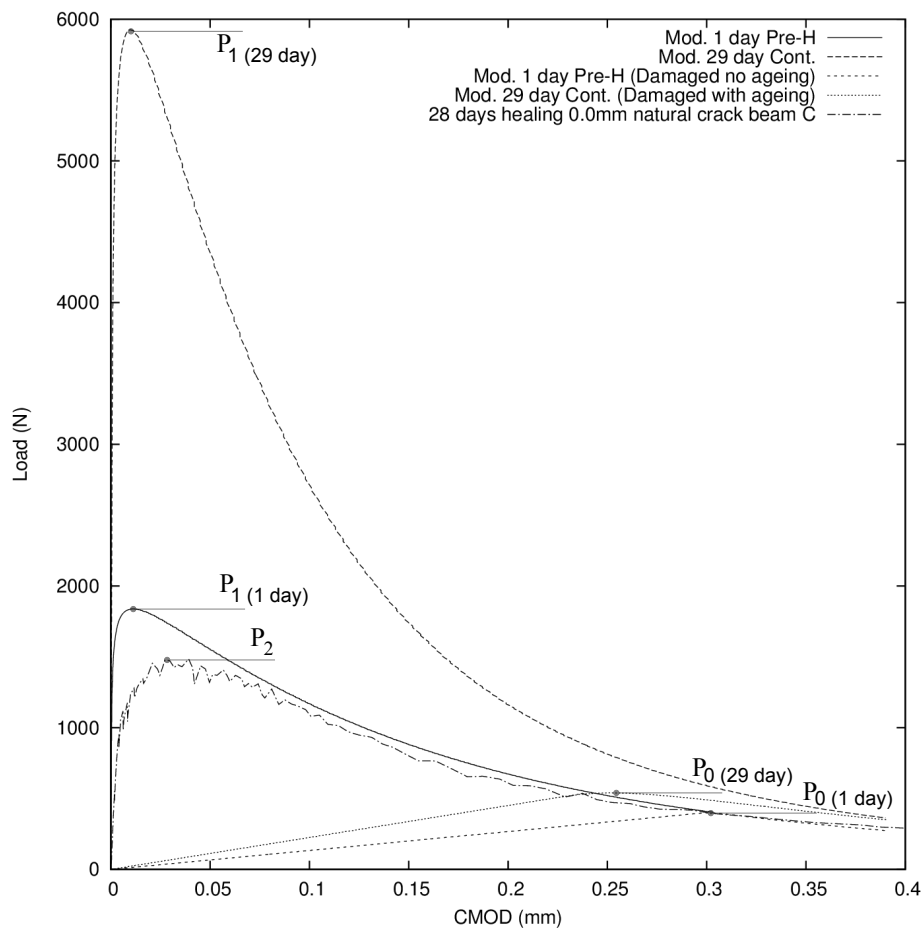


Figure 6.14: The effect of the ageing material properties on the strength increase in the uncracked ligament

Table 6.10: Load at various positions on Figure 6.14

Loading position	$P_{0(1day)}$	$P_{0(29days)}$	$P_{1(1day)}$	$P_{1(29day)}$	$P_2$
Load ( $N$ )	400	540	1838	5924	1503

## Conclusions

The volumetric self-healing model proved to be a useful tool in understanding the impact of the different damaging mechanisms after healing and could be used as a development tool in the future. Using a micromechanical model means that the model is mechanistic in nature and requires very few parameters, which can all be determined from macroscopic experiments. The modelling work showed that even though the micro-scale healing properties were difficult to obtain, as shown by Chapter 5, an inverse parameter identification exercise can be used to find these parameters. In essence, further development of this micromechanical model could provide guidance on which area and what parameters to focus on in future experiments.

The novel approach of applying the solidification principle to a healing model at the micromechanical scale allows a range of loading scenarios to be considered. This is the first time, to the authors knowledge, that this behaviour has been achieved for cementitious materials through micromechanical modelling.

The model is presented within the framework of a constitutive driver, allowing the healing effects to be captured under different loading conditions. Since only the uniaxial loading scenario was considered in this chapter, there is scope to examine in further detail the impact of other loading conditions on the mechanical strength gain of the healing mechanisms. The fact that this micromechanical model was able to be included in a macroscopic layered beam model shows that it can also be incorporated into a finite element model.

At the micromechanical model scale, future developments could allow for healing taking place simultaneously with micro-cracking. Furthermore, since only a single mechanical component of the healing model was considered here, there is potential to combine this with developing and ageing material properties, such as solidification and continued hydration of the matrix material. Chapters 3 and 4 showed that the approach used can be developed to include many aspects of real materials. Once this ageing process is included, other elements such as predicting when and how much healing material arrives in the micro-cracks could be considered. This work is the first and essential step towards achieving a full hygro-thermo-chemo-mechano micro-scale model capable of representing the characteristic response of a self-healing cementitious material.

# Chapter 7

## Conclusions and Future Work

In the introduction, the overall objectives and aims for the work in this thesis were set out. The completed work addresses the mechanical aspect of a thermo-hygro-chemo-mechanical model for self-healing cementitious materials. This chapter reviews the findings of the research work. The novel micromechanical model presented in Chapter 3 and 4 is summarized along with the experimental results from Chapter 5 and the micromechanical self-healing model from Chapter 6. There are several lines of research arising from this work which should be pursued. These suggestions are included in Section 7.2.

### 7.1 Conclusions

- A new micromechanical constitutive model was presented describing a two-phase composite material model with inelastic strains in the matrix. This allowed time-dependent behaviour to be considered. The inelastic strains are introduced in an Eshelby (1959) inclusion based micromechanical solution considering the compatibility equation and constrained strain. The non-dilute inclusions were homogenised using the Mori & Tanaka (1973) approach.
- Early age volumetric shrinkage strains in the matrix and mechanically applied loading both result in micro-cracking. These have been represented by volumetric and directional (anisotropic) micro-cracking components in the constitutive equation. Volumetric cracking is represented using a scalar damage variable and directional cracking is added using the approach of Budiansky & O'Connell (1976). This separation, between the isotropic and directional micro-cracking components, is clearly shown using stress and strain path loadings. The two micro-cracking components work seamlessly together, as shown by the reasonable response of the model when representing a shear softening response.

- The addition of the exterior point Eshelby theory, containing matrix inelastic strains, enabled the use of realistic experimentally derived micro-cracking parameters. The amplification of stresses at the matrix/inclusion interface drives the crack initiation criterion and evolution parameters. This was particularly evident in the simulation of a two-phase composite undergoing free shrinkage.
- The micromechanical model, in particular the homogenised scheme adopted, was successfully validated using a 3D FE discretization of the composite. The Eshelby based solution meant that micro-scale constitutive relationship is simulated in a computationally convenient manner. The elastic solution, for example, is computed in a fraction of a second compared to 30 minutes for an idealised meso-scale concrete FE analysis. Furthermore, the constitutive driver algorithm, being driven by total stress, total strain or shrinkage potential of the matrix, means that the constitutive relationship is suitable for further development as a FE constitutive model.
- The performance of the model is demonstrated by simulating the autogenous drying behaviour of concrete. The combination of volumetric solidification, hydration modelling and shrinkage in the matrix allowed quantification of the micro-cracking effects during drying. The importance of including micro-cracking can be seen when the solution results are compared with experimental data. This work could form the basis of a cementitious material design tool. The overall effect of shrinkage on a cementitious composite can be described by knowing the cement paste shrinkage with time, aggregate volume fraction and material properties of the components.
- Even though the application has focused on shrinkage and ageing in cementitious materials the model can be applied to other non-specific inelastic strains in the matrix and other materials which contain inelastic strains in the matrix.
- Healing in cementitious materials is traditionally measured from cracks on the outer surface of a specimen or by measuring crack permeability. These are associated with improving environmental conditions or durability of concrete. Mechanical strength recovery is readily measured from the flexural strength using a three point bending test at the macro-scale. However, the scale at which the healing takes place is at the micro-scale. Investigations were carried out to identify techniques for measuring strength of healed materials at the micro-scale. The most suitable technique appeared to be hardness testing. However, the hardness tests performed did not provide valuable information

for quantifying autogenous healing in cementitious materials. The high degree of variation meant that results cannot be relied upon.

- Experiments carried out on concrete and mortar samples showed that autogenous healing does readily occur under laboratory conditions. The evidence gathered through qualitative observations and quantitative mechanical strength results provided an insight into the development of autogenous healing material over time. Autogenous healing was examined for early age concrete and mortar with different crack widths where the first loading stage occurred 24 hours after casting. The healing mechanism was seen to be continued hydration, as evidenced by visual inspection, SEM and XRD results. It was found that the smaller the crack width the greater the strength recovery. Furthermore, increased healing time led to increased strength recovery. A natural crack, closed after loading and cured fully in water showed the greatest degree of autogenous self-healing and mechanical strength recovery.
- The strength recovery percentage shown by the natural cracks, in particular the closed crack, provides confidence significant healing can be achieved and could form part of a system for managing the strength and durability of structures post-damage. It should be noted that the large CMOD reached in unreinforced beams meant that the majority of the material strength had been lost. Nevertheless, mechanical recovery for a concrete beam with a natural crack healed in water over 28 days was approximately 70 % of the original peak load. It is noted that this mechanical recover is approximately 20 % of the actual control peak load when tested at 29 days.
- A novel self-healing micromechanical model for cementitious materials has been developed focusing on mechanical strength regain. The model is based on the basic two-phase composite model described in Chapter 3 of this thesis and uses the findings from the autogenous healing experimental results for validation.
- Healing is incorporated into the equivalent local stress equation of the (micro) crack-plane relationship. This stress equation has contributions from the uncracked original material and from the proportion of micro-cracks that have healed. A solidification strain ensures that the stress of the overall material does not change at the instant of healing and a further micro-cracking parameter is included to allow the healed material to also micro-crack.
- The amount of healing and strength of this new material can be specified and controlled. Different micro-cracking criteria and evolution functions are used

for the original and healed material. This means that the model is highly configurable.

- A simplified version of the self-healing model, that only considers volumetric behaviour, proved to be a useful tool in understanding the impact of the different damaging mechanisms after healing. The mechanistic nature of the micromechanical model meant that it required very few material parameters, all of which can be determined from macro-scale experiments. This is accomplished using an inverse parameter identification exercise using experimental load CMOD data.
- The novel approach of applying the solidification principle to a healing model and having a constitutive driver numerical implementation means that a range of loading scenarios can be considered. For example, considering the impact of healing when a beam remains under stress due to applied load.
- The constitutive self-healing micromechanical model was also incorporated into a macroscopic layered beam model. This layered beam model allowed straight forward comparison with experimental results. These comparisons were favourable and showed that the healing model is applicable to a range of cementitious materials.
- A layered beam model was used to investigate the impact of ageing material properties and found that increasing the material strength of the uncracked ligament had a limited effect on the overall strength recovery.
- This work is the first and essential step towards achieving a full thermo-hygro-chemo-mechanical micro-scale model capable of representing the characteristic response of a self-healing cementitious material. The concept used in this work of adding components to a basic formulation leads to the creation of a comprehensive micromechanical model for cementitious materials.

## **7.2 Recommendations for future work**

This research has made a contribution towards understanding the autogenous healing that occurs in concrete structures. This alternative approach of using self-healing to manage the deterioration of structures, will require an extensive and comprehensive research programme, before being fully incorporated into the design process. This study has raised a number of interesting questions, in both the modelling and experimental work, that if developed further would increase the understanding of autogenous healing in cementitious materials.

There are many possible developments for a future micromechanical model. Firstly, the performance of the current model could be further examined by considering how the mechanical strength gain changes with other loading conditions and healing mechanism. To simulate loading scenarios, other than uniaxial loading, further targeted experiments would be required. Autonomic healing experiments could also be simulated using the healing micromechanical model. There is potential to combine this current healing model with developing and ageing material properties, similar to the work in Chapter 4, examining the impact of healing with time. However, this model would still only be able to solve an instantaneous healing problem. A major development in the capability of the micromechanical model would be one where the healing could take place as the micro-cracks develop. Therefore, resulting in continual damage and concurrent healing which would be particularly relevant to predicting early age concrete response.

Only single mechanical components were considered in this research for both inelastic strains and the healing model. Other components, such as plastic deformation, rough crack contact recovery and creep could be added, resulting in a numerical model which has a range of compatible mechanical components which can be chosen as required. Once a micromechanical model has the required components, the goal would be to implement the code in a commercial FE structural analysis package to allow wide dissemination and use in industry. Another important aspect to consider when modelling healing, is predicting when and how much healing material arrives in the micro-cracks. This would require combining the mechanical model with a thermo-hygro-chemical model.

This micromechanical model could provide guidance on which aspect and what parameters to focus on in future experiments. For example, the micromechanical healing model was most sensitive to the healing efficiency parameter ( $h$ ) and extensive inverse parameter identification could be carried out to find a measurement of healing that can be related directly to the healing efficiency.

In order to make use of autogenous healing in design, there is a need to fully understand the processes at a laboratory scale. This research has shown that there are limited comparable experimental studies on mechanical strength recovery of autogenous healing. This is, in part, due to there not being a standard test for measuring mechanical healing and due to the wide range of variables to be considered when working with cementitious materials. Future experiments, in combination with a micromechanical model, could find out how these variables impact on the healing. The limited number of experiments carried out during this investigative experimental work are not sufficient to be able to predict statistical relationships. Further experimental work should ensure that there are sufficient numbers of experiments to give trends and provide confidence limits for healing with different degrees of

damage.

Future experiments could revisit the indentation techniques used here, but this would only be worthwhile if the micro-indenter apparatus was capable of recording a dynamic response. A relationship between the mechanical strength recovery of autogenous healing and permeability could be examined, but again this would require a suitably designed experiment. In a real structure the serviceability loading, often responsible for causing cracking, is likely to remain in place during any healing process. Experiments, which can provide results for healing under-load conditions, would be useful to validate the proposed model.

The author would like to mention that the self-healing modelling work in this thesis will be developed and extended as part of a research grant called 'Materials for Life (M4L): Biomimetic multi-scale damage immunity for construction materials' from EPSRC with reference EP/K026631/1. The M4L project, a consortium between Cardiff University, University of Cambridge and University of Bath will develop a multi-scale system using a range of interdisciplinary technologies to promote and enable self-healing in construction materials. Inspired by nature, the project will address a range of damage scenarios at a range of spatial and temporal scales over the whole life cycle. The self-healing micromechanical model will play a key role in this project.

# Appendix A

## Direct Tensor Notation

Table A.1 shows the direct tensor font notation and Table A.2 shows the direct tensor operation notation. These are used throughout this thesis unless otherwise stated.

Table A.1: Direct tensor notation font

Notation	Physical quantity	Font description
$s$	= scalar or zero order tensor	(light face italic small)
$\mathbf{v}$	= vector or first order tensor	(boldface roman small)
$\boldsymbol{\sigma}$	= second order tensor	(boldface greek)
$\mathbf{T}$	= third order tensor	(boldface italic capital)
$\mathbf{F}$	= fourth-order tensor	(boldface san serif capital)

Table A.2: Tensor operation notation

Direct tensor notation	Summation convention
$a = \mathbf{b} \cdot \mathbf{c}$	$a = b_i c_i$
$\boldsymbol{\alpha} = \mathbf{b} \otimes \mathbf{c}$	$\alpha_{ij} = b_i c_j$
$\boldsymbol{\alpha} = \boldsymbol{\beta} \cdot \boldsymbol{\gamma}$	$\alpha_{ik} = \beta_{ij} \gamma_{jk}$
$a = \boldsymbol{\beta} : \boldsymbol{\gamma}$	$a_i = \beta_{ij} \gamma_{ij}$
$\mathbf{A} = \boldsymbol{\beta} \otimes \boldsymbol{\gamma}$	$A_{ijkl} = \beta_{ij} \gamma_{kl}$
$\boldsymbol{\alpha} = \mathbf{B} : \boldsymbol{\gamma}$	$\alpha_{ij} = B_{ijkl} \gamma_{kl}$
$\mathbf{A} = \mathbf{B} \cdot \mathbf{C}$	$A_{ijmn} = B_{ijkl} C_{klmn}$

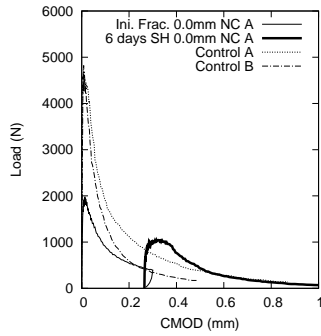
$\otimes$  is referred to as the dyadic product,  $\cdot$  is called the dot product and  $:$  is termed the tensor contraction. Tensor operations follow notation used by Voyiadjis & Kattan (2006) and Nemat-Nasser & Hori (1999). The summation convention is based on Einstein's summation of repeated indices.



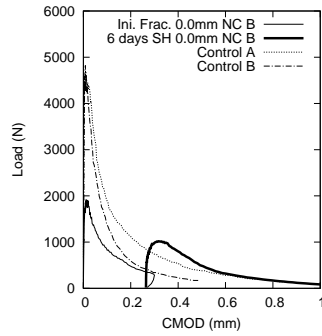
# Appendix B

## Experimental results

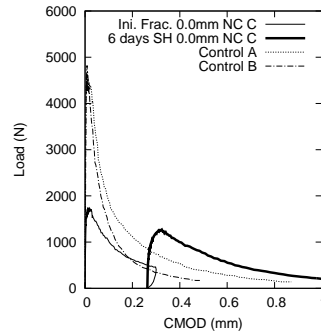
- Figure B.1: Autogenous healing 0.0 mm natural crack Set 1 Load-CMOD
- Figure B.2: Autogenous healing 0.18 mm natural crack Set 2 Load-CMOD
- Figure B.3: Autogenous healing 0.30 mm natural crack Set 3 Load-CMOD
- Figure B.4: Autogenous healing 0.1 mm narrow notch Set 4 Load-CMOD
- Figure B.5: Autogenous healing 0.2 mm narrow notch Set 5 Load-CMOD
- Figure B.6: Autogenous healing 0.3 mm narrow notch Set 6 Load-CMOD
- Figure B.7: Load-CMOD for 13 days self-healing narrow notch Set 7 and 8
- Figure B.8: Load-CMOD for 27 days self-healing narrow notch Set 7 and 8
- Figure B.9: Load-CMOD for 41 days self-healing narrow notch Set 7 and 8
- Figure B.10: Load-CMOD for 55 days self-healing narrow notch Set 7 and 8
- Figure B.11: SEM Images Set 7
- Figure B.12: Time lapse Set 7
- Table B.1: Anchor Scan Parameters: X'Pert Highscore PANalytical software



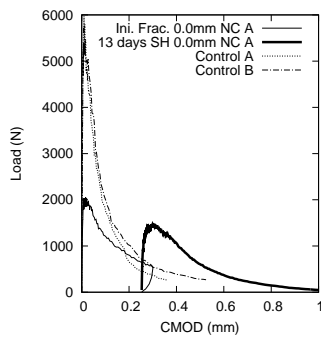
(a) 6 days SH beam A



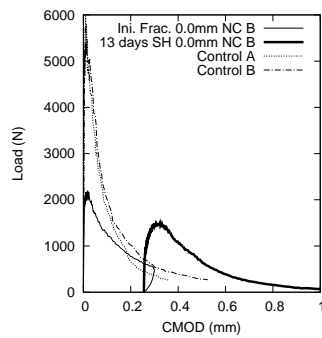
(b) 6 days SH beam B



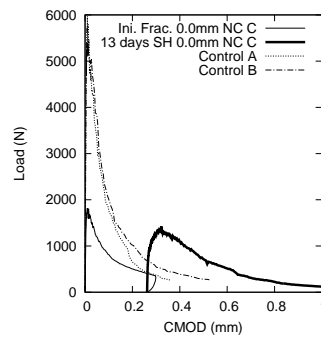
(c) 6 days SH beam C



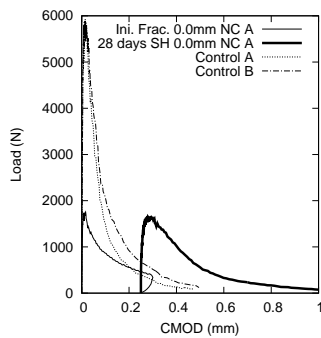
(d) 13 days SH beam A



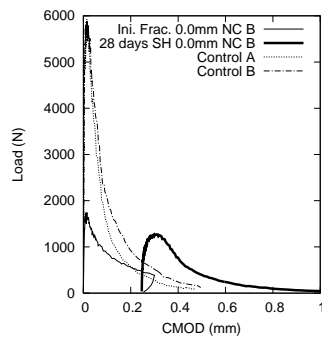
(e) 13 days SH beam B



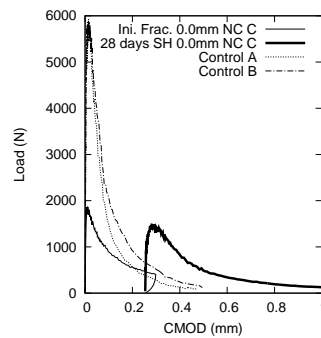
(f) 13 days SH beam C



(g) 28 days SH beam A



(h) 28 days SH beam B



(i) 28 days SH beam C

Figure B.1: Autogenous healing 0.0 mm natural crack (NC) Set 1 Load-CMOD

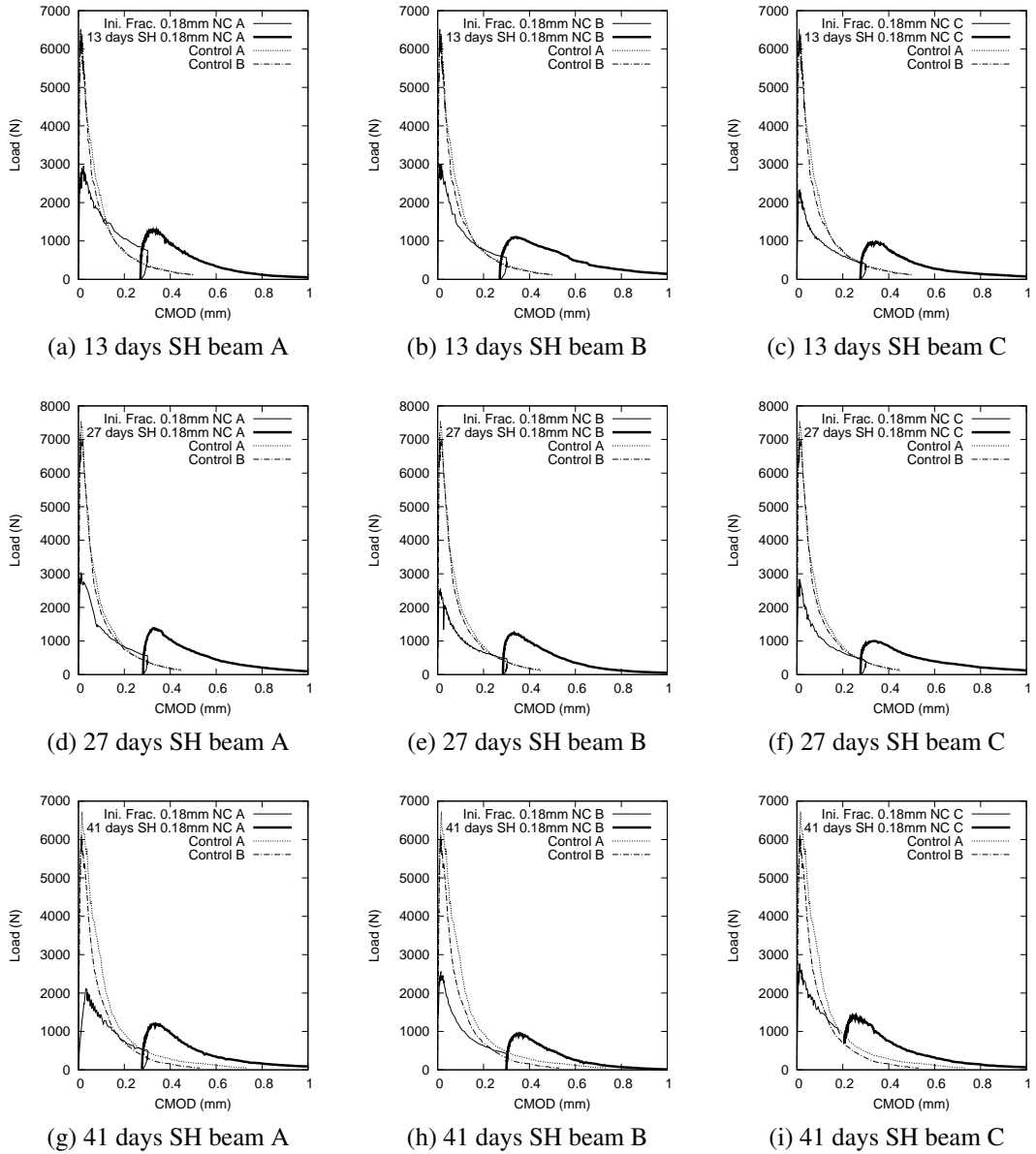


Figure B.2: Autogenous healing 0.18 mm natural crack (NC) Set 2 Load-CMOD

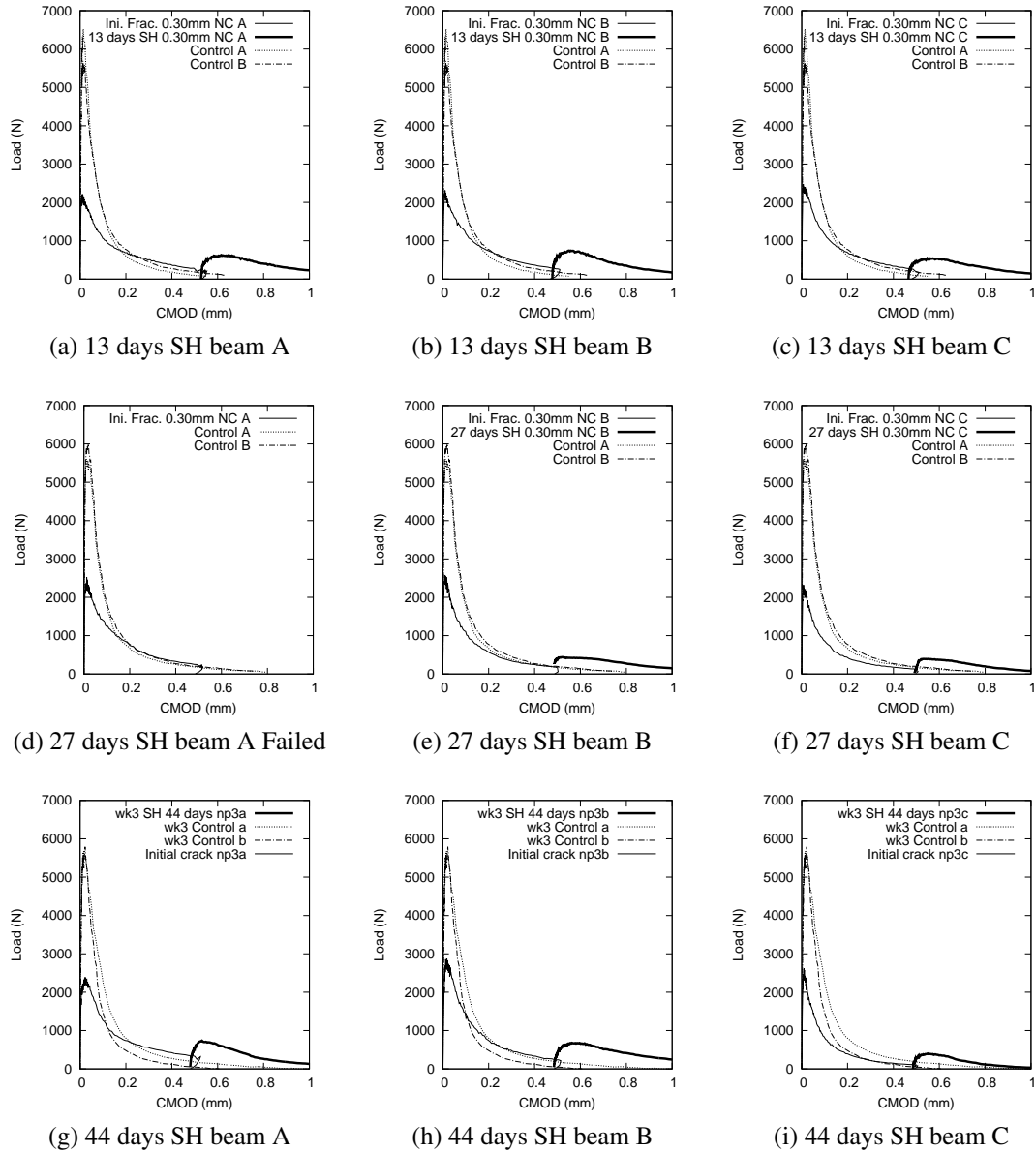
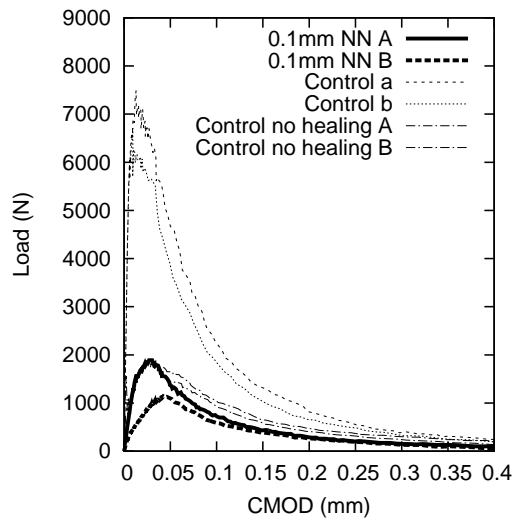
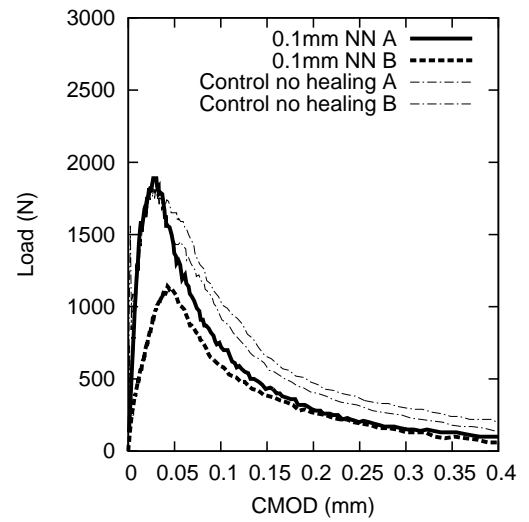


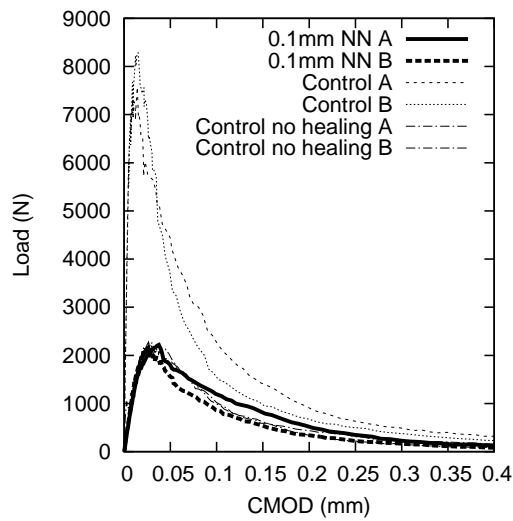
Figure B.3: Autogenous healing 0.30 mm natural crack (NC) Set 3 Load-CMOD



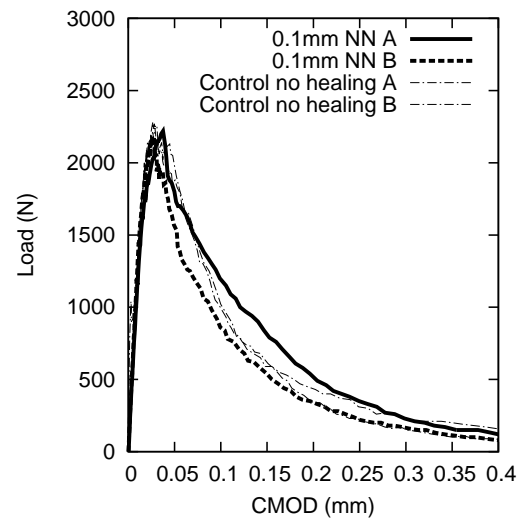
(a) 13 days SH



(b) 13 days SH magnified

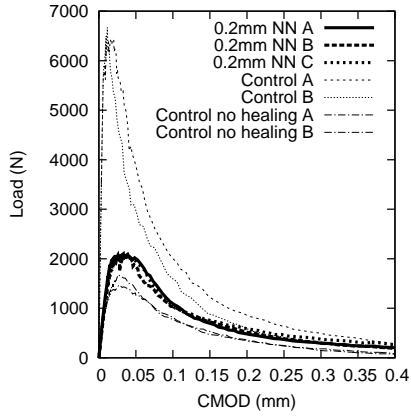


(c) 27 days SH

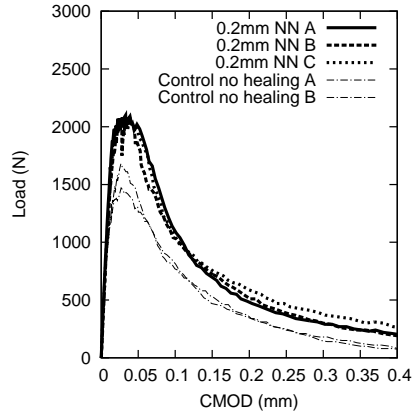


(d) 27 days SH magnified

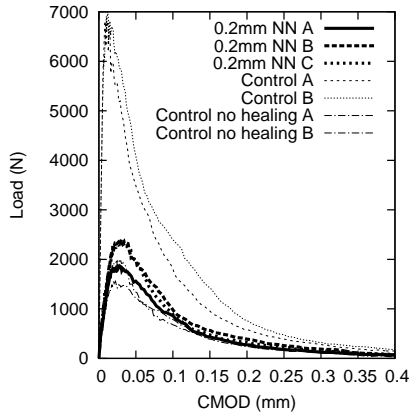
Figure B.4: Autogenous healing 0.1 mm narrow notch (NN) Set 4 Load-CMOD



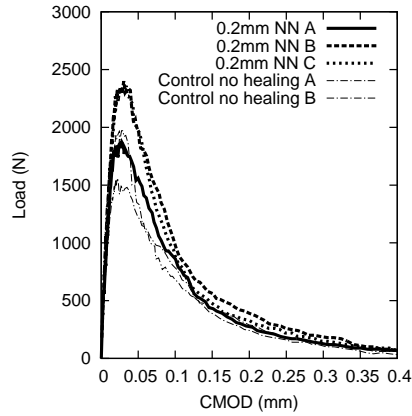
(a) 13 days SH



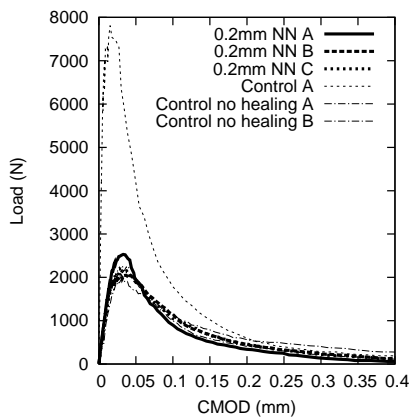
(b) 13 days SH magnified



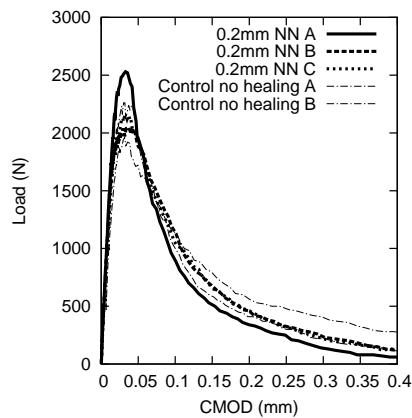
(c) 27 days SH



(d) 27 days SH magnified

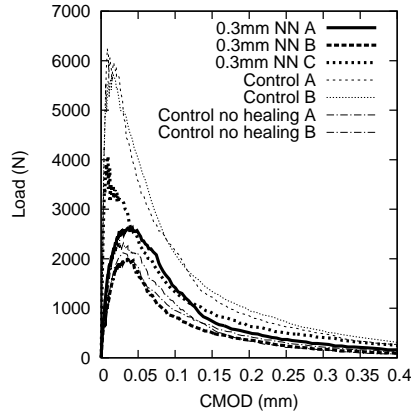


(e) 35 days SH

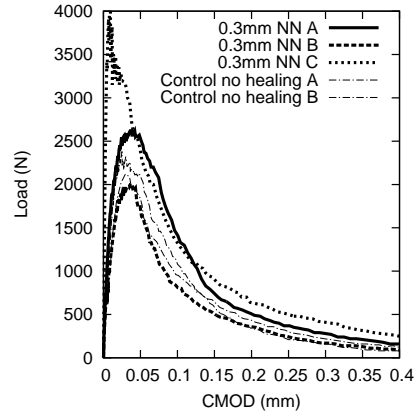


(f) 35 days SH magnified

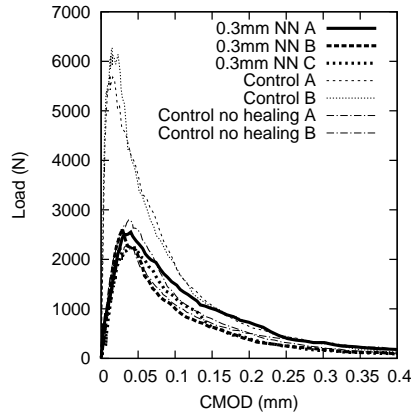
Figure B.5: Autogenous healing 0.2 mm narrow notch (NN) Set 5 Load-CMOD



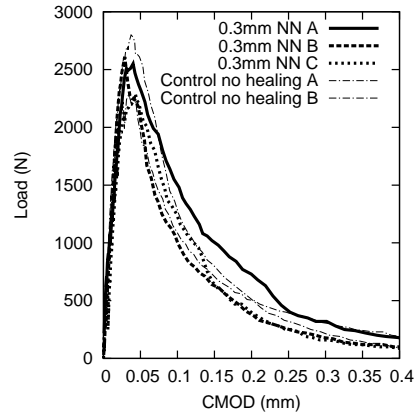
(a) 13 days SH



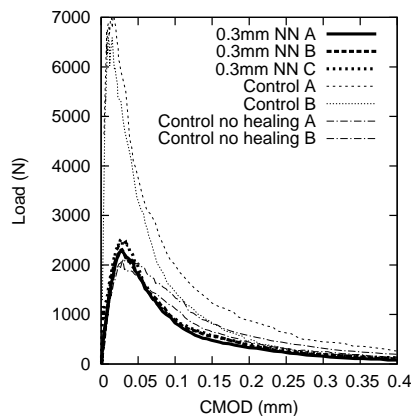
(b) 13 days SH magnified



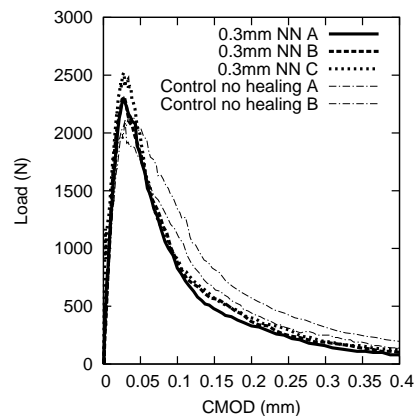
(c) 27 days SH



(d) 27 days SH magnified

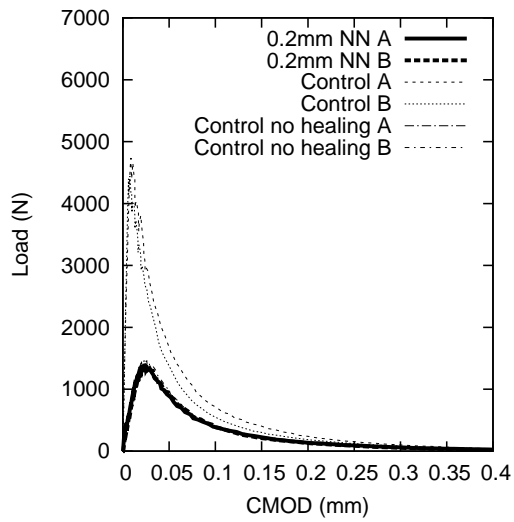


(e) 41 days SH

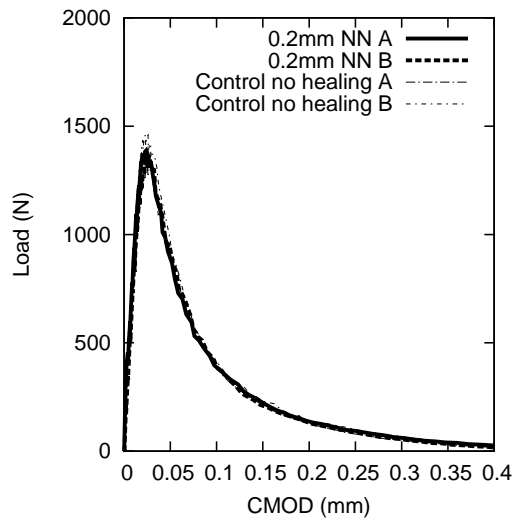


(f) 41 days SH magnified

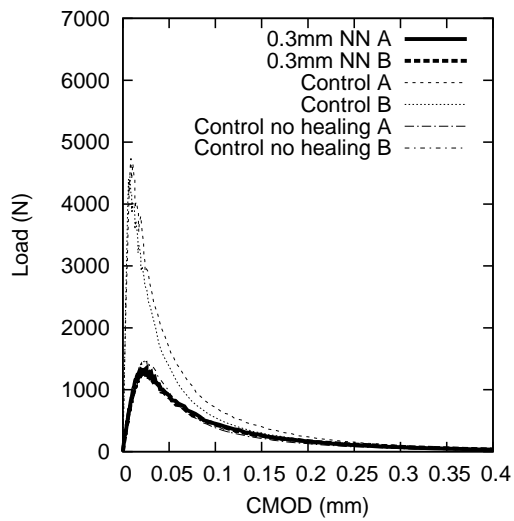
Figure B.6: Autogenous healing 0.3 mm narrow notch (NN) Set 6 Load-CMOD



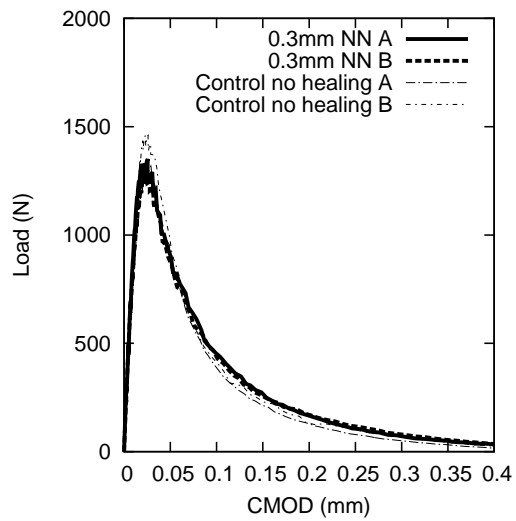
(a) 13 days SH 0.2 mm



(b) 13 days SH 0.2 mm magnified

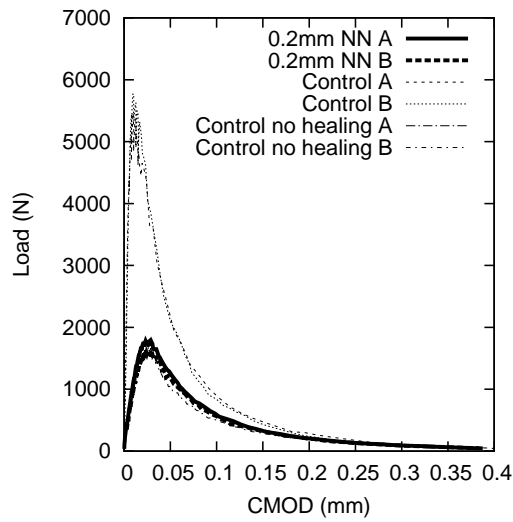


(c) 13 days SH 0.3 mm

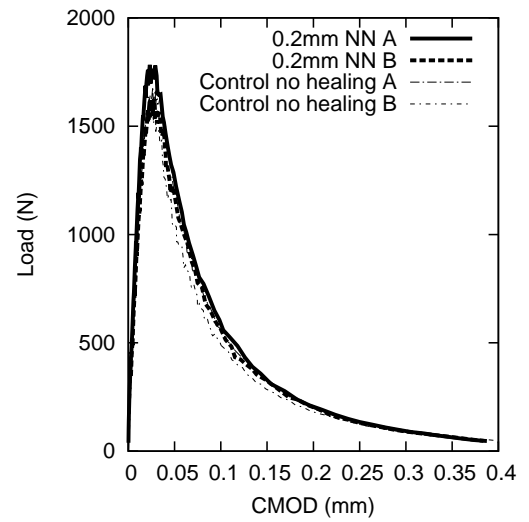


(d) 13 days SH 0.3 mm magnified

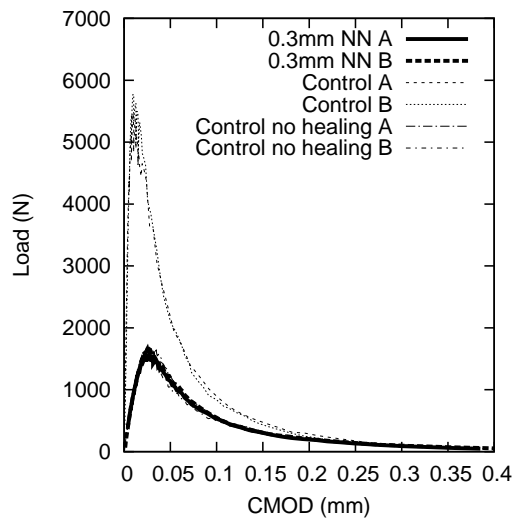
Figure B.7: Load-CMOD for 13 days self-healing narrow notch (NN) Set 7 and 8



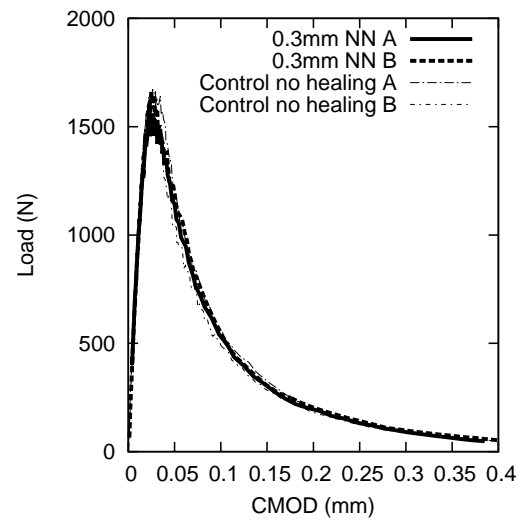
(a) 27 days SH 0.2 mm



(b) 27 days SH 0.2 mm magnified

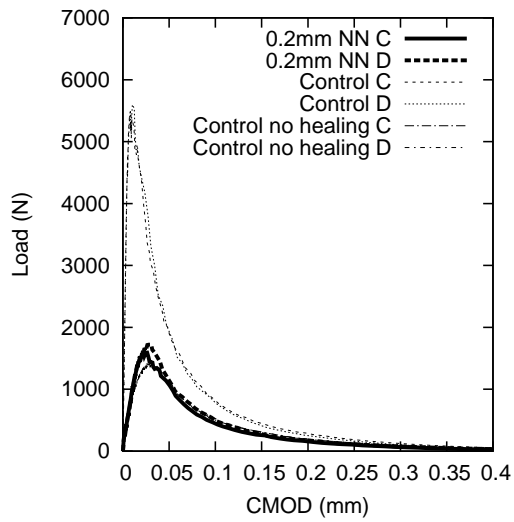


(c) 27 days SH 0.3 mm

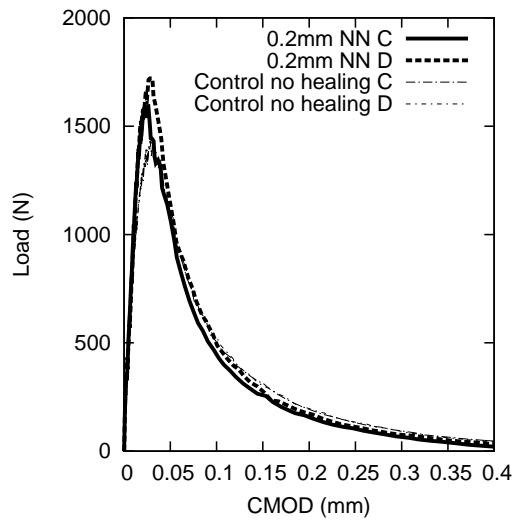


(d) 27 days SH 0.3 mm magnified

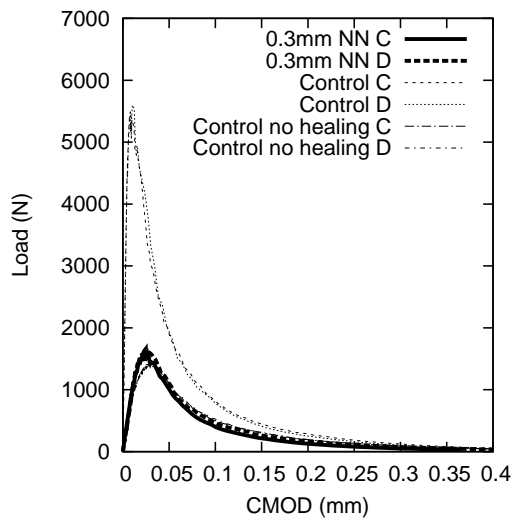
Figure B.8: Load-CMOD for 27 days self-healing narrow notch (NN) Set 7 and 8



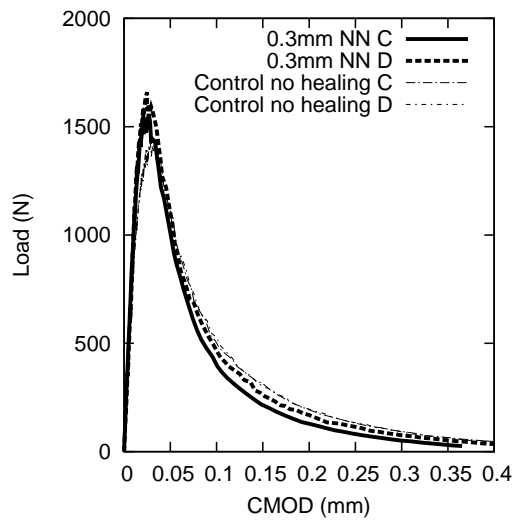
(a) 41 days SH 0.2 mm



(b) 41 days SH 0.2 mm magnified

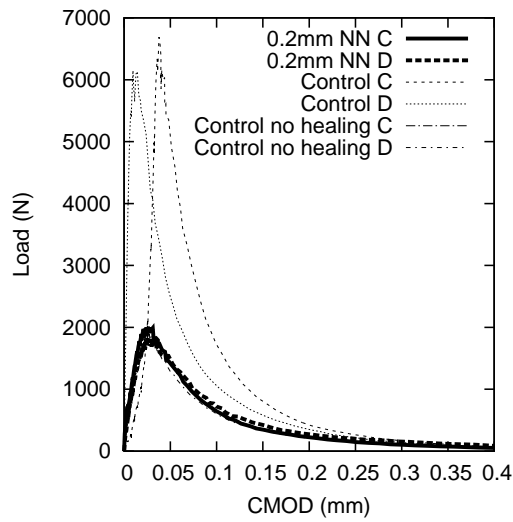


(c) 41 days SH 0.3 mm

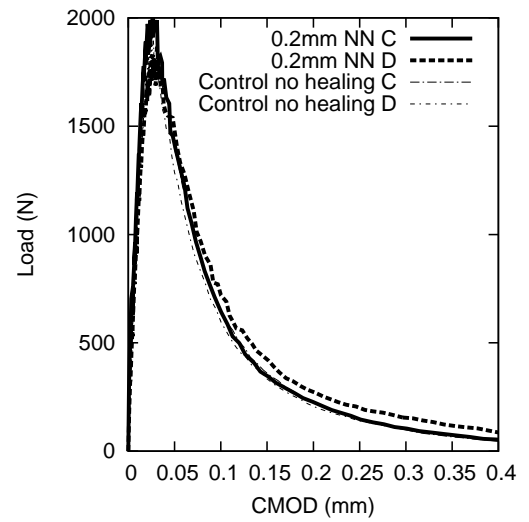


(d) 41 days SH 0.3 mm magnified

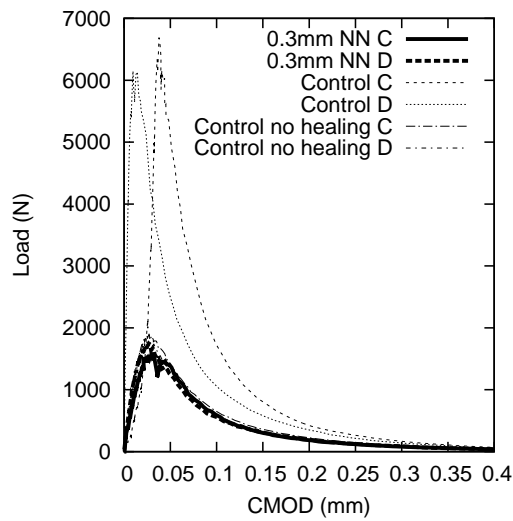
Figure B.9: Load-CMOD for 41 days self-healing narrow notch (NN) Set 7 and 8



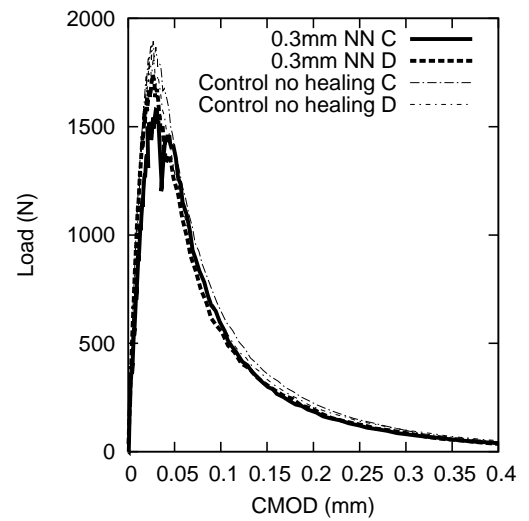
(a) 55 days SH 0.2 mm



(b) 55 days SH 0.2 mm magnified

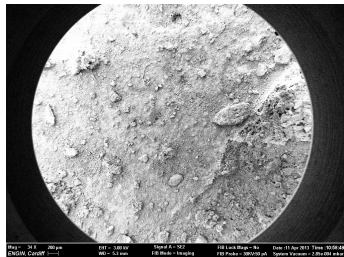


(c) 55 days SH 0.3 mm

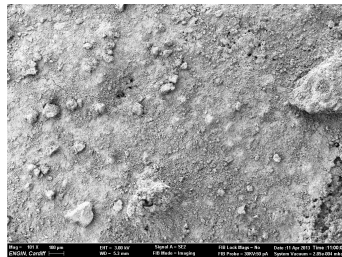


(d) 55 days SH 0.3 mm magnified

Figure B.10: Load-CMOD for 55 days self-healing narrow notch (NN) Set 7 and 8



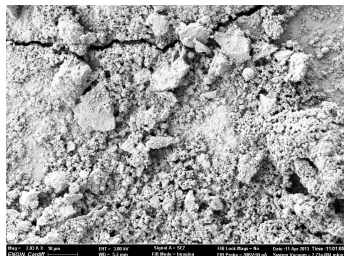
(a) Flat surface 34x mag



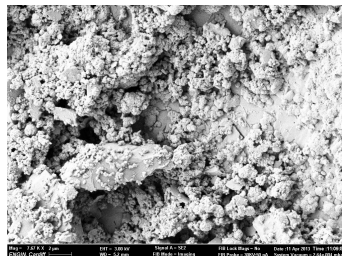
(b) Flat surface 101x mag



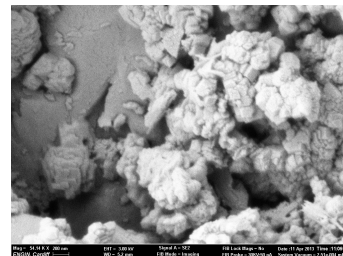
(c) Flat surface 312x mag



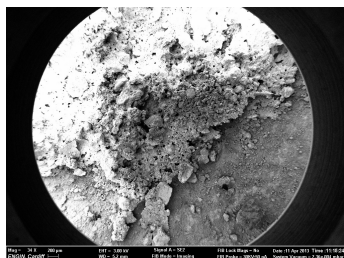
(d) Flat surface 2.03Kx mag



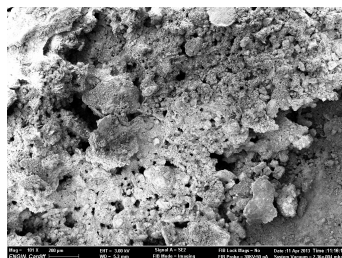
(e) Flat surface 7.67Kx mag



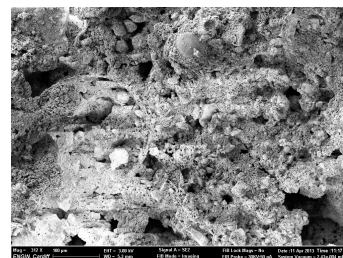
(f) Flat surface 54.14Kx mag



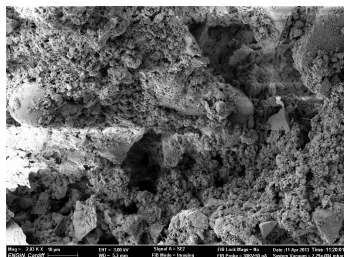
(g) SH surface 34x mag



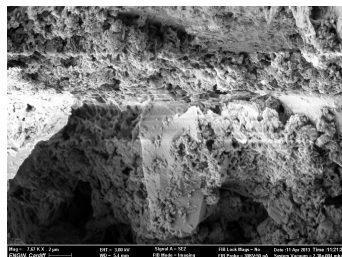
(h) SH surface 101x mag



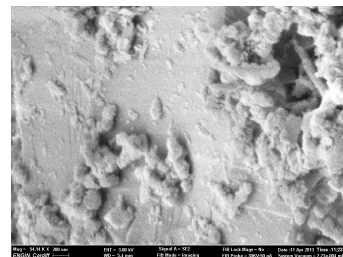
(i) SH surface 312x mag



(j) SH surface 2.03Kx mag

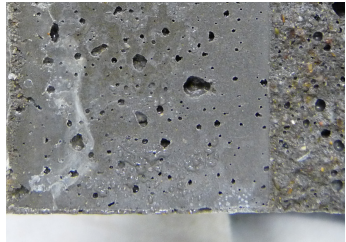


(k) SH surface 7.67Kx mag



(l) SH surface 54.14Kx mag

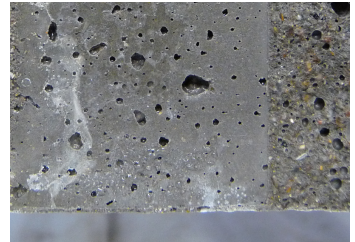
Figure B.11: SEM Images Set 7



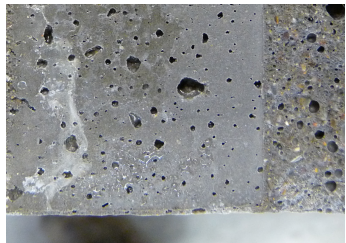
(a) 0 min



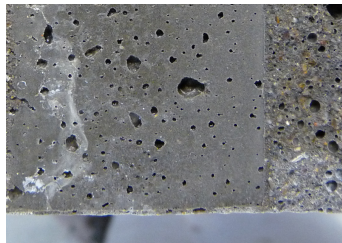
(b) 1 min



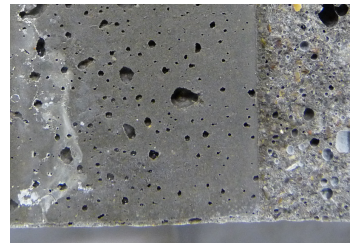
(c) 3 min



(d) 6 min



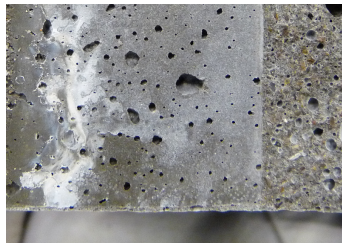
(e) 10 min



(f) 15 min



(g) 20 min



(h) 30 min



(i) 40 min



(j) 50 min



(k) 60 min



(l) 150 min

Figure B.12: Time lapse Set 7

Table B.1: Anchor Scan Parameters: X'Pert Highscore PANalytical software

Dataset Name	concrete sample
File name	concretesample.RD
Sample Identification	concrete sample
Comment	X'Pert Industry
Measurement Date/Time	20/06/2013 15:38:00
Raw Data Origin	PHILIPS-binary (scan) (.RD)
Scan Axis	Gonio
Start Position [ $^{\circ}2\theta$ ]	5.0000
End Position [ $^{\circ}2\theta$ ]	80.0000
Step Size [ $^{\circ}2\theta$ ]	0.0200
Scan Step Time [s]	0.5000
Scan Type	Pre-set time
Offset [ $^{\circ}2\theta$ ]	0.0000
Divergence Slit Type	Fixed
Divergence Slit Size [ $^{\circ}$ ]	1.0000
Specimen Length [mm]	10.00
Receiving Slit Size [mm]	0.0500
Measurement Temperature [ $^{\circ}\text{C}$ ]	0.00
Anode Material	Cu
K-Alpha1 [ $\text{\AA}$ ]	1.54060
K-Alpha2 [ $\text{\AA}$ ]	1.54443
K-Beta [ $\text{\AA}$ ]	1.39225
K-A2/K-A1 Ratio	0.50000
Generator Settings	0 mA, 0 kV
Diffractionmeter Type	PW1710
Diffractionmeter Number	1
Goniometer Radius [mm]	173.00
Dist. Focus-Diverg. Slit [mm]	91.00
Incident Beam Monochromator	No
Spinning	No

# References

- Abrams, D. (1925), 'Autogeneous healing of concrete', *Concrete* **27**(2), 50.
- Abu Al-Rub, R. K. & Darabi, M. K. (2012), 'A thermodynamic framework for constitutive modeling of time- and rate-dependent materials. part i: Theory', *International Journal of Plasticity* **34**, 61–92.
- Abu Al-Rub, R. K., Darabi, M. K., Little, D. N. & Masad, E. A. (2010), 'A micro-damage healing model that improves prediction of fatigue life in asphalt mixes', *International Journal of Engineering Science* **48**(11), 966–990.
- Ahn, T. & Kishi, T. (2010), 'Crack self-healing behavior of cementitious composites incorporating various mineral admixtures', *Journal of Advanced Concrete Technology* **8**(2), 171–186.
- Alfredsson, K. S. & Stigh, U. (2004), 'Continuum damage mechanics revised: A principle for mechanical and thermal equivalence', *International Journal of Solids and Structures* **41**(15), 4025–4045.
- Bažant, Z. & Oh, B. (1985), 'Microplane model for progressive fracture of concrete and rock', *Journal of Engineering Mechanics* **111**(4), 559–582.
- Bažant, Z. P. (1995), 'Creep and shrinkage prediction model for analysis and design of concrete structures-model b3', *Materials and Structures* **28**, 357–365.
- Bažant, Z. P. (2001), 'Prediction of concrete creep and shrinkage: past, present and future', *Nuclear Engineering and Design* **203**(1), 27–38.
- Bažant, Z. P., Hauggaard, A. B., Baweja, S. & Ulm, F. (1997), 'Microprestress-Solidification theory for concrete creep. i: Aging and drying effects', *Journal of Engineering Mechanics* **123**(11), 1188–1194.
- Bažant, Z. P. & Prasannan, S. (1989), 'Solidification theory for concrete creep: I. formulation', *Journal of Engineering Mechanics* **115**(8), 1691–1703.
- Bažant, Z. P. & Xi, Y. (1994), 'Drying creep of concrete: constitutive model and new experiments separating its mechanisms', *Materials and Structures* **27**(1), 3–14.
- Barbero, E. J., Elgileerirgl, L., Greco, F., Lon'etti, P. & J, E. (2005), 'Continuum damage-healing.Mechanics with application to.Self-healing composites', *International Journal of Damage Mechanics* **14**, 51–81.

- Barbero, E. J. & Luciano, R. (1995), ‘Micromechanical formulas for the relaxation tensor of linear viscoelastic composites with transversely isotropic fibers’, *International Journal of Solids and Structures* **32**(13), 1859–1872.
- Baroghel-Bouny, V. (1994), Characterization of Cement Pastes and Concretes - Methods, Analysis, Interpretations., PhD thesis, Laboratoire Central des Ponts et Chaussées, Paris.
- Baroghel-Bouny, V., Thiéry, M. & Wang, X. (2011), ‘Modelling of isothermal coupled moisture–ion transport in cementitious materials’, *Cement and Concrete Research* **41**(8), 828–841.
- Bazant, Z. & Pijaudier-Cabot, G. (1989), ‘Measurement of characteristic length of nonlocal continuum’, **115**(4), 755–767.
- Beltzung, F. & Wittmann, F. H. (2005), ‘Role of disjoining pressure in cement based materials’, *Cement and Concrete Research* **35**(12), 2364–2370.
- Benboudjema, F., Meftah, F., Sellier, A., Torrenti, J. M. & Heinfling, G. (2001), ‘On the prediction of delayed strains for concrete subjected to drying and loading simultaneously’, *Proc. (CONCREEP) Creep, shrinkage and durability mechanics of concrete and other quasi-brittle materials* **6**, 245–250.
- Benboudjema, F., Meftah, F. & Torrenti, J. M. (2005), ‘Interaction between drying, shrinkage, creep and cracking phenomena in concrete’, *Engineering structures* **27**(2), 239–250.
- Benveniste, Y. (1987), ‘A new approach to the application of Mori-Tanaka’s theory in composite materials’, *Mechanics of Materials* **6**(2), 147–157.
- Bernard, O., Ulm, F. J. & Lemarchand, E. (2003), ‘A multiscale micromechanics-hydration model for the early-age elastic properties of cement-based materials’, *Cement and Concrete Research* **33**(9), 1293–1309.
- Blees, M. H., Winkelman, G. B., Balkenende, A. R. & Den Toonder, J. M. J. (2000), ‘The effect of friction on scratch adhesion testing: application to a sol–gel coating on polypropylene’, *Thin Solid Films* **359**(1), 1–13.
- Boh, B. & Sumiga, B. (2008), ‘Microencapsulation technology and its applications in building construction materials’, *RMZ–Materials and Geoenvironment* **55**(3), 329–344.
- Bohm, H. J. (1998), ‘A short introduction to basic aspects of continuum micromechanics’, *CDL-FMD Report* **3**.
- Brandeis, F. (1937), ‘Autogenous healing of concrete’, *Beton und Eisen* **36**, 12.
- Brenchich, A. & Gambarotta, L. (2001), ‘Isotropic damage model with different tensile-compressive response for brittle materials’, *International Journal of Solids and Structures* **38**(34), 5865–5892.
- Brinson, L. C. & Lin, W. S. (1998), ‘Comparison of micromechanics methods for effective properties of multiphase viscoelastic composites’, *Composite Structures* **41**(3-4), 353–367.

- Brokenshire, D. R. (1995), A study of torsion fracture tests, PhD thesis, UWCC.
- BS EN 12390-3 (2009), *BS EN 12390-3:2009 - Testing hardened concrete - Compressive strength of test specimens*, BSi, Brussels.
- BS EN 12390-5 (2009), *BS EN 12390-5:2009 - Testing hardened concrete - Flexural strength of test specimens*, BSi, Brussels.
- BS EN 12504-2 (2012), *BS EN 12504-2:2012 - Testing concrete in structures Non-destructive testing. Determination of rebound number*, BSi, Brussels.
- BS EN 197-1 (2011), *Cement - Part 1: Composition, specifications and conformity criteria for common cements*, BSi, Brussels.
- BS EN 843-4 (2005), *BS EN 843-4:2005 - Advanced technical ceramics. Mechanical properties of monolithic ceramics at room temperature. Vickers, Knoop and Rockwell superficial hardness – BSI British Standards*, BSi, Brussels.
- Budiansky, B. & O’Connell, R. (1976), ‘Elastic-moduli of a cracked solid’, *International Journal of Solids and Structures* **12**(2), 81–97.
- Caner, F. & Bažant, Z. (2013), ‘Microplane model m7 for plain concrete. i: Formulation’, *Journal of Engineering Mechanics* **139**(12), 1714–1723.
- Carol, I., Rizzi, E. & Willam, K. (2001), ‘On the formulation of anisotropic elastic degradation. i. theory based on a pseudo-logarithmic damage tensor rate’, *International Journal of Solids and Structures* **38**(4), 491–518.
- Castaneda, P. (1996), ‘Exact second-order estimates for the effective mechanical properties of nonlinear composite materials’, *Journal of the Mechanics and Physics of Solids* **44**(6), 827–862.
- Castaneda, P. & Willis, J. (1995), ‘The effect of spatial distribution on the effective behavior of composite materials and cracked media’, *Journal of the Mechanics and Physics of Solids* **43**(12), 1919–1951.
- Chaboche, J., Kruch, S., Maire, J. & Pottier, T. (2001), ‘Towards a micromechanics based inelastic and damage modeling of composites’, *International Journal of Plasticity* **17**(4), 411–439.
- Chen, D., Shen, W. Q., Shao, J. F. & Yurtdas, I. (2013), ‘Micromechanical modeling of mortar as a matrix-inclusion composite with drying effects’, *International Journal for Numerical and Analytical Methods in Geomechanics* **37**(9), 1034–1047.
- Chen, W.-F. (2007), *Plasticity in Reinforced Concrete*, J. Ross Publishing, New York.
- Clear, C. A. (1985), ‘The effects of autogenous healing upon the leakage of water through cracks in concrete’.
- Counto, U. J. (1964), ‘The effect of the elastic modulus of the aggregate on the elastic modulus, creep and creep recovery of concrete’, *Magazine of Concrete Research* **16**(48), 129–138.

- Darabi, M. K., Abu Al-Rub, R. K. & Little, D. N. (2012), 'A continuum damage mechanics framework for modeling micro-damage healing', *International Journal of Solids and Structures* **49**(3-4), 492–513.
- Darabi, M. K., Abu Al-Rub, R. K., Masad, E. A. & Little, D. N. (2013), 'Constitutive modeling of fatigue damage response of asphalt concrete materials with consideration of micro-damage healing', *International Journal of Solids and Structures* **50**(19), 2901–2913.
- Davies, R. E. & Jefferson, A. D. (2012), The simulation of time dependent behaviour of cement bound materials with a micro-mechanical model, in '1st International Conference on Numerical Modelling Strategies for Sustainable Concrete', SSCS, Aix en Provence, France.
- Davies, R. E. & Jefferson, A. D. (2013), The simulation of inelastic strains and fracture in a two-phase composite using a micromechanical model, in 'International Conference on Computational Mechanics (CM13)', ACME, Durham, UK.
- de Borst, R. (2002), 'Fracture in quasi-brittle materials: a review of continuum damage-based approaches', *Engineering Fracture Mechanics* **69**(2), 95–112.
- de Borst, R. & Guitiérrez, M. A. (1999), 'A unified framework for concrete damage and fracture models including size effects', *International Journal of Fracture* **95**(1-4), 261–277.
- de Rooij, M. R., Van Tittelboom, K., De Belie, N. & Schlangen, E. (2013), *Self-Healing Phenomena in Cement-Based Materials: State-of-the-Art Report of RILEM Technical Committee 221-SHC: Self-Healing Phenomena in Cement-Based Materials*, Springer, Bagneux, France.
- De Schutter, G. (2002), 'Finite element simulation of thermal cracking in massive hardening concrete elements using degree of hydration based material laws', *Computers & Structures* **80**(27-30), 2035–2042.
- Desmorat, R., Gatuingt, F. & Ragueneau, F. (2007), 'Nonlocal anisotropic damage model and related computational aspects for quasi-brittle materials', *Engineering Fracture Mechanics* **74**(10), 1539–1560.
- Desrumaux, F., Meraghni, F. & Benzeggagh, M. L. (2001), 'Generalised moritanaka scheme to model anisotropic damage using numerical eshelby tensor', *Journal of Composite Materials* **35**(7), 603–624.
- Dry, C. (1994), 'Matrix cracking repair and filling using active and passive modes for smart timed release of chemicals from fibers into cement matrices', *Smart Materials and Structures* **3**(2), 118–123.
- Dry, C. (2000), 'Three designs for the internal release of sealants, adhesives, and waterproofing chemicals into concrete to reduce permeability', *Cement and Concrete Research* **30**(12), 1969–1977.
- Dunn, M. L. & Ledbetter, H. (1997), 'Elastic-plastic behavior of textured short-fiber composites', *Acta materialia* **45**(8), 3327–3340.

- Dunn, S. C. (2011), A Novel Self-Healing Shape Memory Polymer-Cementitious System, PhD thesis, Cardiff University.
- Dutra, V. F., Maghous, S. et al. (2010), 'A micromechanical approach to elastic and viscoelastic properties of fiber reinforced concrete', *Cement and Concrete Research* **40**(3).
- Dvorak, G. J. (1992a), 'Transformation field analysis of inelastic composite materials', *Proceedings of the Royal Society of London. Series A: Mathematical and Physical Sciences* **437**(1900), 311.
- Dvorak, G. J. (1992b), 'Transformation field analysis of inelastic composite materials', *Proceedings of the Royal Society of London. Series A: Mathematical and Physical Sciences* **437**(1900), 311.
- Edvardsen, C. (1999), 'Water permeability and autogenous healing of cracks in concrete', *ACI Materials Journal-American Concrete Institute* **96**(4), 448–454.
- EN 1990 (2002), *Base Eurocode : Basis of structural design*, BSi, London.
- EN 1992 (2008), *Eurocode 2 : Design of concrete structures*, BSi, London.
- England, G. L. (1965), Method of estimating creep and shrinkage strains in concrete from properties of constituent materials, in 'ACI Journal Proceedings', Vol. 62, pp. 1411–1420.
- Eshelby, J. D. (1957), 'The determination of the elastic field of an ellipsoidal inclusion, and related problems', *Proceedings of the Royal Society of London. Series A, Mathematical and Physical Sciences* **241**(1226), 376–396.
- Eshelby, J. D. (1959), 'The elastic field outside an ellipsoidal inclusion', *Proceedings of the Royal Society of London. Series A, Mathematical and Physical Sciences* p. 561–569. 00930.
- Fan, S. & Li, M. (2013), Characterization of distributed damage and self-healing in cementitious materials based on time-dependent 3-d x-ray computed microtomography (micro-CT), in '4th International Conference of Self-Healing Materials', ICSHM2013, Ghent University; Delft University of Technology, Ghent.
- Feenstra, P. & de Borst, R. (1995), 'A plasticity model and algorithm for mode-I cracking in concrete', *International Journal for Numerical Methods in Engineering* **38**(15), 2509–2529.
- Ferretti, E. (2004), 'A discussion of strain-softening in concrete', *International Journal of Fracture* **126**(1), L3–L10.
- fib (2013), *CEB-FIP Model Code for Concrete Structures 2010*, John Wiley & Sons, Lausanne, Switzerland.
- Fichant, S., La Borderie, C. & Pijaudier-Cabot, G. (1999), 'Isotropic and anisotropic descriptions of damage in concrete structures', *Mechanics of Cohesive-frictional Materials* **4**(4), 339–359.

- Gambarotta, L. (2004), 'Friction-damage coupled model for brittle materials', *Engineering fracture mechanics* **71**(4-6), 829–836.
- Gardner, D., Jefferson, A., Hoffman, A. & Lark, R. (2014), 'Simulation of the capillary flow of an autonomic healing agent in discrete cracks in cementitious materials', *Cement and Concrete Research* **58**, 35–44.
- Gawin, D., Pesavento, F. & Schrefler, B. A. (2008), 'Modeling of cementitious materials exposed to isothermal calcium leaching, considering process kinetics and advective water flow. part 1: Theoretical model', *International Journal of Solids and Structures* **45**(25–26), 6221–6240.
- Ghosh, S. K. (2009), *Self-Healing Materials: Fundamentals, Design Strategies, and Applications*, Wiley Online Library, Weinheim.
- Giry, C., Dufour, F. & Mazars, J. (2011), 'Stress-based nonlocal damage model', *International Journal of Solids and Structures* **48**(25–26), 3431–3443.
- Glanville, W. H. (1931), *The permeability of Portland cement concrete*, Vol. Technical paper 3, Building Research, Watford.
- Granger, S., Loukili, A., Pijaudier-Cabot, G. & Chanvillard, G. (2005), Mechanical characterization of the self-healing effect of cracks in ultra high performance concrete (UHPC), in 'Proceedings Third International Conference on Construction Materials, Performance, Innovations and Structural Implications, ConMat', Vol. 5, p. 22–24.
- Granger, S., Loukili, A., Pijaudier-Cabot, G. & Chanvillard, G. (2007a), 'Experimental characterization of the self-healing of cracks in an ultra high performance cementitious material: Mechanical tests and acoustic emission analysis', *Cement and Concrete Research* **37**(4), 519–527.
- Granger, S., Pijaudier-Cabot, G. & Loukili, A. (2007b), 'Mechanical behavior of self-healed ultra high performance concrete: from experimental evidence to modeling', in *Proc. FRAMCOS* **6**.
- Grassl, P. & Jirásek, M. (2006), 'Damage-plastic model for concrete failure', *International journal of solids and structures* **43**(22), 7166–7196.
- Grassl, P., Lundgren, K. & Gylltoft, K. (2002), 'Concrete in compression: a plasticity theory with a novel hardening law', *International Journal of Solids and Structures* **39**(20), 5205–5223.
- Han, D. J. & Chen, W.-F. (1985), 'A nonuniform hardening plasticity model for concrete materials', *Mechanics of materials* **4**(3), 283–302.
- Hannant, D. & Keer, J. (1983), 'Autogenous healing of thin cement based sheets', *Cement and Concrete Research* **13**(3), 357–365.
- Hashin, Z. & Shtrikman, S. (1963), 'A variational approach to the theory of the elastic behaviour of multiphase materials', *Journal of the Mechanics and Physics of Solids* **11**(2), 127–140. 03065.

- Hearn, N. (1998), 'Self-sealing, autogenous healing and continued hydration: What is the difference?', *Materials and Structures* **31**(8), 563–567.
- Hearn, N. (1999), 'Effect of shrinkage and load-induced cracking on water permeability of concrete', *ACI Materials Journal* **96**(2), 234–242.
- Hill, R. (1963), 'Elastic properties of reinforced solids: some theoretical principles', **11**(5), 357–372.
- Hill, R. (1965), 'Continuum micro-mechanics of elastoplastic polycrystals', *Journal of the Mechanics and Physics of Solids* **13**(2), 89–101.
- Hilloulin, B., Grondin, F., Matallah, M. & Loukili, A. (2013), Numerical modelling of autogenous healing and recovery of mechanical properties in ultra-high performance concrete, in 'Proceedings of the 4th International Conference on Self-Healing Materials', Ghent, Belgium.
- Hirsch, T. J. (1962), Modulus of elasticity of concrete affected by elastic moduli of cement paste matrix and aggregate, in 'ACI Journal Proceedings', Vol. 59 of 3, pp. 427–451.
- Homma, D., Mihashi, H. & Nishiwaki, T. (2009), 'Self-healing capability of fibre reinforced cementitious composites', *Journal of Advanced Concrete Technology* **7**(2), 217–228.
- Hua, C., Acker, P. & Ehlacher, A. (1995), 'Analyses and models of the autogenous shrinkage of hardening cement paste: I. modelling at macroscopic scale', *Cement and Concrete Research* **25**(7), 1457–1468.
- Huang, H. & Ye, G. (2012), 'Simulation of self-healing by further hydration in cementitious materials', *Cement and Concrete Composites* **34**(4), 460–467.
- Igarashi, S., Kunieda, M. & Nishiwaki, T. (2009), 'Technical committee on autogenous healing in cementitious materials JCI-TC075B'.
- Isaacs, B., Lark, R., Jefferson, T., Davies, R. & Dunn, S. (2013), 'Crack healing of cementitious materials using shrinkable polymer tendons', *Structural Concrete* **14**(2), 138–147.
- Jacobsen, S., Marchand, J. & Hornain, H. (1995), 'SEM observations of the microstructure of frost deteriorated and self-healed concretes', *Cement and Concrete Research* **25**(8), 1781–1790.
- Jacobsen, S. & Sellevold, E. J. (1996), 'Self healing of high strength concrete after deterioration by freeze/thaw', *Cement and Concrete Research* **26**(1), 55–62.
- Jefferson, A. & Bennett, T. (2010), 'A model for cementitious composite materials based on micro-mechanical solutions and damage-contact theory', *Computers & Structures* **88**(23-24), 1361–1366.
- Jefferson, A. D. (2003), 'Craft- a plastic-damage-contact model for concrete. i. model theory and thermodynamic considerations', *International Journal of Solids and Structures* **40**, 5973–5999.

- Jefferson, A. D. (2010), Finite element material models for concrete, in 'Proceedings of The Tenth International Conference on Computational Structures Technology', Valencia.
- Jefferson, A. D. & Bennett, T. (2007), 'Micro-mechanical damage and rough crack closure in cementitious composite materials', *International Journal for Numerical and Analytical Methods in Geomechanics* **31**(2), 133–146.
- Jefferson, A. D., Joseph, C., Lark, R., Isaacs, B., Dunn, S. & Weager, B. (2010), 'A new system for crack closure of cementitious materials using shrinkable polymers', *Cement and Concrete Research* **40**(5), 795–801.
- Jendele, L., Cervenka, J., Saouma, V. & Pukl, R. (2001), On the choice between discrete or smeared approach in practical structural FE analyses of concrete structures, in '4th International Conference on Analysis of Discontinuous Deformation Glasgow, Scotland UK'.
- Jennings, H. M. & Bullard, J. W. (2011), 'From electrons to infrastructure: Engineering concrete from the bottom up', *Cement and Concrete Research* **41**(7), 727–735.
- Jiang, Q., Sun, G., Zhang, Y. & Liu, Z. (2012), 'Observation of microstructure formation process of cement paste using non-destructive methods', *Magazine of Concrete Research* **64**(11), 957–965.
- Jirásek, M. & Havlásek, P. (2014), 'Microprestress–solidification theory of concrete creep: Reformulation and improvement', *Cement and Concrete Research* **60**, 51–62.
- Jonkers, H. M., Thijssen, A., Muyzer, G., Copuroglu, O. & Schlangen, E. (2010), 'Application of bacteria as self-healing agent for the development of sustainable concrete', *Ecological Engineering* **36**(2), 230–235.
- Joseph, C. (2008), Experimental and numerical study of the fracture and self-healing of cementitious materials, PhD, Cardiff University.
- Joseph, C., Jefferson, A. D., Isaacs, B., Lark, R. & Gardner, D. (2010), 'Experimental investigation of adhesive-based self-healing of cementitious materials', *Magazine of Concrete Research* **62**(11), 831–843.
- Ju, J. & Sun, L. (2001), 'Effective elastoplastic behavior of metal matrix composites containing randomly located aligned spheroidal inhomogeneities. part i: micromechanics-based formulation', *International Journal of Solids and Structures* **38**(2), 183–201.
- Ju, J. W. & Sun, L. Z. (1999), 'A novel formulation for the exterior-point eshelby's tensor of an ellipsoidal inclusion', *Journal of Applied Mechanics* **66**(2), 570–574.
- Kachanov, L. M. (1999), 'Rupture time under creep conditions', *International Journal of Fracture* **97**(1-4), 11–18.
- Kachanov, M. L. (1982), 'A microcrack model of rock inelasticity part i: Frictional sliding on microcracks', *Mechanics of Materials* **1**(1), 19–27.

- Karpov, E. G., Grankin, M. V., Liu, M. & Ariyan, M. (2012), 'Characterization of precipitative self-healing materials by mechanokinetic modeling approach', *Journal of the Mechanics and Physics of Solids* **60**(2), 250–260.
- Krajcinovic, D. (2000), 'Damage mechanics: accomplishments, trends and needs', *International Journal of Solids and Structures* **37**(1–2), 267–277.
- Landis, E. N., Nagy, E. N. & Keane, D. T. (2003), 'Microstructure and fracture in three dimensions', *Engineering Fracture Mechanics* **70**, 911–925.
- Laws, N. (1973), 'On the thermostatics of composite materials', *Journal of the Mechanics and Physics of Solids* **21**(1), 9–17.
- Laws, N. & McLaughlin, R. (1978), 'Self-Consistent estimates for the viscoelastic creep compliances of composite materials', *Proceedings of the Royal Society of London. Series A, Mathematical and Physical Sciences* **359**(1697), 251–273.
- Lee, H. K. & Ju, J. W. (2007), 'A three-dimensional stress analysis of a penny-shaped crack interacting with a spherical inclusion', *International Journal of Damage Mechanics* **16**(3), 331–359.
- Lee, J. & Fenves, G. (1998), 'Plastic-damage model for cyclic loading of concrete structures', *Journal of Engineering Mechanics* **124**(8), 892–900.
- Leukart, M. & Ramm, E. (2003), 'A comparison of damage models formulated on different material scales', *Computational Materials Science* **28**(3–4), 749–762.
- Leukart, M. & Ramm, E. (2006), 'Identification and interpretation of microplane material laws', *Journal of Engineering Mechanics* **132**(3), 295–305.
- Li, S., Sauer, R. A. & Wang, G. (2007), 'The Eshelby Tensors in a Finite Spherical Domain—Part I: Theoretical Formulations', **74**(4), 770–783.
- Li, V. C., Lim, Y. M. & Chan, Y.-W. (1998), 'Feasibility study of a passive smart self-healing cementitious composite', *Composites Part B: Engineering* **29**(6), 819–827.
- Li, V. C. & Yang, E.-H. (2008), Self healing in concrete materials, in 'Self Healing Materials', Springer, p. 161–193.
- Low, S. R. (2001), *Rockwell Hardness Measurement of Metallic Materials*, Vol. NIST Recommended Practice Guide Special Publication 960-5, National Institute of Standards and Technology, Washington.
- LUSAS (2012), 'LUSAS solver reference manual', <http://www.lusas.com> [Accessed: 18 October 2013]. 14.7 Issue 1.
- Mainguy, M., Coussy, O. & Baroghel-Bouny, V. (2001), 'Role of air pressure in drying of weakly permeable materials', *Journal of Engineering mechanics* **127**(6), 582–592.

- Malzbender, J., den Toonder, J., Balkenende, A. & de With, G. (2002), 'Measuring mechanical properties of coatings: a methodology applied to nano-particle-filled sol-gel coatings on glass', *Materials Science and Engineering: R: Reports* **36**(2-3), 47-103.
- Mathcad (2010), 'Mathcad help manual', <http://www.ptc.com/product/mathcad> [Accessed: 18 October 2013]. Version 15.0.
- Mazars, J. (1986), 'A description of micro- and macroscale damage of concrete structures', *Engineering Fracture Mechanics* **25**(5-6), 729-737.
- Mergheim, J. & Steinmann, P. (2013a), Macroscopic modelling of self-healing thermoset materials, in 'Proceedings of the 4th International Conference on Self-Healing Materials', Ghent, Belgium.
- Mergheim, J. & Steinmann, P. (2013b), 'Phenomenological modelling of self-healing polymers based on integrated healing agents', *Computational Mechanics* **52**(3), 681-692.
- Miao, S., Wang, M. & Schreyer, H. (1995), 'Constitutive models for healing of materials with application to compaction of crushed rock salt', *Journal of Engineering Mechanics* **121**(10), 1122-1129.
- Mihai, I. C. & Jefferson, A. D. (2011), 'A material model for cementitious composite materials with an exterior point eshelby microcrack initiation criterion', *International Journal of Solids and Structures* **48**, 3312-3325.
- Monchiet, V., Gruescu, C., Cazacu, O. & Kondo, D. (2012), 'A micromechanical approach of crack-induced damage in orthotropic media: application to a brittle matrix composite', *Engineering Fracture Mechanics* **83**, 40-53.
- Mondal, P. (2008), Nanomechanical properties of cementitious materials, PhD thesis, Northwestern University.
- Mondal, P., Shah, S. P. & Marks, L. (2007), 'A reliable technique to determine the local mechanical properties at the nanoscale for cementitious materials', *Cement and Concrete Research* **37**(10), 1440-1444.
- Mor, A., Monteiro, P. J. & Hester, W. T. (1989), 'Observations of healing of cracks in high-strength lightweight concrete', *Cement, concrete and aggregates* **11**(2), 121-125.
- Mori, T. & Tanaka, K. (1973), 'Average stress in matrix and average elastic energy of materials with misfitting inclusions', *Acta Metallurgica* **21**(5), 571-574.
- Mosley, W. H., Bungey, J. H. & Hulse, R. (2012), *Reinforced concrete design: to Eurocode 2*, Palgrave Macmillan, Basingstoke; New York.
- Mounanga, P., Cherkaoui, K., Khelidj, A., Courtial, M., Noirfontaine, M.-N. d. & Dunstetter, F. (2012), 'Extrudable reactive powder concretes: hydration, shrinkage and transfer properties', *European Journal of Environmental and Civil Engineering* **16**(sup1), s99-s114.

- Mura, T. (1987), *Micromechanics of defects in solids*, 2nd, rev. ed. edn, M. Nijhoff Distributors for the U.S. and Canada Kluwer Academic Publishers, Dordrecht Netherlands; Boston; Hingham MA USA.
- Nemat-Nasser, S. & Hori, M. (1999), *Micromechanics: overall properties of heterogeneous materials*, Elsevier, Amsterdam; New York.
- Neville, A. M. & Brooks, J. J. (2010), *Concrete Technology*, 2 edn, Prentice Hall, London.
- Neville, A. M., Dilger, W. H. & Brooks, J. J. (1983), *Creep of plain and structural concrete*, Construction Press, London; New York.
- Ngo, D. & Scordelis, A. C. (1967), Finite element analysis of reinforced concrete beams, in 'ACI Journal Proceedings', Vol. 64, pp. 152–163.
- Nguyen, G. & Korsunsky, A. (2008), 'Development of an approach to constitutive modelling of concrete: Isotropic damage coupled with plasticity', *International Journal of Solids and Structures* **45**(20), 5483–5501.
- Oden, J. T., Belytschko, T., Babuska, I. & Hughes, T. J. R. (2003), 'Research directions in computational mechanics', *Computer Methods in Applied Mechanics and Engineering* **192**(7-8), 913–922.
- ONS (2014), 'Construction statistics reference table 2.8 - no. 14, 2013 edition', <http://www.ons.gov.uk> [Accessed: 1 August 2014].
- Parks, J., Edwards, M., Vikesland, P. & Dudi, A. (2010), 'Effects of bulk water chemistry on autogenous healing of concrete', *Journal of Materials in Civil Engineering* **22**(5), 515–524.
- Pavlina, E. J. & Van Tyne, C. J. (2008), 'Correlation of yield strength and tensile strength with hardness for steels', **17**(6), 888–893.
- Pensee, V. & Kondo, D. (2003), 'Micromechanics of anisotropic brittle damage: comparative analysis between a stress based and a strain based formulation', *Mechanics of materials* **35**(8), 747–761.
- Pensée, V., Kondo, D. & Dormieux, L. (2002), 'Micromechanical analysis of anisotropic damage in brittle materials', *Journal of Engineering Mechanics* **128**(8), 889–897.
- Perelmuter, M. (2013), Bridged crack approach to model materials self-healing, in 'Proceedings of the 4th International Conference on Self-Healing Materials', Ghent, Belgium.
- Pichler, B. & Dormieux, L. (2010a), 'Cracking risk of partially saturated porous media-part i: Microporoelasticity model', *International Journal for Numerical and Analytical Methods in Geomechanics* **34**(2), 135–157.
- Pichler, B. & Dormieux, L. (2010b), 'Cracking risk of partially saturated porous media-part II: application to drying shrinkage', *International Journal for Numerical and Analytical Methods in Geomechanics* **34**(2), 159–186.

- Pichler, B. & Hellmich, C. (2011), 'Upscaling quasi-brittle strength of cement paste and mortar: A multi-scale engineering mechanics model', *Cement and Concrete Research* **41**(5), 247–476.
- Pichler, B., Hellmich, C. & A. Mang, H. (2007), 'A combined fracture micromechanics model for tensile strain softening in brittle materials, based on propagation of interacting microcracks', *International Journal for Numerical and Analytical Methods in Geomechanics* **31**(2), 111–132.
- Pichler, B., Hellmich, C., Eberhardsteiner, J., Wasserbauer, J., Termkhajornkit, P., Barbarulo, R. & Chanvillard, G. (2013), 'Effect of gel–space ratio and microstructure on strength of hydrating cementitious materials: An engineering micromechanics approach', *Cement and Concrete Research* **45**, 55–68.
- Pichler, B., Hellmich, C. et al. (2010), 'Estimation of influence tensors for eigenstressed multiphase elastic media with nonaligned inclusion phases of arbitrary ellipsoidal shape', *Journal of Engineering Mechanics* **136**, 1043–1053.
- Pichler, C. & Lackner, R. (2008), 'A multiscale creep model as basis for simulation of early-age concrete behavior', *Computers and Concrete* **5**(4), 295–328.
- Pichler, C. & Lackner, R. (2009), 'Upscaling of viscoelastic properties of highly-filled composites: Investigation of matrix-inclusion-type morphologies with power-law viscoelastic material response', *Composites Science and Technology* **69**(14), 2410–2420.
- Pichler, C., Lackner, R. & Mang, H. A. (2007), 'A multiscale micromechanics model for the autogenous-shrinkage deformation of early-age cement-based materials', *Engineering fracture mechanics* **74**(1-2), 34–58.
- Pickett, G. (1956), Effect of aggregate on shrinkage of concrete and a hypothesis concerning shrinkage, in 'ACI Journal Proceedings', Vol. 52, pp. 581–590.
- Prado, E. P. & Van Mier, J. G. M. (2003), 'Effect of particle structure on mode I fracture process in concrete', *Engineering fracture mechanics* **70**(14), 1793–1807.
- Rashid, Y. R. (1968), 'Ultimate strength analysis of prestressed concrete pressure vessels', *Nuclear Engineering and Design* **7**(4), 334–344.
- Reinhardt, H.-W. & Jooss, M. (2003), 'Permeability and self-healing of cracked concrete as a function of temperature and crack width', *Cement and Concrete Research* **33**(7), 981–985.
- Remmers, J. J. & de Borst, R. (2008), Numerical modelling of self healing mechanisms, in 'Self Healing Materials', Springer, p. 365–380.
- Richardson, M. G. (2002), *Fundamentals of durable reinforced concrete (Modern Concrete Technology)*, Spon Press, London.
- Saiidi, M., Sadrossadat-Zadeh, M., Ayoub, C. & Itani, A. (2007), 'Pilot study of behavior of concrete beams reinforced with shape memory alloys', *Journal of Materials in Civil Engineering* **19**(6), 454–461.

- Sanahuja, J. (2013), 'Effective behaviour of ageing linear viscoelastic composites: Homogenization approach', *International Journal of Solids and Structures* **50**(19), 2846–2856.
- Sanahuja, J. & Dormieux, L. (2010), 'Creep of a CSH gel: a micromechanical approach', *Anais da Academia Brasileira de Ciências* **82**, 25–41.
- Sanahuja, J., Dormieux, L. & Chanvillard, G. (2007), 'Modelling elasticity of a hydrating cement paste', *Cement and Concrete Research* **37**(10), 1427–1439.
- Scheiner, S., Hellmich, C. et al. (2009), 'Continuum microviscoelasticity model for aging basic creep of early-age concrete', *Journal of Engineering Mechanics* **135**(4), 307–323.
- Schimmel, E. C. & Remmers, J. J. C. (2006), 'Development of a constitutive model for self-healing materials', [http://repository.tudelft.nl/assets/uuid:6ad6ebfd-aa1c-46f1-a9d5-c17109b8a423/Schimmel\\_2006.pdf](http://repository.tudelft.nl/assets/uuid:6ad6ebfd-aa1c-46f1-a9d5-c17109b8a423/Schimmel_2006.pdf) [Accessed: 11 September 2014]. Delft Aerospace Computational Science, Report DACS-06-003.
- Schindler, A. K. & Folliard, K. J. (2005), 'Heat of hydration models for cementitious materials', *ACI materials journal* **102**(1), 24–33.
- Schlangen, E., Ter Heide, N. & Van Breugel, K. (2006), Crack healing of early age cracks in concrete, in 'ECF16', Alexandroupolis, Greece.
- Siddiqi, Z. A. (2009), *Concrete structures*, Help Civil Engineering Publisher, Lahore, Pakistan.
- Simo, J. C. & Ju, J. W. (1987), 'Strain- and stress-based continuum damage models—I. formulation', *International Journal of Solids and Structures* **23**(7), 821–840.
- Snoeck, D., Tittelboom, K. V., Steuperaert, S., Dubruel, P. & Belie, N. D. (2012), 'Self-healing cementitious materials by the combination of microfibres and superabsorbent polymers', *Journal of Intelligent Material Systems and Structures* **0**(0), 1–12.
- Soroker, V. J. & Denson, A. J. (1926), 'Autogenous healing of concrete', *Zement* **25**.
- Stroud, A. (1972), *Approximate Calculation of Multiple Integrals*, Prentice Hall, Englewood Cliffs, N.J.
- Stutzman, P. E. (2000), 'Scanning electron microscopy in concrete petrography', *Materials Science of Concrete Special Volume: Calcium Hydroxide in Concrete, Proceedings-Anna Maria Island-FL* p. 59–72.
- Sun, C., Saffari, P., Ranade, R., Sadeghipour, K. & Baran, G. (2007), 'Finite element analysis of elastic property bounds of a composite with randomly distributed particles', *Composites Part A: Applied Science and Manufacturing* **38**(1), 80–86.

- Tandon, G. P. & Weng, G. J. (1988), 'A theory of particle-reinforced plasticity', *Journal of applied mechanics* **55**, 126–134.
- Taqiuddin, Z., Voyiadjis, G. & Almasri, A. (2012), 'Formulation and verification of a concrete model with strong coupling between isotropic damage and elastoplasticity and comparison to a weak coupling model', *Journal of Engineering Mechanics* **138**(5), 530–541.
- Taylor, G. (1938), 'Plastic strain in metals', *Journal of the Institute of Metals* **62**, 307–324.
- Ter Heide, N. (2005), Crack healing in hydrating concrete, PhD thesis, TU Delft: MSc-thesis.
- Ter Heide, N. & Schlangen, E. (2007), Selfhealing of early age cracks in concrete, in 'Proceedings of the First international conference on Self Healing Materials'.
- Thomas, J. J. & Jennings, H. M. (2006), 'A colloidal interpretation of chemical aging of the c-s-h gel and its effects on the properties of cement paste', *Cement and Concrete Research* **36**(1), 30–38.
- Ulm, F.-J., Zhang, Q., Termkhajornkit, P., Roy, R. L., Gartner, E., Vandamme, M. & Zuber, B. (2013), Creep properties of cementitious materials from indentation testing: Significance, influence of relative humidity, and analogy between c-s-h and soils, in 'Mechanics and Physics of Creep, Shrinkage, and Durability of Concrete', American Society of Civil Engineers, pp. 48–61.
- USGS (2014), 'U.S. geological survey, mineral commodity summaries', <http://minerals.usgs.gov/minerals/pubs/commodity/cement> [Accessed: 1 August 2014].
- Van Breugel, K. (2007), 'Is there a market for self-healing cement-based materials?', in '1st International Conference on Self-healing Materials, Noordwijk, Holland', ICSHM2007, Noordwijk aan Zee, Netherlands.
- van Breugel, K. (2011), 'Structural systems for protection against extreme events', *Structural Concrete* **12**(1), 5–12.
- van Mier, J. G. M. (1997), *Fracture processes of concrete: Assessment of material parameters for fracture models*, CRC Press, Boca Raton.
- Van Tittelboom, K. & De Belie, N. (2013), 'Self-healing in cementitious materials—a review', *Materials* **6**(6), 2182–2217.
- Van Tittelboom, K., De Belie, N., De Muynck, W. & Verstraete, W. (2010), 'Use of bacteria to repair cracks in concrete', *Cement and Concrete Research* **40**(1), 157–166.
- Van Tittelboom, K., De Belie, N., Van Loo, D. & Jacobs, P. (2011), 'Self-healing efficiency of cementitious materials containing tubular capsules filled with healing agent', *Cement and Concrete Composites* **33**(4), 497–505.

- Van Tittelboom, K., Gruyaert, E., Rahier, H. & De Belie, N. (2012), 'Influence of mix composition on the extent of autogenous crack healing by continued hydration or calcium carbonate formation', *Construction and Building Materials* **37**, 349–359.
- Vliet, K. J. V., Pinson, M. B., Thomas, J. J., Bonnaud, P. A., Pellenq, R. J.-M., Strekalova, E. G., Masoero, E., Bažant, M. Z., Ji, Q., Manzano, H., Ulm, F.-J. & Jennings, H. M. (2013), Water isotherms, shrinkage and creep of cement paste: Hypotheses, models and experiments, *in* 'Mechanics and Physics of Creep, Shrinkage, and Durability of Concrete', American Society of Civil Engineers, pp. 134–141.
- Voyiadjis, G. Z. & Kattan, P. I. (2006), *Advances in damage mechanics metals and metal matrix composites with an introduction to fabric tensors*, Elsevier, Amsterdam; Boston; London.
- Voyiadjis, G. Z., Shojaei, A. & Li, G. (2011), 'A thermodynamic consistent damage and healing model for self healing materials', *International Journal of Plasticity* **27**(7), 1025–1044.
- Walraven, J. C. & Reinhardt, H. W. (1981), 'Concrete mechanics. part a: Theory and experiments on the mechanical behavior of cracks in plain and reinforced concrete subjected to shear loading', *NASA STI/Recon Technical Report N 82*.
- Weng, G. J. (1988), 'Theoretical principles for the determination of two kinds of composite plasticity- inclusions plastic vs. matrix plastic', *Mechanics of composite materials* pp. 193–208.
- White, S. R., Sottos, N. R., Geubelle, P. H., Moore, J. S., Kessler, M. R., Sriram, S. R., Brown, E. N. & Viswanathan, S. (2001), 'Autonomic healing of polymer composites', *Nature* **409**(6822), 794–797.
- Willam, K. J. & Warnke, E. P. (1975), Constitutive models for triaxial behaviour of concrete, *in* 'Proceedings of the International Association of Bridge Structural Engineering', Vol. 19, Zurich, Switzerland, pp. 1–30.
- Willam, K., Pramono, E. & Sture, S. (1989), Fundamental issues of smeared crack models, *in* S. P. Shah & S. E. Swartz, eds, 'Fracture of Concrete and Rock', Springer New York, pp. 142–157.
- Wilson Instruments (2004), *Fundamentals of Rockwell Hardness Testing - document WB1226*, Wilson Instruments, An Instron Company, Norwood, MA 02062-2643 USA.
- Windslow, D. (1981), 'A rockwell hardness test for portland cement concrete'. Joint Highway Research Project, Indiana Department of Transportation and Purdue University, Publication FHWA/IN/ JHRP-81/12.
- Wu, M., Johannesson, B. & Geiker, M. (2012), 'A review: Self-healing in cementitious materials and engineered cementitious composite as a self-healing material', *Construction and Building Materials* **28**(1), 571–583.

- Xi, Y. & Jennings, H. M. (1997), 'Shrinkage of cement paste and concrete modelled by a multiscale effective homogeneous theory', *Materials and Structures* **30**(6), 329–339.
- Yang, T., Keller, B., Magyari, E., Hametner, K. & Günther, D. (2003), 'Direct observation of the carbonation process on the surface of calcium hydroxide crystals in hardened cement paste using an atomic force microscope', *Journal of Materials Science* **38**(9), 1909–1916.
- Ye, G. & van Breugel, K. (2007), Potential use of HYMOSTRUC cement hydration model for self-healing of microcracks in cementitious materials, in 'Proceedings of the First International Conference on Self Healing Materials', Noordwijk aan Zee, The Netherlands.
- Yi, S. T., Kim, J. K. & Oh, T. K. (2003), 'Effect of strength and age on the stress-strain curves of concrete specimens', *Cement and Concrete Research* **33**(8), 1235–1244.
- Zaoui, A. (2002), 'Continuum micromechanics: survey', *Journal of Engineering Mechanics* **128**(8), 808–816.
- Zhang, J., Hou, D. & Han, Y. (2012), 'Micromechanical modeling on autogenous and drying shrinkages of concrete', *Construction and Building Materials* **29**, 230–240.
- Zhang, Y., Pichler, C., Yuan, Y., Zeiml, M. & Lackner, R. (2013), 'Micromechanics-based multifield framework for early-age concrete', *Engineering Structures* **47**, 16–24.
- Zhong, W. & Yao, W. (2008), 'Influence of damage degree on self-healing of concrete', *Construction and Building Materials* **22**(6), 1137–1142.
- Zhu, Q. Z., Kondo, D. & Shao, J. F. (2008), 'Micromechanical analysis of coupling between anisotropic damage and friction in quasi brittle materials: role of the homogenization scheme', *International Journal of Solids and Structures* **45**(5), 1385–1405.
- Zhu, Q. Z., Kondo, D. & Shao, J. F. (2009), 'Homogenization-based analysis of anisotropic damage in brittle materials with unilateral effect and interactions between microcracks', *International Journal for Numerical and Analytical Methods in Geomechanics* **33**(6), 749–772.
- Zhu, Q. Z., Shao, J. F. & Kondo, D. (2011), 'A micromechanics-based thermodynamic formulation of isotropic damage with unilateral and friction effects', *European Journal of Mechanics-A/Solids* **30**(3), 316–325.